THESE DE DOCTORAT

NANTES UNIVERSITE

ECOLE DOCTORALE N° 602
Sciences de l'Ingénierie et des Systèmes
Spécialité : *Energétique – Thermique - Combustion*

Par

Ahmad FAWAZ

Optimisation topologique basée sur la méthode de densité des échangeurs de chaleur à plaques

Thèse présentée et soutenue à Nantes, le 04/11/2024
Unité de recherche : Laboratoire de thermique et Energie de Nantes (CNRS UMR 6607)

Rapporteurs avant soutenance :

Qiuwang WANG	Professor, KLTFSE, Xi'an Jiaotong University
Raphael BOICHOT	Maître de conférences (HDR), Grenoble INP, SIMAP UMR 5266

Composition du Jury :

Président :	Lounès TADRIST	Professeur des universités, IUSTI, Aix-Marseille Université
Examinateurs :	Alain BASTIDE	Professeur des universités, PIMENT, Université de La Réunion
	Yilin FAN	Chargé de recherche (HDR), CNRS, LTeN, Nantes Université
Directrice de thèse :	Lingai LUO	Directrice de recherche, CNRS, LTeN, Nantes Université
Co-directeur de thèse :	Steven LE CORRE	Professeur des universités, LTeN, Nantes Université
Co-encadrant de thèse :	Yuchao HUA	Chercheur, LTeN, Nantes Université

CONTENT

ACKNOWLEDGEMENTS

First, I would like to thank my supervisors Steven Le Corre, Lingai Luo, Yuchao Hua and Yilin Fan for their support, guidance and encouragement throughout my Ph.D. journey. Their critical feedback and suggestions have been indispensable in helping me navigate the challenges of my research.

I would like to extend my thanks to the members of my thesis committee, Qiuwang Wang, Raphael Boichot, Lounès Tadrist and Alain Bastide, for their valuable, constructive feedback and suggestions, which has significantly enhanced the quality of my thesis.

I would also like to express my deep appreciation to the staff, faculty, and laboratory services of LTeN for providing me with essential resources, including computational tools, experimental equipment, and measurement platforms. Their unwavering support and encouragement have been instrumental in enabling me to pursue my research and overcome the challenges of my PhD journey.

I would like to acknowledge the valuable contributions of my research participants Gwenael Biotteau, Julien Aubril, and Stephane Roux, whose willingness to share their experiences and insights has been crucial to the success of the experimental work of my research. I am also deeply grateful to all my colleagues, particularly Mosbah Kiwan, Ziad Maksassi, Adrien Le Reun, Matthis Baltazar, Rafic Nader, Sourour Traouli, Elia Missi, Rita Moussallem, Jean Daoud, Baoshan Xie, Madi Halidi, and Antonio Della Volpe, who have provided me with professional suggestions in the practice of presentation, and a supportive and stimulating academic community.

I would like to express my deepest gratitude to my family for their unwavering love and support throughout my PhD journey. Their steadfast belief in me has been a constant source of motivation and inspiration, and I could not have reached this milestone without their encouragement and support.

Finally, I would like to give my gratitude to the Region Pays de la Loire for supporting this PhD project financially.

ABSTRACT

Heat exchangers (HXs) play a critical role in various energy systems, which can largely influence their overall efficiency. Most recently, the interest in the topology optimization (TO) for heat transfer problems is growing rapidly, which can derive innovative thermal designs. Therefore, the present thesis investigates the utility of the density-based TO for dual-flow HX unit with narrow design domain, along with CFD (computational fluid dynamics) and experimental verifications. A convergent-divergent (C-D) design of fins is acquired using a topology generator (TG), of which efficacy can be proven by the CFD simulations, despite an identified deficiency in the velocity field of the TG-derived topology. Furthermore, upon the resolution of this deficiency, a new topology has been acquired by allocating the generated solids in proximity to the adiabatic boundaries for maximizing the thermo-hydraulic performance of the HX unit with moderate conductive material. High fidelity numerical approaches are employed to examine the efficacy of this new design through a comparative analysis with a benchmark case, and experiments are conducted to validate the numerical results. Both numerical and experimental approaches demonstrate that the TO-derived HX unit has the best thermo-hydraulic performance, reflecting its feasibility in practice. Furthermore, detailed physical interpretations are delivered to analyze the underlying physics behind the obtained topologies.

RESUME

Les échangeurs de chaleur (HX) jouent un rôle essentiel dans divers systèmes énergétiques, ce qui peut grandement influencer leur efficacité globale. Plus récemment, l'intérêt pour l'optimisation topologique (TO) pour les problèmes de transfert de chaleur connaît une croissance rapide, ce qui peut donner lieu à des conceptions thermiques innovantes. Par conséquent, la présente thèse étudie l'utilité du TO basé sur la densité pour les unités HX à double flux avec un domaine de conception étroit, ainsi que la CFD (dynamique des fluides computationnelle) et des vérifications expérimentales. Une conception convergente-divergente (C-D) d'ailettes est acquise à l'aide d'un générateur de topologie (TG), dont l'efficacité peut être prouvée par les simulations CFD, malgré une déficience identifiée dans le champ de vitesse de la topologie dérivée du TG. De plus, après résolution de cette déficience, une nouvelle topologie a été acquise en allouant les solides générés à proximité des limites adiabatiques pour maximiser les performances thermohydrauliques de l'unité HX avec un matériau conducteur modéré. Des approches numériques haute-fidélité sont utilisées pour examiner l'efficacité de cette nouvelle conception à travers une analyse comparative avec un cas de référence, et des expériences sont menées pour valider les résultats numériques. Les approches numériques et expérimentales démontrent que l'unité HX dérivée du TO présente les meilleures performances thermohydrauliques, reflétant sa faisabilité en pratique. De plus, des interprétations physiques détaillées sont fournies pour analyser la physique sous-jacente aux topologies obtenues.

SYNTHESE DE THESE (EN FRANÇAIS)

Cette thèse, financée par la Région Pays de la Loire et menée au sein du Laboratoire de Thermique et Energie de Nantes (LTeN) se concentre sur l’optimisation topologique basée sur la méthode de densité des échangeurs de chaleur à plaques. Les échangeurs de chaleur sont largement reconnus pour leur importance primordiale dans les systèmes énergétiques. Ils sont dispersés dans plusieurs secteurs industriels et ils jouent un rôle crucial dans de nombreux processus industriels en permettant un transfert efficace de l’énergie thermique, ce qui en fait l’un des dispositifs thermiques les plus impactants sur l’efficacité globale des systèmes énergétiques. Par conséquent, la manière d’augmenter les performances des échangeurs de chaleur est depuis longtemps un sujet brûlant pour les ingénieurs et les chercheurs.

Pour améliorer les performances des échangeurs de chaleur, de nombreuses recherches ont été menées, reflétant l'importance considérable des échangeurs de chaleur sur l'efficacité globale des systèmes énergétiques. Dans la littérature, trois principales techniques d'optimisation sont utilisées pour optimiser la configuration des échangeurs de chaleur dans le but d'obtenir de meilleures performances, l'optimisation de la taille, de la forme et de la topologie. L'optimisation de la taille/forme contient un nombre relativement faible de variables de conception. En revanche, l'optimisation topologique peut avoir le nombre maximal de variables de conception, et ainsi des performances maximisées peuvent être théoriquement obtenues sans aucune géométrie prédéfinie. Avec l'essor rapide de TO au cours des dernières années, il est prévu que l'optimisation topologique devienne une technique de pointe pour la conception thermique.

La première partie de ce travail propose une revue détaillée de la littérature sur l'optimisation topologique (TO) des échangeurs de chaleur (HX). Divers algorithmes pour l'optimisation topologique des HX sont dispersés dans la littérature, tandis qu'une revue complète et comparative de leurs caractéristiques, avantages, inconvénients et limites fait toujours défaut. Par conséquent, cette partie vise à combler le manque de littérature en fournissant un examen complet de l'état de l'art sur l'optimisation topologique des HX au cours des dernières décennies, afin d'indiquer la feuille de route technologique la plus prometteuse. Chaque étape de l'optimisation topologique, c'est-à-dire la paramétrisation de la conception, la modélisation du transfert de chaleur, l'optimisation et la réalisation finale, est analysée avec soin dans la section correspondante, en mettant en évidence les principaux avantages, inconvénients et défis. Nos statistiques démontrent que l'optimisation topologique actuelle, bien que bien développée et rapidement améliorée, présente encore de nombreuses limitations dans la gestion des HX industriels qui contiennent des structures et des modèles d'écoulement complexes. Finalement, trois schémas émergents, à savoir l'apprentissage automatique, la réduction de l'ordre des modèles et le déplacement des composants morphables, visant à améliorer l'efficacité de l'optimisation topologique sont également discutés.

La littérature actuelle met moins l'accent sur (1) Fournir un examen détaillé des contraintes et des limitations associées au TO actuel pour le transfert de chaleur conjugué ; (2) Réaliser le TO sur des domaines de conception étroits réalistes, qui peuvent correspondre à des HX compacts ; (3) Exécuter le TO sur des HX à double flux car les HX travaillent en pratique fréquemment avec au moins deux flux ;(4) Effectuer une validation expérimentale des HX acquis par le TO car l'approche expérimentale est considérée comme une étape indispensable pour valider les modèles numériques ; (5) Fournir des interprétations physiques des conceptions dérivées du TO.

La deuxième partie de cette thèse aborde la génération de topologie basée sur la méthode de densité dans un domaine 2D qui représente une unité élémentaire d'un échangeur de chaleur à plaques à contre-courant (PHE). L'objectif du générateur de topologie (TG) est de maximiser l'efficacité, ce qui donne lieu à une nouvelle topologie d'ailettes convergentes-divergentes. En raison de la grande sensibilité des paramètres de réglage du TG (y compris le nombre de Reynolds, le nombre de Prandtl et le rapport de conductivité thermique), leurs effets sur les topologies acquises sont étudiés. Pour évaluer l'efficacité de cette nouvelle ligne directrice de conception des ailettes proposée, un HX (échangeur de chaleur) simplifié avec une distribution d'ailettes rectangulaires convergentes-divergentes (C-D) est introduit et comparé aux structures acquises par TG et à une conception d'ailettes uniformes conventionnelles. L'analyse comparative est réalisée en effectuant un ensemble de simulations de dynamique des fluides computationnelle (CFD) sur les cinq structures (trois obtenues par TG, une simplifiée et une conventionnelle) dans deux cas différents (cas 1 : eau-eau, cas 2 : eau-huile comme fluides de travail respectivement à froid et à chaud) qui englobent une large gamme de nombres de Reynolds. Les résultats montrent une amélioration thermohydraulique des HX obtenus par TG et simplifiés par rapport au nombre conventionnel avec une amélioration du nombre de critères d'évaluation des performances (PEC) jusqu'à environ 23 % et 10 % pour le cas 1 et jusqu'à 36 % et 16 % pour le cas 2, respectivement. Finalement, une interprétation physique détaillée de la topologie générée est fournie. Enfin, une déficience dans la méthodologie employée a été identifiée en examinant le champ de vitesse de la topologie dérivée, ce qui en fait un processus de génération (TG) plutôt qu'un processus d'optimisation (TO). Cette partie actuelle fournit une nouvelle ligne directrice pour la conception des ailettes inspirée des caractéristiques topologiques, qui pourrait être très utile pour améliorer les performances thermohydrauliques des HX.

La troisième partie de notre thèse se penche sur la résolution du problème rencontré identifié dans la partie précédente, principalement présenté par l'inadéquation de l'imperméabilité maximale imposée pour atteindre une vitesse nulle de la phase solide. Pour rectifier ce problème, la valeur de l'imperméabilité est augmentée, imposant simultanément une contrainte sur la chute de pression maximale autorisée à l'intérieur des canaux d'écoulement. Cette double stratégie est obligatoire pour atténuer les problèmes potentiels de blocage dans les canaux d'écoulement de l'échangeur de chaleur (HX), découlant de l'imposition d'une valeur d'imperméabilité élevée sur la phase solide. Le même domaine de conception utilisé au chapitre 3, représentant l'unité périodique dans l'échangeur de chaleur à plaques à contre-courant (PHE), est utilisé dans ce chapitre pour le processus d'optimisation topologique (TO). L'objectif de TO est de maximiser la chaleur échangée, conduisant à une nouvelle topologie caractérisée par l'introduction de solides conducteurs modérés (Stainless Steel) dans la région centrale des canaux de l'échangeur de chaleur. Afin de valider expérimentalement la méthodologie de conception dans les chapitres suivants, un domaine de conception supplémentaire est introduit en excluant les effets de périodicité aux limites supérieure et inférieure du domaine de conception. Cette décision est motivée par les défis associés à la représentation précise du flux thermique périodique local (variable) sur les plaques supérieure et inférieure de l'unité HX à l'aide d'un équipement expérimental. Conformément à l'objectif TO susmentionné, une nouvelle allocation d'ailettes a été acquise pour les HX à double flux utilisant un matériau à conductivité modérée (Stainless Steel), où les solides sont positionnés près des parois isolées. Un examen approfondi des effets des paramètres d'entrée TO sur la topologie dérivée a été effectué.

La quatrième partie de cette thèse fournit une étude numérique 3D à l'aide du solveur FLUENT d'ANSYS basé sur la méthode FVM (méthode des volumes finis) sur la structure optimisée avec TO pour le problème de conception 2 (DP2) introduit dans la partie précédente. La raison du choix de la topologie optimale pour DP2 (parois supérieure et inférieure isolées du HX) et non pour DP1 (condition limite périodique thermique sur les parois supérieure et inférieure du HX) est la difficulté associée à la représentation d'un flux de chaleur local variable sur les plaques supérieure et inférieure de l'unité HX à l'aide d'un équipement expérimental. Cette sélection facilite la validation expérimentale de la topologie optimale pour DP2, qui sera abordée dans la prochaine partie. Dans le but d'effectuer une analyse comparative, deux unités HX supplémentaires ayant des ailettes rectangulaires avec une répartition solide identique et opposée de la conception optimisée TO sont introduites et nommées respectivement unités HX simplifiées et de référence. Les résultats numériques démontrent que l'allocation de solides à proximité de l'isolation comme dans les unités HX optimisées et simplifiées se traduit par une performance thermohydraulique améliorée par rapport au positionnement solide à la paroi d'interface du HX comme dans le cas de référence, précisément lorsque des matériaux solides à conductivité faible/modérée (c'est-à-dire Stainless Steel) sont utilisés dans le HX. De plus, une interprétation physique est effectuée pour interpréter l'intensification thermique présentée dans les unités HX optimisées et simplifiées par rapport au cas de référence. L'étape d'interprétation physique révèle que le positionnement de solides à conductivité modérée (Stainless Steel) près de l'isolation du HX réduit simultanément les résistances thermiques convectives et conductrices conduisant à une augmentation des performances globales.

La dernière (cinquième) présente l'approche expérimentale pour évaluer expérimentalement les performances thermohydrauliques des unités HX (échangeur de chaleur) étudiées (optimisées, simplifiées et de référence) numériquement dans la partie précédente dans le but de valider la méthodologie de conception TO. Les trois unités HX sont fabriquées en utilisant le procédé de découpe au jet d'eau et un dispositif expérimental est construit, permettant l'évaluation des performances globales des unités HX usinées, tandis que la thermographie IR (infrarouge) est utilisée pour comparer et valider les champs de température locaux. Les résultats expérimentaux acquis sont comparés aux résultats numériques obtenus grâce à l'analyse CFD présentée dans partie précédente, démontrant une bonne concordance entre eux, confirmant la robustesse et la supériorité de l'unité HX optimisée par le TO par rapport à la conception de référence.

Nomenclature

Abbreviation

AI	Artificial intelligence
AM	Additive manufacturing
BO	Bayesian optimization
C-D	Convergent-divergent
CM	Conventional manufacturing
CNC	Computer numerical control
CV	Control volume
CFD	Computational fluid dynamics
DP1	Design problem 1
EA	Evolutionary algorithm
EDM	Electrical discharge machining
FEA	Finite element analysis
FEM	Finite element method
FVM	Finite volume method
GA	Genetic algorithm
GCMMA	Globally convergent MMA
GP	Gaussian process
HX	Heat exchanger
IR	Infrared
LBM	Lattice Boltzmann method
LSF	Level-set Function
LSM	Level-set Method
ML	Machine learning
MMC	Moving morphable components
MMA	Method of Moving Asymptotes
MOR	Model order reduction

MOSQP	Multi-objective SQP
NS	Navier-Stokes
NSGA	Non-dominated Sorting Genetic Algorithm
PDE	Partial differential equation
PHE	Plate heat exchanger
RAMP	Rational approximation of material properties
RANS	Reynolds averaged Navier-Stokes
SF	Single flow
SIMP	Solid isotropic material with penalization
SLA	Stereolithography
SLP	Sequential linear programming
SQP	Sequential quadratic programming
TD	Temperature dependent
Ti	Temperature independent
TG	Topology generation
TO	Topology optimization
VOF	Volume of the fluid method
XFEM	Extended finite element method

Symbols

Q	Heat transfer rate [W]
U	Overall heat transfer coefficient [$W.m^{-2}.K^{-1}$]
ΔT_m	Logarithmic mean temperature difference [K]
A	Heat transfer area [m^2]
λ	Physical property
γ	Design variables
q	Penalization coefficient
$\emptyset$	Level-set function
X	Location vector
t	Time [s]

ρ	Density [kg.m^{-3}]
v	Velocity [m.s^{-1}]
P	Pressure [Pa]
μ	Dynamic viscosity [Pa.s]
C_p	Specific heat capacity [J.kg^{-1}.K^{-1}]
k	Thermal conductivity [W.m^{-1}.K^{-1}]
Sr	Heat Source [W]
α	Inverse permeability
F	Brinkmann coefficient
Re	Reynolds number
Pr	*Prandtl number*
Nu	*Nusselt number*
C_k	Thermal conductivity ratio
n	Normal vector
L	Characteristic length [m]
ϵ	Effectiveness
v_f	Volume fraction
L	Langragian function
R_u	Residual of the momentum equation
R_T	Residual of the energy equation
$\lambda_{u,T}$	Adjoint variables
R	Filter radius [m]
β	Projection slope
γ_β	Projection point
Er	Relative error
ΔP	Pressure drop [Pa]
f	Friction coefficient
D_h	Hydraulic diameter [m]
l	Length [m]
h	Convective heat transfer coefficient [W.m^{-2}.K^{-1}]

PEC	Performance evaluation criteria
$cos\theta$	Synergy field
∇T	Temperature gradient vector [K]
S	Volumetric heat capacity [J.m^{-3}.K^{-1}]
Da	Darcy number
b	Convexity parameter
C_s	Volumetric heat capacity ratio
E	Energy [W]
Ω	Design domain
R_{th}	Thermal resistance [W.K^{-1}]
Bi	Biot number
p	Penalization parameter
∇	Gradient operator
n	Index number for the pressure drop constraint

Subscript

s	Solid
f	Fluid
0	Reference
in	Inlet
$cold$	Cold fluid
hot	Hot fluid
max	Maximum
min	Minimum
out	Outlet
k	Iteration number
p	Projected
f	Filtered
b	Bulk mean
w	wall

Superscript

T	Transpose operator
*	Dimensionless
k	Iteration number

Diacritic

$\overline{X}$	Mean operator

Chapter 1: General introduction

1.1 Context

Heat exchangers (HXs) are thermal devices that exchange heat between different mediums (e.g., fluid-fluid, fluid-solid) with or without direct contact for generally realizing various fundamentals, like, cooling, drying, and heating, etc. They play a crucial role in many industrial processes by allowing the thermal energy transfer efficiently, which make them one of the most impactful thermal devices on the overall efficiency of the energy systems. Therefore, how to increase the HX's performance has been for a long time a hot topic for engineers and researchers.

For improving the performance of HXs, many researches have been conducted, reflecting the extensive importance of HXs on the global efficiency of energy systems. In the literature, three main optimization techniques are employed to optimize the configuration of the HXs for the purpose of achieving improved performances, size, shape and topology optimization. The size/shape optimization holds relatively small number of design variables. By contrast, the TO (topology optimization) can have the maximum number of design variables, and thus maximized performance can be theoretically achieved without any predefined geometry. With the rapid rise of TO in the recent years, it is anticipated that TO may became a leading technique for thermal design.

1.2 Research gaps

However, according to the TO of HXs literature [1], several research gaps can be identified as follows:

- Lack of research on TO for multiple flow HXs with narrow domains that correspond to compact HXs.
- Lack of in-depth investigation of the TO's input parameters setting.
- Lack of comprehensively addressing the limitations of the density-based TO.

- Lack of experimental test and validation specifically for dual-flow HXs.
- Lack of physical interpretations for the TO-derived designs.

1.3 Main objective of the thesis

Therefore, the main objective of the thesis is to investigate the utility of density-based TO approach for dual-flow HXs with narrow domains, along with the CFD verifications, experimental tests, and physical analyses.

1.4 Thesis outline

The present thesis dissertation is structured and decomposed into the following chapters:

Chapter 2: Topology optimization of heat exchangers: A review

This chapter presents a comprehensive literature review on the TO of HXs over the past decades. The different approaches utilized in the literature for each stage of the TO are discussed by highlighting their advantages and disadvantages. Furthermore, a statistical analysis is performed to illustrate the utilization percentage of each method within the literature, facilitating the identification of the literature's gaps. Lastly, emerging approaches that aims to increase the efficiency of the TO are also discussed.

Chapter 3: Convergent-divergent design of fins for improving the thermo-hydraulic performance of heat exchangers assisted by a dual-flow topology generator

In this chapter, the density-based topology generation is conducted on a counter-flow HX unit, resulting in a novel fins distribution with a convergent-divergent (C-D) arrangement that have not been reported in the literature. The effect of several TG (topology generator)'s input parameters on the acquired topology has been investigated. Thereafter, CFD (computational fluid dynamics) simulations are conducted to accurately evaluate the thermo-hydraulic performance of the TG-acquired topologies and compare it with different configurations. In addition, a detailed physical interpretation of the generated C-D topology is provided. At the end of this chapter, an identified issue in the velocity field of the generated topology has been presented and discussed. The identified deficiency in the employed methodology classifies it as a topology generation process rather than a topology optimization one.

Chapter 4: Density-based topology optimization of dual-flow heat exchanger with moderate conductive material

This chapter addresses the density-based TO for two counter-flow HX units (DP1 & DP2) employing moderate conductive material (Stainless Steel) with the intention of resolving the identified problem of chapter 3 regarding the velocity field of the generated topology. An in-depth investigation analysis is performed to test the effect of various TO's parametric setting on the derived topology. Upon resolving the identified issue, the investigation stage reveals a significantly different topologies compared to those obtained in chapter 3 (C-D), reflecting the high influence of the TO's input parameters on the acquired topologies.

Chapter 5: Performance evaluation of the topology-optimized thermo-fluidic structure with insulated side walls: A 3D computational fluid dynamic analysis

This chapter numerically studies the TO-optimized HX unit for DP2 presented in the preceding chapter 4 by performing a 3D CFD analysis. Two additional HX designs (simplified and benchmark) are introduced to perform a comparative analysis with the TO-optimized HX in the laminar region. Multiple criteria are employed to compare and assess the thermo-hydraulic performance of the three HX units (TO-optimized, simplified and benchmark). Moreover, a detailed physical interpretation is delivered to analyze the underlying physics behind the TO-derived design.

Chapter 6: Experimental validation of the topology optimization design methodology

In this chapter, the experimental approach is presented with the intention of validating the TO's design methodology and the numerical model through the comparison of the HX's thermo-hydraulic performance evaluated experimentally and numerically (CFD results of the previous chapter 5). Moreover, the IR thermography is employed to validate and measure the fluid local temperature distribution.

Chapter 7: Conclusions and perspectives

This chapter summarizes the primary conclusions of the preceding chapters and offers perspectives for future research directions.

Chapter 2: Topology optimization of heat exchangers: A review

Chapter Summary

This chapter presents a detailed comprehensive literature review on the topology optimization (TO) of heat exchangers (HXs). Various algorithms for TO of HXs are dispersed in the literature, while a comprehensive and comparative review on their features, advantages, disadvantages, and limitations, is still lacking. Therefore, this chapter aims at filling the literature gap by providing a comprehensive state-of-the art review on the TO for HXs over the past decades, so as to indicate the most promising technology roadmap. Each stage of the TO, i.e., the design parametrization, the heat transfer modeling, the optimization, and the final realization, is analyzed carefully in the corresponding section, with highlighting the major pros, cons and challenges. Our statistics demonstrate that the current TO, though well-developed and fast improved, still have numerous limitations in handling the industrial HXs that hold the complicate structures and flow patterns. Eventually, three emerging schemes, i.e. machine learning, model order reduction, and moving morphable components, aimed to improve the efficiency of TO are also discussed.

Keywords of the Chapter:

Topology optimization, Heat exchangers, Conjugate heat transfer, Additive manufacturing, Machine learning.

2.1 Introduction

Energy, environment and sustainable development are closely related topics, while energy is at the center of the sustainable development paradigm. All energy conversion systems involve the heat transfer via fluid flows. More than two thirds of energy is lost in the energy conversion chain, from capture, conversion, transport, production, distribution, storage to end use. Increasing energy efficiency has been identified as one of the main challenges for energy systems and has attracted increasing attention from the academic and industrial communities [2]–[4].

The heat exchanger is a classical component [5]–[7] and the basic element not only for all systems and processes of energy conversion, production and use but also for many industries (food, cosmetics, medical, textile, chemical, metallurgical, materials, building, embedded systems, aeronautics, aerospace...). Exchangers are everywhere, indispensable, in different forms, to meet various needs, and are often subject to strong functional and operational constraints, objects of permanent challenges and infinite innovations. This is a highly applied research topic that requires fundamental sciences such as thermodynamics, transport phenomena, fluid mechanics, materials, combined with high-performance numerical methods and optimization tools. The objective is to increase their overall performance. The key points are the intensification of heat transfer on the one hand, and the optimized management of fluid flows on the other hand, at each scale, structural and temporary [7]–[10]. Therefore, how to improve the thermal performance of HXs has long been a hot topic in the research community of energy engineering.

Many theorems and methodologies have been developed for enhancing the heat transfer rate of HXs at the given pressure loss [11]–[15]. Starting with the basic heat transfer equation for HXs [11]:

$$Q = UA\Delta T_m \quad (1)$$

where Q is the heat transfer flux (W), U is the overall heat transfer coefficient (W.m^{-2}.K^{-1}), A is the heat transfer surface area (m^2) and ΔT_m is the mean temperature difference or the heat flux driving force (K). U is composed of conduction and convection coefficients which are associated to the transport properties. Both coefficients (conduction and convection) could be magnified by enhancing the thermal properties of the HX material and by affecting the fluid flow pattern near to the heat transfer surfaces, respectively. Moreover, it is evident that also increasing A and enhancing the distribution of the heat transfer driving force (ΔT_m) will also intensify heat transfer. For all these three aspects, a determinant factor is the shape/form/arrangement of the solid-fluid interface within the HX, on which the size/shape/topology optimization methods could be employed to play a critical role.

In general, the optimization of HXs can be classified into three types: the size optimization, the shape optimization and the topology optimization (TO). The size/shape optimization has been well developed for years [16]–[18], which refers to the design process that searches for the optimal size or shape in the given configuration or arrangement for a specific HX [19]. Nevertheless, the size/shape optimization could not significantly change the prescribed configuration or arrangement of HXs set by designers, which may limit the optimization performance. In practice, good performance improvement can still be achieved with the careful selection of the initial structures and optimization criteria [20]. Different from the size/shape optimization, the TO act directly on the topology of the (interface) geometry by spatially optimizing the distribution of fluid or solid phase and their connectivity, within a defined domain, which may attain any topology that minimize/maximize the optimization objective under some constraints. In theory, it holds the possibly maximum degrees of freedom in optimization, though in practice, the optimization objectives and constraints can also have a significant influence on the final results. In recent years, the TO has been regarded as a groundbreaking technique to obtain the innovative designs of HXs with greatly improved effectiveness, and has drawn more and more attention of researchers.

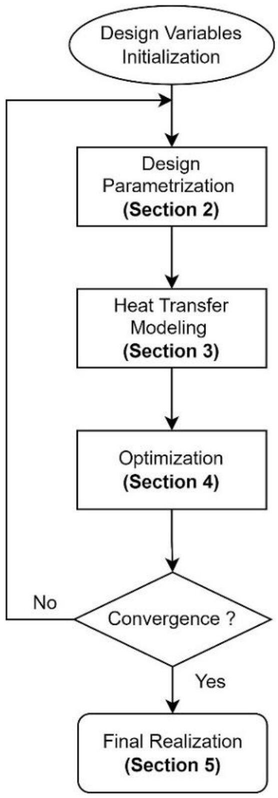

Figure 2.1: The basic stages (the corresponding section) in the TO process.

Figure 2.1 shows a representative workflow of TO that includes four basic stages: (1) Design parametrization, (2) Heat transfer modeling, (3) Optimization process, and (4) Final realization. Compared to structural TO for mechanics, the issues that limit the TO's utilization for the HXs can emerge in each stage of the TO process. The HXs involve the conjugate flow and heat transfer [21]. Thus, the fluid problems should be solved during the iteration process of TO, leading to large computational expenses. This is actually the major obstacle for the practical utilization of TO for the real HXs of which the intermediate or final interface structures/topologies can be really complicated. Meanwhile, the mixing among different flows should be avoided by carefully designing the parametrization scheme, when updating the geometry of the solid phase that separates different fluids [22]. Additionally, maximizing the heat transfer rate is not always the only goal when designing HXs; the pressure loss should also be considered. To address this issue, the weighted-sum objective function [23] or a multiple-objective optimizer, such as NSGA-II [24], should be employed. Moreover, even if the rapid development of additive manufacturing (AM) techniques has greatly improved the ability to realize the optimized designs obtained by the TO, there are still some manufacturing constraints when applying a specific AM technique [25], and the proper post-treatments on the TO-derived structures are highly needed [26]. Actually, there are few researches that consider the fabricating constraints in the TO of HXs. Researchers have proposed some specific solutions for the issues mentioned above, which are dispersed among the literature. In the past years, several review articles were published to cover the literature of TO for microfluidic devices [27], heat transfer systems [28], fluid-based problems [29]. However, a comprehensive and comparative review on different TO stage's features, advantages, disadvantages, and limitations, is still lacking particularly for HXs.

Here, we will analyze and compare the researches on the TO for HXs in the most recent years with the main objectives of defining a research guideline for more enhancement and development in the TO of HXs by providing a brief understanding of different methods employed in all TO stages for HX applications which will also help and clarify the implementation procedure for researchers. However, there have been few TO researches handling such practical multi-flow HXs. In fact, most of the TO papers just deal with a specific element (such as a duct) within the whole HX structure. In order to extend the coverage of our review, the papers for single-flow heat sinks and fins that involves the physics of conjugate heat transfer are also included, while the pure heat conduction, the radiation, the phase change (evaporation, condensation), transient operations (thermal energy storage for example), and exothermic/endothermic reaction problems are excluded for clarity. According to this inclusion criteria, 112 articles published in the past fifteen years are covered in this review, which can well reflect the mostly-recent progress in the TO for HXs.

The present chapter is organized following the procedure of TO, that is, each stage of TO will be discussed in the corresponding section. Those common approaches are presented, with emphasis in the issues that limit their utilization for the practical HXs. Afterwards, some new trends in this area aimed to improve the efficiency, like the integration of machine learning techniques, will also be covered in Section 6. A series of statistics, comparative tables and figures will be given in each section to demonstrate the features, advantages, disadvantages, and limitations of the developed schemes in the TO of HXs.

2.2 Design Parametrization

Design parametrization refers to the representation of variables determining the design configurations which determines the relationship between the design variables (e.g., the density distribution that determines the flow paths in the density-based TO problems) and the physical properties by the interpolation functions. Its sensitive representation strongly affects the TO's output results [30]. Furthermore, the design parametrization can vary from TO types, problem descriptions, and physical phenomena. It should be carefully chosen according to the problem's features, considering both efficiency and accuracy. As given in Tab. 2.1, there are three main types of parametrization methods: Density-based, Level set and Direct explicit.

Table 2.1: Summary and comparison of design parametrization methods

Parametrization	Advantages	Disadvantages
Density-based	• Fixed mesh; • Well developed in TO for years.	• No interface described; • Numerical instabilities; • Modified governing equations.
Level-set	• Crisp description of interface profile; • No re-meshing in general.	• Slow convergence; • Results dependent on initial configurations; • Numerical artifacts.
Direct explicit	• Interface described explicitly; • Straight-forward & relatively simple.	• Applicable only for simple geometries.

2.2.1 Density-based method

The density-based method is the most popular means, which was first proposed by Bendsøe [31] in 1989. It is based on representing the design domain by densities or porosities to parametrize the fluid and solid phases. Researches started with the single-flow problems from Borrvall and Petersson [32]. Their representation of design variables (the density γ) consists of assigning $\gamma = 0$ for the solid phase or non-existing fluid phase, and $\gamma = 1$ for the fluid phase. The governing equation need be modified by introducing a fictitious force (the detailed equations will be given in Sec.3), which is determined by an inverse permeability (α) for each element, with α_{min} corresponding to $\gamma = 1$ (fluid region) and α_{max} corresponding to $\gamma = 0$ (solid region). In the elements of solid with $\gamma = 0$, the fictitious force is maximum to block the flowing of fluid. During the iteration process, the inverse permeability (α) is changing continuously in every element, which is determined by an interpolation function. Taking the widely-used SIMP (solid isotropic material with penalization) [31] as an example, it is given by,

$$\lambda(\rho) = \lambda_{max} + (\lambda_{min} - \lambda_{max})\gamma^{q} \tag{2}$$

where $q > 1$ is a penalization coefficient to minimize the presence of the gray elements, i.e. the ones of partial density from 0 to 1, $\lambda_{min}, \lambda_{max}$ are the minimum and maximum physical properties values (e.g., thermal conductivity), respectively. Note that the gray elements are usually regarded to hold no physical meaning and thus should be avoided by adjusting q. Thereafter, the above density-based representation with the different penalization functions, including SIMP and RAMP (rational approximation of material properties), etc., have been utilized in a wide range of single-flow HX problems [33]–[98]. Additionally, some other researchers [99]–[115] used an opposite representation of design parametrization by assigning $\gamma = 1$ for the solid phase or non-existing fluid phase and $\gamma = 0$ for the fluid phase. Note that no evidence demonstrates that such different representation of solid and liquid phases will significantly affect the solutions or efficiency of TO in the single-flow heat transfer problems. Currently, the first kind of representation accounts for the largest portion in the published articles, as shown in Fig. 2.2b.

Furthermore, the density-based method was extended to the multi-flow HE problems, which involve two or more fluids separated by one or more solid phases [22], [114], [116]–[120]. For instance, Kobayashi et al. [119] used one density (γ) to describe the multi-fluid problem by assigning $\gamma = 0$ for fluid 1, $\gamma = 1$ for fluid 2 and intermediate values ($0 < \gamma < 1$) for the solid phase. Tang et al. [114] divided a dual flow heat transfer problem into two independent one-flow and one-solid sub-problems, and thus one design variable (density) is used for both sub-problems.

The density-based method has shown its high efficiency by avoiding the re-meshing process at each iteration. As for the interpolation functions, the RAMP has proved the ability to penalize the larger range of design variables compared to the SIMP function [121]. In fact, the majority of TO publications are based on the density-based method, as shown in Fig. 2.2a. However, some numerical issues are usually encountered, like the mesh-dependent results, the bad formation of solid/fluid cells in the optimized structure in which they are ordered similarly to the checkerboard configurations, and the intermediate densities values, etc. [122]. To remedy these instabilities, densities filters and projections should be implemented [122],[123]. More importantly, it is not able to exactly describe the interface between different phases due to the element by element updating procedure, and thus not suitable for the problems where the interfacial profiles or the properties near the interfaces are important [124].

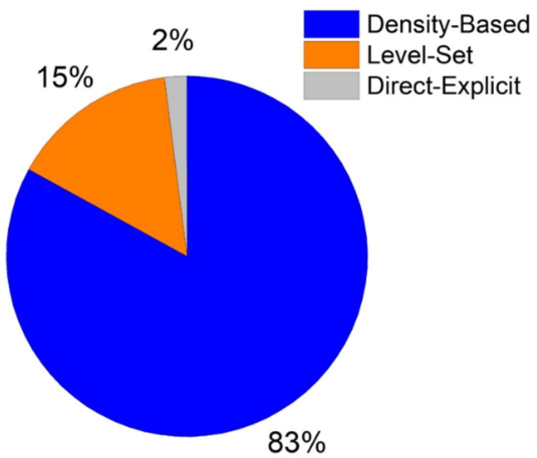

(2.a) Publication percentage of different design parametrization methods

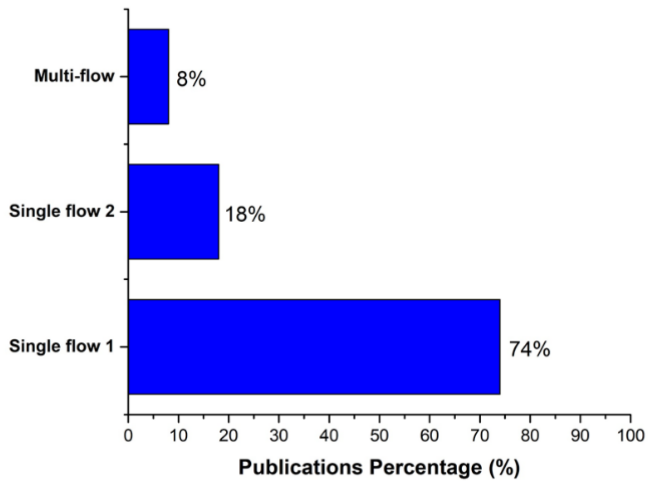

(2.b) Publication percentage of Density-based different design parametrization. Single flow 1 (ρ=1 fluids, ρ=0 solids). Single flow 2 (ρ=0 fluids, ρ=1 solids)

Figure 2.2: Publications statistics for design parametrization methods in TO of heat exchangers (until 24-February-2024).

2.2.2 Level set method

The level-set method (LSM) was first developed by Osher and Sethian [125], for the purpose of well defining the interface between phases. Most of the time, it implicitly describes the interface between multiple phases by a level-set function (LSF) [126]–[128], which allows a clear description of the interfaces and improves the accuracy of the responses captured at the boundaries. The design parametrization of LSM is given by,

$$\begin{cases} \emptyset(\boldsymbol{X}) > 0 \Leftrightarrow (\text{Material Phase}) \\ \emptyset(\boldsymbol{X}) = 0 \Leftrightarrow (\text{Interface}) \\ \emptyset(\boldsymbol{X}) < 0 \Leftrightarrow (\text{Void}) \end{cases} \tag{3}$$

where $\emptyset$ is the level-set function and $\boldsymbol{X}$ is the location vector of the design domain. The LSF is set to be zero at the interface, and the nodal values of LSF can be solved based on a governing equation or interpolated on the computational domain by a space function called "basis functions". The LSM has also been applied in the TO of HXs [109], [118], [129]–[141]. Feppon et al. [132] even used the LSM to deal with the 2D and 3D HXs involving two fluids. Furthermore, the LSF can be described in an explicit way [135],[142]. Li et al. [142] suggested a component-based level-set parametrization to describe explicitly the solid/fluid interface for the TO of a micro-channel heat sink.

The clear and crisp description of interface in the LSM makes it a good option for the problems where the interfacial profiles or the properties near the interfaces really matter. Generally in the LSM, re-meshing is not needed, except in the case of conforming discretization (referring to the conforming discretization section in Ref. [143]). In this sense, the LSM can be well suitable for the HXs where heat transfer rate is largely determined by the flow velocity and temperature fields near the solid-liquid or liquid-solid-liquid interfaces. However, the dependence of output results on the initial configurations can significantly affect the accuracy and efficiency of LSM [143]. Another disadvantage is the slow convergence compared to the density-based method [143]. Moreover, similar to the density-based method, the regularization techniques are always necessary to avoid numerical artifacts and enhance the convergence rate in the LSM [143].

2.2.3 Direct explicit method

Direct explicit parametrization permits to describe interfaces in a direct way. One or several functions or arrays are used to describe the interfacial profiles explicitly. Among the literature, the direct explicit parametrization is very well established for shape optimization [144]–[146]. However, the direct explicit method is only applicable for some simple problems. As for TO of HXs, it is infrequently applied (see Figure 2.2.a), though it can eliminate the numerical artifacts encountered by the implicit representations [147]. For example, Mekki et al. [148] proposed an explicit voxel parametrization for optimizing the 2D fins of a HX: each voxel can represent either solid or liquid, and can be iteratively switched during the optimization process. Moreover, Shimoyama and Komiya [149] suggested a new explicit parametrization by representing the 3D lattice-structured heat sink using a point/edge system. However, up to date, there has been no published research that used the direct explicit method in the TO for complex HX problems.

2.3 Heat transfer modeling

The conjugate heat transfer in HXs is characterized by four equations, i.e., (a) continuity eq, (b) momentum eq, and energy balance eq (c) for fluids, (d) for solids,

$$
\begin{aligned}
&\frac{\partial \rho_f}{\partial t} + \nabla.(\rho_f v) = 0 \quad (a)\\
&\rho_f \left(\frac{\partial v}{\partial t} + v.\nabla v\right) = -\nabla P + \mu_f.\nabla^2 v + F \quad (b)\\
&\rho_f C_{pf} \frac{\partial T}{\partial t} + \rho_f C_{pf} v.\nabla T = \nabla.\left(k_f \nabla T\right) + Sr \quad (c)\\
&\rho_s C_{ps} \frac{\partial T}{\partial t} = \nabla.(k_s \nabla T) + Sr \quad (d)
\end{aligned}
\tag{4}
$$

where C_{pf} and C_{ps} are the specific heat at constant pressure for fluid and solid phases respectively ($J.kg^{-1}.K^{-1}$), k_s and k_f are the thermal conductivities for solid and fluid phase respectively ($W.m^{-1}.K^{-1}$), v the velocity ($m.s^{-1}$), T the temperature (K), P the pressure (Pa), μ_f the fluid dynamic viscosity (Pa.s), ρ_f and ρ_s are the fluid and solid phases densities ($kg.m^{-3}$), t is the time (s), Sr is the heat source term (W) and F is the fictious force equal to $-\alpha v$, where α is the inverse permeability. This friction force is an indispensable term specifically in density-based TO which represents the solid phase force on the fluid phase. Nevertheless, this friction term is infrequently used in level set TO; in the direct explicit case, it is not needed. In the TO, the governing equations should be solved at each iteration to compute the objective function values. Apparently, the solver efficiency and accuracy will greatly affect the performance of TO. Furthermore, these numerical solvers encountered some difficulties to correctly and efficiently simulate turbulent flows which is usually described by the velocity, pressure chaotic changes and unsteady eddies. In decades, several solvers have been developed to solve Eq. (5), as given in Tab. 2.2. In the majority of HXs applications, some acceptable simplifications and assumptions are made to simplify the numerical modeling e.g., steady-state, temperature independent thermo-physical properties for fluid and solid phases, incompressible flows, etc. Additionally, some rare exceptional studies dealt with some more complicated conditions, e.g. temperature dependent thermo-physical properties [61].

Table 2.2: Summary and comparison of the solvers in TO of HXs

Methods	Advantages	Disadvantages
FEM	• High availability in TO; • Flexible with a wide range of physics.	• Not ensuring the conservation law locally; • Numerical instabilities for convection.
FVM	• Ensuring the conservation law locally; • Suitable for CFD problems.	• Relatively low availability in TO; • Tough to design higher order schemes with high accuracy; • High requirement of mesh quality especially for complex geometries.
XFEM	• Well capturing interfaces.	• Very low availability in TO; • Not ensuring the conservation law locally.
LBM	• Ensuring the conservation law locally; • Able to consider the size effects at microscale; • Easy-meshing.	• Very low availability in TO; • Difficulties in handling the multiphase flow, compressibility and 3D extension; • Memory intensive.

2.3.1 Finite element method (FEM)

The FEM is one of the well-developed techniques for solving partial differential equations. It was first proposed by Hrennikoff [150] and McHenry [151] on structural problems. FEM consists of discretizing the domains into small domains called “finite elements” to transform a continuous problem into a discrete one. Thereafter, the governing equations are integrated over each element by the weighted residual methods [152], e.g., Galerkin method. The elemental matrices are then formulated and assembled into the global discretized system of equations that enable to calculate the unknown variables at each node. FEM has proved its high flexibility of being applied to a wide range of physics with highly accurate results [153].

In the TO of HXs, the solvers based on the FEM have been extensively used for the steady-state laminar flow in both the 2D and 3D cases [22],[33]–[38], [45],[47],[49]–[56], [60]–[63], [65]–[79], [81], [83]–[85], [87], [89]–[99], [102], [104], [107]–[113], [115], [117]–[120], [131]–[134], [136], [137], [141], [154]–[156]. As for the single-flow HXs, for instance, Dede et al. [47],[102] used the FEM solver in the TO of a liquid cooled heat sink, and Matsumori et al. [33] optimized the channels of a HE using the FEM-integrated TO. In the multi-flow HX cases, the FEM was adopted in the TO by Papazoglou [22]. Sun et al. [37] executed the TO on a fin and tube HE using the FEM-based COMSOL Multiphysics software. Different from the preceding references, under laminar transient conditions, Zeng et al. [57] performed a TO on a 3D heat sink using a finite element solver. On the other hand, few researches on the TO of HXs involving the turbulent flow have also been conducted mainly using the FEM to solve the RANS (Reynolds averaged Navier-Stokes) equations [41],[62],[86],[100],[142],[157]. For example, Zhao et al. [100] adopted the Darcy-flow and RANS models for the TO of cooling channels problems under steady state conditions: the FEM-based commercial software (COMSOL Multiphysics) was employed to simulate the turbulent flow in the channels.

The combination of density-based method and FEM is the most convenient transfer from the TO of structural mechanics to that of conjugated heat transfer. In decades, a series of algorithms and codes have been developed, and recently the TO module has even been integrated in the FEM-based commercial software. Owing to such high availability, the FEM is currently the mostly-used solver in the TO of HXs, as illustrated in Fig. 2.3. However, in the FEM, the conservation law is not well guaranteed locally for each finite element [158]. This may lead to the numerical instabilities of the conjugate heat transfer problems [159], which can largely affect the performance of the TO of HXs.

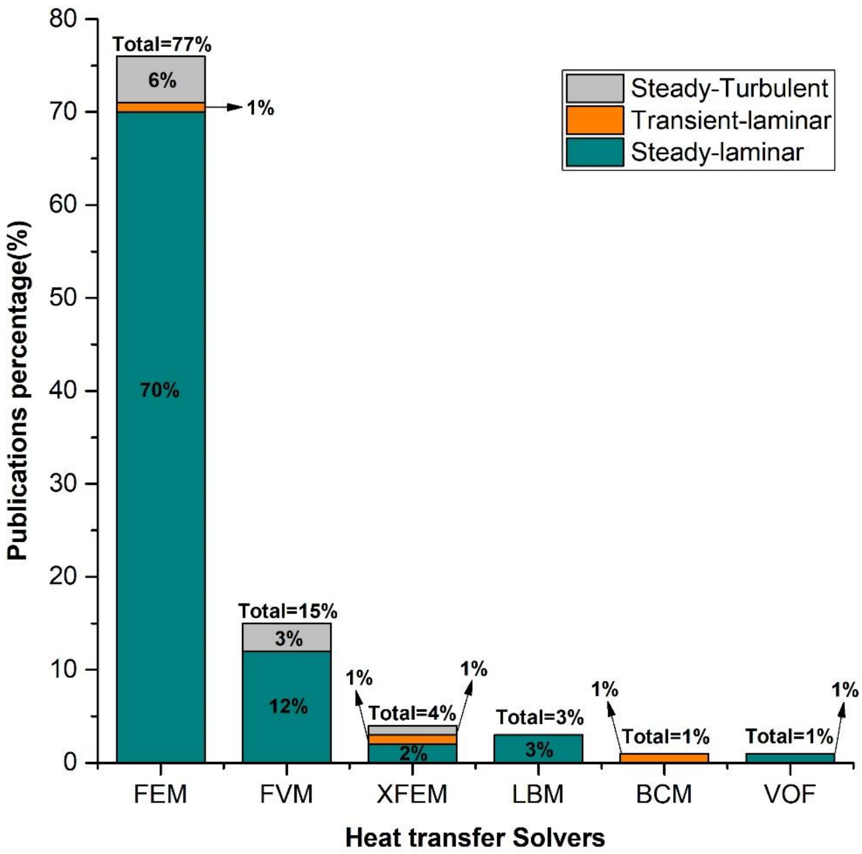

Figure 2.3: Publications percentages for different solvers used in the TO of HXs under different conditions (until 24- February-2024).

2.3.2 Finite volume method (FVM)

The FVM is discretizing the design domain into a group of control-volumes (CVs) by directly integrating the governing equations over each CV, and the divergence theorem is applied to transform the CV integration into boundaries summation over each CV [160]–[162]. It has shown its robustness and stability in CFD (computational fluid dynamics) problems [163].

FVM was first used in the TO of heat conduction by Gersborg-Hansen et al. [164]. Then, it was implemented in a TO algorithm for the steady-state laminar flow HXs [39],[44],[46],[59],[64],[82],[88],[103],[114],[116],[139],[148],[149]. Tawk et al. [116] optimized both parallel and counter-flow HXs using the FVM-based TO for thermo-hydraulic enhancement purposes. Recently, the open-source library OpenFoam based on FVM becomes popular to solve the flow problems. It has also been applied for TO of HXs [46],[148] on few cases.

As for the HXs involving turbulent flow, Kontoleontos et al. [101] used the FVM to solve the Spalart-Allmaras turbulence model in the TO of a thermal-fluid problem. In the same idea, Dilgen et al. [43] studied the turbulence effect on a heat sink using the *k-w* model at steady state conditions. With the intention of studying the turbulence effects inside a square tube HE, the FVM was applied by Pietropaoli et al. [106] to solve the RANS equations in the TO; then, they carried out a detached eddy simulation (DES) to evaluate the thermal performance of optimized structure. Ghosh et al. [80] used a FVM-based software (OpenFoam) to model the turbulent flow inside a cooling duct.

The FVM ensures the conservativeness over every CV [162], which makes it a good option for CFD problems. In fact, the majority of authors that used the FEM- based TO mentioned in Subsection 3.1 performed the CFD analyses using FVM solvers to evaluate the performance of the TO-derived structures, which underscores the advantages of the FVM over the FEM in CFD applications. However, the portion of the FVM-based TO of HXs to date happens to be rather small, as shown in Fig. 2.3. The low availability of the FVM-based TO programs may be the major reason for that. Moreover, the optimized results in the FVM-based TO can be mesh dependent, without integrating a proper filter [28]; it becomes difficult to design high order schemes that obtain a good accuracy using the FVM [165].

2.3.3 Extended finite element method (XFEM)

The XFEM extends the approach of the FEM by adding enrichment degrees of freedom on the nodes near the discontinuities to improve the description of discontinuities [166],[167]. The XFEM was first used on the 2D cracks by Belytschko and Black [168] to study the crack propagation and interfaces.

As a very valuable attempt, Coffin and Maute [135] combined the XFEM and the LSM in the TO for the 2D and 3D, steady-state and transient single-flow heat transfer problems dominated by natural convection. Moreover, Lin et al. [138] performed a topology optimization using the LSM-XFEM coupling to optimize the channel topology for a 2D heat sink under steady-state conditions. Recently, Noël and Maute [157] suggested a TO using XFEM for the intention of optimizing the solid/fluid interface to intensify the exchanged heat in the turbulent region.

Thanks to the features of XFEM and LSM, the interface is well captured during the iterative optimization process, while the computational burden increases at the same time. In the XFEM-based TO, the description of the interface can be improved, however adding new degrees of freedom at the nodes near the interfaces induces a high algorithmic complexity that strongly increases the computational time. As demonstrated by Fig. 2.3, XFEM was scarcely used as a numerical solver for the TO of HXs. The same as the FEM, some instability problems are encountered due to the deficiency of conservative fluxes at each element [158]. Additionally, particularly for transient problems due to the rapid change of the physical properties (like temperature jumps near the interface), small time steps are required to capture it when using the XFEM [169].

2.3.4 Lattice Boltzmann method (LBM)

The LBM is a mesoscale method used for solving transport governing equations described at the macroscopic scale [170],[171]. A set of Boltzmann transport equations are designed to correspond to the macroscopic governing equations, and then are solved in the representation of lattice gas.

The LBM is a relatively young technique compared to the FEM and the FVM. There are few researchers attempted to integrate the LBM in the TO of flow and heat transfer problems [40],[58],[130],[140]. Yaji et al. [58] implemented a TO based on LBM to optimize the flow channels topology of a 2D thermo-fluid problem. For instance, the LBM was adopted by Dugast et al. [130] for the TO of a 2D thermal fluid problem.

The LBM has showed its robustness and accuracy in the heat and mass transfer problems, particularly in the micro-scale cases where the size effects become significant [172]. It ensures the local conservation law, and has the advantages when dealing with the problems of complicated interfaces and size effects at the microscale. In this sense, the LBM-based TO may be promising for the multiscale HXs. However, the LBM has difficulties in handling with the multiphase flow, compressibility and 3D extension. Moreover, due to the iterative propagation step, the LBM is a memory-intensive method [173]. Importantly, the integration of LBM with TO is still at a starting stage, which is far from mature for practical applications.

2.4. Optimization

After computing the objective function(s) using the heat transfer solvers, an optimization process is conducted to renew the design variables (defined in the parametrization stage), in order to minimize or maximize the objective function(s) under specific constraints. The objective functions serve as the optimization criteria and may influence the final topologies. Regarding the thermal performance, there have been at least 10 different objective functions among the literature of TO, including minimizing average temperature rise, minimizing thermal compliance, minimizing thermal resistance, maximizing exchanged heat, and maximizing recoverable thermal power. Optimization criteria of HXs where the subject of long discussions in the community of heat transfer [12],[14],[174]. For instance, in the view of thermodynamics, minimizing the exergy destruction can also be an objective function of heat transfer optimization. However, to our best knowledge, there has been no research that carefully investigates the influence of objective functions on the TO of HXs up to date. Additionally, the hydraulic performance of HXs can serve as either the constraint or one of the objective functions. Regarding the hydraulic performance, the choices of optimization criteria (or constraints) are not that diverse: minimizing the pressure drop and the energy dissipation (loss) of flow are the common ones. In addition, as illustrated by Fig. 2.4b, the majority of the researchers dealt with single objective functions. Some of these studies take an advantage to enhance the thermo-hydraulic performance simultaneously by dealing with a single objective function and setting the other objective as an optimization constraint. On the other hand, other groups of researchers employed the weighted sum or the true multi-objective optimization for the same purpose of intensifying the heat transfer and improving the hydraulic performance concurrently of HXs. The optimizer, which is the core part of TO algorithm, determines the evolution of design domains and thus the final output result by the TO. Table 2.3 lists some commonly-used optimizers.

Table 2.3: Summary and comparison of the optimizers in TO of HXs

Optimizers	Advantages	Disadvantages
Gradient-based	• Mostly efficient for the large-design-variable-number problems; • High availability in TO.	• Deficiency in multi-objective problems; • Local optima.
GA (Genetic Algorithm)	• Gradient-free; • Global optima; • Efficient in multi-objective problems.	• Slow convergence; • Randomness.
Bayesian	• Efficient in big data problems.	• Expensive and complex computation; • Scalability weakness with the number of objective function evaluations.

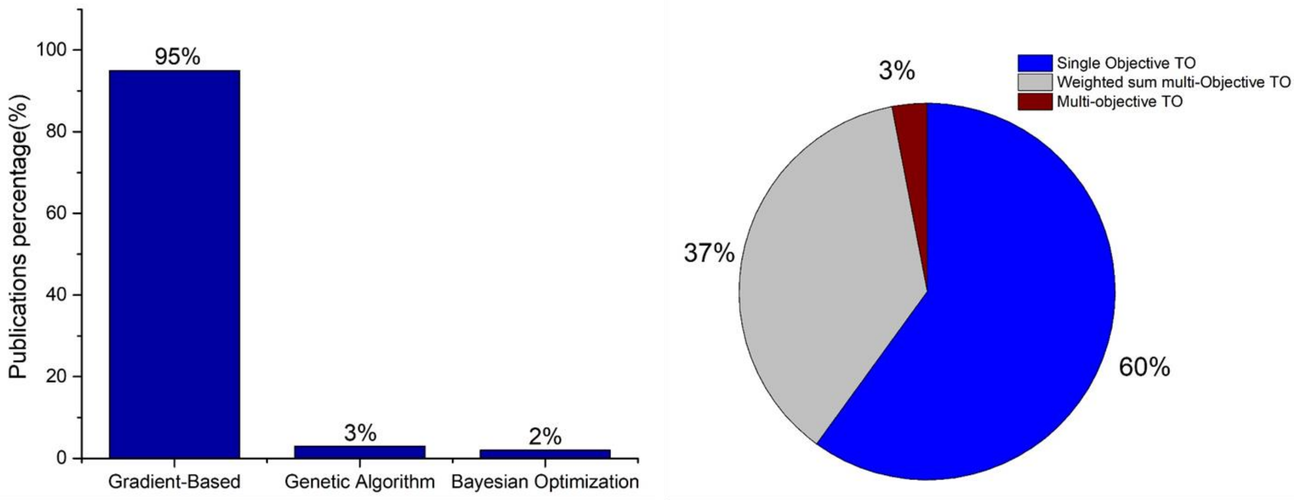

(a) Different optimization techniques

(b) Optimization types

Figure 2.4: Publications percentages for different optimization techniques in the TO of heat exchangers (until 24- February-2024) (a) Different optimization techniques;(b) Optimization types.

2.4.1 Gradient-based optimization

The gradient-based method also called "sensitivity analysis" is based on computing the gradients of the objective functions with respect to the design variables. These gradients represent the variation of the objective function with respect to the design variables at each iteration and are often solved using the adjoint method [175]. The adjoint method has shown its high efficiency in computing the objective function gradients [176]. The optimizer renews the design variables based on these gradient values.

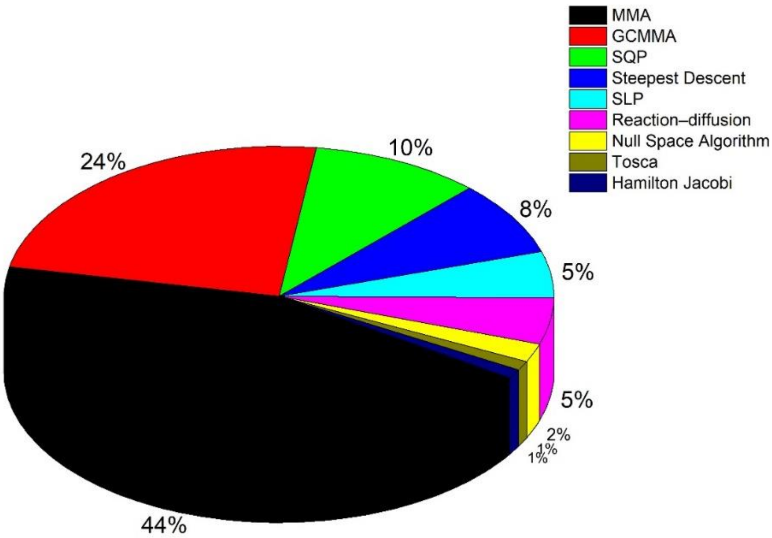

Figure 2.5: Publications percentages of the optimizers used in gradient-based TO of heat exchangers (until 24- February-2024).

As illustrated in Fig. 2.5, several gradient-based optimizers are utilized in the TO of HXs, including MMA (Method of Moving Asymptotes) [177](44%), GCMMA (Globally convergent MMA) [178](25%), SLP (Sequential linear programming) [179](6%), SQP (Sequential quadratic programming) [180](9%), Steepest descent [181](8%), Tosca [182](1%), Reaction-diffusion [183](4%), Hamilton-Jacobi [109](1%) optimizers, and Null Space algorithm [184](2%). These gradient- based optimizers hold the different mathematical natures and thus the distinct applications. The detailed explanation on their mathematical characteristics are beyond the scope of our review, and can be found in the relevant references.

The utilization of gradient-based optimizers is the mainstream in the TO not limited to the problems of HXs [22],[33]–[114], [116]–[120],[130]–[142],[154],[155],[157]. According to Fig. 2.4a, more than 90% of papers on the TO of HXs utilize the gradient-based optimizers. This is mainly because its efficiency in handling problems involving such large number of design variables (usually equal to the number of nodes in the solver) [185]. Additionally, some gradient-based multi-objective algorithms have been developed, like MOSQP (Multi-objective

SQP) [186], which has been employed in the structural TO [112]; however, up to date there has been no published work on the TO of HXs using such algorithm. Additionally, the gradient-based optimization can converge to a local optimum when the objective function has several local optimums [134], and thus sometimes we may need re-optimization by setting different initial configurations.

2.4.2 Genetic algorithm (GA)

The GA is a stochastic evolutionary algorithm (EA) based on the biology of chromosomes and genes [187]. This evolutionary algorithm obtains the optimized solution(s) after several generations. Each generation starts by generating the initial population randomly to increase its diversity. Then, the fitness values are evaluated for each chromosome in the population using fitness function(s), i.e. objective function(s). The parent chromosomes are selected from the initial population using natural selection processes, e.g. roulette wheel [188]. The children are then obtained by the combination of two parents using crossover [189]. Thereafter, the mutation process based on randomness is applied on the children to mutate one or more of their genes before moving to the next generation. Finally, the elitism stage [190] moves one chromosome to the next generation without being edited by the crossover and mutation.

The GA have been developed by many researchers in different fields including heat transfer [191]. As for the TO of HXs, few researchers implemented the GA for generating optimized topologies [62],[129],[148],[149],[192]. Yaji et al. [62] proposed a multi-fidelity TO for a heat sink using EA main stages (selection, crossover, mutation). They first performed a low fidelity optimization problem based on Darcy flow model using ε-constrained method [193]. According to low fidelity results, a high-fidelity evaluation was executed using Navier–Stokes equations. Then, a non-dominated sorting strategy (NSGA II) was employed to select the optimal pareto front.

The GA method avoids the gradient computation of the objective function (s) at each iteration. In theory, it will obtain the global optima, and screen the influence from the initial guess [191]. Moreover, the GA is a good option for the multi-objective problems, since it handles a group of candidates simultaneously, which is of advantage to derive the Pareto front

[24]. Having similar stochastic behaviors, other evolutionary algorithms (e.g., Particle Swarm Optimization) could be also tested with the TO of HXs which may possess more efficiency than the GA in some cases. Despite the merits of GA, it has been rarely coupled with the TO of HXs, as shown in Fig. 2.4a. This is mainly attributed to the slow convergence of GA [191], which significantly increases the computational time of the TO.

2.4.3 Bayesian optimization (BO)

The BO is an optimization technique based on machine learning concept. It initially rose thanks to the work by Kushner [194], Zhilinskas [195] and Mockus [196]. Then it was popularized after the paper by Jones et al. [197]. The BO is composed of two main parts: statistical modeling and acquisition function. In the Bayesian statistical modeling section, a random set is initially generated. After that, the mean vector and the covariance matrix are calculated based on Gaussian process (GP) regression for the whole set. The acquisition function is then calculated and its optimum value is used to optimize the objective function for the next step (more details referring to section 4 in Ref. [198]).

The BO is a sequential optimization method that solves tasks in a sequence way. Due to its high data efficiency structure, the BO has shown its robustness in the big data applications [199]. Some structural TO problems have been studied by integrating the BO; for example, Lynch et al. [200] investigated a simple structural TO problem (i.e., minimizing the compliance of a 2D beam) to show the possibility of integrating BO in the TO for HXs. In fact, the concept of BO was also employed by Yoshimura et al. [129] and Shimoyama and Komiya [149] to handle HX problems. Both references built a Kriging surrogate model [201] to efficiently evaluate an approximated objective function which will emphatically diminishes the computational time. Apparently, the utilization of BO in the TO of HXs is very limited, and even less than that of GA up to date. The expensive and complex computation of the acquisition function optimization procedure at each iteration [202] may be a reason. Indeed, another disadvantage of BO is the scalability weakness which is represented by the asymptotically increase of the computational time when evaluating the objective function for a new sampling point or when computing the objective function derivatives [203].

2.5 Final Realization

The optimized complex structures obtained by the TO are generally difficult to be fabricated using the conventional manufacturing (CM) techniques. Therefore, additive manufacturing (AM) techniques also called as 3D printing have been applied to manufacture those very complex structures [26],[204]. Table 2.4 compares CM and AM for fabricating the TO-derived structures of HXs. AM is an additive technique that build the structure by adding layers, while the CM techniques are subtractive, which remove material from the structure. Generally, the AM can remove the fabrication shackles of the CMs, but the equipment and materials of metallic AM are still very expensive currently [205]. Importantly, due to the restrictions of AM accuracy, some constraints, including length scale, connectivity, and overhang constraints, etc., should be subjected to the optimized structures obtained by the TO [25]. Those constraints are critically essential to eliminate the un-manufacturable features of the optimized structures. More details of those constraints can be found in Ref.[26].

Table 2.4: Comparison between AM and CM for TO of HXs

Techniques	Advantages	Disadvantages
AM	• Manufacturing ability for complex geometries; • High manufacturability efficiency for complex geometries.	• Relative limited understanding on the manufacturing constraints on the TO optimized structures; • Expensive equipment and materials; • Limited to prototype fabrication; • Limited choices of materials.
CM	• High availability; • High productivity; • Cheap equipment compared to AM.	• Limited manufacturability for TO-derived structures; • Slow fabrication and repairing process for complex TO-derived structures

As for the area of HXs optimization, referring to Fig. 2.6, only few researchers (about 18%) have manufactured the optimized structures obtained by the TO and tested them in practice. As a tradeoff, some researchers realized and tested the engineering simplified version of TO-resulted geometry due to the fabrication difficulty, the advantages of TO being partially or totally lost [59].

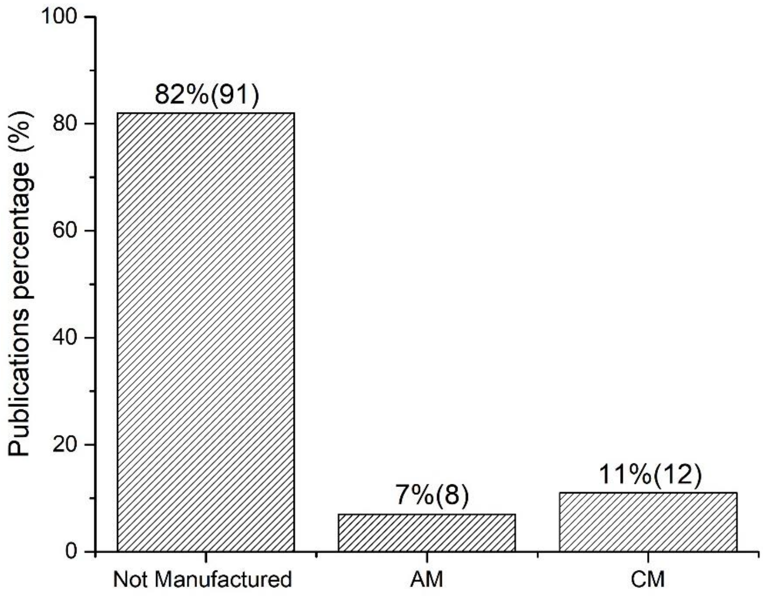

Figure 2.6: Publication Statistics for final realization statuses of optimized HEs. Percentage (Numbers) of publications (until 24- February-2024).

Using AM techniques, some researchers fabricated the TO-optimized HXs to validate their numerical results [42],[55],[69],[84],[93],[112],[155],[206]. For example, Lei et al. [69] manufactured the optimized structure of a passive HX by the TO using 3D stereolithography (SLA) printing technique assisted with investment casting process.. On the other hand, the CM methods [34],[45],[50],[52],[59]–[61],[75],[91],[92], [102],[142], have also been utilized to fabricate some HXs obtained by the TO (mainly the 2D topologies, such as the 2D heat sinks). For instance, as referred by Koga et al. [34], the electrical discharge machining (EDM) was used to manufacture the optimized structure of a heat sink with the help of CNC (computer numerical control) milling. Figures 2.7(a) and (b) illustrate the heat sinks fabricated by the AM [112] and the CM [52] techniques, respectively. Apparently, the AM method can attain more complex structures especially in the 3D case. Note that since the majority of current researches on the TO of HXs does not conduct the final realization of designed structures, there have been rare discussions on the fabricating constraints on the TO-optimized HXs, which should be improved in the further work. One recent paper mention the integration between AM and TO precisely the implementation of the overhang constraint in the TO for HXs [207].

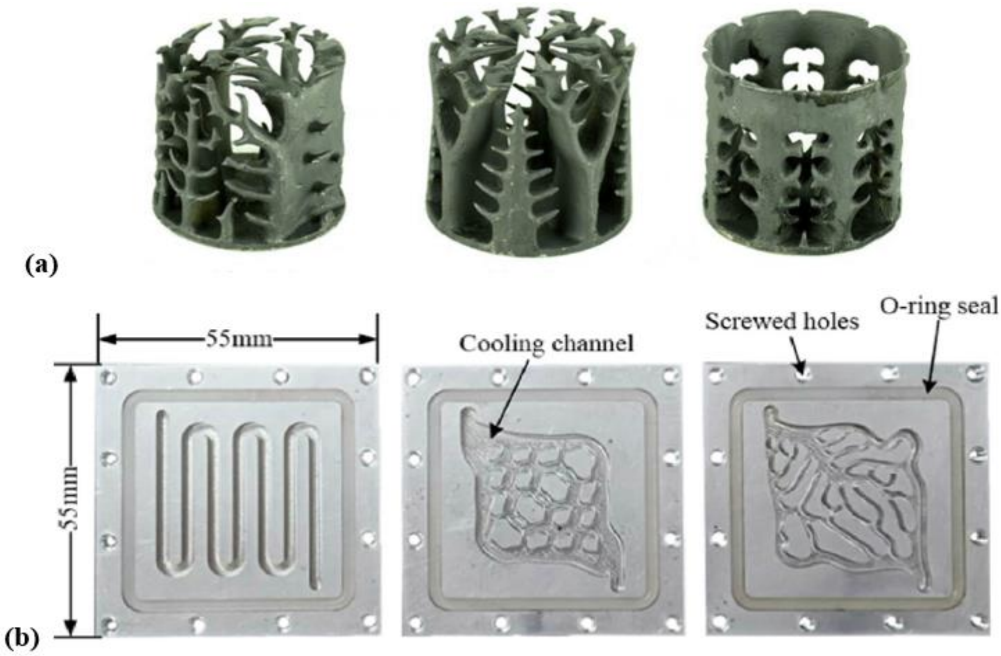

Figure 2.7: (a) Heat sinks manufactured using the AM technique (the SLA printing assisted with investment casting) [69]; (b) Heat sink channels manufactured using the CM technique (the CNC) [52].

Furthermore, in order to give a complete comparison among the existing literature, the papers on the TO of HXs analyzed in the sections above, i.e., Design parametrization, Heat transfer modeling, Optimization, and Final realization, are summarized in Tab. 2.5.

Table 2.5: Summary of researches on TO of HXs analyzed in the sections above.

No.	Reference	Year	Parametrization	Solver	Objective Function	Optimizer	Final Realization
1	Dede [47]	2009	Density (SF1)[1]	FEM	Min (Mean Temperature & Energy Dissipation)	Gradient (MMA)	Not [4]
2	Yoon [108]	2010	Density (SF2)[2]	FEM	Min (Thermal Compliance)	Gradient (MMA)	Not
3	Dede [102]	2012	Density (SF2)	FEM	Min (Mean Temperature & Energy Dissipation)	Gradient (MMA)	CM (N/A)
4	Kontoleontos et al. [101]	2012	Density (SF2)	FVM	Min (Pressure Drop) & Max (Temperature Difference)	Gradient(S-D)	Not
5	Matsumori et al. [33]	2013	Density (SF1)	FEM	Max (Heat Generation)	Gradient (SQP)	Not
6	Marck et al. [64]	2013	Density (SF1)	FVM	Min (Pressure Drop) & Max (The Recoverable Thermal Power)	Gradient (MMA)	Not
7	Koga et al. [34]	2013	Density (SF1)	FEM	Min (Pressure Drop) & Max (Dissipated Heat)	Gradient (SLP)	CM (EDM, CNC)
8	Oevelen et al. [44]	2014	Density (SF1)	FVM	Min (Thermal Resistance)	Gradient (MMA)	Not
9	Alexandersen et al. [65]	2014	Density (SF1)	FEM	Min (Thermal Compliance)	Gradient (MMA)	Not
10	Yaji et al. [134]	2015	LSM	FEM	Max (Heat Generation)	Gradient (R-D)	Not
11	Papazoglou [22]	2015	Density (Multi-flow)	FEM	Max (Exchanged Heat)	Gradient (MMA)	Not
12	Yaji et al. [58]	2015	Density (SF1)	LBM	Min (Pressure Drop) & Max (Exchanged Heat)	Gradient (MMA)	Not
13	Coffin and Maute [135]	2015	LSM	XFEM	Min (Average Temperature)	Gradient (GCMMA)	Not
14	Łaniewski-Wołłk et al. [40]	2016	Density (SF1)	LBM	Max (Exchanged Heat)	Gradient (MMA)	Not
15	Qian and Dede [66]	2016	Density (SF1)	FEM	Min (Average Temperature & Dissipation Energy)	Gradient (MMA)	Not
16	Zhou et al. [154]	2016	Parametrization of [208]	FEM	Max (Reaction Flux)	Gradient (TOSCA)	Not
17	Alexendersen et al. [67]	2016	Density (SF1)	FEM	Min (Thermal Compliance)	Gradient (MMA)	Not
18	Li et al. [156]	2016	Density (N/A[3])	FEM	Min (Heat Potential Capacity)	N/A	Not
19	Yoshimura et al. [129]	2017	LSM	BCM	Min (Pressure Drop) & Max (Bulk Mean Temperature	GA & BO	Not

20	Haertel and Nellis [35]	2017	Density (SF1)	FEM	Max (Thermal Conductance)	Gradient (GCMMA)	Not
21	Zhao et al. [100]	2017	Density (SF2)	FEM	Min (Mean Temperature)	Gradient (MMA)	Not
22	Qian et al. [68]	2017	Density (SF1)	FEM	Min (RMS Temperature & Energy Dissipation)	Gradient (MMA)	Not
23	Sato et al. [136]	2018	LSM	FEM	Max (Heat Generation) & Min (Energy Dissipation)	Gradient (R-D)	Not
24	Haertel et al. [36]	2018	Density (SF1)	FEM	Min (Thermal Resistance)	Gradient (GCMMA)	Not
25	Zeng et al. [45]	2018	Density (SF1)	FEM	Min (Pressure Drop)	Gradient (GCMMA)	CM (CNC)
26	Dilgen et al. [43]	2018	Density (SF1)	FVM	Min (Average Temperature)	Gradient (MMA)	Not
27	Dugast et al. [130]	2018	LSM	LBM	Min (Mean Temperature) & Max (Exchanged Heat)	Gradient(S-D)	Not
28	Ramalingom et al. [103]	2018	Density (SF2)	FVM	Min (Pressure Drop) & Max (Recoverable Thermal Power)	Gradient(S-D)	Not
29	Santhanakrishnan et al. [109]	2018	Density (SF2), LSM	FEM	Min (Thermal Compliance)	Gradient (MMA, H-J)	Not
30	Lei et al. [69]	2018	Density (SF1)	FEM	Min (Thermal Compliance)	Gradient (MMA)	AM (SLA)
31	Sun et al. [37]	2018	Density (SF1)	FEM	Min (Pressure Drop)	Gradient (GCMMA)	Not
32	Lurie et al. [110]	2018	Density (SF2)	FEM	Min (Pressure Drop & Energy Dissipation)	Gradient (MMA)	Not
33	Saglietti et al. [38]	2018	Density (SF1)	FEM	Max (Exchanged Heat)	Gradient (MMA)	Not
34	Pietropaoli et al. [105]	2018	Density (SF2)	VOF	Min (Stagnation Pressure Drop) & Max (Temperature Gain)	Gradient(S-D)	Not
35	Makhija and Beran [99]	2018	Density (SF2)	FEM	Min (Average Temperature)	Gradient (GCMMA)	Not
36	Lv and Liu [48]	2018	Density (SF1)	N/A	Max (Heat Dissipation) & Min (Energy Dissipation)	Gradient (MMA)	Not
37	Subramaniam et al. [39]	2019	Density (SF1)	FVM	Min (Pressure Drop) Max (Recoverable Thermal Power)	Gradient (MMA)	Not

38	Saviers et al. [155]	2019	N/A	FEM	Max (Exchanged Heat)	Gradient (GCMMA)	AM (SLA)
39	Yu et al. [70]	2019	Density (SF1)	FEM	Min (Thermal Compliance & Energy Dissipation)	Gradient (MMA)	Not
40	Asmussen et al. [104]	2019	Density (SF2)	FEM	Min (Thermal Compliance)	Gradient (MMA)	Not
41	Zhang and Gao [53]	2019	Density (SF1)	FEM	Max (Heat Generation)	Gradient (MMA)	Not
42	Jahan et al. [111]	2019	Density (SF2)	FEM	Min (Thermal Compliance)	Gradient (MMA)	Not
43	Kobayashi et al. [49]	2019	Density (SF1)	FEM	Max (Heat Extraction)	Gradient (SLP)	Not
44	Tawk et al. [116]	2019	Density (Multi-flow)	FVM	Min (Pressure Drop) & Max (Exchanged Heat)	Gradient (MMA)	Not
45	Zeng and Lee [50]	2019	Density (SF1)	FEM	Min (Pressure Drop)	Gradient (GCMMA)	CM (CNC)
46	Yan et al. [51]	2019	Density (SF1)	FEM	Min (Maximum Temperature)	Gradient (MMA)	Not
47	Li et al. [60]	2019	Density (SF1)	FEM	Min (Pressure Drop) & Max (Exchanged Heat)	Gradient (SQP)	CM (CNC)
48	Li et al. [52]	2019	Density (SF1)	FEM	Min (Dissipation Energy) & Max (Exchanged Heat)	Gradient (SQP)	CM (CNC)
49	Dong and Liu [71]	2019	Density (SF1)	FEM	Min (Thermal Resistance & Pressure Drop & Energy Dissipation)	Gradient (SQP)	Not
50	Ghosh and Kapat [46]	2019	Density (SF1)	FVM	Min (Pressure Drop) & Max (Temperature Rise)	Gradient(S-D)	Not
51	Hu et al. [72]	2019	Density (SF1)	FEM	Min (Mean Temperature & Energy Dissipation)	Gradient (GCMMA)	Not
52	Kambampati et al. [131]	2020	LSM	FEM	Min (Thermal Compliance)	Gradient (SLP)	Not
53	Zhang et al. [54]	2020	Density (SF1)	FEM	Max (Exchanged Heat)	Gradient (GCMMA)	Not
54	Zeng et al. [57]	2020	Density (SF1)	FEM	Min (Average Temperature)	Gradient (GCMMA)	Not
55	Sun et al. [73]	2020	Density (SF1)	FEM	Min (Average Temperature)	Gradient (MMA)	Not
56	Zhang et al. [74]	2020	Density (SF1)	FEM	Min (Average Temperature)	Gradient (GCMMA)	Not
57	Francisco et al. [112]	2020	Density (SF2)	FEM	Max (Thermal Conductivity)	Gradient (MMA, MOSQP)	AM (N/A)
58	Høghøj et al. [117]	2020	Density (Multi-flow)	FEM	Min (Enthalpy Difference)	Gradient (MMA)	Not

59	Troya et al. [118]	2020	Multi-flow, LSM	FEM	Max (Exchanged Heat)	Gradient (MMA, NSA)	Not
60	Lee et al. [113]	2020	Density (SF2)	FEM	Min (Thermal Resistance)	Gradient (MMA)	Nolt
61	Feppon et al. [132]	2021	LSM	FEM	Max (Exchanged Heat)	Gradient (NSA)	Not
62	Pietropaoli et al. [106]	2021	Density (SF2)	FVM	Min (Stagnation Pressure Drop) & Max (Temperature Rise)	Gradient (S-D)	Not
63	Dong and Liu [63]	2021	Density (SF1)	FEM	Min (Energy Dissipation) & Max (Recoverable Thermal Power)	Gradient (GCMMA)	Not
64	Kobayashi et al. [119]	2021	Density (Multi-flow)	FEM	Max (Exchanged Heat)	Gradient (SLP)	Not
65	Mekki et al. [148]	2021	Explicit	FVM	Max (Exchanged Heat) & Min (Pressure Drop)	GA	Not
66	Lee et al. [59]	2021	Density (SF1)	FVM	Min (Average Temperature & Dissipation Energy)	Gradient (GCMMA)	CM (Laser cutting)
67	Mario et al. [133]	2021	LSM	FEM	Max (Exchanged Heat) & Min (Energy Dissipation)	Gradient (R-D)	Not
68	Zhao et al. [77]	2021	Density (SF1)	FEM	Min (Average Temperature)	Gradient (GCMMA)	Not
69	Zhou et al. [75]	2021	Density (SF1)	FEM	Min (Temperature Difference, Average Temperature, Energy Dissipation)	Gradient (MMA)	CM (Machining)
70	Han et al. [55]	2021	Density (SF1)	FEM	Min (Temperature Difference & Energy Dissipation & Average Temperature)	Gradient (GCMMA)	AM (N/A)
71	Mo et al. [42]	2021	Density (SF1)	N/A	Min (Average Temperature & Energy Dissipation)	Gradient (MMA)	AM (N/A)
72	Ghasemi and Elham [107]	2021	Density (SF2)	FEM	Min (Thermal Resistance & Pressure Drop)	Gradient (GCMMA)	Not
73	Liu et al. [76]	2021	Density (SF1)	FEM	Min (Pumping Power, Mean and Standard Deviation of The Temperature)	Gradient (GCMMA)	Not
74	Liu et al. [56]	2021	Density (SF1)	FEM	Max (Exchanged Heat) & Min (Energy Dissipation)	Gradient (MMA)	Not
75	Zhao et al. [41]	2021	Density (SF1)	FEM	Min (Average Temperature Rise)	Gradient (MMA)	Not

76	Tang et al. [114]	2021	Density (SF2, Multi-flow)	FVM	Min (Mean Temperature & Pressure Drop)	Gradient (MMA)	Not
77	Chen et al. [78]	2021	Density (SF1)	FEM	Max (Heat Generation)	Gradient (SQP)	Not
78	Yaji et al. [62]	2021	Density (SF1)	FEM	Max (Exchanged Heat) & Min (Energy Dissipation)	Gradient (SLP), GA	Not
79	Li et al. [142]	2021	LSM	FEM	Min (Average Temperature)	Gradient (MMA)	CM (Milling)
80	Ghosh et al. [80]	2021	Density (SF1)	FVM	Max (Gained energy) & Min (Power lost)	Gradient (S-D)	Not
81	Qian et al. [61]	2021	Density (SF1)	FEM	Min (RMS[5] Temperature & Energy Dissipation)	Gradient (MMA)	CM (CNC)
82	Shimoyama and Komiya [149]	2022	Explicit	FVM	Max (Heat transfer rate) & Min (Material cost)	GA & BO	Not
83	Li et al. [137]	2022	LSM	FEM	Min (Thermal Compliance)	Gradient (R-D)	Not
84	Yu et al. [82]	2022	Density (SF1)	FVM	Min (Maximum Temperature)	Gradient (MMA)	Not
85	Zhou et al. [84]	2022	Density (SF1)	FEM	Min (Energy Dissipation, Average Temperature & Temperature Difference)	Gradient (GCMMA)	AM (N/A)
86	Zou et al. [83]	2022	Density (SF1)	FEM	Min (Average temperature & Pumping power)	Gradient (SQP)	Not
87	Marshall and Lee [85]	2022	Density (SF1)	FEM	Min (Pressure in fin area of the fluid)	Gradient (N/A)	Not
88	Yeranee et al. [86]	2022	Density (SF1)	FEM	Min (Pressure Drop)	Gradient (GCMMA)	Not
89	Lin et al. [138]	2022	LSM	XFEM	Min (Average Temperature)	Gradient (GCMMA)	Not
90	Xie et al. [79]	2022	Density (SF1)	FEM	Min (Pressure Drop)	Gradient (GCMMA)	Not
91	Huang et al. [81]	2022	Density (SF1)	FEM	Min (Average Temperature)	Gradient (SQP)	Not
92	Xia et al. [96]	2023	Density (SF1)	FEM	Max (Heat generation), Min (Energy dissipation)	Gradient (SQP)	Not
93	Rogié and Andreasen [98]	2023	Density (SF1)	FEM	Min (Mean temperature)	Gradient (MMA)	Not
94	Zhang et al. [141]	2023	LSM	FEM	Max (Heat generation), Min (Energy dissipation)	Gradient (MMA)	Not
95	Zhang et al. [94]	2023	Density (SF1)	FEM	Max (Heat transfer rate)	Gradient (GCMMA)	Not
96	Petrovic et al. [206]	2023	Density (SF1)	FEM	Max (Heat transfer rate)	Fictitious interface	AM (3D printer)

						energy	
97	Noël and Maute [157]	2023	LSM	XFEM	Min (Average Temperature)	Gradient (GCMMA)	Not
98	Luo et al. [140]	2023	LSM	LBM	Min (Mean temperature), Min (pressure drop)	Gradient (R-D)	Not
99	Wang et al. [87]	2023	Density (SF1)	FEM	Max (Heat transfer rate) & Min (Energy Dissipation)	Gradient (MMA)	Not
100	Wang et al. [88]	2023	Density (SF1)	FVM	Min (Maximum temperature)	Gradient (MMA)	Not
101	Wang et al. [209]	2023	Density (SF1)	FEM	Max (heat transfer), Max (outlet enthalpy), Max (solid temperature), Min (kinetic energy difference)	Gradient (SQP)	Not
102	Lee et al. [120]	2023	Density (Multi-flow)	FEM	Max (Heat source)	Gradient (GCMMA)	Not
103	Zhan et al. [91]	2023	Density (SF1)	FEM	Max (heat generation)	Gradient (SQP)	CM (CNC)
104	Tang et al. [93]	2023	Density (SF1)	FEM	Min (temperature difference), Min (Mean temperature), Min (pressure drop)	Gradient (N/A)	AM (3D printer)
105	Wu [89]	2023	Density (SF1)	FEM	Min (temperature variation),Min (Energy dissipation)	Gradient (SQP)	Not
106	Sun et al. [92]	2023	Density (SF1)	FEM	Max (Heat generation), Min (Energy dissipation)	Gradient (MMA)	CM (CNC)
107	Zhong et al. [97]	2024	Density (SF1)	FEM	Min (Mean temperature), Min (Energy dissipation)	Gradient (MMA)	Not
108	Wang et al. [95]	2024	Density (SF1)	FEM	Min (Mean temperature)	Gradient (MMA)	N/A
109	Navah et al. [115]	2024	Density (SF2)	FEM	Min (Mean temperature)	N/A	Not
110	Adil et al. [90]	2024	Density (SF1)	FEM	Min (total mass)	Gradient (MMA)	Not
111	Chen et al. [139]	2024	LSM	FVM	Max (Heat transfer rate) & Min (drag force)	Gradient (S-D)	Not
112	Li et al. [192]	2024	Explicit	FVM	Min (Peak temperature)	GA	Not

[1] SF1: single flow with ρ=1 fluids, ρ=0 solids; [2] SF2: single flow with ρ=0 fluids, ρ=1 solids; [3] N/A: Not Announced; [4] Not: Not Manufactured; [5] RMS: Root mean square

2.6 Some New Trends

Here, we will move to discuss of some emerging schemes aimed to improve the efficiency (i.e., reducing computational time and memory storage) of TO not limited to the area of HXs. Currently many of these novel schemes are designed for the structural TO problems; nevertheless, it is possible to transfer some of them to deal with the HXs problems.

2.6.1 Machine learning (ML)

With the rapid development in the recent years, the ML technique (a subset of AI) has become a powerful tool to handle various engineering problems. As for transport phenomena, the ML has exhibited the ability of predicting their solutions [197]–[200], due to its high potential of learning from existing data-sets. Using different strategies, the ML algorithms can be coupled with the density-based TO mainly for the structural problems at the present stage [214]–[217]. As for the TO of HXs, a data driven TO based on EA was suggested by Yaji et al. [62] for a heat sink under forced convection. In this research, a variational autoencoder [218] was implemented to perform the crossover operation by generating a new dataset. In a recent study, Wang et al. [88] proposed a deep learning assisted with the TO of 3D coolant channels for the purpose of accelerating the optimization process and increasing the performance simultaneously. The ML proved the ability of increasing the TO efficiency by predicting the optimized structures for heat transfer problems with negligible time [88],[219]. However, currently the research combining the ML and the TO for HXs is still rare, which may be attributed to the complexity of conjugating heat transfer (especially the fluid flow part) and the complicated structures of HXs. It requires more studies to clarify how to integrate the ML in the TO involving fluids and whether the ML can improve the efficiency.

2.6.2 Model order reduction (MOR)

The MOR is an approach aiming to decrease the complexity of models. It reduces the full original model into a reduced one by capturing the fundamental characteristics and neglecting the unimportant ones under certain accuracy [220]. The MOR methods were first proposed in 1980s [221]–[223]. For instance, Zhao et al. [100] proposed a poor man’s approach to reduce the computational time for the TO of cooling channels: a simplified model was derived by imposing the Darcy flow model on NS equation and neglecting the effect of body force term. In the TO of a heat sink, Asmussen et al. [104] suggested a reduced order model by making some assumptions on the governing equations, which significantly reduce the number of degree of freedoms. Even with a high simplification, the reduced model obtains the subjectively analogous results with the full-based model [224]. Nevertheless, the simplifications are largely dependent on the knowledge of designers, and a poor simplification may degrade the accuracy and even cause severe computational issues represented mainly by unrealistic results and modeling problems. For instance, when the MOR technique is applied to NS equations under unsteady conditions or for turbulent flows, some computational problems frequently emerge [225].

2.6.3 Moving morphable components (MMC)

The MMC-based TO was originally proposed in 2014 by Guo et al. [226] then enhanced by Zhang et al. [227] for the 2D structural problems. Thereafter, the MMC method is extended to the 3D TO [228],[229]. It represents the design domain by using several structural components. In the optimization process, the mathematical features described by center coordinates, width, length and inclination angles of these components are updated for achieving an optimized structure. In 2019, Yu et al. [70] proposed a density-based TO for a 2D heat transfer problem using the MMC. To take an advantage over the traditional MMC, Li et al. [142] utilized the quadratic Bézier curve permitting for more movement flexibility of the component. In a recent attempt, Yu et al. [82] suggested a component-based representation of the heat source distribution with various-intensities for the TO of a liquid cooled heat sink. The MMC-based TO can obtain optimized shapes in an explicit way, which can avoid the post-processing problems, like intermediate design variables, and checkboards, etc. [226]. Furthermore, the number of design variables is reduced compared to other implicit techniques, which may decrease the computational cost [227]. However, the design (including its geometry and initial distribution) of the domain components, that significant influences both the efficiency and the accuracy of the MMC-based TO, largely depends on the experience of designers. Moreover, as yet, it has been limited to some 2D HX problems, which may be attributed to the difficulties of explicit methods in describing the solid/fluid interface for 3D complex structures [147].

2.7 Conclusions and Perspectives

The present chapter provides a comprehensive review on the literature of the TO for HXs in the most recent years. Each stage of the TO is analyzed carefully with the statistical figures and comparison tables. Our review shows that the current TO methods are not powerful enough yet to handle the industrial HXs in energy systems: (a) the majority of the researches only deal with the 2D single-flow problems with single objective, limited to the relatively simple flow patterns (like the laminar flow and the turbulence described by the Reynolds-averaged models); (b) merely a small portion of work has manufactured and tested the TO-obtained structures in practice, and few discussions have been conducted on the fabricating constraints of the TO-obtained HXs. Currently, a combination of the density-based method, the FEM, and the gradient-based optimization is the most popular TO method for HXs, since it is a straight-forward transfer from the structural mechanics to the conjugate heat transfer. However, the conjugate heat transfer holds some very different features compared to the structural mechanics, which may not be well addressed in the framework initially developed for the structural TO. Furthermore, three emerging schemes, i.e., ML, MOR, and MMC, aimed to improve the efficiency of TO are discussed. They are initially designed for the structural TO problems and show good performance in that area. Some of them have been extended to handle some simple heat transfer problems, and there has been limited evidence to prove that they are effective in improving the efficiency of the TO for conjugate heat transfer. Apparently, future effort is still required for the TO of HXs, particularly to:

(1) Provide a detailed examination of the constraints and limitations associated with the current TO for conjugate heat transfer.
(2) Conduct the TO on realistic narrow design domains, which may correspond to compact HXs.
(3) Execute the TO on dual flow HXs.
(4) Perform experimental validation of the TO-acquired HXs.
(5) Provide physical interpretations of the TO-derived designs.
(6) Perform an in-depth investigation of various TO’s input parameter setting impact on the derived topology.
(7) Test the effect of the fluid temperature dependent properties on the TO-acquired topology for dual flow HXs.

(8) Investigate the effect of the different gradient optimizers on the TO-acquired topologies.

The recognition of these literature gaps serves as a compelling motivation for us to undertake the research of this Ph.D. by using numerical and experimental approaches to elaborate the limitation of the current TO and propose novel optimized HX designs, which will be presented in the following chapters.

Chapter 3: Convergent-divergent design of fins for improving the thermo-hydraulic performance of heat exchangers assisted by a dual-flow topology generator

Chapter Summary

This chapter addresses the density-based topology generation within a 2D domain that represents one elementary unit of a counter-flow plate heat exchanger (PHE). The objective of the topology generator (TG) is to maximize the effectiveness, resulting in a novel convergent–divergent fin topology. Due to the high sensitivity of the TG setting parameters (including Reynolds number, Prandtl Number and thermal conductivity ratio), their effects on the acquired topologies are investigated. To assess the efficacy of this newly-proposed design guideline of fins, a simplified HX (heat exchanger) with convergent-divergent (C-D) rectangular fin distribution is introduced and compared with the TG-acquired structures and a conventional uniform fin design. The comparative analysis is performed by conducting a set of computational fluid dynamic (CFD) simulations on the five structures (three TG-obtained, one simplified and one conventional) under two different cases (case1: water-water, case2: water-oil as cold and hot working fluids respectively) that encompass a wide range of Reynolds numbers (300-3000). The results show a thermo-hydraulic improvement of the TG-acquired and simplified HXs compared to the conventional one with an enhancement in the performance evaluation criteria (PEC) number up to about 23% and 10% for case 1 and up to 36% and 16% for case 2, respectively. Eventually, a detailed physical interpretation of the generated topology is delivered. Lastly, a deficiency in the employed methodology has been identified by scrutinizing the velocity field of the derived topology, which make it a generation process (TG) rather than an optimization one (TO). The current chapter provides a novel guideline for fin design inspired by topological features, which could be much helpful to improve the thermo-hydraulic performance of HXs.

Keywords of the Chapter:

Topology generator, Heat exchanger, Convergent-divergent, Conjugate heat transfer, fin design.

3.1 Introduction

How to improve the performance of HXs has been for a long time an essential topic in both industrial and academic communities. Over the past decades, tremendous active and passive methods have been developed for improving the effectiveness of HXs [230]. It has been well demonstrated that the techniques utilizing extended surfaces as fins are the most effective ones in practice to enhance heat transfer rates by disrupting fluid flows and increasing surface areas, with the drawback of largely-increased hydraulic loss [231], [232]. Reducing the hydraulic losses is as crucial as intensifying the exchanged heat in the HXs, particularly for the HX applications that operate under low to moderate pumping power as the gasket plate heat exchangers (PHE).

The proper design of extended surface i.e. fins, including shape, size, and arrangement, is of importance for achieving a good trade-off between heat transfer rate enhancement and pumping power requirement, especially for compact HXs like PHE [233],[234]. At the beginning stage, researchers generally designed fins intuitively based on their physical background and understandings [235]–[237]. Afterwards, with the development of computer techs, optimal designs of fins become possible with the assistance of numerical simulation and various optimization algorithms. Size/shape optimization of fins, which cannot significantly alter the prescribed configuration or arrangement set by designers, has been developed for years [238]–[241]. Most recently, topology optimization (TO), which acts on the topology of geometry by spatially optimizing the distribution of fluid and solid phases and thus theoretically holds maximum degrees of freedom in optimization, has attracted increasing attention from researchers [242], [243], [1].

The acquired topological configurations by the TO are conspicuously affected by the choice of input parameters justifying the notable sensitivity of the TO to these input parameters. Currently, the TO is mainly conducted on one-flow HXs (more than 90%), according to the statistics in our recent review paper [1] that covers most of the relevant publications in the past two decades, while the HXs in practice frequently work with at least two flows. Moreover, the majority of design problems generally introduce the wide (Length/width < 2) design domains that allows the structures to evolve freely to generate highly complex structures [244]–[246], but this may contradict with some actual applications where the fluid area is considerably restricted as in compact HXs. In addition, in-depth physical interpretation on the optimized structures is always needed for better understanding and possible generalization of TO-derived results.

Considering the issues above, the present chapter employs the dual-flow density-based topology generation to handle the heat transfer within the narrow 2D design domain (Length/width=25) that corresponds to one periodic unit within counter dual-flow PHEs under steady-state and laminar conditions. A relatively generalizable design guideline of fins with convergent-divergent distribution, which may achieve the simultaneous thermo-hydraulic improvement, is acquired using a TG and verified with a series of CFD simulations. Moreover, the underlying mechanisms behind the obtained fin topology are analyzed carefully based on the synergy field theory [247].

Finally, upon scrutinizing the acquired topology, the deficiency in the impermeability intensity is evident, as it fails to enforce a zero velocity in the solid phase. This inadequacy discovered in the employed methodology classifies it as a topology generation process rather than a topology optimization (TO) one.

3.2 Problem Formulation of the Topology generator

3.2.1 Simplification and Assumptions

Due to the massive computational time and cost of the topology generation process, it is difficult to conduct it on an industrial heat exchanger that holds the complicated structure and flow patterns. Accordingly, the 3D industrial PHE is simplified to a 2D counter flow PHE's unit as seen in Fig. 3.1. Based on this simplification, several reasonable assumptions are considered:

(1) The 2D counter flow PHE's unit is insulated, no heat loss to the surrounding
(2) The effect of heat and mass transfer is neglected in the third direction.
(3) The fluid properties are assumed to be temperature independent
(4) Steady-state conditions

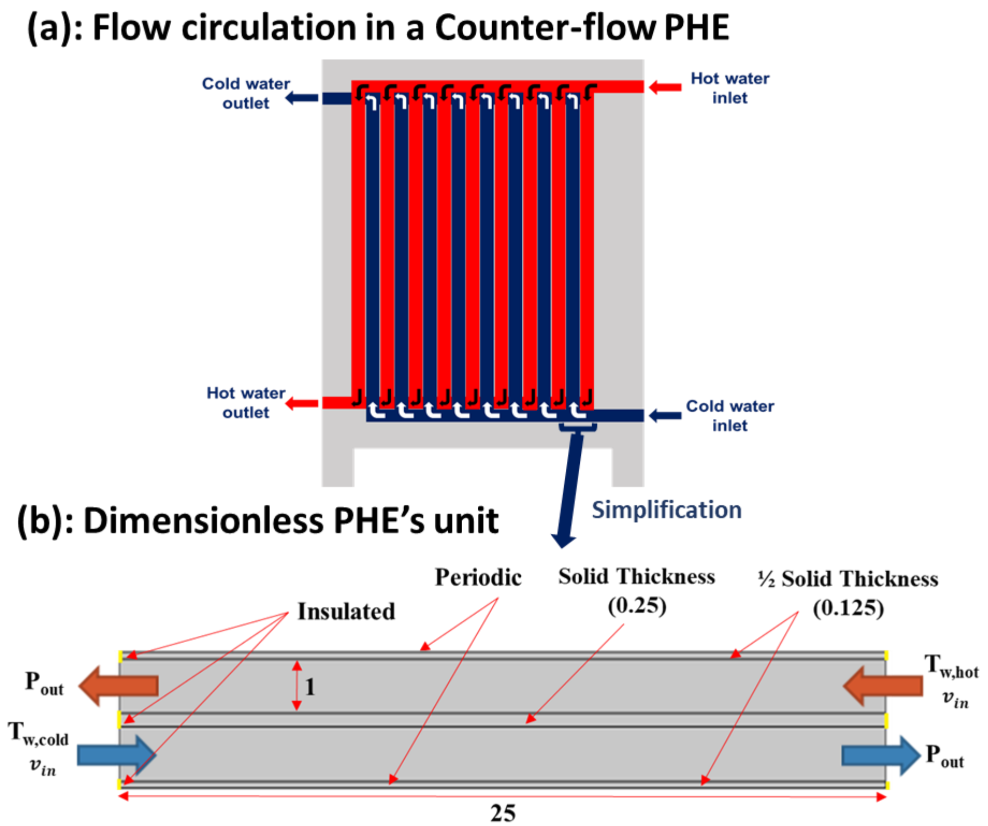

Figure 3.1: (a): Flow circulation in counter-flow PHE, **(b):** simplified dimensionless PHE's unit.

3.2.2 Conjugate heat transfer modeling

The conjugate heat transfer physics in HXs combines the fluid dynamics and heat transfer models. The incompressible and steady-state fluid flow in the HX is modelled using the dimensionless continuity and momentum equations which are given as respectively [60]:

$$\nabla^*.\boldsymbol{v}^* = 0$$
$$(\boldsymbol{v}^*.\nabla^*)\boldsymbol{v}^* = -\nabla^*P^* + \frac{1}{Re}.\nabla^{*2}\boldsymbol{v}^* - \boldsymbol{F}(\gamma) \tag{5}$$

where $\boldsymbol{v}^*$ is the dimensionless velocity vector, P^* the dimensionless pressure field, γ is the design variables and *Re* is the Reynolds number. The dimensionless variables are defined with respect to the width of the channel denoted as L, and a characteristic speed designated as the inlet velocity v_{in}. These dimensionless variables are determined based on the subsequent formulations:

$$\nabla^* = L\nabla$$
$$v^* = \frac{\boldsymbol{v}}{v_{in}} \tag{6}$$
$$P^* = \frac{P - P_{out}}{\rho v_{in}^2}$$

where P_{out} is the outlet pressure (Pa) and ρ is the density of the fluid (kg/m^3). Moreover, the Re denotes the ratio between the inertia over the viscous terms defined as:

$$Re = \frac{\rho v_{in} D_h}{\mu} \tag{7}$$

μ is the fluid viscosity and D_h is the hydraulic diameter or characteristic length of the design domain. In the density-based topology generation, the Momentum equation needs to be modified by adding a Brinkman friction $\boldsymbol{F}$ coefficient to dominate the design domain treated as porous medium which can be defined as follow:

$$\boldsymbol{F}(\gamma) = \alpha^*(\gamma)\boldsymbol{v}^* \tag{8}$$

where α^* is the dimensionless inverse permeability that must be interpolated between the solid and fluid phases to define the optimized flow path (the detailed interpolation function equations will be discussed in the TG section).

The heat transfer will be studied in the solids that are dominated by conduction and in the fluids that are dominated by convection. The steady-state dimensionless energy equation is utilized to model the heat transfer of the HX.

$$RePr_f(\boldsymbol{v}^*.\nabla^* T^*) - \nabla^*.(C_k(\gamma)\nabla^* T^*) = 0 \tag{9}$$

where Pr_f is the fluid Prandtl number that represents the ratio of the momentum over the thermal diffusivity, C_k is the thermal conductivity ratio between the solid and fluid phases and T^* is the dimensionless temperature field. The previous mentioned parameters can be expressed as:

$$Pr_f = \frac{\mu C_p}{k_f}$$
$$C_k = \frac{k_s}{k_f} \tag{10}$$
$$T^* = \frac{T - T_{in,cold}}{T_{in,hot} - T_{in,cold}}$$

where k_f & k_s are the thermal conductivity of the solid and fluid respectively (W.m^{-1}.K^{-1}) , C_p is the specific heat of the fluid phase (J.kg^{-1}.K^{-1}), μ is the fluid dynamic viscosity (Pa.s) and $T_{in,cold}$, $T_{in,hot}$ are the inlet temperatures of the cold and hot fluid respectively (K). It is noteworthy to mention that the primary objective of the governing equation's non-dimensionalization is the reduction of the TG's input parameters, which will facilitate the parametric investigation study (presented in section 3.5) by allowing a concentrated analysis on the crucial TG's input parameters.

3.2.3 Boundary Conditions

As illustrated in Fig. 3.1b, a set of Dirichlet boundary conditions are imposed at the inlet of each fluid by setting a uniform velocity and temperature profiles as follow:

$$\begin{gathered} -\boldsymbol{v}^{*}.\boldsymbol{n} = 1 \Longleftrightarrow \text{on } \Gamma_{in,cold} \text{ and } \Gamma_{in,hot} \\ T^{*} = 0 \Longleftrightarrow \text{on } \Gamma_{in,cold} \\ T^{*} = 1 \Longleftrightarrow \text{on } \Gamma_{in,hot} \end{gathered} \tag{11}$$

where $\boldsymbol{n}$ is the normal vector to the corresponding boundary outwardly oriented to the design domain. Similarly, a uniform pressure and outflow conditions are set at the outlet boundaries of fluid flows as hydraulic and thermal boundary conditions respectively.

$$\begin{gathered} P^{*} = 0 \Longleftrightarrow \text{on } \Gamma_{out,cold} \text{ and } \Gamma_{out,hot} \\ -\boldsymbol{n}.\nabla T^{*} = 0 \Longleftrightarrow \text{on } \Gamma_{out,cold} \text{ and } \Gamma_{out,hot} \end{gathered} \tag{12}$$

The six yellow boundaries of the HX mentioned in the Fig. 3.1b are assumed to be insulated i.e., no heat loss to the surrounding. In addition, a periodic boundary condition is assigned at the top and bottom boundaries of the HX to consider the heat transfer effect from the upper and lower units.

3.3 Topology generator (TG)

In this subsection, the detailed methodology the density-based (porosity-based) topology generation on a dual-flow 2D HX unit is presented.

3.3.1 Design Parametrization

The density-based parametrization is based on representing the design domain (Fluid channels in the present case) by densities or porosities (design variables) to parametrize the fluid and solid phases. In this study, the initial density distribution has been set to an intermediate design variable, γ_i=0.5, i.e., each mesh element is composed initially of a porous medium that contains 50% fluid and 50% solid. Throughout the TO procedure, the density values (γ) can exhibit a continuous variation ranging from 0 (fluid) to 1 (solid). As for the interpolation scheme, the inverse permeability is interpolated between the solid and fluid phases using the following formula [244]:

$$\alpha^*(\gamma) = \alpha^*_{max} * q * \frac{\gamma}{q + 1 - \gamma}$$
$$\alpha^*_{max} = \frac{L\alpha_{max}}{\rho v_{in}} \tag{13}$$

where α^*_{max} is the maximum impermeability value and q is a penalization coefficient.

When the value of γ=0, $\alpha \rightarrow 0$, $f \rightarrow 0$, which implies that the water can freely flow through this element and the fluid phase is occupied in this element. By contrast, when the value of γ=1, $\alpha \rightarrow \alpha_{max}$, $f \rightarrow f_{max}$, a huge frictional force is applied on the fluid flow to ensure its negligible velocity, which is consistent with the behavior of the solid phase. Concerning the thermal properties interpolation, the thermal conductivity ratio can be interpolated between solid and fluid phases using the classical SIMP (solid isotropic material with penalization) interpolation function [248].

$$C_k(\gamma) = 1 + (C_k - 1)\gamma^p \tag{14}$$

where p is a penalty factor. In order to avoid the mixing of both fluids during the topology generation procedure, the separating solid is considered as fixed solid and excluded from the design domain.

3.3.2 Finite element analysis (FEA)

The governing equations (GEs) presented in Eqs. (5), (9) are discretized in space and solved using Finite element method (FEM). Due to the weak coupling between the two physics (fluid flow and heat transfer), the FEM solver implemented in COMSOL 6.0 is used to sequentially solve the multiphysics problem starting by computing the velocity distribution using Eqs (5) from a pressure initial guess. Then, the velocity field is substituted in the energy equation (Eq.9) to calculate the temperature distribution over the HX. As for the GE's space discretization, a fine mesh with mapped quadratic P1 linear element is built.

3.3.3 Objective and constraints

In this research, the primary objective of the TG is to maximize the effectiveness (ϵ) of the HX which can be expressed as [249]:

$$\epsilon = \frac{\left(\rho C_p\right)_{cold} \times \int_{\Gamma out,cold} \boldsymbol{v}^* T^* \, d\Gamma - \int_{\Gamma in,cold} \boldsymbol{v}^* T^* \, d\Gamma}{\left(\rho C_p\right)_{min} \times \int_{\Gamma in,hot} \boldsymbol{v}^* T^* \, d\Gamma - \int_{\Gamma in,cold} \boldsymbol{v}^* T^* \, d\Gamma} \tag{15}$$

To constraint the non-linear problem, a set of constraints have been imposed. First, a relaxation is applied on the design variable γ to transform it from discrete to continuous $\gamma \in [0,1]$. Moreover, the governing equations presented in Eqs. (5) & (9) should be also set as a constraint to ensure that their residuals will be zero in each iteration. Eventually, a solid fraction is imposed to constraint the amount of solid generated in the flow channels. Thus, the TG's mathematical problem can be summarized as follows:

$$\begin{aligned} &Find\ \gamma \\ &Max\ \epsilon\ (Eq.15) \\ &s.t \begin{cases} 0 \le \gamma \le 1 \\ Eqs.(5),(9) \\ \int_{\Omega} \gamma d\Omega \le v_{fs} \end{cases} \end{aligned} \tag{16}$$

where v_{fs} is the maximum allowed solid volume fraction and Ω is the design domain.

3.3.4 Discrete Adjoint analysis and topology updates

Due to the implicit dependency of the state variables (pressure, velocity and temperature) and the objective function with the design variable, it is impossible to calculate the derivative (sensitivity) of the objective function directly. The discrete adjoint method is used to perform the sensitivity analysis [250]. It consists of transforming the constrained problem into unconstrained by setting up a Lagrangian function that requires the multiplication of the constraints by Lagrange multiplier (adjoint variables):

$$L = \epsilon + \lambda_u^{\mathrm{T}} R_u + \lambda_T^{\mathrm{T}} R_T \tag{17}$$

where R_u and R_T are the residuals of the momentum and energy equations respectively, λ_u and λ_T are the adjoint variables vector. The total derivative of the lagrangian function with respect to the design variables (γ) can be written as follows:

$$\frac{dL}{d\gamma} = \frac{d\epsilon}{d\gamma} + \lambda_u^{\mathrm{T}} \frac{dR_u}{d\gamma} + \lambda_T^{\mathrm{T}} \frac{dR_T}{d\gamma} \tag{18}$$

Then, the chain rule is used to compute the derivative of the Lagrange function:

$$\begin{aligned} \frac{dL}{d\gamma} = \frac{d\epsilon}{d\gamma} + \lambda_u^{\mathrm{T}} \frac{dR_u}{d\gamma} + \lambda_T^{\mathrm{T}} \frac{dR_T}{d\gamma} + \left(\frac{d\epsilon}{du} + \lambda_u^{\mathrm{T}} \frac{dR_u}{du}\right) \frac{du}{d\gamma} \\ + \left(\frac{d\epsilon}{dT} + \lambda_T^{\mathrm{T}} \frac{dR_T}{dT}\right) \frac{dT}{d\gamma} \end{aligned} \tag{19}$$

The discrete adjoint approach assumes the verification of the adjoint vector with the equation multiplied by du/dγ and dT/dγ, to avoid the computation of such difficult terms. Accordingly, the adjoint equations can be formulated as follow:

$$\begin{gathered} \left(\frac{dR_T}{dT}\right)^{\mathrm{T}} \lambda_T = \left(-\frac{d\epsilon}{dT}\right)^{\mathrm{T}} \\ \left(\frac{dR_u}{du}\right)^{\mathrm{T}} \lambda_u = -\left[\left(\frac{d\epsilon}{du}\right)^{\mathrm{T}} + \left(\frac{dR_T}{du}\right)^{\mathrm{T}} \lambda_T\right] \end{gathered} \tag{20}$$

Upon the computation of the adjoint variables (λ_u,λ_T) through the aforementioned adjoint equations (Eq. 20), the sensitivities of the objective function can be directly assessed using Equation 18. Furthermore, the sensitivities computed are subsequently projected back, employing the chain rule also in this process:

$$\frac{d\epsilon}{d\gamma} = \frac{d\epsilon}{d\gamma} + \frac{d\epsilon}{d\gamma_p} \frac{d\gamma_p}{d\gamma_f} \frac{d\gamma_f}{d\gamma} \tag{21}$$

where γ_f and γ_p are the filtered and projected design variables. The $(d\gamma_p)/(d\gamma_f)$ term of Eq. 21 is determined through the differentiation of the hyperbolic projection equation (Equation 23), as elaborated in the subsequent section. The generation process is carried out using the FEM (Finite element method)-based software COMSOL multiphysics. Thereafter, the globally convergent method of moving asymptotes (GCMMA) [251], which is built in the COMSOL software package, is used with 0.1 external move limits to iteratively updates the design variables distribution. The global optimization process is judged to be converged when the criterion $|L_k - L_{k-1}| < 1 \times 10^{-3}$ is achieved.

3.3.5 Filter and projection

During the topology generation, filters are necessary to avoid the numerical instabilities (checkerboard, mesh dependency, local optimum, etc.) caused by the ill-posedness of the TG problems [252]. To avoid this issue, filters and projection techniques are adopted to control the computed design variables. For the filtering technique, the Helmholtz PDE filter [253] is adopted to obtain an averaged filtered design variables γ_f:

$$\gamma_f = R^2 \nabla^2 \gamma_f + \gamma \tag{22}$$

where *R* is the filter radius which is considered as the mesh element size in the current study. After the filtering process, an intermediate density area near the solid-fluid interface is generated. In order to reduce it, the filtered design variables are projected using the smooth Heaviside hyperbolic tangent projection [254]:

$$\gamma_p = \frac{\tanh\left(\beta\left(\gamma_f - \gamma_\beta\right)\right) + \tanh\left(\beta\gamma_\beta\right)}{\tanh\left(\beta\left(1 - \gamma_\beta\right)\right) + \tanh\left(\beta\gamma_\beta\right)} \tag{23}$$

where γ_p is the projected design variable, β is the projection slope and γ_β is the projection point.

3.3.6 Continuation scheme

A continuation strategy is applied on the penalization coefficients (*q* and *p*) of the interpolation functions and the projection slope (β). The continuation sequence is chosen to attenuate a possible convergence to a local optimum. The proposed continuation scheme is composed of six steps as shown in Tab. 3.1. For the first three steps, the parameters values are set to low values to stabilize the topology generation process and guarantee better sensitivity scaling by giving the optimizer some freedom. Then, the parameters values are slowly increased in the last steps to acquire more precise physical models by penalizing the intermediate densities and sharping the interfaces. The continuation strategy leads to better performance and gives more stability to the topology generation process than starting with the final parameters values which often leads to fast convergence to a local optimum in such a non-convex optimization problem [67].

Table 3.1: Continuation scheme for damping and projection coefficients

Step	1	2	3	4	5	6
q	0.01	0.01	0.01	0.03	0.05	0.1
p	1	1	1	2	3	3
β	1	2	4	4	8	8

3.3.7 TG setting parameters

The values of the TG's input parameters are summarized in the Table 3.2. First, the Reynolds number (Re) is computed according to the inlet boundaries for simplicity and the hydraulic diameter (D_h) is assumed to be double of the height of an infinite wide channel [255],[256]. The maximum impermeability (α_{max}) is set to 10^4 to avert the convergence difficulties caused by high impermeability values [246], [257]. Additionally, the solid fraction (v_{fs}) in the generation process is set to 0.2 (20%) i.e., the created solids in the flow channels are constrained to 20% of the area of both channels. As mentioned in section 3.3.1, the solid plates (20% of the whole HX area) presented in Fig. 3.1 are excluded from the TG's design domain, thus the total solid fraction (solid generated inside flow channels + three fixed plates) of the HX is 20%+20%=40%. The acquired topology is strongly influenced by the input parameter of the TG [258], emphasizing the high sensitivity of the essential parameters (Re, Pr_f, C_k) of the dimensionless governing equations presented in Eqs.1&5. A thorough examination of the impact of these parameters on the resulting topology will be extensively discussed in the results section. Eventually, the projection point γ_β of the hyperbolic projection process is set to 0.5.

Table 3.2: TG parameters

Parameter	Value
Re	200 - 1000
Pr_f	6.85- 600
C_k	50 - 450
α_{max}	10^4
v_{fs}	0.2 (20%)
γ_β	0.5

3.4 CFD validation Methodology

For the purpose of validating the design methodology and accurately evaluating the thermo-hydraulic performances, a set of computational fluid dynamics (CFD) simulations is conducted on the TG-derived HXs using the FEM solver of COMSOL [255]. The CFD validation analysis is a mandatory stage since the density-based TG is unable to accurately evaluate the performance of the generated topologies due to the governing equations modification, low mesh quality (no boundary layers, fixed mesh) and the existence of intermediate porosities at the solid/fluid interface after achieving the convergence criteria.

3.4.1 Thresholding

At the end of the topology generation process, the interface of the obtained topologies is not clear (pure solid or fluid) and some intermediate densities still exist which hold the non-physical meaning. Therefore, a predefined threshold is applied on the design variable to allow the extraction of the TG-derived HX geometry for verification process as depicted by Figure 3.2. The threshold value (γ_{th}) is taken as 0.5 i.e. 50% of the intermediate densities are taken as solid (γ_{th} ≥0.5) and the other 50% as fluid ($\gamma_{th} < 0.5$) [259].

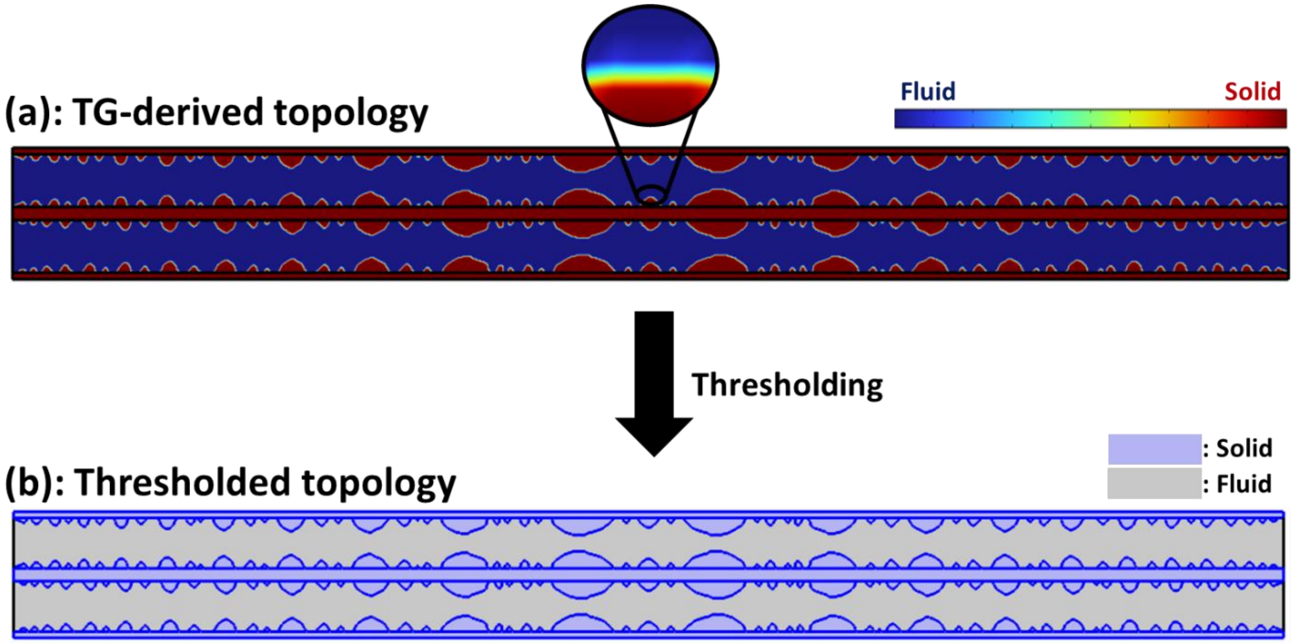

Figure 3.2: (a): TG-derived, **(b):** Thresholded topology.

3.4.2 Governing equations

In the CFD validation analysis, the dimensional governing equations (continuity, momentum and energy equations) of the conjugate heat transfer physics are set up without any modification in the momentum equation as in the topology generation process, assuming for steady-state and incompressible flow conditions:

$$\begin{gathered} \nabla.\boldsymbol{v} = 0 \\ \rho_f(\boldsymbol{v}.\nabla)\boldsymbol{v} = -\nabla P + \mu_f.\nabla^2 v \\ \rho_f C_{pf}\boldsymbol{v}.\nabla T - \nabla.(k_s \nabla T) = 0 \end{gathered} \tag{24}$$

where v is the velocity (m.s^{-1}), P the pressure (Pa), μ_f the fluid dynamic viscosity (Pa.s), ρ_f the fluid density (kg.m^{-3}) , k_s is the solid thermal conductivity (W.m^{-1}.K^{-1}), C_{pf} is the specific heat at constant pressure for fluid (J.kg^{-1}.K^{-1}) and T is the temperature (K). In conjunction with the previous mentioned equations, the k-ε model is employed to simulate the fluid flow inside the HX in the laminar and turbulent regions. A good mesh quality with eight boundary layers is built to discretize the governing equations in space using P1 elements.

3.4.3 Dimensionalization of the HX unit, boundary conditions and physical properties

In order to evaluate the realistic and practical thermo-hydraulic performance, the non-dimensional design domain utilized in topology generation is transformed to a dimensional one by specifying the value of the width of the flow channel to 4 mm. Accordingly, the remaining dimensions of the HX unit are also dimensionalized as illustrated by Fig. 3.3.

As for the boundary conditions, a uniform velocity and temperature profiles are imposed at the inlets. The inlet temperatures are set to 20℃ and 80℃ for the cold and hot fluid respectively. Moreover, zero outlet pressure with outflow conditions are assigned as outlet hydraulic and thermal boundary conditions respectively. Furthermore, a periodic boundary condition is assigned at the top and bottom boundaries of the whole HX to consider the heat transfer effect from the upper and lower units. The boundary conditions imposed on the HX unit are summarized as below:

$$\begin{gathered}
-\boldsymbol{v}.\boldsymbol{n} = v_{in} \Longleftrightarrow \text{on } \Gamma_{in,cold} \text{ and } \Gamma_{in,hot} \\
T = 20℃ \Longleftrightarrow \text{on } \Gamma_{in,cold} \\
T = 80℃ \Longleftrightarrow \text{on } \Gamma_{in,hot} \\
P = 0 \Longleftrightarrow \text{on } \Gamma_{out,cold} \text{ and } \Gamma_{out,hot} \\
-\boldsymbol{n}.\nabla T = 0 \Longleftrightarrow \text{on } \Gamma_{out,cold} \text{ and } \Gamma_{out,hot}
\end{gathered} \tag{25}$$

where $\boldsymbol{n}$ is the normal vector to the corresponding boundary outwardly oriented to the design domain. In the current work, the numerical verification process is divided into 2 parts (*Case* 1&2). Case 1: the thermo-hydraulic performance is evaluated and compared under similar inlet velocity (Re_{hot}=300-3000; Re_{cold}=109.4-1094.5) and fluid material (water) for the cold and hot fluids. Case 2: different inlet velocities ($Re_{cold}/Re_{hot}=10$) with fluid material (cold fluid → water, hot fluid →oil) are assigned for the cold and hot fluid. In both cases, the structures are simulated in the laminar and turbulent regions (Re_{hot}=30-300; Re_{cold}=300-3000). The primary objective behind evaluating the performance of the HX units under varied conditions is to ascertain that the superiority of the proposed design guideline can remain effective in different cases. The water and oil physical properties are considered as temperature dependent using the fitting polynomials given in Table 3.3. By contrast, the temperature dependence on Aluminum physical properties is ignored as shown in Table 3.3 below. Furthermore, the expansion characteristics of the solid material are disregarded in our numerical analysis.

Table 3.3: Physical properties of fluid and solid used for the numerical simulation (283 K <T< 363) [271], [272]

Water	Density [kg.m^{-3}]	$\rho = -9\times10^{-8}T^4 + 3\times10^{-5}T^3 - 6.8\times10^{-3}T^2 + 2.78T + 1000.2$
	Specific heat [J kg^{-1} K^{-1}]	$C_P = 2\times10^{-6}T^4 - 6\times10^{-4}T^3 + 5.48\times10^{-2}T^2 - 2.18T + 4208.6$
	Viscosity [Pa s]	$\mu = 3\times10^{-11}T^4 - 7\times10^{-9}T^3 + 8\times10^{-7}T^2 - 5\times10^{-5}T + 0.0017$
	Thermal conductivity [W m^{-1} K^{-1}]	$k = -4\times10^{-10}T^4 + 10^{-7}T^3 - 2\times10^{-5}T^2 + 2.5\times10^{-3}T + 0.5557$
Oil	Density [kg.m^{-3}]	$\rho = 7.34\times10^{-5}T^2 - 0.639T + 1068.7$
	Specific heat [J kg^{-1} K^{-1}]	$C_P = 0.00115T^2 + 3.476T + 761.4$
	Viscosity [Pa s]	$\mu = 2.48\times10^{-11}T^6 - 5.16\times10^{-8}T^5 + 4.47\times10^{-5}T^4 - 0.02T^3 + 5.36T^2 - 741.17T + 42669.2$
	Thermal conductivity [W m^{-1} K^{-1}]	$k = 1.54\times10^{-7}T^2 - 2.063\times10^{-4}T + 0.192$
Aluminum	Density [kg.m^{-3}]	$\rho = 2700$
	Specific heat [J kg^{-1} K^{-1}]	$C_P = 900$
	Thermal conductivity [W m^{-1} K^{-1}]	$k = 237$

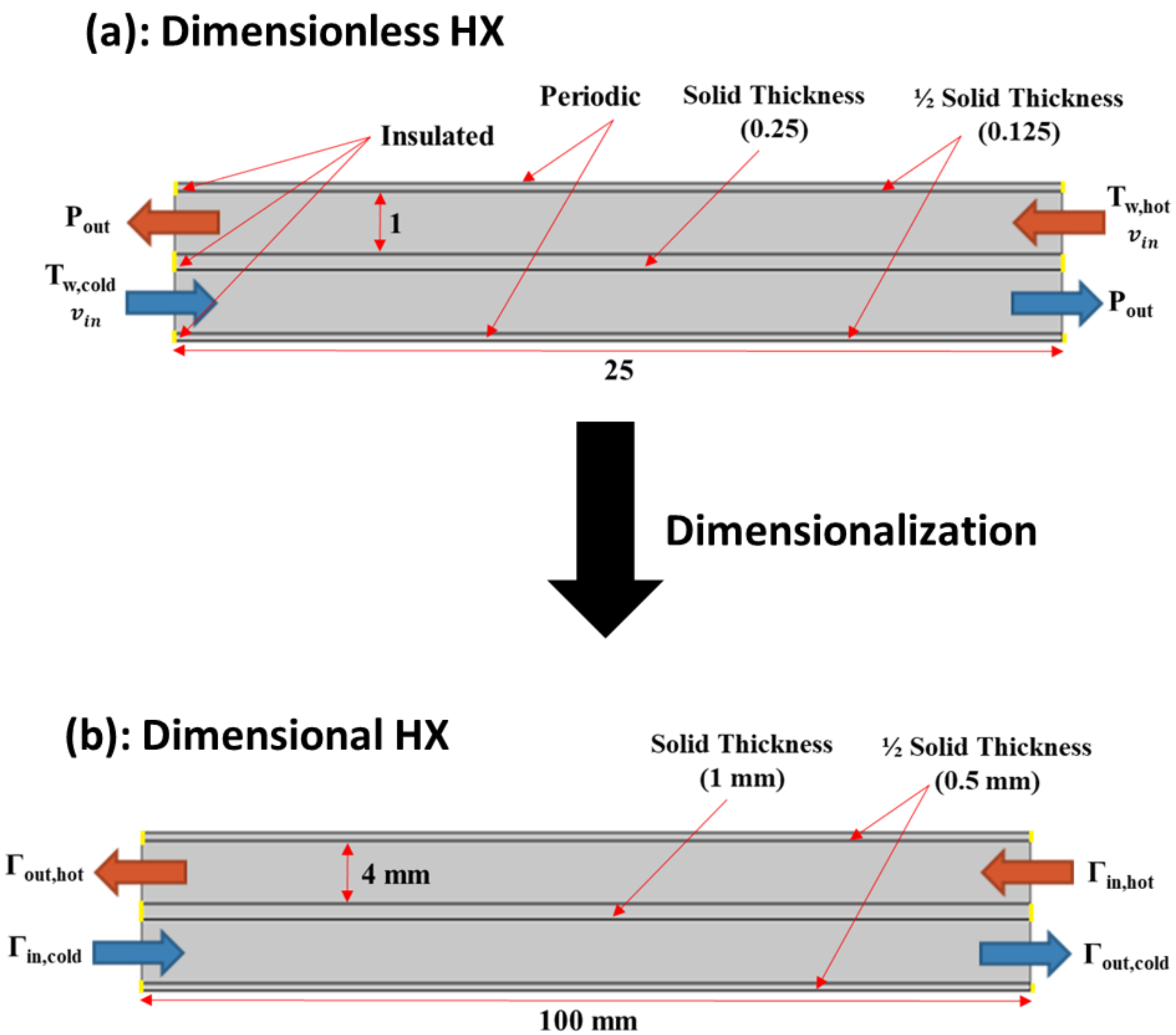

Figure 3.3: (a) : Dimensional, **(b) :** Dimensionless HX unit.

3.4.4 Mesh dependency

A mesh dependency study is executed to ensure the reliability of the numerical simulation. First, a coarse mesh is built to discretize the HX unit. Then, the mesh is refined by a certain factor following the methodology proposed by Celik et al. [260] until the after-mentioned stopping criteria is satisfied:

$$Er(\Delta P) = \left|\frac{\Delta P^k - \Delta P^{k+1}}{\Delta P^k}\right| < 2\% \ \& \ Er(T_{out}) = \left|\frac{T_{out,cold}^k - T_{out,cold}^{k+1}}{T_{out,cold}^k}\right| < 2\% \qquad (26)$$

where k is the index of the mesh dependency test, ΔP is the total pressure drop (Pa), $T_{out,cold}$ is the cold flow outlet temperature (°C) and Er is the relative error. As an example, for Re_{hot} = 3000 (Re_{cold}= 1094.5), the details about the mesh dependency study are given in Table 3.4. As seen that the numerical results become mesh independent when the number of elements hit 1257338.

Table 3.4: Mesh dependency test at Re_{hot} = 3000

Elements number	ΔP (Pa)	Error (ΔP) (%)	$T_{out,cold}$ (°C)	Error ($T_{out,cold}$) (%)
201455	418.2	--	32.5	--
581295	390	7.2%	30.8	5.51%
1257338	373.2	4.5%	29.88	3.07%
3125008	369.03	1.07%	29.7	0.6%

3.4.5 Theoretical verification

In order to validate the accuracy of the numerical results, we perform a comparative analysis between the computed empirical Nusselt number (*Nu*) and friction coefficient (*f*), obtained through the COMSOL solver for the bare HX unit depicted in Figure 4.4f, with their corresponding empirical values calculated employing the Sieder-Tate Nusselt number correlation [261] and the friction coefficient correlation for parallel plates [262], as described below:

$$Nu = 1.86 \times Re^{\frac{1}{3}} \times Pr^{\frac{1}{3}} \times \left(\frac{D_h}{l}\right)^{1/3} \times \left(\frac{\mu_b}{\mu_w}\right)^{0.14}$$

$$f = \frac{96}{Re} \tag{27}$$

where μ_b is the viscosity at the bulk mean temperature (Pa.s), μ_w is the viscosity at the wall temperature (Pa.s), l is the length of the HX unit (m). Figure 3.4 clearly demonstrates a significant level of congruity between the numerical and the correlated results.

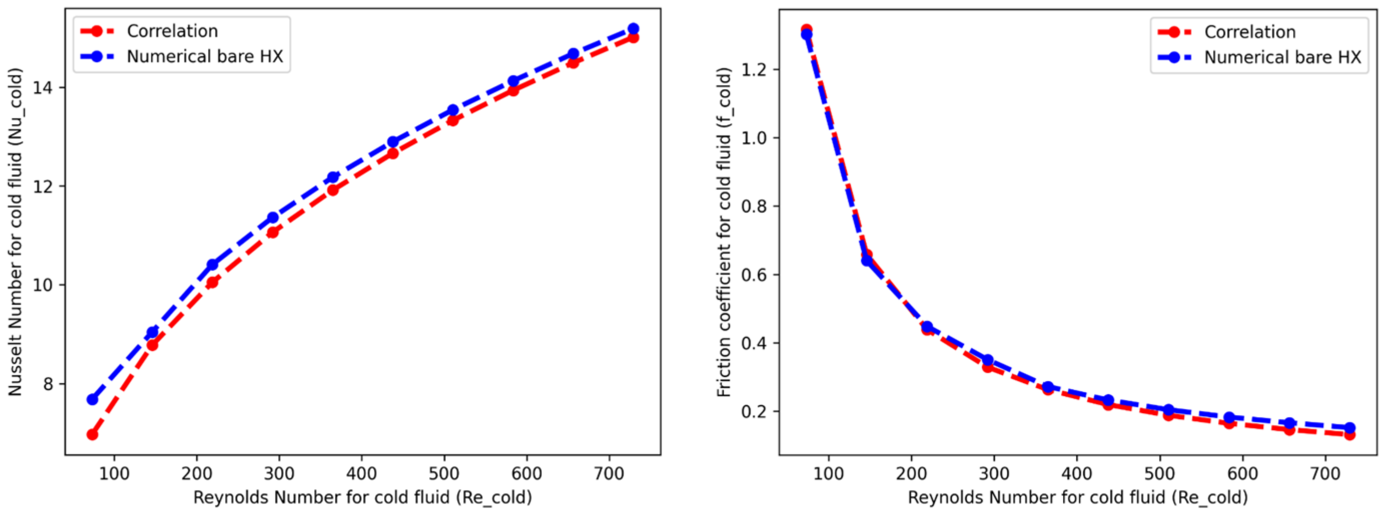

(a): Nusselt Number (*Nu*) Vs Reynolds number (*Re*) **(b)** : Friction coefficient (*f*) Vs Reynolds number (*Re*)

Figure 3.4: Comparison of the numerical results with empirical correlations of the bare HX.

3.5 Results and Discussions

3.5.1 TG-results and the influence of parameters

We investigate firstly the effect of the three essential parameters in the dimensionless TG represented by *Re*, Pr_f & C_k. By increasing the *Re* & Pr_f, the convective term in the energy equation is intensified, thereby causing an increase in the minimum width of the flow channel, as illustrated in Figures 3.5 & 3.6. This elucidates that with the increase of the convection term, the flow force exceeds the force exerted by the appeared solids (from top and bottom of the flow channel), resulting in an unhindered fluid flow through the channel.

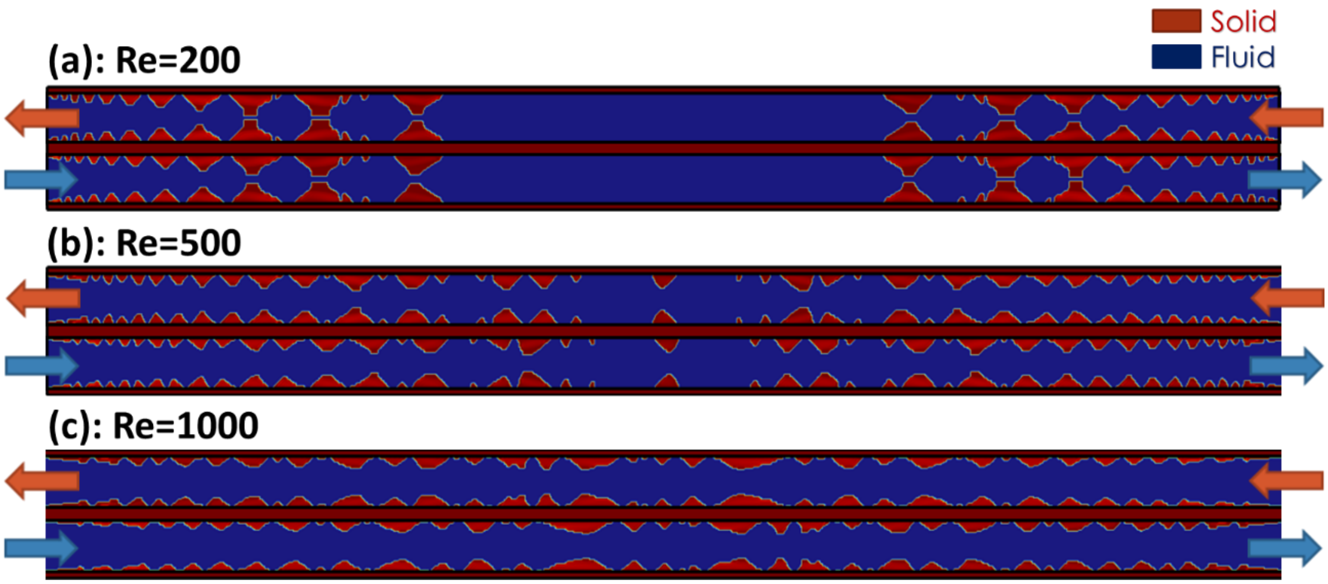

Figure 3.5: Acquired topologies at **(a)** Re=200, **(b)** Re=500,**(c)** Re=1000 with Pr_f=6.85 & C_k=10.

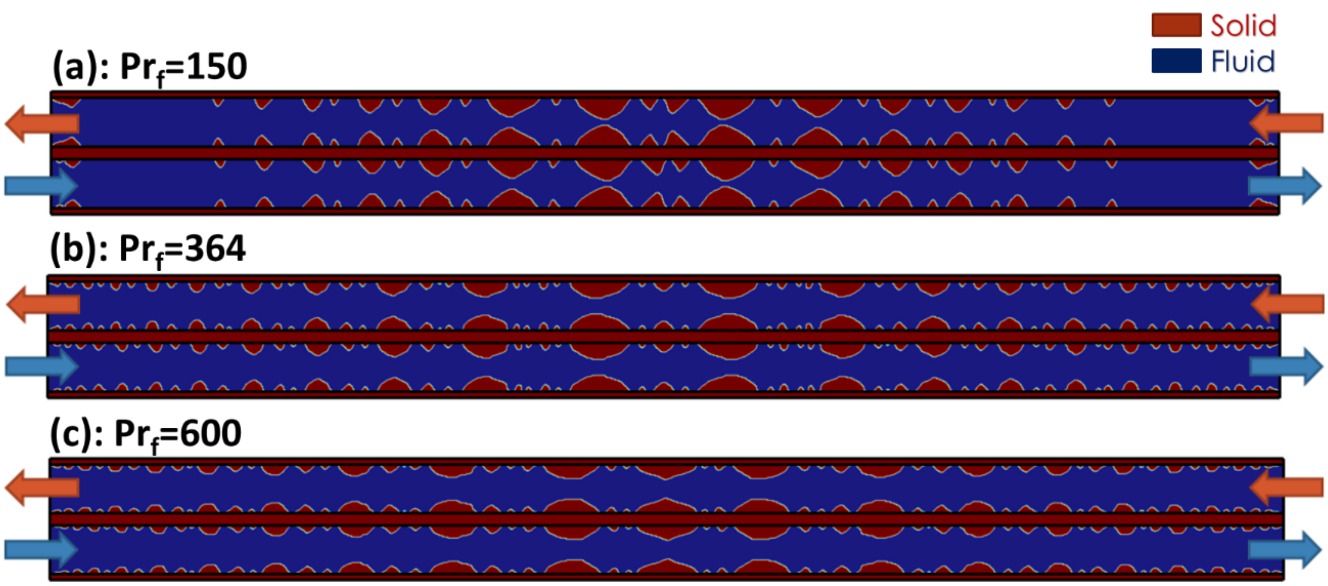

Figure 3.6: Acquired topologies at **(a)** Pr_f=6.85, **(b)** Pr_f=364, **(c)** Pr_f=600 with Re=100 and C_k=150.

In contrast, elevating the conduction term of the energy equation through an increase of the thermal conductivity ratio (C_k) results in a reduction of the minimal distance of the flow channel as depicted by Fig 3.7. This implies that as the conduction term increases, the generated solids attempt to block the fluid flow by impeding its passage.

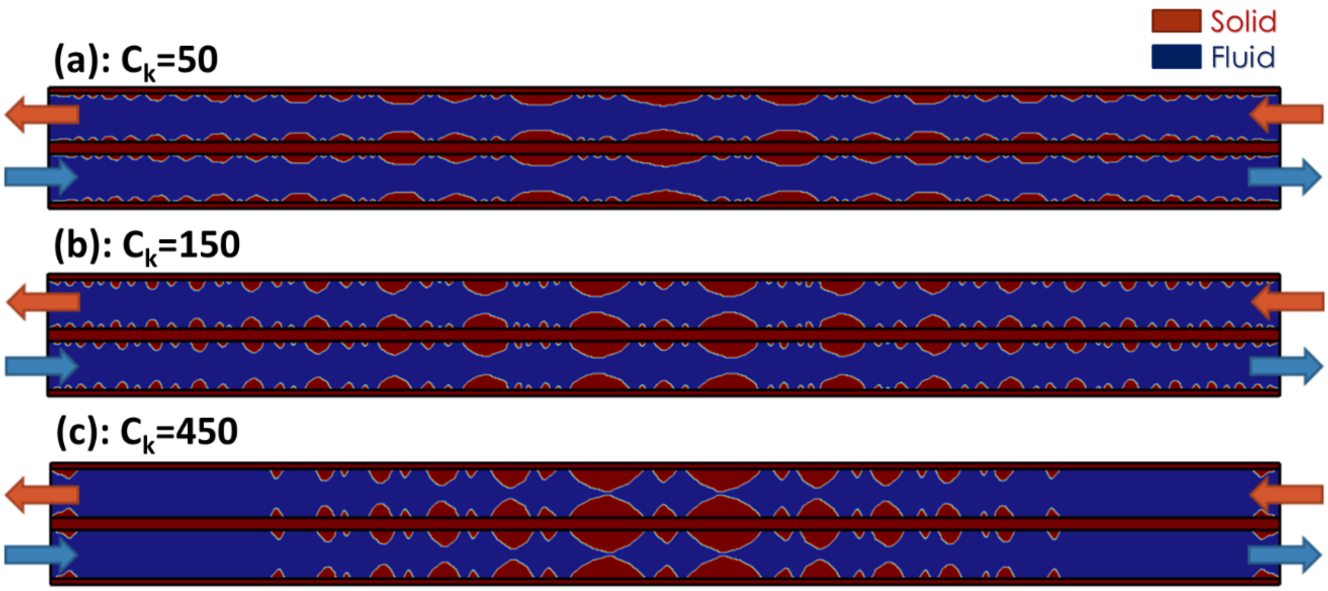

Figure 3.7: Generated topologies at **(a)** C_k=50, **(b)** C_k=150, **(c)** C_k=450 with Re=100 & Pr_f=364.

All topologies depicted in the previous figures show the irregular fin geometries emerged along the solid wall, the symmetry about the vertical axis at the middle of the HX unit. Most importantly, the convergent-divergent arrangement feature i.e. the height and width of the fins increase gradually until the center of the HX unit and then it decreases.

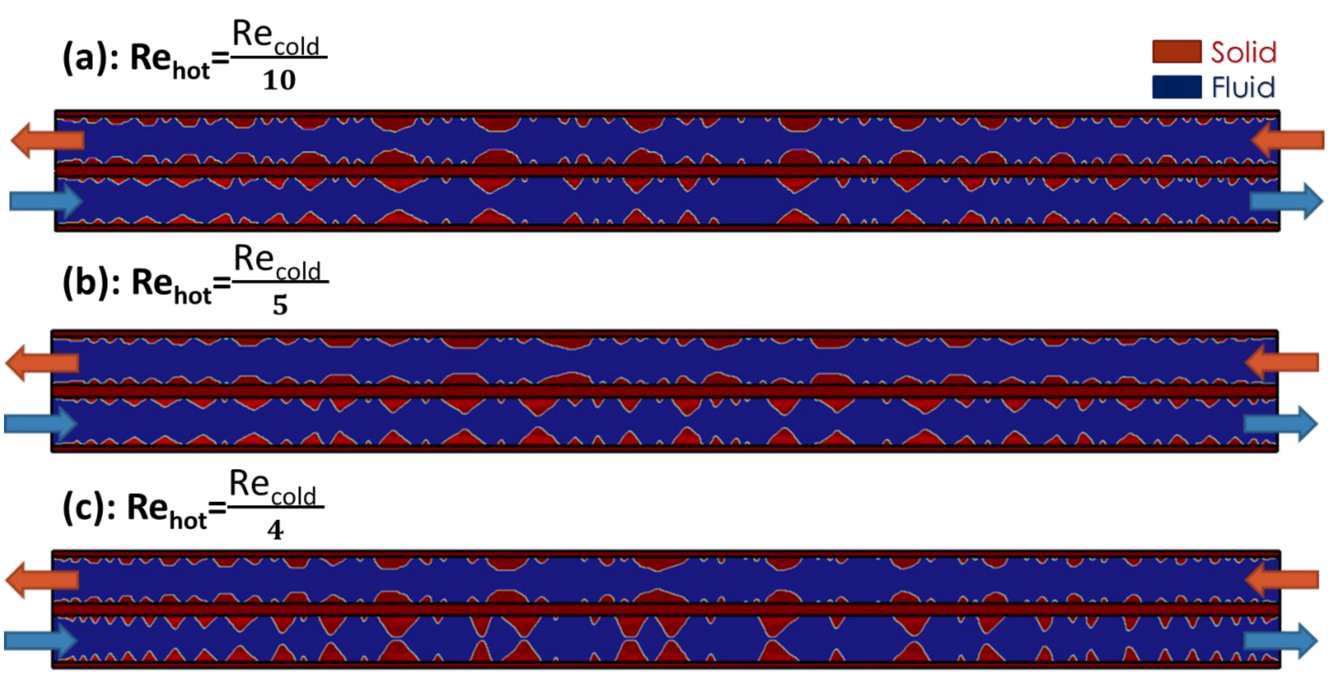

Figure 3.8: Effect of Reynolds number ratio (Re_{cold}/Re_{hot}) on the acquired topologies for Pr_{cold}=6.85, Pr_{hot}=364, $C_{k(cold)}$=10, $C_{k(hot)}$=61.

The previous topologies are acquired using the same fluid material and inlet velocity for the hot and cold fluids. To observe whether the features will be conserved under different conditions, dissimilar fluid material (Pr_{cold} = 6.85 & Pr_{hot} = 364) and inlet velocities are imposed for the cold and hot fluids. As exemplified by Fig 3.8, the symmetry is disrupted while the irregular and C-D distribution features are maintained under different Reynolds number ratio between the cold and hot fluids. The Reynolds number ratio should be also carefully set, beyond the defined range in Fig 3.8 for the prescribed values of Pr_f (Pr_{cold}=6.85 & Pr_{hot}=364) and C_k (C_{kcold} =25, C_{khot} =150), the blocking issues will occur in the cold or hot fluid channels. This blocking phenomenon can be attributed to the disparity in convective heat transfer rates between channels, where a higher rate in one channel leads to an increase in the minimal distance and then decrease in the amount of solid within that channel. Concurrently, to maintain the imposed solid fraction within the flow channels during the topology generation, a compensatory increase in solid content must occur in the other channel leading to a decrease in the minimal distance and then the blocking of the channel.

In the topology generation, the initial guess holds significant importance as it directly influences the obtained results. Correspondingly, two different initial densities distribution using rectangular and circular fins are suggested instead of starting with a uniform density distribution as the topologies acquired previously. As illustrated by Fig 3.9, all acquired topologies using rectangular and circular fins as initial guess possess the C-D distribution features with a remarkable difference in the acquired fins distribution. Numerically, a marginal difference of 0.06% has been observed in the optimal value of the objective function when employing initially rectangular and circular fins, in comparison to the result obtained using a uniform initial density distribution. The difference in the optimum value is negligible and may be explained by the utilization of the continuation scheme in topology generation that can leads to maximized performance for different initial setting.

In summary, the acquired topologies by the TG are strongly affected by the input parameters. Hence, a limitation of setting for a compromise between convection and conduction terms should be considered. Surpassing the limited ranges of parameters inevitably leads to the emergence of flow channel’s blocking issues. Additionally, the C-D distribution feature is conserved irrespective of the prevailing conditions while the symmetry feature is lost when fluid material and the inlet Reynolds number are changed for the cold and hot fluids.

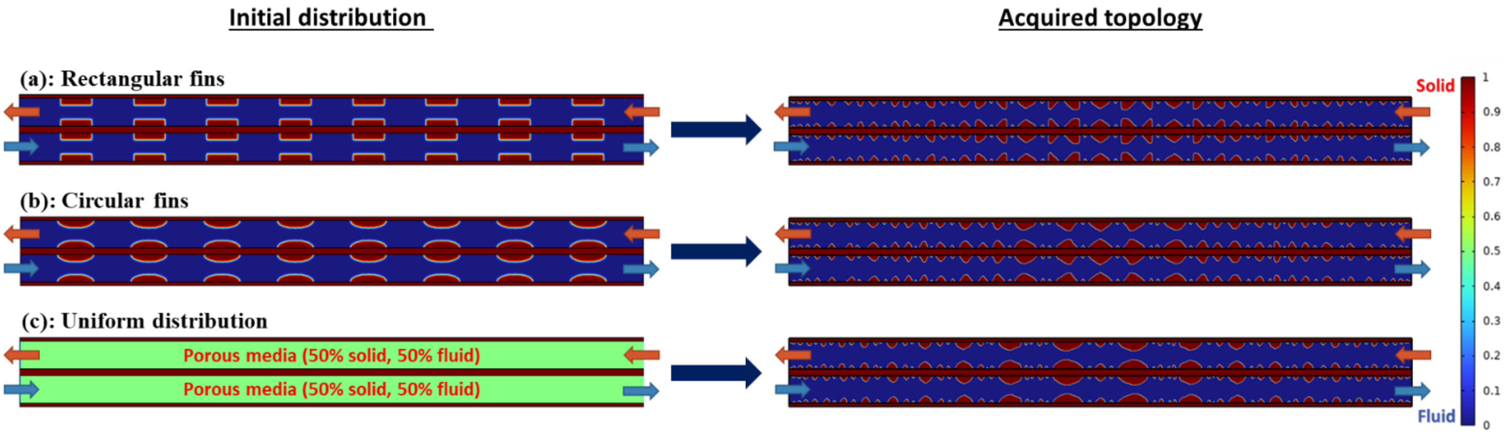

Figure 3.9: Generated topologies by starting with **(a):** Rectangular fins, **(b):** Circular fins, **(c):** uniform distribution as initial topology for Re=100, Pr_f=364, C_k =150.

3.5.2 Investigated HX units

The two TG-derived HX units presented in Fig 3.5c & 3.7b are randomly selected as benchmarks for the numerical comparison stage (cases 1&2) and named TG-HX1 and TG-HX2 respectively. For more consistency between the TG and the case 2 (different fluids: water-oil and inlet conditions: $Re_{cold}/Re_{hot}=10$) of the CFD analysis, the generated HX acquired under different fluid material (Pr_{cold}=6.85, Pr_{hot}=364) and different inlet conditions ($Re_{cold}/Re_{hot}=10$) presented in figure 3.8.a is selected for the CFD investigation stage under case 2 conditions. Moreover, a HX unit with conventional fin design (Constant fin height 1 mm and width 5 mm) having rectangular shapes (as illustrated by Fig 3.10e) is introduced to compare its thermo-hydraulic performance with the TG-acquired HX units. To make a fair comparison, all HX units have the same solid fraction (36%), boundary conditions and dimensions. The investigated HX units are presented in Fig 3.10. Eventually, the overall (external) dimensions of the 2D investigated HX units are 0.1 m $\times$ 0.01 m with a flow channel of 0.04 m wide. The detailed dimensions of the 2D HX units can be found in Fig. 3.3.

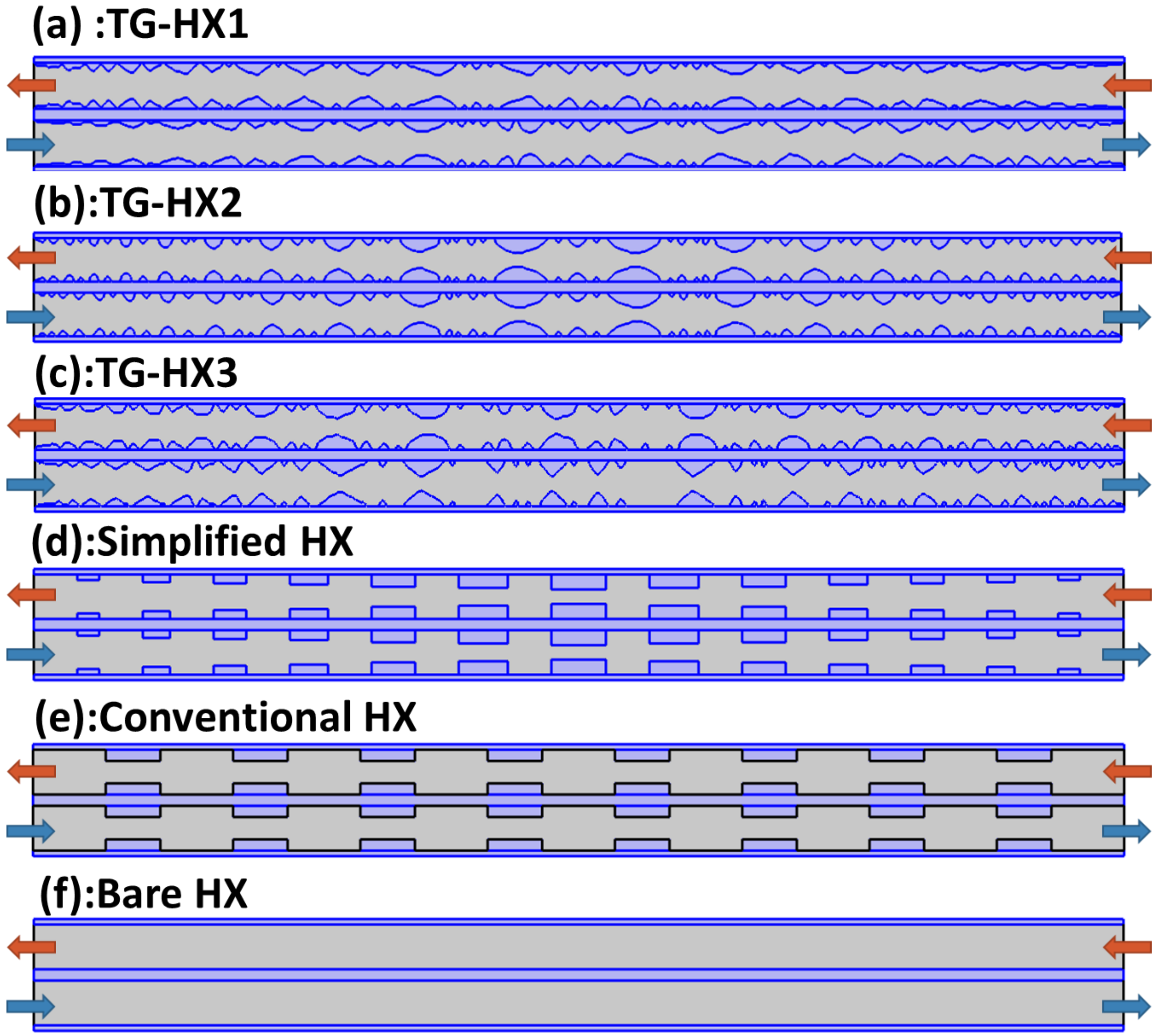

Figure 3.10: (a): TG-HX1, **(b):** TG-HX2, **(c):** TG-HX3, **(d):** Simplified HX, **(e):** Conventional HX and **(f):** Bare HX

3.5.3 The convergent-divergent design

Taking the inspiration from the generated fins that are mainly featured by the convergent-divergent distribution, a simplified HX unit with convergent-divergent arrangement of fins is designed with a minimal channel height (1.3 mm) using analogous rectangular shapes of the conventional design as seen in Fig. 3.10d.

3.5.4 Parameters definition for thermo-hydraulic performance evaluation

For the purpose of evaluating the thermal performance of the HXs, the Nusselt number (Nu) that represents the convective over the conduction heat transfer in the fluid is selected as criteria and evaluated using the following equation:

$$Nu = \frac{hD_h}{\overline{k_f}} \tag{28}$$

where h is the convective heat transfer coefficient ($W.m^{-2}.K^{-1}$) and $\overline{k_f}$ is the fluid average thermal conductivity ($W.m^{-1}.K^{-1}$). As demonstrated by Fig 3.11a, The Nusselt number exhibits an improvement in the TG-obtained and simplified HX units compared to the conventional one, across a broad range of Reynolds number in both cases 1 and 2. This enhancement can be elucidated by the higher local flow velocity within the TG-generated and simplified HX's flow channels (smaller minimal distance) when compared with the local flow velocity within the channels of the conventional HX unit. Subsequently, this will lead to an intensification of the convective heat transfer coefficient h and then the improvement of the Nu.

To assess the hydraulic performance of the HX units, the friction coefficient is evaluated for all HX units using the Darcy–Weisbach equation presented as follow [263]:

$$f = \frac{2\Delta P D_h}{\bar{\rho} l \bar{v}^2} \tag{29}$$

where $\bar{\rho}$ is the fluid average density ($kg.m^{-3}$), $\bar{v}$ is the average velocity in the flow channel ($m.s^{-1}$) and l is the length of the HX (m). Fig. 3.11b exemplifies that the friction coefficient of the generated and simplified HX units is higher compared to the conventional one. The observed augmentation in the friction coefficient can be attributed to the presence of several tiny fin structures inside generated structures, as well as to the disparity of the minimal distance inside the flow channels for the TG-derived and simplified HX units compared to the conventional design.

To consider the thermal and hydraulic performance simultaneously, the PEC (performance evaluation criteria) which fractionally combine the Nusselt number with friction coefficient is evaluated for the three HX units. As seen in Eq. 30, the friction coefficient undergoes an exponentiation of 1/3 as prescribed by the methodology of Webb and Eckert [264].

$$PEC = \frac{Nu/Nu_0}{(f/f_0)^{1/3}} \tag{30}$$

where the Nu_0 and f_0 are the Nusselt number and the friction coefficient for the Conventional HX.

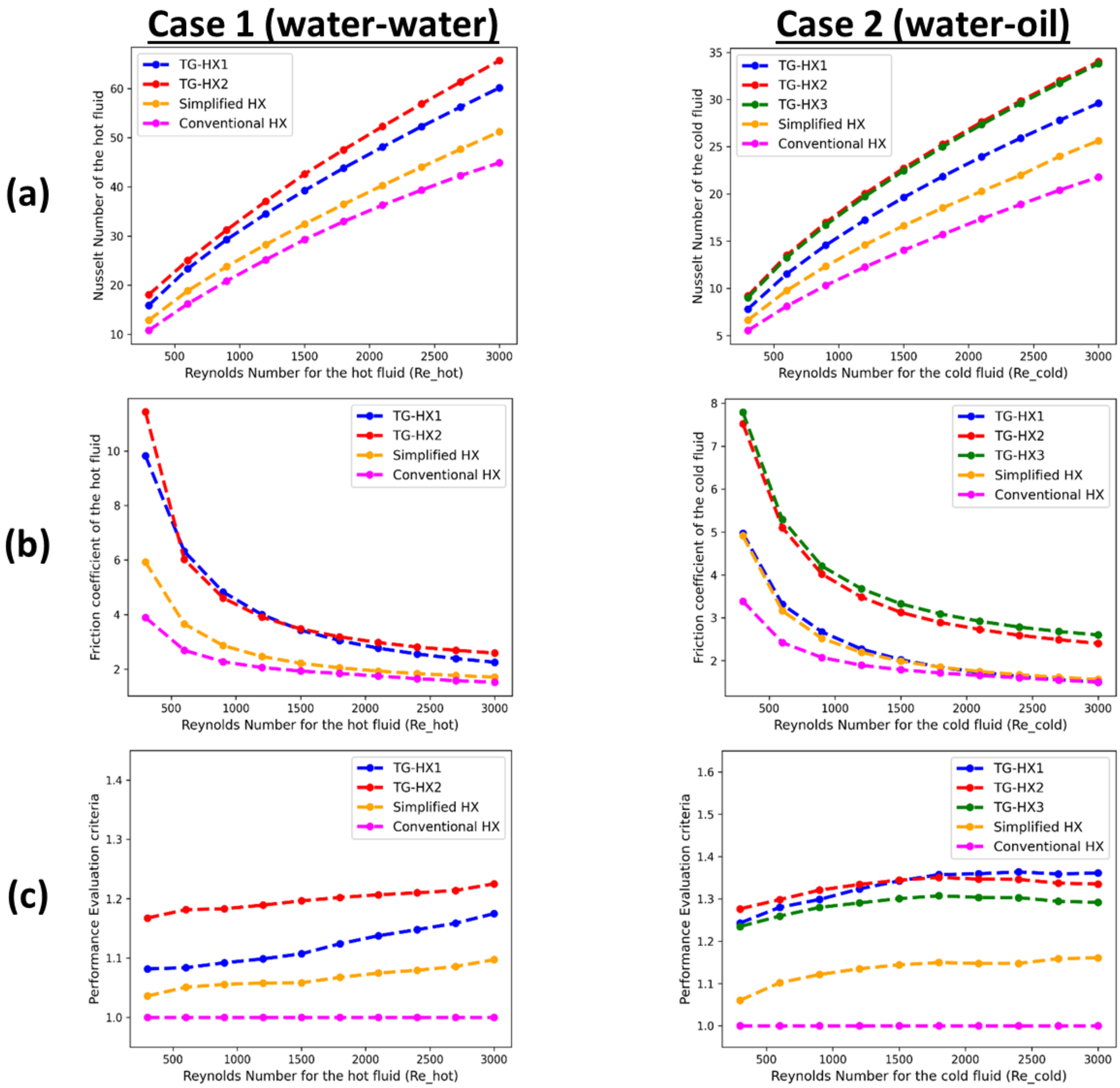

Figure 3.11: Variation of **(a):** the Nusselt Number (*Nu*), **(b):** friction coefficient (*f*) and **(c):** Performance evaluation criteria (PEC) with respect to the Reynolds number for all HX units in cases 1 & 2.

The thermo-hydraulic performance of the TG-generated and simplified HXs surpasses that of the conventional one under a broad range of Reynolds numbers, as illustrated in Figure 3.11c. This superiority is observed in both cases 1 and 2 with enhancement up to 22.5% and 9.7% and up to 36.11% and 16.08%, respectively.

To provide a more reliable and comprehensive comparison of the simultaneous thermo-hydraulic performance and to avoid the limitations of the PEC number, the heat transfer rate of all HXs are plotted under the same pumping power for case 1, as depicted in figure 3.12. The results indicate that the heat transfer rate is intensified in the generated and simplified designs compared to the conventional case with a maximum improvement rate up to 16.4% and 5.8%, respectively, under the same pumping power.

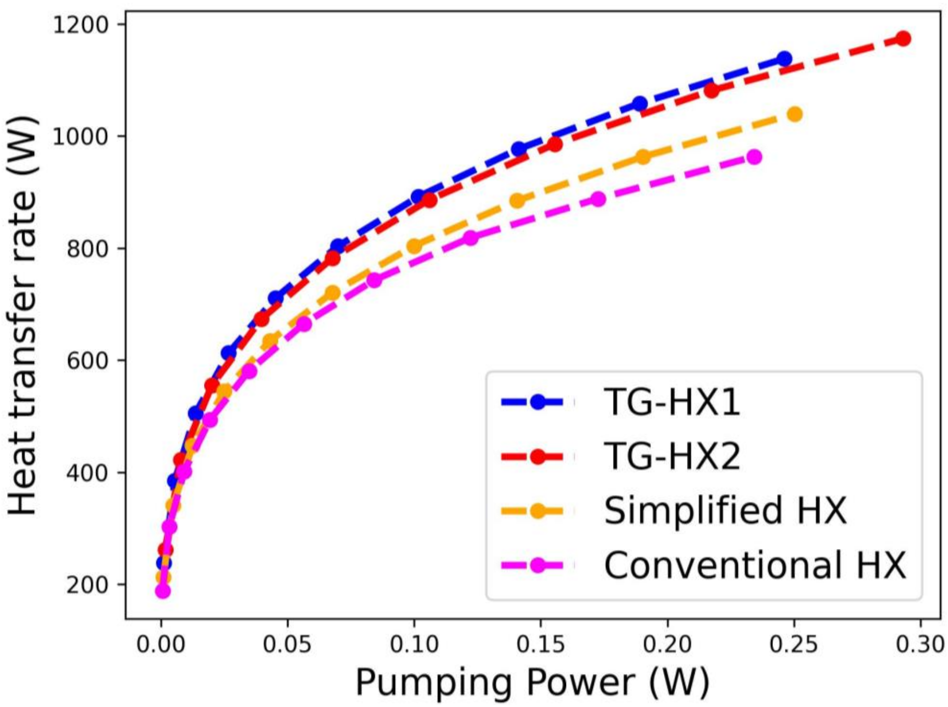

Figure 3.12: Variation of heat transfer rate with respect to the pumping power for all HX units in case 1.

3.5.5 Physical interpretation

Figure 3.13 depicts (a) the normalized velocity contours, (b) the normalized local velocity, (c) the normalized local pressure gradient, (d) the normalized local heat transfer coefficient over the TG-HX2 at Re_{hot}=300.

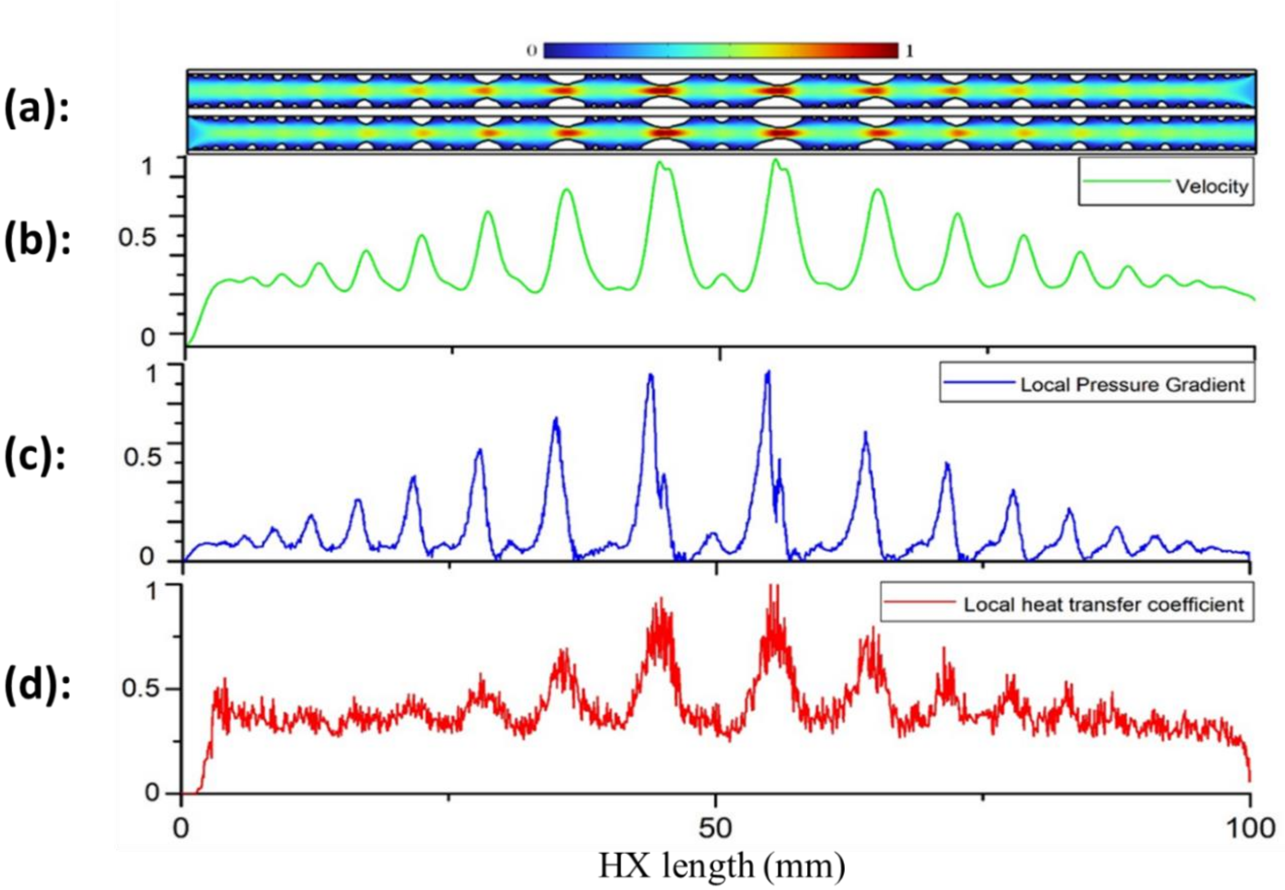

Figure 3.13: Normalized **(a):** velocity contours, **(b):** velocity plot, **(c):** local pressure drop, **(d):** local heat transfer coefficient based on their maximum value over the TG-HX2 at Re_{hot}=300.

The flow channels inside the TG-HX2 are decomposed into two sections (Convergent and divergent). In the convergent section, the current fin distribution attempts to gradually increase the convective heat transfer by increasing the velocity of the fluid resulting in an augmentation of the local heat transfer coefficient and pressure drop. Thereafter, in the divergent section, the C-D design seeks to progressively decrease the fluid velocity, which will simultaneously reduce the local pressure drop and heat transfer coefficient. The proportional variation of the local heat transfer coefficient and pressure drop with respect to the velocity behavior could be proved and confirmed by the following equations [263]:

$$\Delta P = \frac{f\bar{\rho}l\bar{v}^2}{2D_h}$$
$$h = \frac{\overline{k_f}Nu}{D_h} \leftrightarrow Nu \propto v \tag{31}$$

As presented in Eq. 31, the variation of pressure drop is proportional to the magnitude of velocity. Similarly, the heat transfer coefficient is commensurable with the Nusselt number, which is correlated to the velocity. Apparently, the TG-derived design of fins intensifies the convective thermal performance of the HX unit in the convergent section and improves its hydraulic performance in the divergent section for the purpose of achieving the simultaneous thermo-hydraulic enhancement. Besides, regarding the fluctuations in all plots, this could be explained by the flow disturbance and eddies generated inside the channels.

Additionally, one of the most important parameters to evaluate the convective heat transfer is the included angle between the velocity vector and the temperature gradient [10]-[14]. By referring to the dimensionless energy equation, increasing the Re or Pr_f will directly enhance the heat transfer which has been considered as a classical and well-known method in the literature to enhance the heat transfer. In fact, increasing the dot product of the velocity and temperature gradient ($\vec{v}.\overrightarrow{\nabla T}$) could also magnify the heat transfer. Therefore, the synergy field number of the included angle could be expressed as:

$$\cos\theta = \frac{\boldsymbol{v}.\overrightarrow{\nabla T}}{\|\boldsymbol{v}\| \times \left\|\overrightarrow{\nabla T}\right\|} \tag{32}$$

where θ is the incident angle between $\vec{v}$ and $\overrightarrow{\nabla T}$ are the velocity and temperature gradient vectors respectively, $\|\vec{v}\|$ and $\left\|\overrightarrow{\nabla T}\right\|$ are the magnitude of the velocity and temperature gradient vectors respectively. Figure 3.14a demonstrates that the absolute value of the synergy field number $|cos\theta|$ is locally increased thanks to the generated vortex (Flow swirls) between the fins. This flow swirls induces a change in the direction of the fluid velocity vector leading to an increase in the included angle between the velocity and temperature gradient vectors. Besides, Figure 3.14b illustrates that the absolute value of the averaged synergy field number for the TG-derived and simplified HX units are larger than the conventional one under a wide range of Re. The superior synergy field number of the TG-derived and simplified designs demonstrates a higher convective thermal performance compared to the conventional case, elucidating the high efficacy of the C-D design of fins (as in the TG-acquired and simplified) in improving the convective thermal performance. This will elucidate that the synergy field was a good indicator for reflecting the thermal performance advantage of the TG-derived and simplified HXs over the benchmark case. The good representation of thermal performance confirms the reliability of the synergy field when the convection effect dominates over the conduction one, as in the present CFD analysis a high conductive material (Aluminum) is used resulting in a negligible conduction resistance. In the following chapters, a moderate conductive material (stainless steel) will be used in the TO and CFD analysis. Therefore, the synergy field will not be employed to assess thermal performance, as it has proven to be an unreliable indicator when low/moderate conductive materials are used.

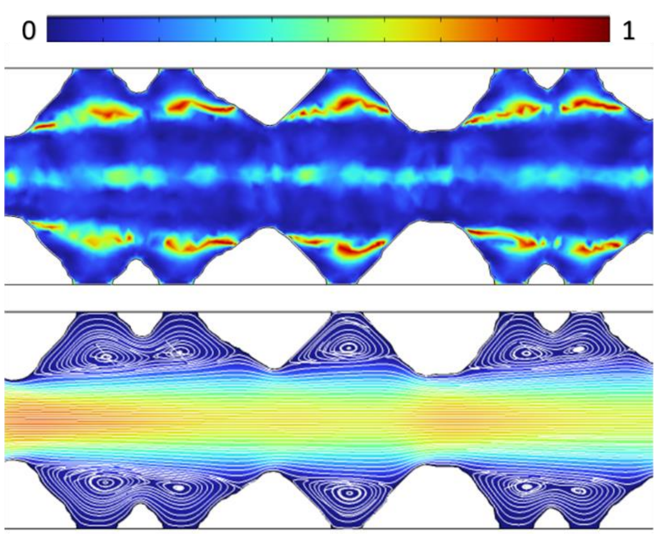

(a): Synergy field number distribution (Top), Velocity streamlines (Bottom)

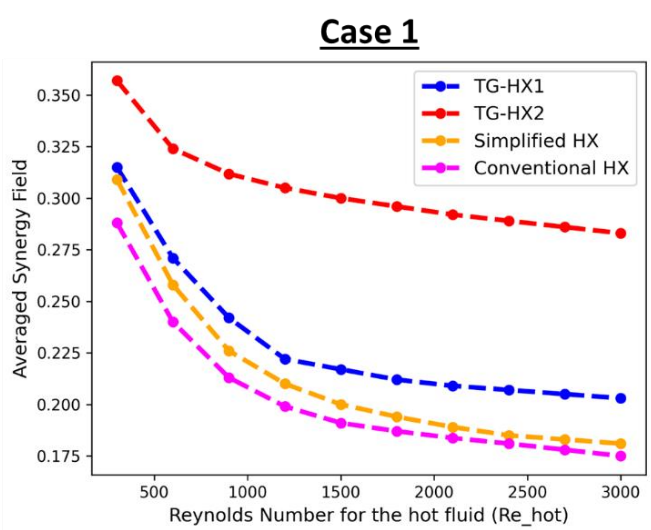

(b): Synergy field number Vs Re

Figure 3.14: Synergy field number variation with regards to the HX's length and Reynolds number.

For further comparison and physical interpretations, the temperature profiles of the TG-HX1, TG-HX2, simplified and conventional HX units along the central vertical axis are plotted and compared under case 1 conditions at Re_{hot} =1200 as illustrated by figure 3.15. Obviously, the temperature profiles of the TG-derived and simplified designs (characterized by the C-D distribution of the fins) tend to have higher temperature of the cold fluid and lower temperature for the hot fluid, simultaneously, compared to the conventional HX unit (featured by uniform fins distribution). This indicates that the cold fluid inside the TG-derived and simplified HX units gained more heat from hot fluid compared to the conventional case at the same positions (x=50 mm) and same conditions (Re_{hot} =1200), which will confirm the thermal performance superiority of the TG-derived and simplified HX units proved previously in figure 3.11a. Moreover, the four investigated HX units can be chronologically classified according to the cold fluid temperature (highest → lowest) as TG-HX2 > TG-HX1 > simplified > benchmark HX unit. This sorted order of the HX units is also validated previously in figure 3.11a that ranks the thermal performances (*Nu*) of the four HX units identically to the aforementioned chronological order.

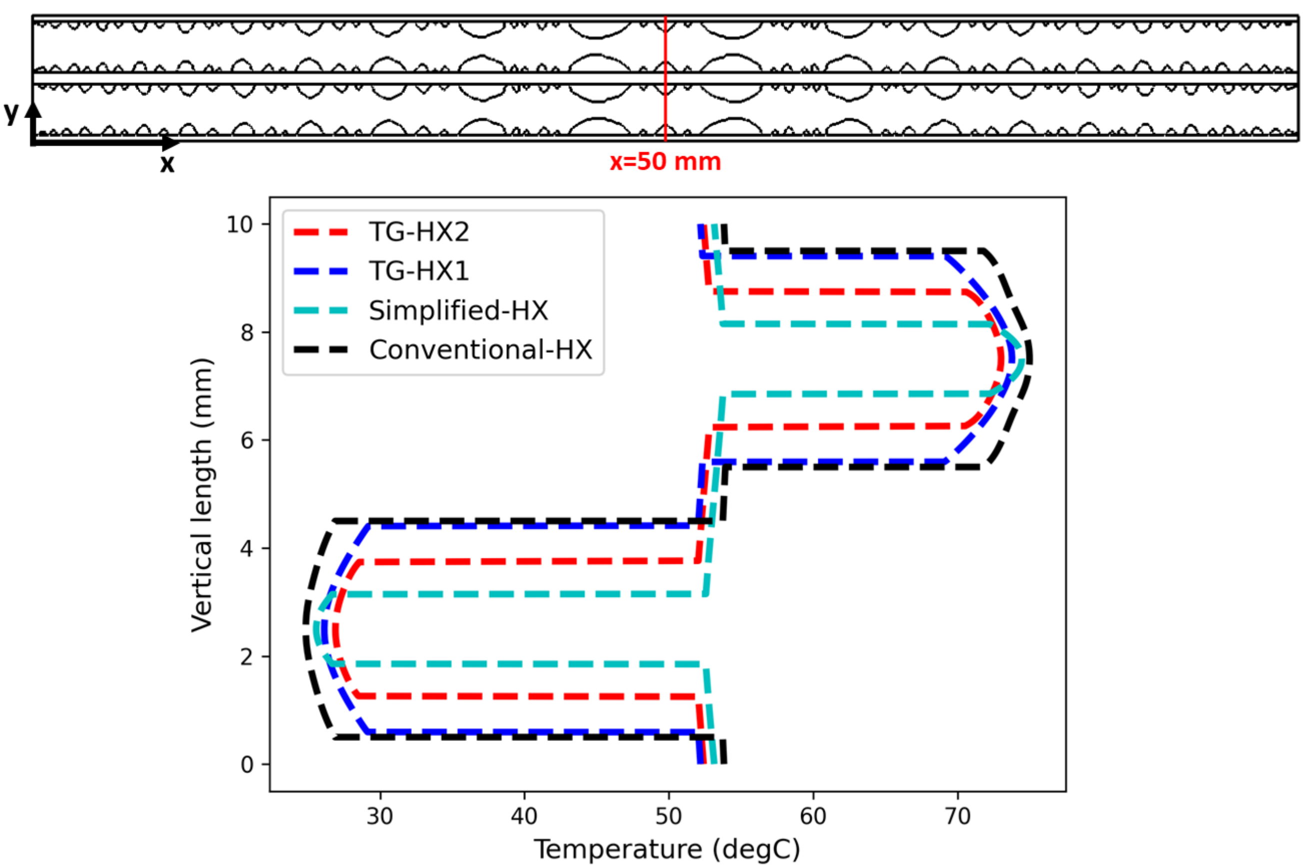

Figure 3.15: Comparison of the temperature profiles of different HX units along their central vertical axis (x=50 mm) under case 1 conditions and at Re_{hot}=1200.

3.5.6 Incompatibility of velocity fields between CFD and TG

The C-D design derived from the TG is proven of good thermal-hydraulic performance in terms of the CFD and physical analysis. However, the incompatibility of velocity fields between CFD and topology generation is found as shown in Fig 3.16. The observation reveals an important velocity in the solid phase as seen in Figure 3.16 of the generated topology depicted in Fig.3.9b, elucidating that the maximal imposed impermeability (which has been widely utilized in the literature of TO for conjugate heat transfer [22], [114], [116]–[120]) was insufficient to enforce zero velocities for the solid phase. This insufficiency may be attributed to the employment of a restricted design domain in the topology generation process. Accordingly, the acquired results could be considered as a novel generated topology rather than an optimized one, while concurrently emphasizing the improvement of the thermo-hydraulic performance resulted from the utilization of the newly generated C-D fins.

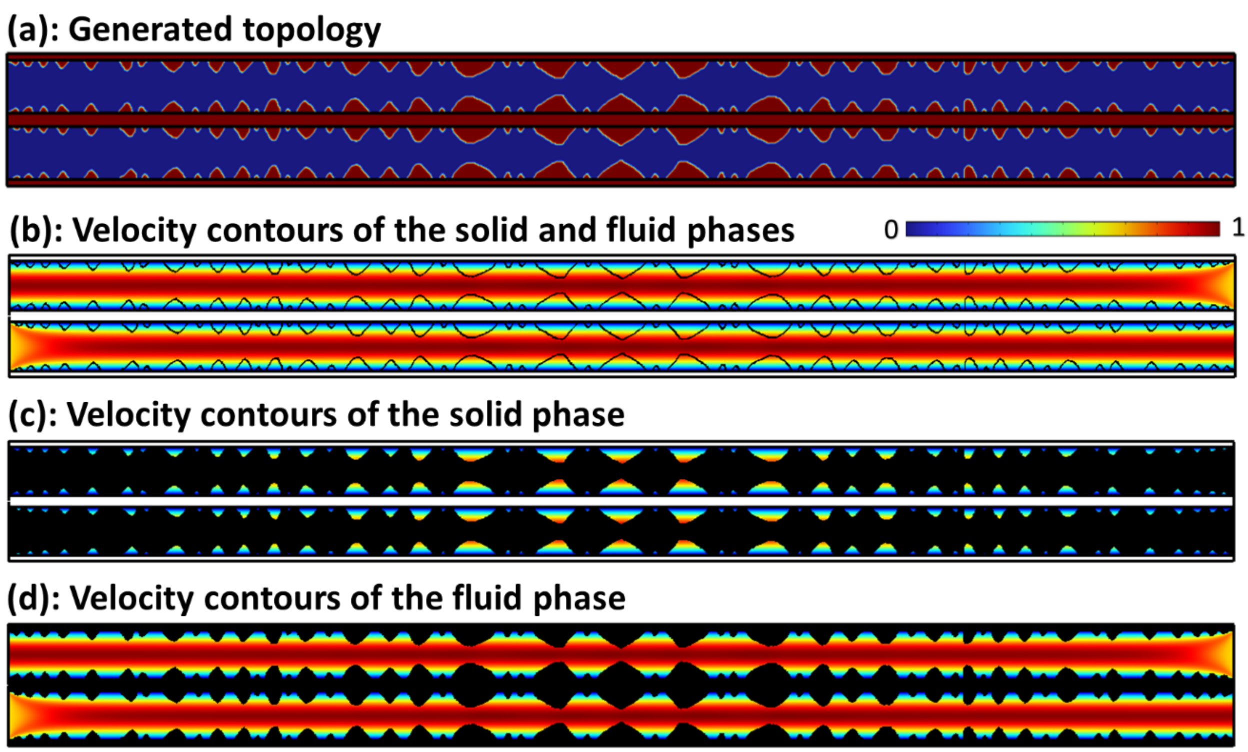

Figure 3.16: **(a):** Generated topology and the corresponding normalized velocity contours for **(b):** solid and fluid phases, **(c):** solid phase and **(d):** fluid phase.

After identifying this nonphysical issue in the velocity field of the generated topology (C-D), it should be noted that the blocking issues encountered in this chapter are not reasonable from a numerical point of view, since the residual of the continuity equation is imposed as a constraint in the optimization process (i.e., the residual of the continuity should be less than or equal a small tolerance). This imposition ensures the conservation of mass in the flow channels at each optimization iteration, which contradicts with the encountered blocking problems.

3.6 Conclusions

In this chapter, a novel fin design with convergent-divergent distribution is generated by using a gradient-based TG. An in-depth examination is carried out to explore the influence of the TG's essential parameters (Re, Pr_f, C_k) on the resulted topologies. According the investigation stage, when the convective heat transfer is increased by increasing the Re & Pr_f, the minimal distance inside the channels increases simultaneously leading to an unhindered flow of the fluid inside the channels. Conversely, when the conduction term is increased by increasing the C_k, the appeared solid tends to obstruct the fluid passage inside the channels. Accordingly, a trade-off between conduction and convection is crucial to avoid the occurrence of fluid passage blockages within the channels. Under the different input parameter settings, the TG-derived geometries are in form of fins and featured essentially by the convergent-divergent distribution along the length of the HX.

Inspired from the preceding feature, a convergent-divergent fin distribution is designed using rectangular shapes. The aim behind introducing such design is to provide a novel guideline for fin design following the essential topological feature with rectangular shapes that could be easy manufactured even with conventional techniques. Moreover, a conventional fin design with uniform distribution is also introduced for comparison. CFD analysis is executed under two different cases (1&2) on four HX units with two TG-derived, one simplified and one conventional designs to compare numerically their thermo-hydraulic performance. Under the same Reynolds number, the TG-acquired and simplified HX units have better thermal performance compared to the HX unit with conventional fins: Nusselt number increase up to 46%, 14% for case1 and 56.16%, 17.68% for case 2, respectively. To characterize the thermal and hydraulic performance simultaneously, the PEC is evaluated for all HX units. It is identified that the advantage of the TG-acquired and simplified HX units over the conventional one with thermo-hydraulic improvement up to 22.5%, 9.7% for case 1 and 36%, 16% for case 2, respectively. The diminishment in performance enhancement observed between the TG-obtained and simplified HXs might be attributed to the omission of several topological features during the design of the simplified HX.

A detailed physical interpretation of this novel fin design guideline is provided by analyzing the local velocity, pressure drop, heat transfer coefficient and synergy field with respect to the HX unit's length. The physical interpretation analysis reveals that the C-D design of fins increases the local velocity in the convergent section and decreases it in the divergent section leading to a proportional variation of the local pressure drop and heat transfer coefficient along the HX unit that can achieve the thermo-hydraulic performance improvement. Moreover, a higher synergy field number is observed for the C-D design of fins compared to the conventional one, reflecting the high ability of the C-D design of fins in intensifying the convective thermal performance of HXs.

The C-D configuration of fins has demonstrated efficacy in enhancing the thermo-hydraulic performance of HXs across laminar and turbulent regimes. Nevertheless, it is essential to characterize the C-D generated fins as a novel topology rather than an optimized design. This distinction arises from the discovered issue presented in section 3.5.6, specifically pertaining to the inadequacy of impermeability intensity in ensuring the zero velocity for the solid phase, which will be carefully investigated in the following chapter 4.

Chapter 4: Density-based topology optimization of dual-flow heat exchanger with moderate conductive material

Chapter Summary

This chapter delves into the resolution of the encountered problem identified in chapter 3, mainly presented by the inadequacy of the maximal imposed impermeability in achieving zero velocity of the solid phase. To rectify this issue, the value of the impermeability is increased, concomitantly imposing a constraint on the maximal allowed pressure drop inside the flow channels. This dual strategy is mandatory to alleviate potential blockage concerns within the heat exchanger (HX) flow channels, stemming from the imposition of a high impermeability value on the solid phase. The identical design domain employed in Chapter 3, representing the periodic unit within the counter-flow plate heat exchanger (PHE), is utilized in this chapter for the topology optimization (TO) process. The objective of TO is to maximize exchanged heat, leading to a new topology characterized by the introduction of the moderate conductive solids (Stainless Steel) in the central region of the heat exchanger channels. In order to experimentally validate the design methodology in subsequent chapters, an additional design domain is introduced by excluding the periodicity effects at the upper and lower boundaries of the design domain. This decision is prompted by challenges associated with accurately representing the periodic local (variable) heat flux on the upper and lower plates of the HX unit using experimental equipment. Pursuant to the aforementioned TO objective, new fins allocation has been acquired for dual-flow HXs using moderate conductive material (Stainless Steel), where the solids are positioned near the insulated walls. A thorough examination of TO input parameters' effects on the derived topology has been conducted. This chapter focuses only on presenting the optimized topologies and extensively examining the effect of the TO's input parameters. The thermo-hydraulic performance evaluation and the physical interpretations of the TO-derived designs are kept to the following chapter 5.

Keywords of the Chapter:

Topology optimization, Heat exchanger, density parametrization, Conjugate heat transfer, gradient optimization, optimal fins allocation, moderate conductive material.

4.1 Introduction

In the present chapter, the density-based TO is employed to handle two distinct design problems. The first design problem corresponds to a periodic unit within the whole Plate Heat Exchanger (PHE), identical to the configuration examined in Chapter 3. The second one diverges by disregarding the periodic effects attributed to the upper and lower units within the PHE. The acquired topologies for the second design problem (DP2) will be numerically and experimentally validated in the forthcoming chapters. The primary objective of this chapter is to address and resolve the unphysical issue identified in Chapter 3, namely the insufficiency of the employed impermeability condition in ensuring zero velocity for the solid phase, which have not been addressed in the literature. It should be noted that the insufficient maximum impermeability value utilized in chapter 3 is widely used in the literature [3]-[6] for the purpose of averting the numerical problems caused by high impermeability value. The main reason behind this insufficiency for the current work may be attributed to the difference in the design problem, boundary conditions and input parameters between the present work and the literature. To ensure that the aforementioned non-physical problem is solved, a scrutinization is conducted on the TO-derived topologies of DP1 and DP2 by evaluating the velocity field of the solid and fluid phases. The examination stage reveals a negligible velocity in the solid phase, indicating the resolution of the deficiency discovered in the methodology of chapter 3. Therefore, this classifies the employed methodology of the present chapter as a topology optimization (TO) process rather than a topology generation one (as in chapter 3). Subsequently, an examination is conducted to analyze the impact of various input parameters of the TO on the resulting topologies. This investigative phase reveals that the topologies obtained for the first (DP1) and second (DP2) design problems primarily exhibit the allocation of generated solids within the central region of the flow channels and in proximity to the insulations on the upper and lower plates, respectively. Ultimately, a crucial limitation, primarily elucidated by the use of a highly conductive material (Aluminum) in the applied methodology, will be discussed and interpreted.

4.2 Problem Formulation of the Topology optimization

4.2.1 Design problems

In this chapter, two design problems are introduced for the topology optimization process. Both design problems correspond to counter-flow Heat Exchanger (HX) units. The first HX unit involves the incorporation of the thermal periodic condition on its top and bottom walls to account for the thermal effect of the upper and lower units within the counter-flow PHE, identified as Design Problem 1 (DP1). The second one assumes the adiabaticity of the top and bottom boundaries, thereby named as Design Problem 2 (DP2). The second approach is adopted for experimental validation in subsequent chapters and to address challenges associated with experimentally representing variable local heat flux across the top and bottom boundaries of the HX unit, acknowledging the complexities arising from the periodicity effect. Both design problems are presented in the illustrated figure below with the corresponding dimensions. As depicted in Figure 4.1b, the dimensions of the second design domain distinguished by insulated walls, have been enlarged to facilitate its fabrication using conventional techniques. Further discussions on the fabrication process will be provided in the forthcoming Chapter 6.

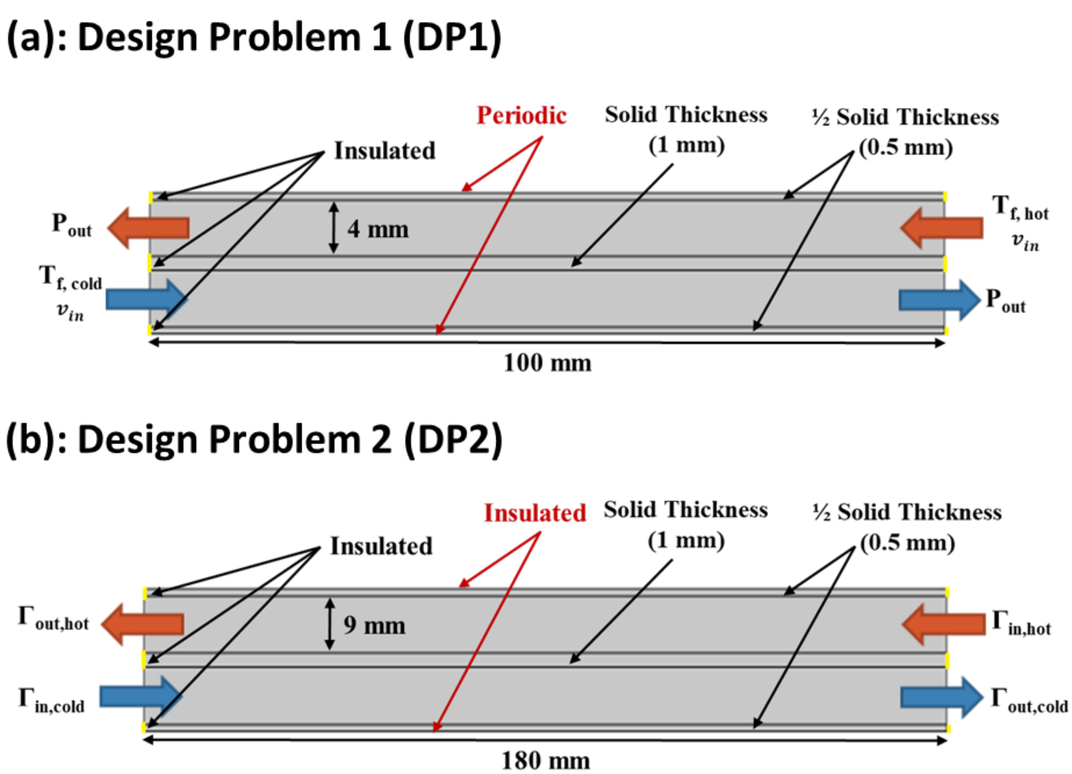

Figure 4.1: (a): Simplified PHE's unit (DP1), **(b):** HX unit with insulated walls (DP2).

4.2.2 Conjugate heat transfer modeling

The conjugate heat transfer physics in HXs combines the fluid dynamics and heat transfer models. The incompressible and steady-state fluid flow in the HX is modelled using the continuity and momentum equations which are given as respectively, assuming for steady-state and incompressible flow conditions:

$$\begin{gathered} \nabla . \boldsymbol{v} = 0 \\ \rho_f (\boldsymbol{v}. \nabla) \boldsymbol{v} = -\nabla P + \mu . \nabla^2 v - \boldsymbol{f}(\gamma) \end{gathered} \tag{33}$$

where $\boldsymbol{v}$ is the velocity (m.s^{-1}), P the pressure (Pa), μ the fluid dynamic viscosity (Pa.s), ρ_f the fluid density (kg.m^{-3}) γ is the TO's design variables. In the density-based topology optimization, the Momentum equation needs to be modified by adding a Brinkman friction $\boldsymbol{f}$ coefficient to dominate the design domain treated as porous medium which can be defined as follow:

$$\boldsymbol{f}(\gamma) = \alpha(\gamma) \boldsymbol{v} \tag{34}$$

where α is the inverse permeability that must be interpolated between the solid and fluid phases to define the optimized flow path (the detailed interpolation function equations will be discussed in the TO section).

Moreover, the Reynolds number of the TO process, which denotes the ratio between the inertia over the viscous terms is defined at the inlets of the HX for simplicity and is expressed as:

$$Re = \frac{\rho_f v_{in} D_h}{\mu} \tag{35}$$

where D_h is the hydraulic diameter (m) and v_{in} is the inlet velocity of the fluid (m.s^{-1}). The heat transfer will be studied in the solids that are dominated by conduction and in the fluids that are dominated by convection. The steady-state energy equation is utilized to model the heat transfer of the HX.

$$S(\gamma) \boldsymbol{v}. \nabla T - \nabla . (k(\gamma) \nabla T) = 0 \tag{36}$$

where T is the temperature field (K), $S(\gamma)$is the volumetric heat capacity interpolation function (J.m^{-3}.K^{-1}) and $k(\gamma)$ is the thermal conductivity interpolation function (W.m^{-1}.K^{-1}). The detailed interpolation function equations will be provided in the TO section (section 4.3).

4.2.3 Boundary Conditions

As illustrated in Fig. 4.1a & 4.1b, a set of Dirichlet boundary conditions are imposed at the inlet of each fluid by setting a uniform velocity and temperature profiles as follow:

$$\begin{gathered} -\boldsymbol{v}.\boldsymbol{n} = v_{in} \Longleftrightarrow \text{on } \Gamma_{in,cold} \text{ and } \Gamma_{in,hot} \\ T = T_{f,cold} \Longleftrightarrow \text{on } \Gamma_{in,cold} \\ T = T_{f,hot} \Longleftrightarrow \text{on } \Gamma_{in,hot} \end{gathered} \tag{37}$$

where $T_{f,cold}$, $T_{f,hot}$ are the inlet temperatures of the cold and hot fluids (K), respectively, and $\boldsymbol{n}$ is the normal vector to the corresponding boundary outwardly oriented to the design domain. Moreover, a uniform pressure and outflow conditions are set at the outlet boundaries of fluid flows as hydraulic and thermal boundary conditions respectively.

$$\begin{gathered} P = 0 \Longleftrightarrow \text{ on } \Gamma_{out,cold} \text{ and } \Gamma_{out,hot} \\ -\boldsymbol{n}.\nabla T = 0 \Longleftrightarrow \text{ on } \Gamma_{out,cold} \text{ and } \Gamma_{out,hot} \end{gathered} \tag{38}$$

Additionally, a periodic boundary condition is assigned at the upper and lower boundaries of TO design domain 1 (DP1), as depicted in Figure 4.1a, to account for the heat transfer effects from the adjacent upper and lower units within the whole HX. In contrast, an adiabatic condition is imposed on the top and bottom walls of TO design domain 2 (DP2), illustrated in Figure 4.1b.

4.3 Topology optimization (TO)

In this subsection, the same methodology presented in chapter 3 for the density-based (porosity-based) topology generation is employed in the present chapter. Specific emphasis is placed on elucidating various modifications of the aforementioned methodology.

4.3.1 Interpolation functions

In the density-based TO procedure, the design variables (densities) values (γ) exhibit a continuous variation ranging from 0 (fluid) to 1 (solid). The incorporation of interpolation functions is essential for the representation of intermediate values of the porous medium. Starting with the impermeability interpolation function, the inverse permeability is interpolated between the solid and fluid phases using the following formula [244]:

$$\alpha(\gamma) = \alpha_{max} * q * \frac{\gamma}{q + 1 - \gamma} \tag{39}$$

where q is a penalization coefficient and α_{max} is the maximum impermeability value.

In this chapter, the value of α_{max} is augmented one order of magnitude comparing to the value used in the preceding chapter 3 to guarantee the attainment of negligible velocity within the solid phase. The adjustment is made in response to the observed limitation, where the utilized value of α_{max} proved insufficient to enforce the desired zero velocity of the solid phase. Moreover, the maximum impermeability value is computed using the following formula [272]:

$$\alpha_{max} = \frac{\mu}{Da.{D_h}^2} \tag{40}$$

where *Da* is the dimensionless Darcy number that represents the permeability effect of the porous medium. Concerning the thermal properties interpolation, the RAMP (rational approximation of material properties) interpolation function is used to interpolate the value of the thermal conductivity and the volumetric heat capacity between the solid and fluid phases. The aim behind using of the RAMP function instead of the classical SIMP (Solid Isotropic Material with Penalization) function, is founded in the demonstrated capability of the RAMP function to penalize a broader range of intermediate design variables when compared with the SIMP function [273]. It is imperative to acknowledge that the alteration in the interpolation function type does not induce a huge modification in the obtained topology. Rather, its purpose is to minimize the intermediate densities intensity within the design domain to the greatest extent possible. Lastly, the thermal conductivity $k(\gamma)$ and volumetric heat capacity $S(\gamma)$ interpolation functions are expressed respectively as follows [274]:

$$\begin{aligned} k(\gamma) &= k_f \frac{(1-\gamma)(C_k(1+b)-1)+1}{C_k(1+(b(1-\gamma))} \\ S(\gamma) &= S_f \frac{(1-\gamma)(C_s(1+b)-1)+1}{C_s(1+(b(1-\gamma))} \end{aligned} \tag{41}$$

where b is the convexity parameter of the function, S_f is the volumetric heat capacity of the fluid phase (J.m^{-3}.K^{-1}), k_f is the thermal conductivity of the fluid phase (W.m^{-1}.K^{-1}), C_k and C_s are the thermal conductivity ratio and the volumetric heat capacity ratio, respectively, between the fluid and solid phases.

4.3.2 Optimization problem formulation

In this research, the primary objective of the TO is to maximize the exchanged heat (Q) between the cold and hot fluids inside the HX which can be expressed as [249]:

$$Q = \int_{out} E\, d\Gamma - \int_{in} E\, d\Gamma = S_f\left(\int_{out} \boldsymbol{v}.T\, d\Gamma - \int_{in} \boldsymbol{v}.T\, d\Gamma \right) \quad (42)$$

where E is the energy (W). To constraint the non-linear problem, a set of constraints have been imposed. First, a constraint is imposed on the maximal pressure drop inside the flow channels to avoid the blocking issues caused by elevating the value of the maximum impermeability. Moreover, the continuous design variable field γ is bounded between 0 (fluid) and 1 (solid). Additionally, the governing equations presented in Eqs. (33) & (36) should be also set as a constraint to ensure that their residuals will be zero in each iteration of the optimization process. Eventually, a solid fraction is imposed to constraint the amount of solid generated in the flow channels. Thus, the TO's mathematical problem can be summarized as follows:

$$\begin{aligned} & Find\ \gamma \\ & Max\ Q\ (Eq.10) \\ & s.t \begin{cases} 0 \le \gamma \le 1 \\ \dfrac{\int_{\Gamma_{in,cold}} P}{n * \Delta P_{bareHX,cold}} - 1 < 0 \\ \dfrac{\int_{\Gamma_{in,hot}} P}{n * \Delta P_{bareHX,hot}} - 1 < 0 \\ \dfrac{\int_{\Omega} \gamma d\Omega}{v_{fs}} - 1 \le 0 \\ Eqs. (33), (36) \end{cases} \end{aligned} \quad (43)$$

where v_{fs} is the maximum allowed solid volume fraction and Ω is the design domain. $\Delta P_{bareHX,cold}$ and $\Delta P_{bareHX,hot}$ are the pressure drop in the cold and hot channels of the bare HX (empty channels) respectively, n is an index number that indicates the intensity of the maximal allowed pressure drop inside the TO-optimized HX relative the bare HX (with empty channels) and Ω is the TO design domain.

4.3.3 Filter and projection

During the topology optimization, filters are necessary to avoid the numerical instabilities (checkerboard, mesh dependency, local optimum, etc.) caused by the ill-posedness of the TO problems [252]. To avoid this issue, filters and projection techniques are adopted to control the computed design variables. For the filtering technique, the Helmholtz PDE filter [253] is adopted to obtain an averaged filtered design variables γ_f:

$$\gamma_f = R^2\nabla^2\gamma_f + \gamma \tag{44}$$

where R is the filter radius which is considered as the mesh element size in the current study. After the filtering process, an intermediate density area near the solid-fluid interface is generated. In order to reduce it, the filtered design variables are projected using the smooth Heaviside hyperbolic tangent projection [254]:

$$\gamma_p = \frac{\tanh\left(\beta\left(\gamma_f - \gamma_\beta\right)\right) + \tanh\left(\beta\gamma_\beta\right)}{\tanh\left(\beta\left(1 - \gamma_\beta\right)\right) + \tanh\left(\beta\gamma_\beta\right)} \tag{45}$$

where γ_p is the projected design variable, β is the projection slope and γ_β is the projection point.

4.3.4 COMSOL implementation

The implementation of the TO models for the 2D counter-flow HX unit is carried out using the Finite Element Method (FEM)-based commercial software COMSOL 6.0. The CFD Module of COMSOL is employed to address the fluid problem (Eq. 33) with a first-order discretization scheme for velocity and pressure. Furthermore, the Heat Transfer Module is utilized to solve the energy equation, employing a first-order discretization scheme for the temperature field. As for the Helmholtz PDE filter, a linear discretization scheme is used and the filter radius is set 1.5 times and twice of the maximum element size for DP1 and DP2, respectively. Triangular mesh is used to discretize the governing equations and the number of elements of the design problems 1 & 2 are 90,000 and 160,000 elements, respectively. The governing equations are subjected to the streamline stabilization scheme, while the upwind stabilization scheme is omitted. The direct solver

PARDISO, integrated into COMSOL, is utilized for solving the discretized governing equation. Furthermore, segregated solver steps are utilized to address the fluid problem, thermal problem, and filter PDE. Gradient optimization is conducted through the utilization of the Optimization Module in COMSOL. This module solves the adjoint problem to furnish the sensitivities of both objective and constraint functions for the globally convergent method of moving asymptotes (GCMMA) [178], serving as the optimizer for iteratively updating the topology throughout the optimization process. A conservative continuation strategy is applied on the penalization coefficients (q and b) of the interpolation functions and the projection slope (β). The continuation sequence is chosen to attenuate a possible convergence to a local optimum. The proposed continuation scheme is composed of ten steps as shown in Tab. 4.1. For the first steps, the parameters values are set to low values to stabilize the topology optimization process and guarantee better sensitivity scaling by giving the optimizer some freedom. Then, the parameters values are slowly increased in the last steps to acquire more precise physical models by penalizing the intermediate densities and sharping the interfaces. The continuation strategy leads to better performance and gives more stability to the topology optimization process than starting with the final parameters values which often leads to fast convergence to a local optimum in such a non-convex optimization problem [67]. It is noteworthy that a less conservative continuation strategy involving a reduction in both the number of continuation steps and model evaluations is feasible, but with an elevated risk of converging towards a poor local optimum.

Table 4.1: Continuation scheme for penalization and projection coefficients

Step	1	2	3	4	5	6	7	8	9	10
q	0.01	0.01	0.01	0.03	0.03	0.08	0.1	0.1	0.1	0.1
b	0.1	0.1	0.1	5	5	20	50	50	50	50
β	1	1	1	2	3	4	5	6	8	8

4.3.5 TO setting parameters

The values of the TO's input parameters are summarized in the Table 4.2. First, the Reynolds number (Re) is computed according to the inlet boundaries for simplicity and the hydraulic diameter (D_h) is assumed to be double of the height of an infinite wide channel [255],[256]. Since the acquired topology has been reported to be strongly influenced by the input parameters of the

TO [31], a thorough examination of the effect of these parameters on the resulting topology will be extensively discussed in the results section. Furthermore, the projection point γ_β of the hyperbolic projection process is set to 0.5. The working fluid employed in the TO is water, while the solid material is Stainless Steel. The properties of both water and Stainless Steel are assumed to be temperature independent, as outlined in Table 4.3.

Table 4.2: TO parameters

Parameter	Design domain 1	Design domain 2
Re	300-500	50-150
D_h [mm]	8	18
Da	10^{-5}	10^{-5}
v_{fs}	(20%)	(5% - 30%)
γ_β	0.5	0.5
n	5-15	3-10
C_k	0.04	0.04
C_s	1.72	1.72
S_f [$J.m^{-3}.K^{-1}$]	4.18e6	4.18e6
R [mm]	0.15	0.5

Table 4.3: Material properties used in the TO [55]

Parameter	water	Stainless Steel	Aluminum
k [$W.m^{-1}.K^{-1}$]	0.61	15	237
ρ [$kg.m^{-3}$]	1000	7800	2700
C_p [$J.kg^{-1}.K^{-1}$]	4182	468	900
μ [Pa.s]	1e-3	-	-

4.4 Results and Discussions

This section is divided into two subsections; the first one presents the TO-optimized topologies for the design problem 1 (DP1) and the second subsection provides the TO-acquired topologies for the design problem 2 (DP2).

4.4.1 TO-optimized results for DP1

4.4.1.1 Correctness of the acquired results

Before starting with the investigation stage to test the effect of the TO's input parameters on the acquired topology for DP1, it is imperative to conduct an examination of the acquired topology. This involves the visualization of velocity contours within the designated domain of the TO to ascertain the resolution of the challenge outlined in chapter 3. Figure 4.2 elucidates the topological configuration derived from the density-based TO for the case denoted as DP1 at Re of 300. Concurrently, the figure 4.2 provides a representation of the velocity field for both the solid and fluid phases. It is evident that the solid phase manifests negligible velocity, indicating that the imposed impermeability effectively enforces a zero velocity for the generated solid within the HX's flow channels. Moreover, the TO-acquired topology DP1 is mainly characterized by the allocation of the irregularly distributed and geometrically distinct solids at the central horizontal axis of the flow channels. According to the velocity field presented in Fig. 4.2a, the TO-derived topology attempt to increase the velocity of the fluid near the walls where heat exchange occurs (heat flux from the hot fluid through the middle plate and periodic heat flux through the lower plate). This will decrease the convective and conduction resistances in the HX unit, thereby leading to an intensification of the exchanged heat.

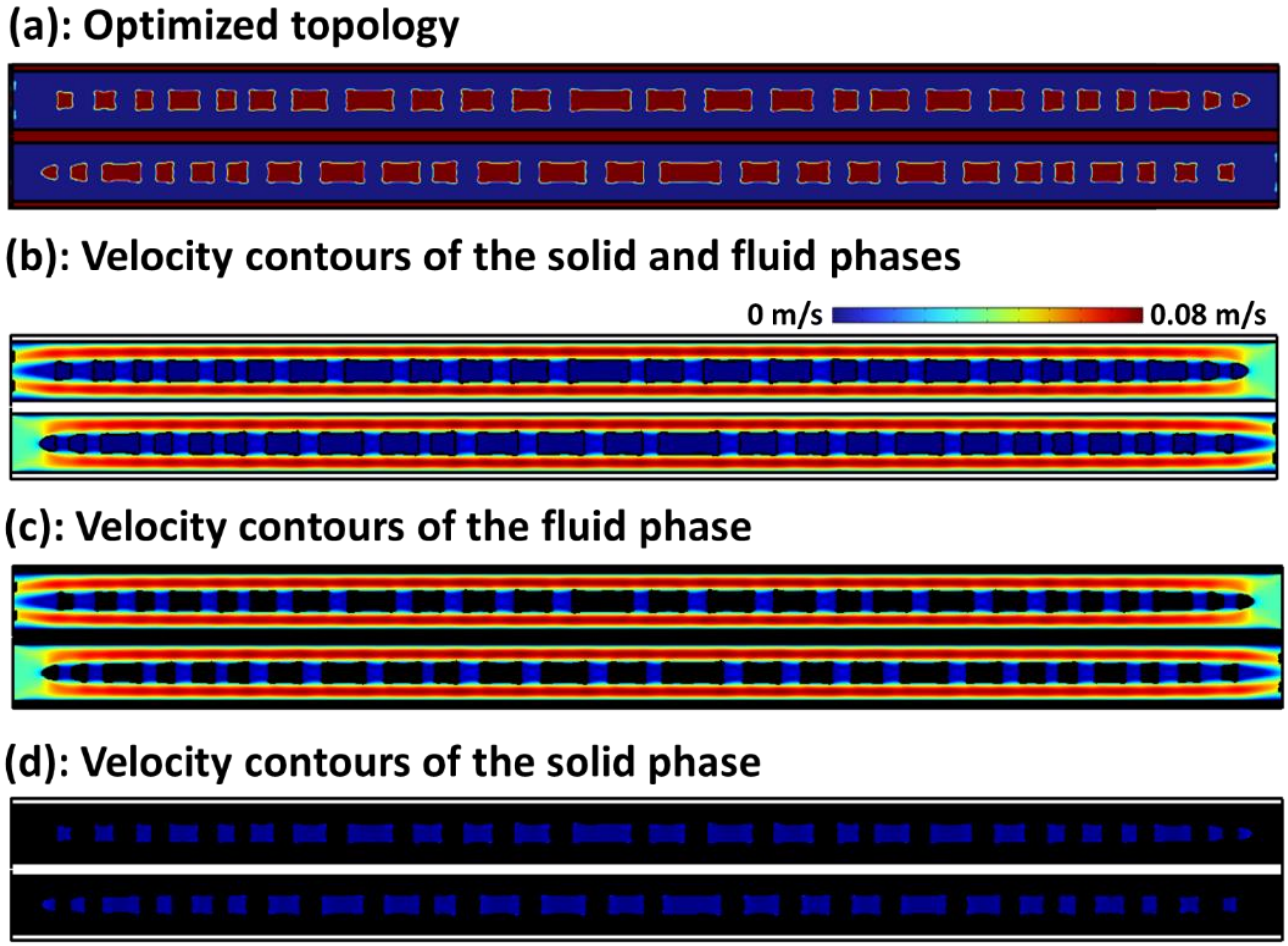

Figure 4.2: Optimized topology with the corresponding velocity contours for **(b):** solid and fluid phases, **(c):** Fluid phase and **(d):** solid phase.

4.4.1.2 Effect of the imposed pressure drop constraint intensity

Figure 4.3 illustrates the obtained topologies across different intensities of the maximum admissible pressure drop. The optimized topologies prominently showcase solid allocations positioned within the central regions of the flow channels. As illustrated, the augmentation of the maximum imposed pressure drop correlates with a concurrent increase in the width of the generated solids, which induces a localized elevation in flow velocity near the walls of the flow channel, thereby resulting in an intensification of the objective function (heat transfer rate).

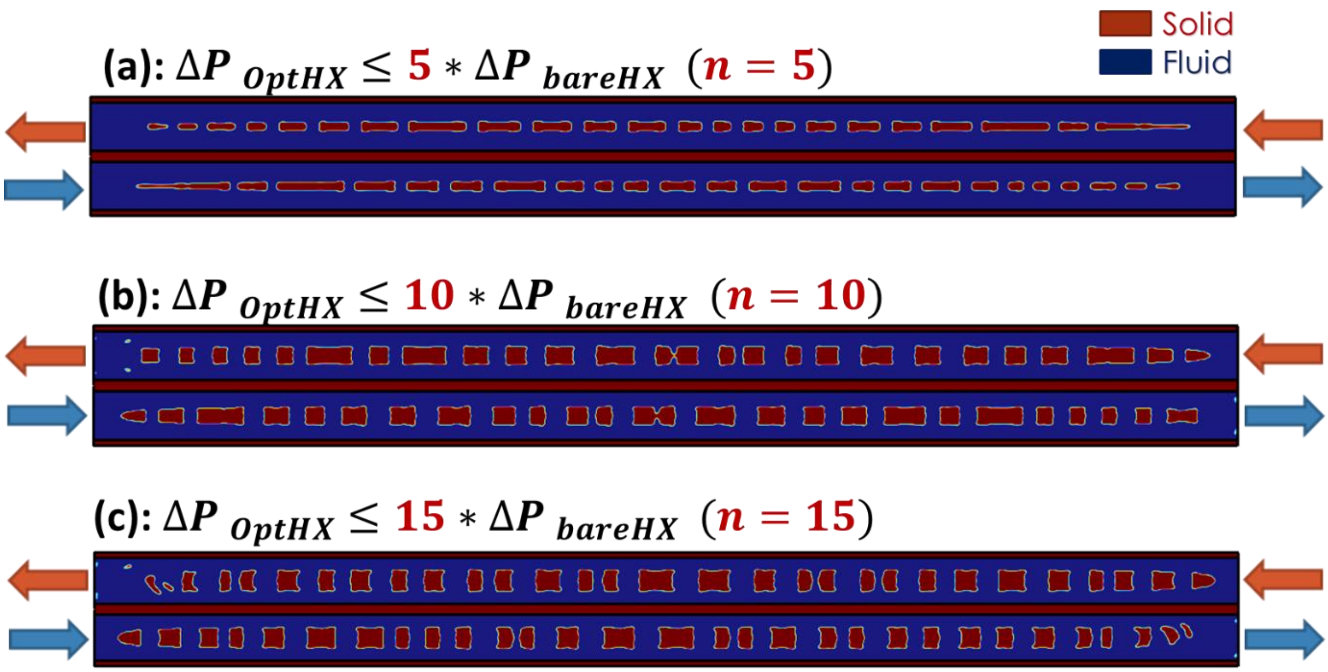

Figure 4.3: TO-derived HXs at **(a):** n=5, **(b):** n=10, **(c):** n=15 under Re=500.

4.4.1.3 Effect of Reynolds number (Re)

The effect of the Reynolds number on the TO-derived topology for DP1 is investigated in this subsection. As depicted by figure 4.4, the acquired topologies at different *Re* maintain the same solid allocation at the central region of the HX's channels with a small difference in the distribution and geometry of the generated solids.

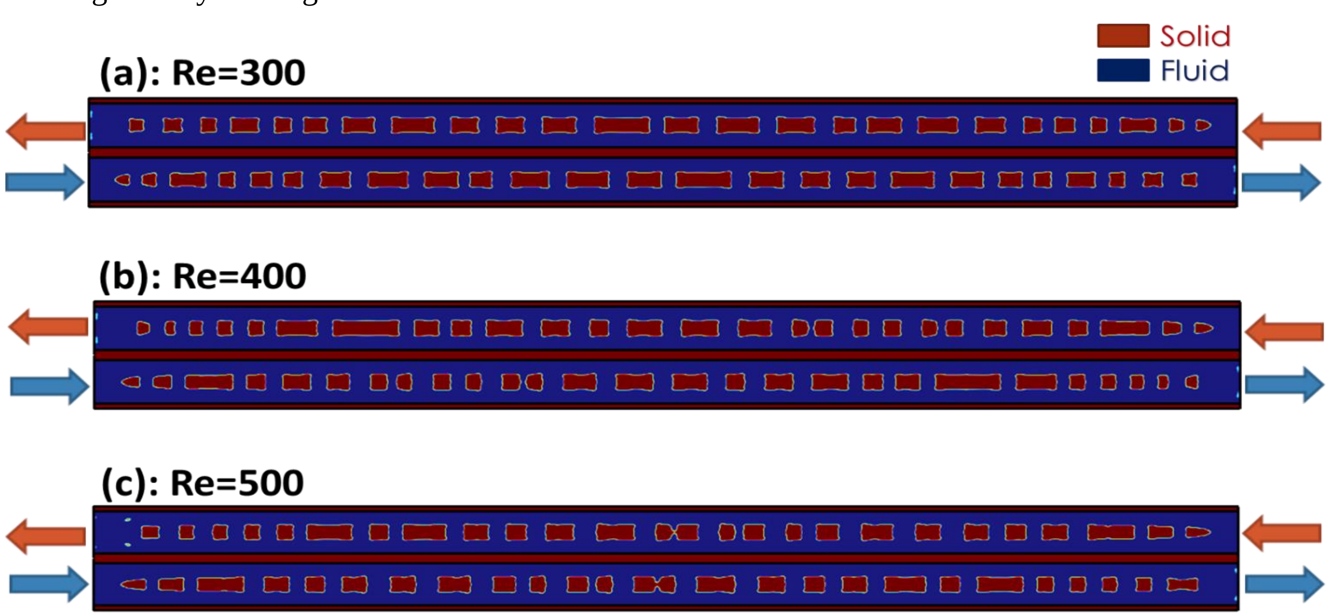

Figure 4.4: Optimized topologies at **(a):** Re=300, **(b):** Re=400, **(c):** Re=500 under n=10.

4.4.1.4 Effect of initial density distribution

Due to high impact of the initial guess in the optimization methods in general, and in the gradient optimization specifically, the effect of the initial density distribution on the derived topology is investigated. Figure 4.5 illustrates the TO-optimized topologies using three different uniform distribution. As seen, all TO-derived structures have similar allocation of the solids in the middle of HX's flow channels, with a small difference in the geometry and distribution of the generated solids and a negligible variation in the optimal value of the objective function. The marginal difference observed can be attributed to the implementation of a conservative continuation scheme, which will diminish the possibility of converging towards poor local minima.

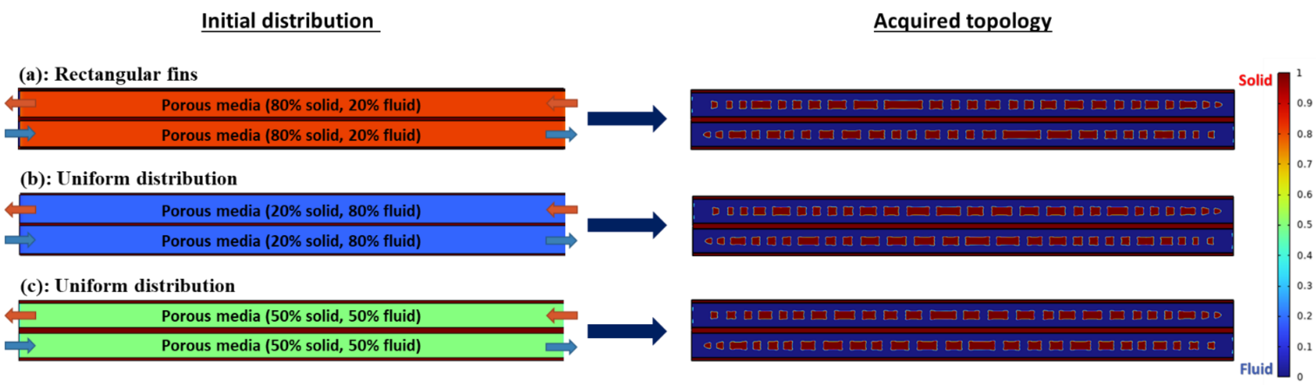

Figure 4.5: Optimized topology using different initial density distribution under *Re*=300, *n*=10.

4.4.1.5 Applicability of TO-design in industrial applications

In this subsection, the applicability of the TO-design on industrial plate heat exchangers (PHEs) is discussed. One possible scenario involves the fabrication of an additional plate embedded with the middle-inserted solids (TO-design presented in previous subsections) and assembled between two actual plates of the PHE. As seen in Figure 4.6a & b, the middle-inserted solids with an approximate thickness of 1 mm, are attached with the additional plate via their cross-sectional area and practically the whole plate assembly with the TO-design can be fabricated as one body (plate) using conventional manufacturing techniques. Therefore, the flow circulation within the PHE's unit is illustrated in figure 4.6c. The purpose of adding an additional plate with the TO-concept in the middle of each PHE's unit is to increase the local velocity of the fluid near the interface walls (where heat is exchanged), leading to an improvement in the PHE's thermal performance.

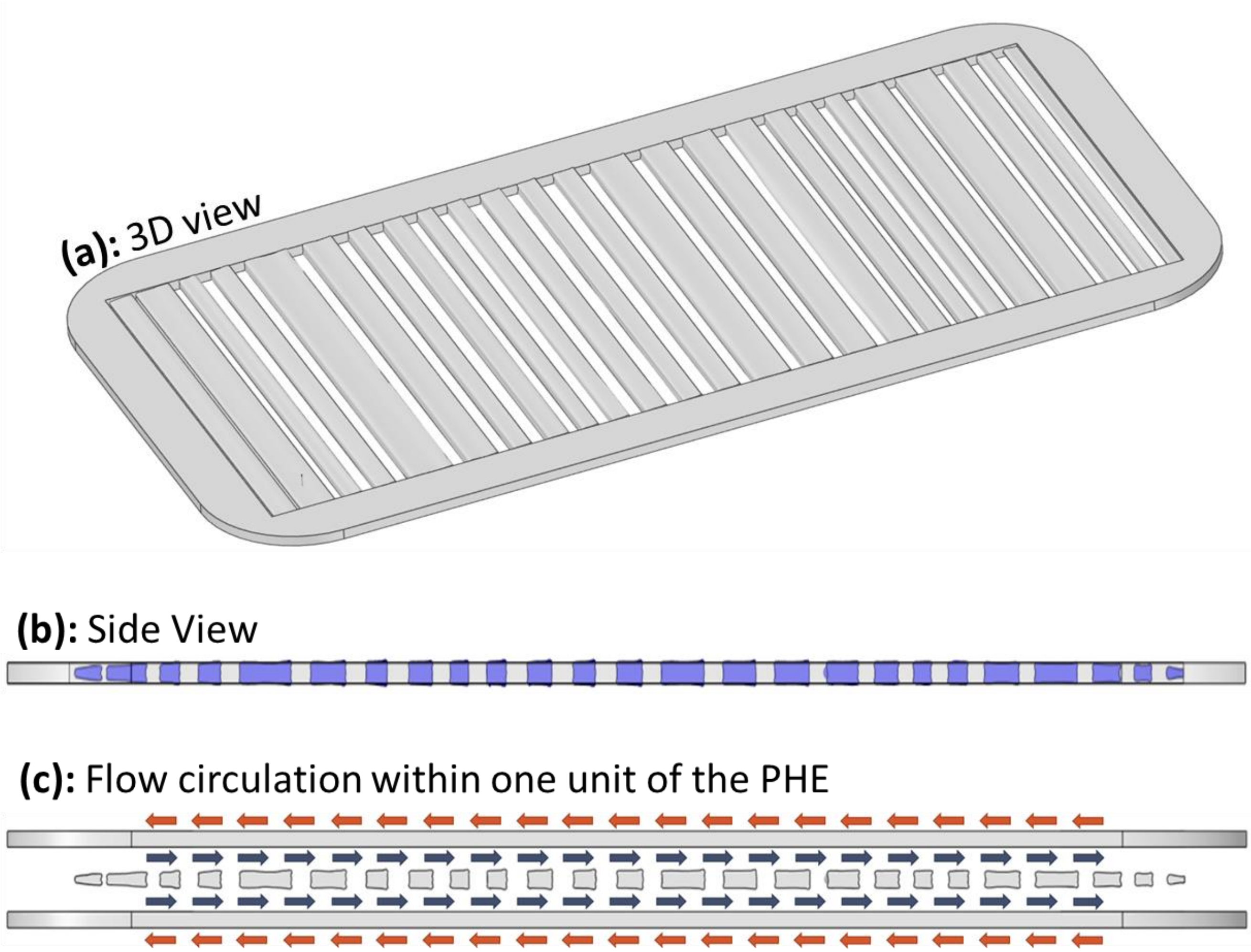

Figure 4.6: Application of the TO-design on an actual Plate heat exchanger

4.4.1.6 Summarization

The optimized configurations for DP1, employing moderately conductive materials (Stainless Steel) in the TO process, are mainly characterized by the concentrated distribution of generated solids within the central region of the fluidic channels of the HX. This central allocation of the solids in the flow channels aims to locally increase the velocity of the fluid near the walls (where heat is exchanged) leading to an augmentation in the convective thermal performance. Additionally, the TO-derived design attempt to decrease the conduction and convection resistance by avoiding the placement of the moderate conductive solids (Stainless Steel) at the interface walls (middle, top and bottom plates) where heat exchange occurs, leading to an intensification of the overall thermal performance.

4.4.2 *TO-optimized results for DP2*

4.4.2.1 Correctness of the acquired results

Similar to the previous subsection 4.4.1, an investigation is undertaken to scrutinize the obtained topology by visualizing the velocity field within the TO's design domain to ensure the resolution of the issues encountered in Chapter 3. Figure 4.7 presents the topological configuration derived from the TO for the DP2 at *Re*=100, accompanied with the representation of the velocity field for both solid and fluid phases. Evidently, the solid phase exhibits negligible velocity, signifying that the imposed impermeability was sufficient to enforce a zero velocity for the generated solid within the flow channels.

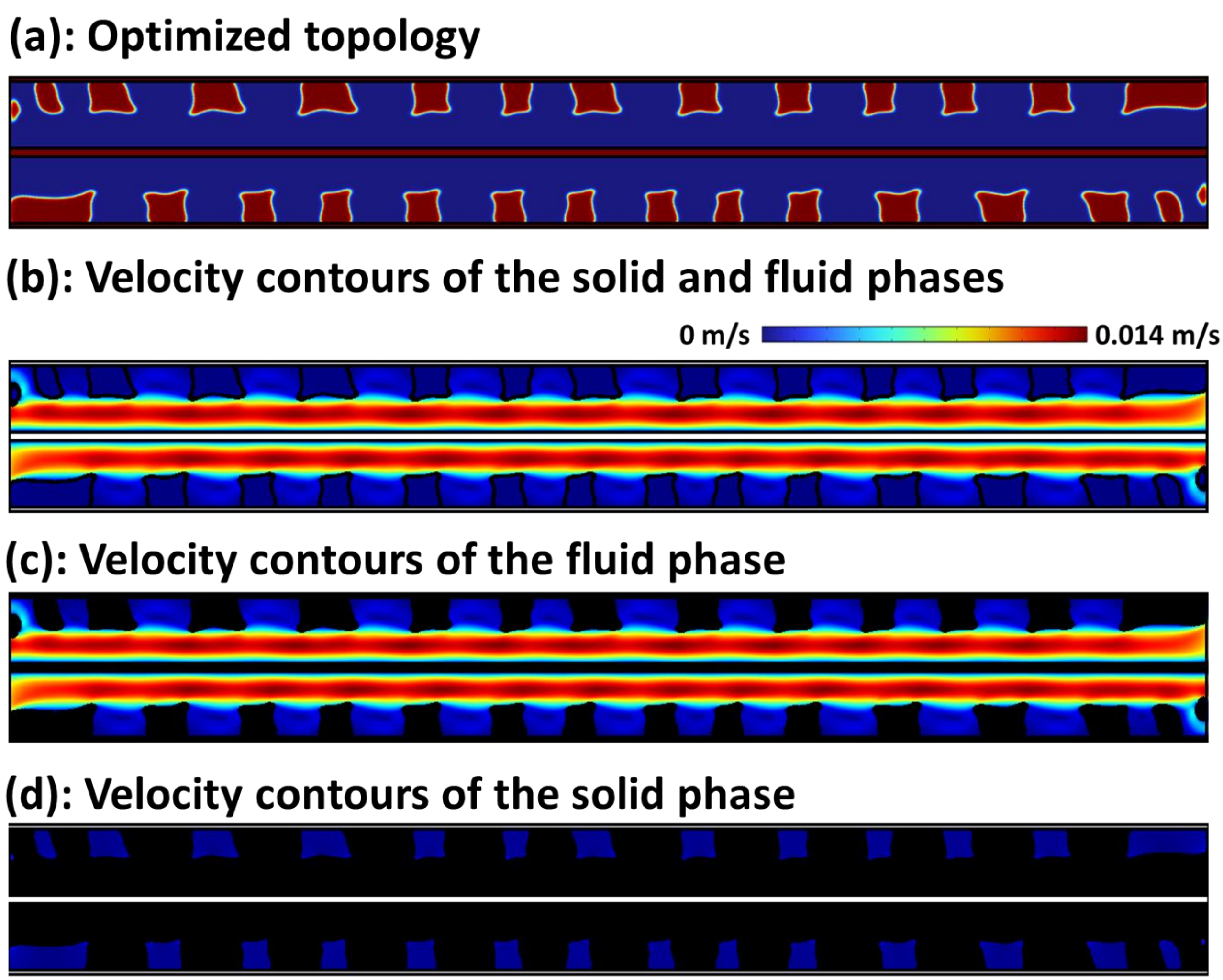

Figure 4.7: Optimized topology and the corresponding velocity contours for **(b):** solid and fluid phases, **(c):** Fluid phase and **(d):** solid phase.

The TO-acquired topology for DP2 is mainly featured by the allocation of the solids on the upper and lower plates of the HX unit (near the insulation). The generated fins are characterized by a curvature towards the HX's middle plate. As illustrated by Fig 4.7b, the TO-derived design for DP2 attempt to increase locally the velocity of the fluid near the walls of the HX's middle plate (the location of heat exchange) leading to an intensification of the exchanged heat, following the same concept of the acquired topology for DP1. Similar to the optimal design for DP1, the TO-derived design for DP2 aims to decrease the conduction and convective resistances of the HX by avoiding the positioning of the moderate conductive solids (Stainless Steel) at the interface walls (where heat is exchanged) of the middle plates.

4.4.2.2 Effect of Reynolds number (Re)

Figure 4.8 shows the acquired topologies for the DP2 at three Reynolds numbers. The optimized topology is distinctly characterized by the strategic placement of solid fins on the upper and lower plates, proximate to the insulation of the HX unit, rather than at the middle wall that separates the hot and cold fluids. Moreover, a conspicuous characteristic includes a distinct inclination in the geometry of the fins directed towards the central plate of the HX unit.

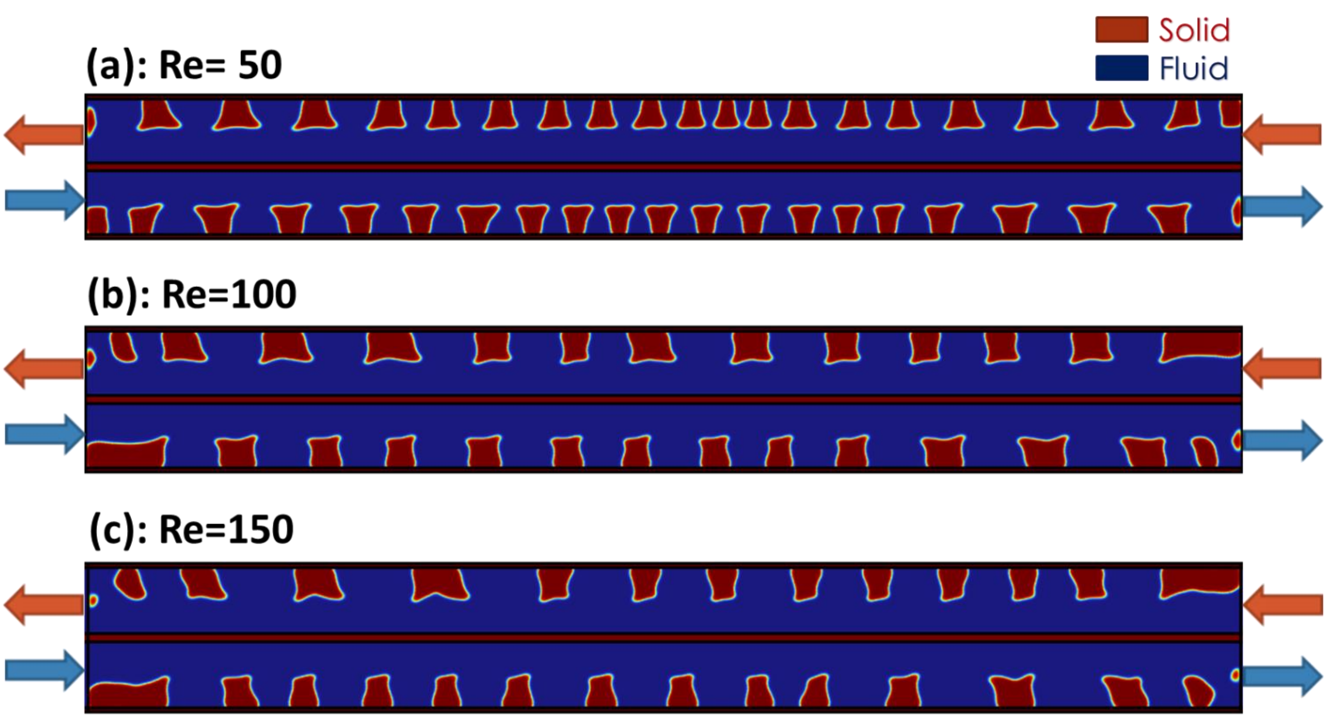

Figure 4.8: Optimized topology at **(a):** *Re*=50, **(b):** *Re*=100, **(c):** *Re*=150.

The physical interpretation behind the acquired topologies will be discussed in details in the upcoming chapter 5.

By increasing the *Re*, there is a concurrent reduction in the number of fins generated within the flow channels. This phenomenon is accompanied by a notable change in the geometry and distribution of the fins, as evidenced in Figure 4.8, which will underscore the pronounced sensitivity of TO-derived topology to the variations of the *Re*.

4.4.2.3 Effect of the imposed pressure drop constraint intensity

Within this subsection, an examination is conducted to investigate the impact of the maximum admissible pressure drop ($n \times \Delta P_{bareHX}$) within the flow channels on the acquired topologies. As the *n* value increases, there is a tendency for the generated solids to reduce the minimal distance within the channels as seen in Fig. 4.9. The narrower channels will increase the local velocity of the fluid leading to an increase in the exchanged heat (objective function). This investigation strongly evidences the crucial necessity of incorporating a pressure drop constraint in the TO process. This constraint is crucial for averting potential blocking issues within the flow channels of the HX.

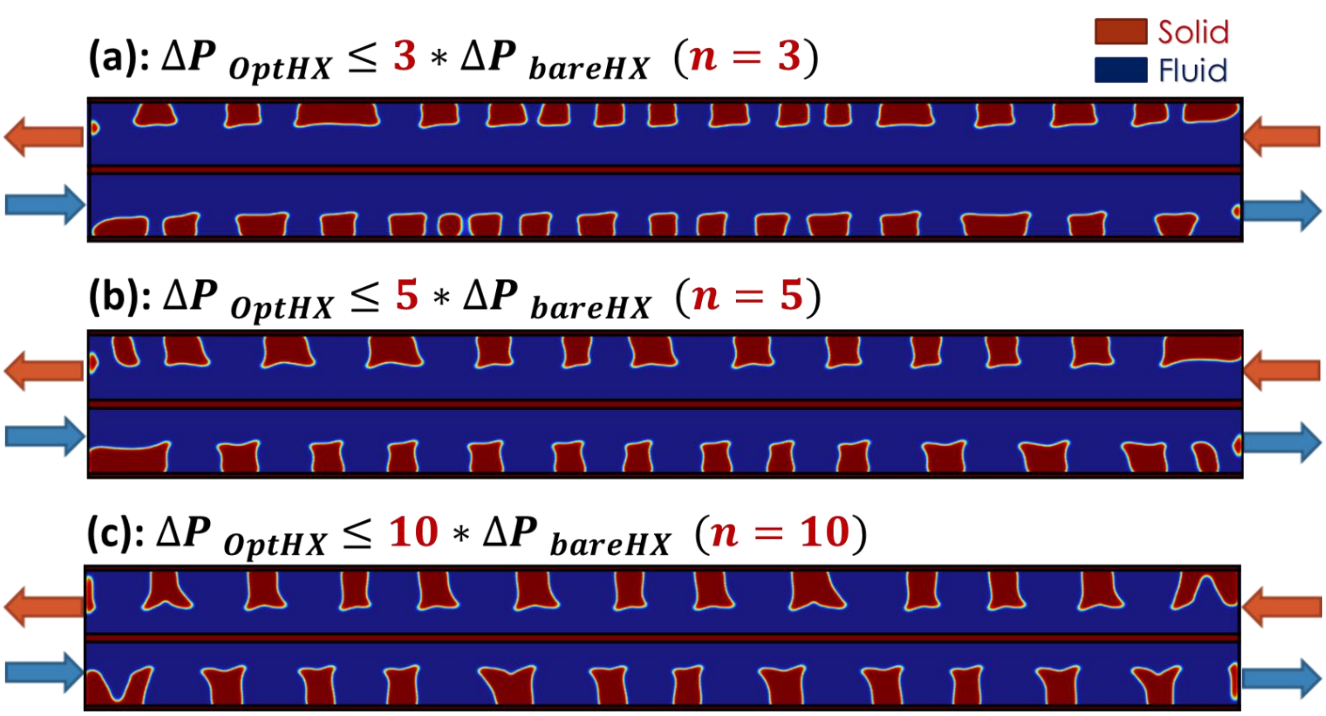

Figure 4.9: TO-derived HXs at **(a)**: *n*=3, **(b)**: *n*=5, **(c)**: *n*=10 under *Re*=100.

4.4.2.4 Effect of initial density distribution

Given the paramount significance of the initial guess in the optimization process, particularly in gradient optimization, various initial distributions of densities are tested, as delineated in Figure 4.10. The visual representation demonstrates that the acquired topologies have similar solid allocations, with a slight difference in the distribution of fins in the flow channels of the HX. Moreover, a negligible difference in the final optimized value of the objective function for the different TO-derived structures has been noted. This underscores the robustness of the employed methodology and the major reason behind this marginal difference may be addressed to the incorporation of a conservative continuation scheme, which will decrease the possibility of converging to a poor local optimum.

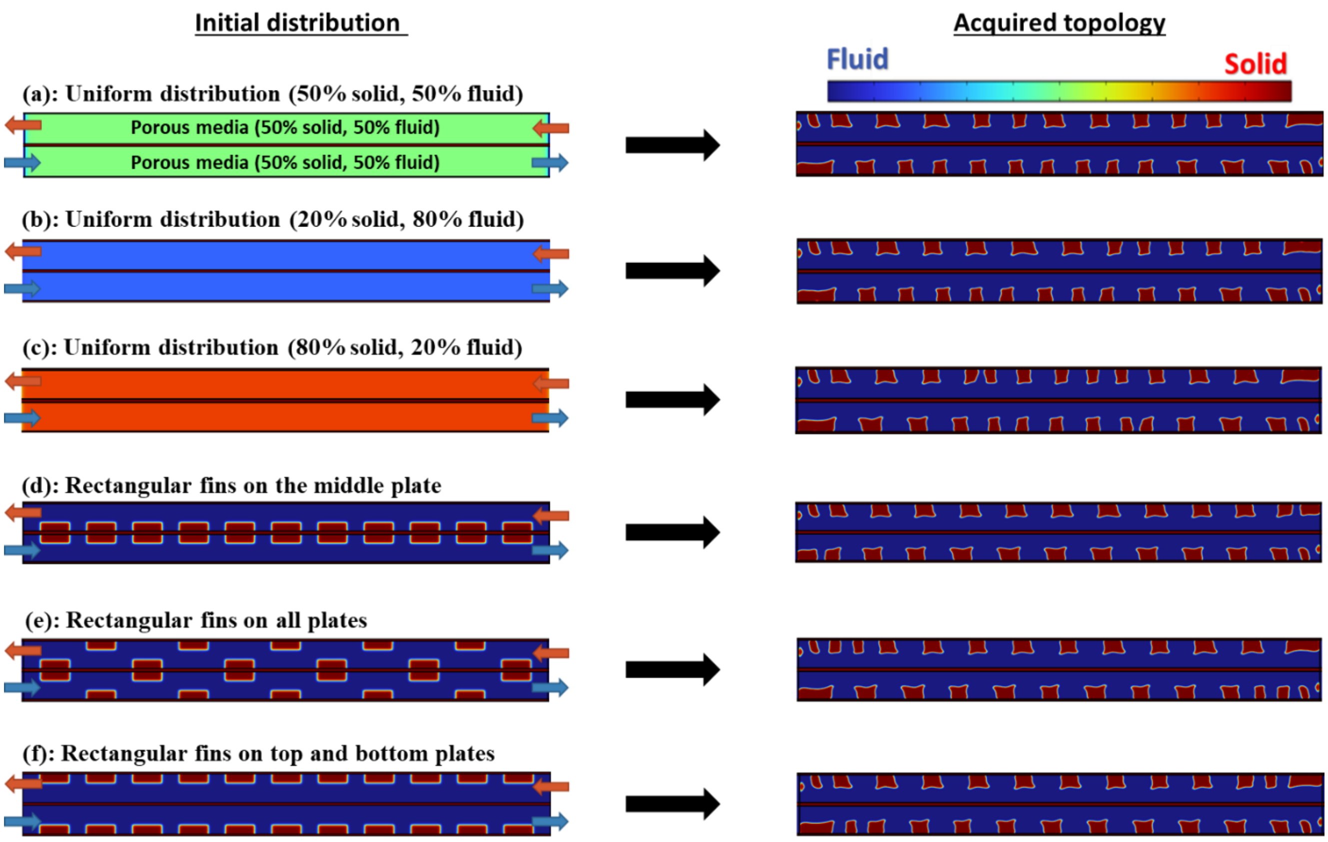

Figure 4.10: Acquired topologies using different initial distribution of the densities at *Re*=100, *n*=5.

4.4.2.5 Effect of final solid fraction

The optimization process incorporates a constraint on the amount of generated solid. The impact of varying the imposed percentage of generated solids on the resulting topology is examined in this subsection. Figure 4.11 clearly demonstrates that the width of the generated solids increases by increasing the imposed solid fraction with maintaining consistent solid allocation on the upper and lower plates of the HX unit. It is noteworthy that the maximum height of the generated solids in the HX's flow channels for the three presented cases is almost identical. This can be explained by the analogous imposed maximal pressure drop (n=5) in the flow channels for the three acquired topologies.

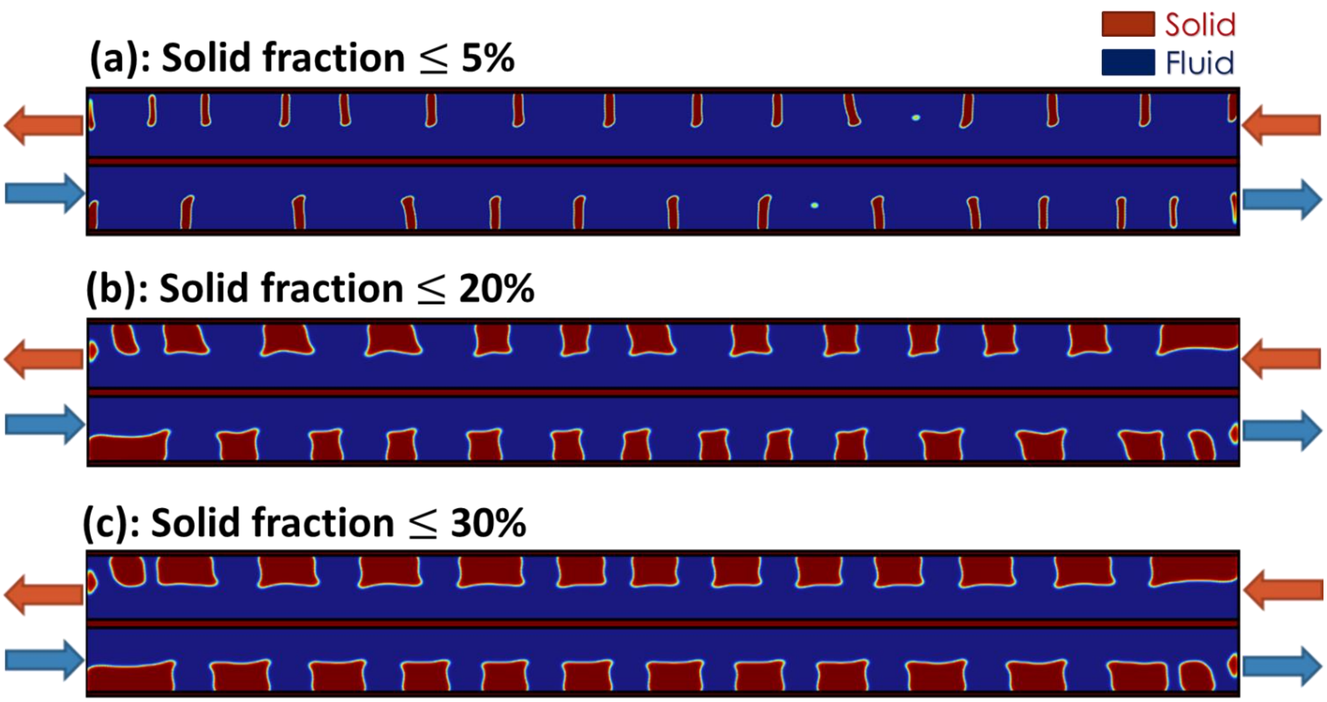

Figure 4.11: Optimized topologies at different imposed solid fraction under *Re*=100, *n*=5.

4.4.2.6 Effect of inlet velocity profile

In this subsection, an examination is conducted on the influence of the inlet velocity profile. Two velocity profiles are considered: a uniform profile and a fully developed profile resembling to the Poiseuille flow.

As illustrated in Figure 4.12, both optimized topologies (derived using the aforementioned velocity profiles) exhibit identical solid allocations, with minor distinctions observed in the quantity, distribution and geometry of the generated fins.

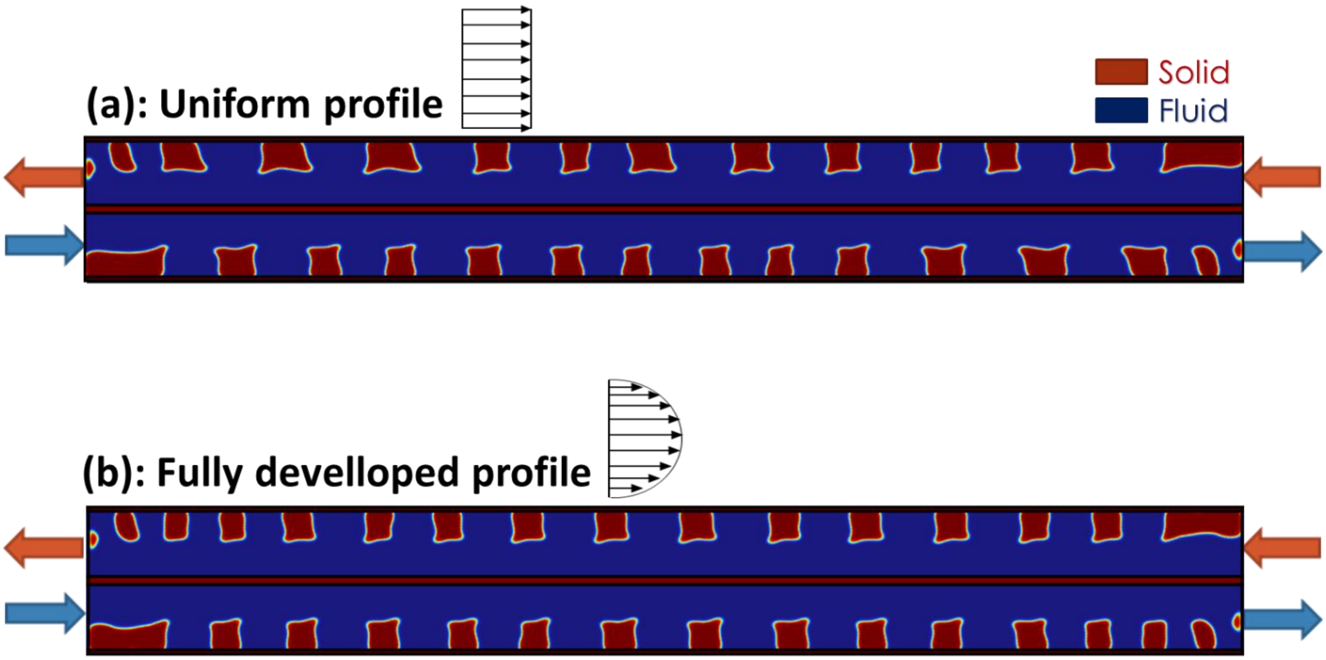

Figure 4.12: Obtained topologies with **(a):** uniform, **(b):** fully developed velocity profile at *Re*=100, *n*=5.

4.4.2.7 Effect of flow arrangement

In theory, the counter-flow arrangement of HXs is anticipated to yield superior thermal performance when compared with the parallel flow configuration. Nevertheless, it is intriguing to explore the impact of different flow arrangements on the resulting topology. As depicted in Figure 4.13, the distribution of the generated fins within the hot fluid channel using parallel flow arrangement is reversed in comparison to the configuration obtained through the counter-flow arrangement. This reversal is accompanied by distinct variations in the geometry and distribution of the fins.

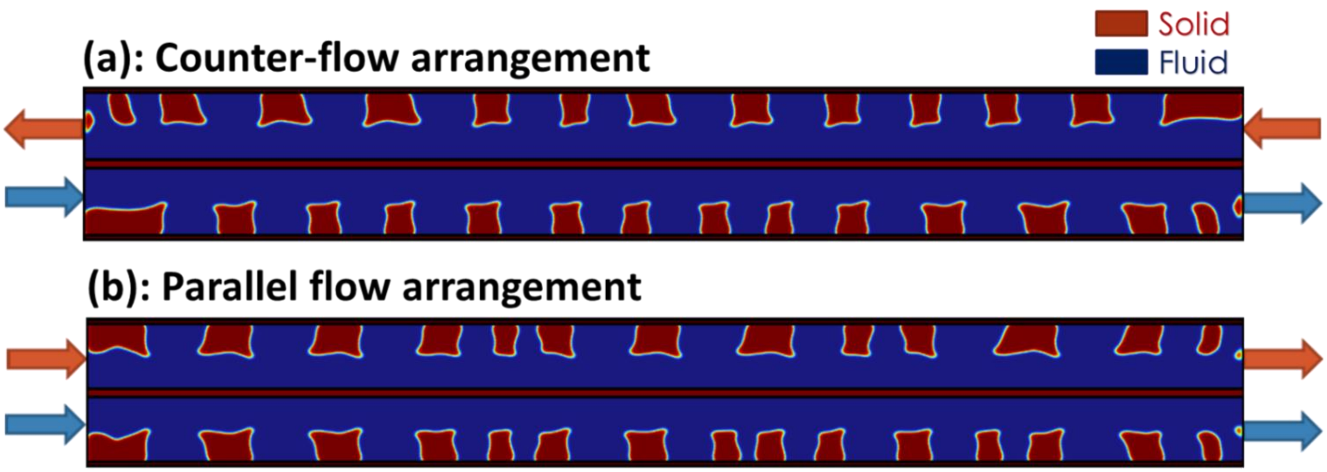

Figure 4.13: Optimized topologies using **(a):** Counter, **(b):** Parallel flow arrangement under *Re*=100, *n*=5.

4.4.2.8 Effect of inlet and outlet position of the flow channels

This investigation subsection delves into studying the impact of the flow inlet/outlets position on the resulting topology. As depicted in Figure 4.14, with two distinct positions of the flow inlets and outlets, the generated fins persist on the upper and lower plates of the HX unit. Notably, there is a significant disparity (compared to the previous obtained topologies) in the height and geometry of the fins under these different inlet/outlet configurations. This disparity in the fin's geometries can be attributed to the higher pressure drop of the bare HX with narrow flow inlets/outlets compared to the one with wide inlets/outlets (as in all previous investigations), which will increase the maximal imposed pressure inside the flow channels leading to an elevation in the fins' height (as demonstrated in section 4.4.2.3).

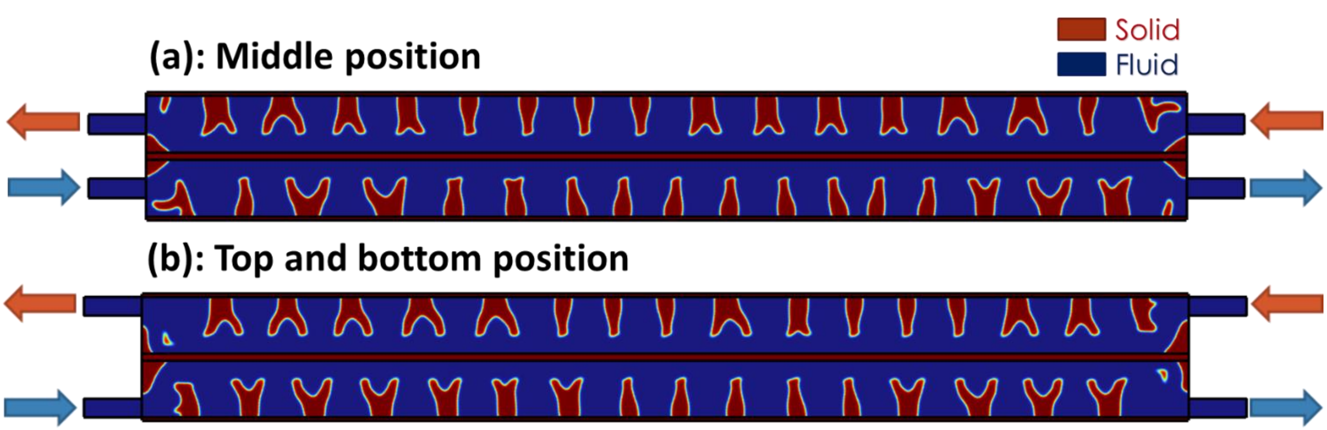

Figure 4.14: Optimized topologies using different inlet/outlet position of the HX flow channels at *Re*=100, *n*=5.

4.4.2.9 Effect of different Reynolds number for cold and hot fluids

In all preceding obtained topologies, the Reynolds number (Re) for both the cold and hot fluids was consistently set to the same value, representing a specific scenario in heat exchanger applications. To consider diverse cases, the TO is executed with different inlet Reynolds numbers for the cold and hot fluids. The outcomes presented in figure 4.15 reveal that altering the Re in the channels of the HX unit induces simultaneous changes in the distribution, geometry, and quantity of fins in both the cold and hot channels without changing the allocation of the generated solid near the insulated walls.

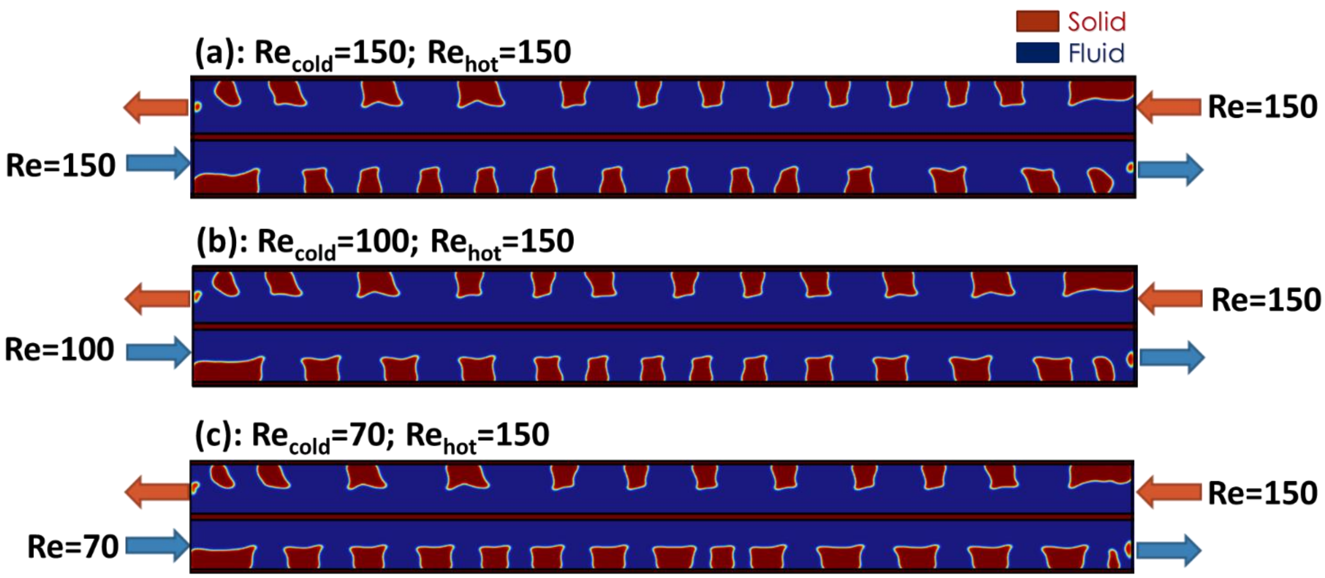

Figure 4.15: Optimized topologies using **(a):** same, **(b) & (c):** different Reynolds number for the cold and hot fluids.

4.4.2.10 Effect of temperature dependent thermo-physical properties of the water

According to the literature, the effect of the temperature dependent (TD) thermo-physical properties of the fluid on the acquired topology is still lacking for dual-flow HXs. Therefore, the effect of utilizing TD-properties of the fluid (water) on the acquired topology is investigated in this subsection. The TD thermo-physical properties of the water are employed in the TO process using the fitting polynomials presented in the table 4.4. As illustrated by figure 4.16, the TO-derived topology using water TD-properties is mainly featured by an inconsistent variation (number and geometry of fins) of the generated solid in the cold and hot fluids unlike the one obtained using Ti-properties (almost the same number and geometry of the fins in the cold and hot channels). The number of fins in the hot channel is decreased compared to the cold one, which can be explained by the disparity of the Reynolds number in the cold and hot channel (same inlet velocity) due to the diminishment of the water density and viscosity with the increase of the temperature. This will elucidate the high influence of the Reynolds number on the acquired topology, reaffirming the conclusion of the subsection 4.4.2.1. Lastly, both topologies (obtained using Ti and TD-properties) presented in the figure 4.16 are tested and compared using high fidelity CFD simulations. The results show a negligible enhancement in the thermo-hydraulic performance of the HX design acquired using TD-properties compared to the one obtained through Ti-properties.

Table 4.4: Fitting polynomials of the water thermo-physical properties (283.15 K <T< 343.15) [275]

Water	*Density [kg.m^{-3}]*	$\rho = -3.3 \times 10^{-7}T^4 + 4.3 \times 10^{-4}T^3 - 0.217T^2 + 47.95T + 2962.83$
	Specific heat [J kg^{-1} K^{-1}]	$C_P = 4.81 \times 10^{-6}T^4 - 6.1 \times 10^{-3}T^3 + 2.98T^2 - 643.2T + 56148.51$
	Viscosity [Pa.s]	$\mu = 2.96 \times 10^{-11}T^4 - 4 \times 10^{-8}T^3 + 2 \times 10^{-5}T^2 - 4.6 \times 10^{-3}T + 0.4$
	Thermal conductivity [W m^{-1} K^{-1}]	$k = -6.4 \times 10^{-11}T^4 + 1.34 \times 10^{-7}T^3 - 9.91 \times 10^{-5}T^2 + 3.2 \times 10^{-2}T - 3$

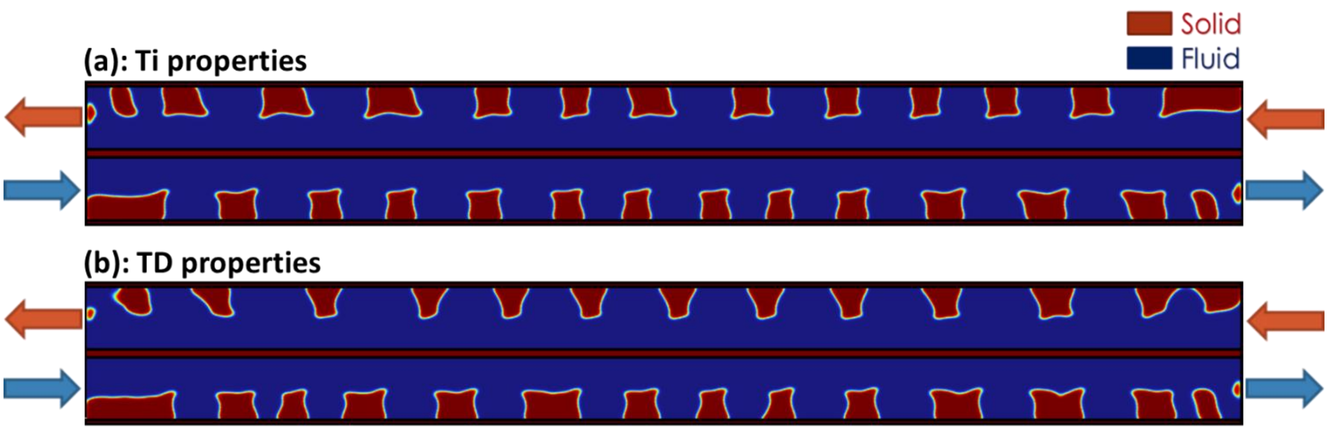

Figure 4.16: TO-acquired topologies using **(a):** Temperature independent and **(b):** Temperature dependent thermo-physical properties of the water at *Re*=100.

4.4.2.11 Effect of different gradient optimizers

In the literature, several gradient optimizers are implemented in the TO for HXs for the purpose of finding the optimum value of a specific objective under several constraints [1]. However, the effect of different gradient optimizers employed in the TO on the acquired topology has not yet been investigated so far [1]. Therefore, three gradient optimizers, including GCMMA, SNOPT (Sparse nonlinear optimizer) [276] and IOPOPT (Interior point optimizer) [277] are utilized and compared in the TO to examine their effect on the acquired topologies under the same input parameters, objective function and constraints. The three investigated gradient optimizers hold different mathematical background and thus the distinct approaches. Detailed explanations behind their mathematical background are beyond the scoop of this chapter and can be found in the mentioned references. As depicted by figure 4.17, a remarkable difference has been observed in the TO-acquired topologies using different gradient optimizers mainly by the distinct geometry and number of the generated fins. Additionally, a negligible difference (about 0.1 %) in the optimum achieved value of the objective function has been observed. This reflects the robustness of the density-based TO method in achieving the maximized performance.

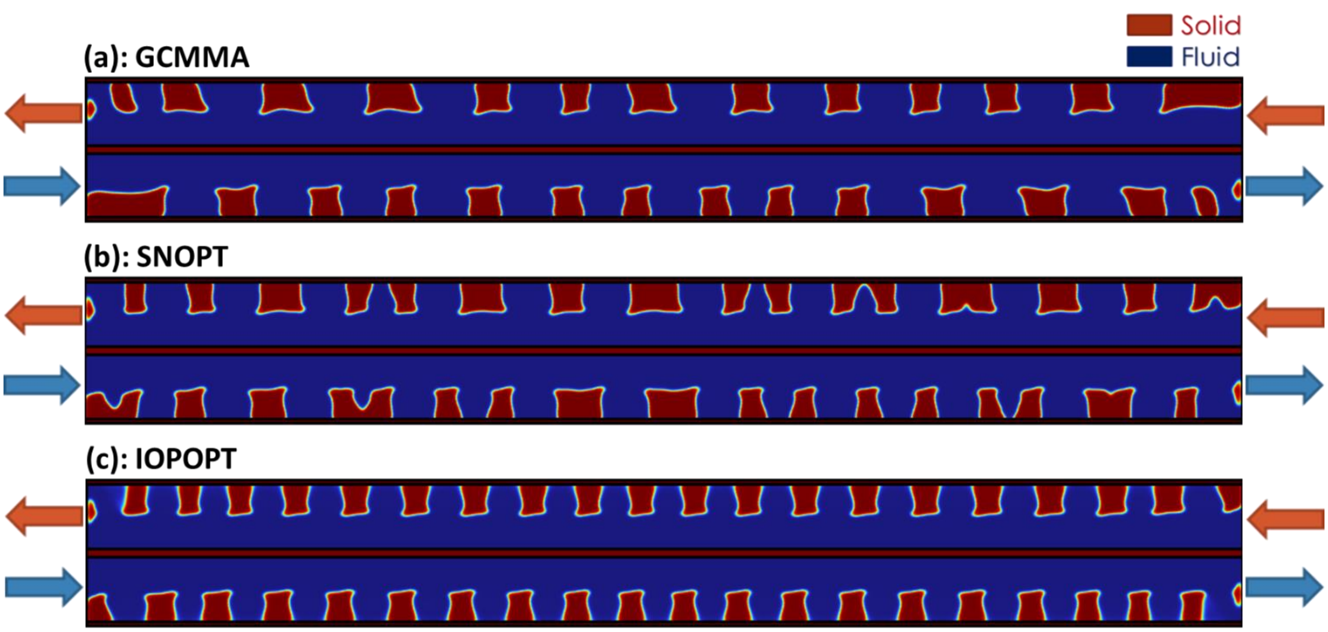

Figure 4.17: TO-derived topologies using **(a):** GCMMA, **(b):** SNOPT and **(c):** IOPOPT gradient optimizers at *Re*=100, *n*=5.

4.4.2.12 Physical interpretation of the TO-optimized topology

For the purpose of physically interpreting the TO-derived design, the evolution of the densities (porosities) and the Peclet number (*Pe*) distributions of the acquired topology presented in Figure 4.10c in the TO process is provided in figure 4.18. Considering the nature of density-based TO methodology, a crucial factor, which could determine the solid arrangement, is the relative intensity between the fluidic convective heat transfer and the solid heat conduction within design domain, which can be characterized by this local *Pe* number [278]:

$$Pe = \frac{S(\gamma) \times \boldsymbol{v} \times D_h}{k(\gamma)} \tag{46}$$

In the flow channels of the HX units, four high Peclet number (or velocity) gradient regions can be identified near the walls of the solid plates due to the imposition of no-Slip boundary condition. Therefore, the TO optimizer will attempt to position the solid fins within these high Peclet number gradient regions to disturb the flow path, thereby intensifying of the objective function (heat transfer rate). Moreover, since moderate conductive material (Stainless Steel) is employed in the TO, the optimizer aims to allocate the solids near the insulation and not at the interface wall.

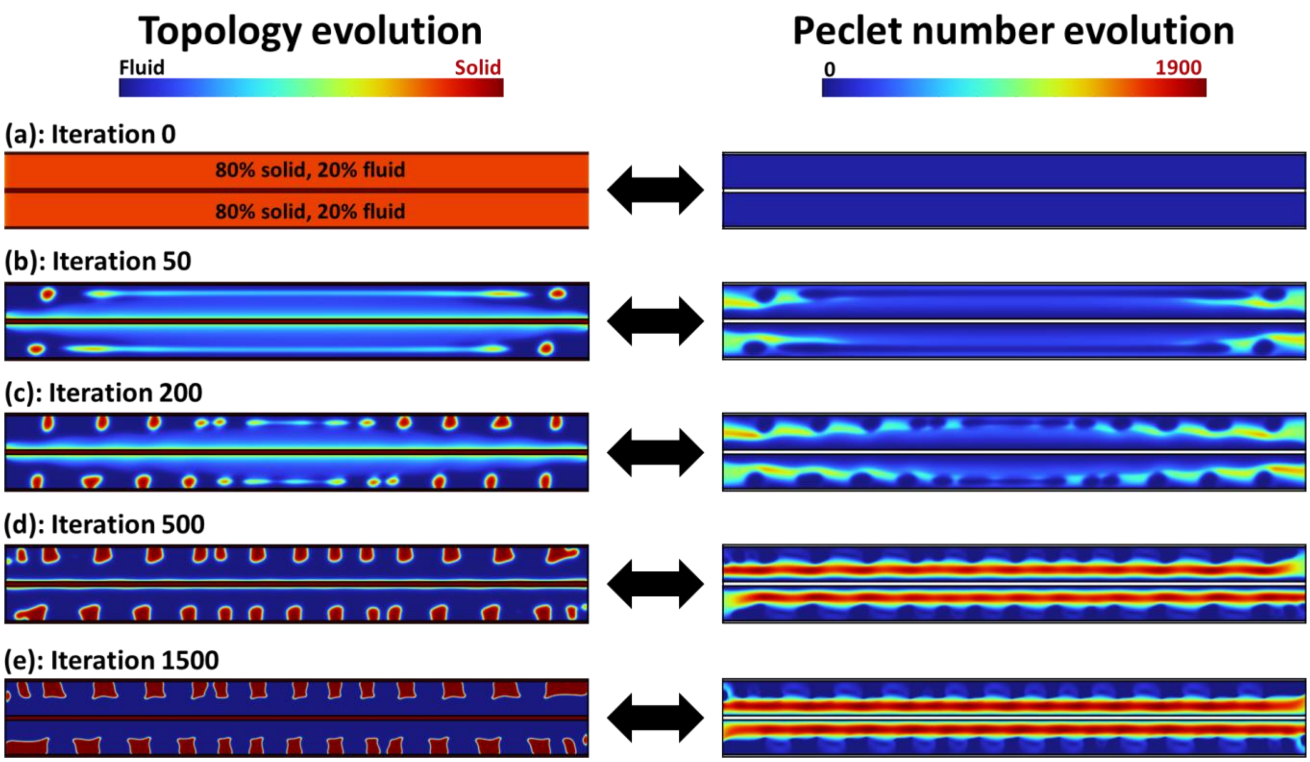

Figure 4.18: Evolution of the density and the Peclet number distributions in the TO process.

This solid allocation strives to locally increase the Peclet number near the walls of the middle plate (where heat is exchanged), consequently resulting in a simultaneous decrease in the convection and conduction resistances and then improving the HX's thermal performance.

4.4.2.13 Limitations of the density-based TO

In preceding investigations, the TO process employed a moderately conductive material (Stainless Steel) with a thermal conductivity of 15 $W.m^{-1}.K^{-1}$. However, transitioning from this moderate conductive material (Stainless Steel) (figure 4.19a) to a highly conductive material (Aluminum) (figure 4.19b) has given rise to notable challenges in the resulting topology. Specifically, the augmentation of thermal conductivity difference between solid and fluid phases has led to the emergence of numerous intermediate densities and partial obstruction of the flow channel outlets as illustrated in the figure 4.19b. The detailed physical properties of the Aluminum employed in the TO are presented in the table 4.3.

Thereafter, several trials were conducted for the purpose of trying to solve the previous encountered problems. First, a higher order of space discretization (P2) for the velocity and temperature fields is used with the intention of ensuring the numerical stability and considering the high gradient of temperature, respectively. As seen in the figure 4.19c, the previous-mentioned problems remain with a small variation in the acquired topology.

Furthermore, the element size is decreased from 0.25 mm to 0.15 mm. As depicted by figure 4.19d, the intensity of intermediate field is diminished with an important variation in the acquired topology and the remaining of the outlet partial blocking issues.

Moreover, the value of the maximum impermeability is increased to penalize the velocities of the intermediate field, however, the partial blocking problem persist with a lot of closed regions as depicted by figure 4.19e. Lastly, the relaxation applied on the convexity parameter of the impermeability interpolation function in the continuation scheme is increased. The relaxation range of the convexity parameter q is expanded by an order of magnitude. Instead of commencing with q=0.01 and ending with q=0.1, the revised relaxation scheme initiates at q=0.01 and ends at q=1. As seen in the figure 4.19f, the intensity of the intermediate densities increases a lot with a marginal unblocking in the outlets. This elucidates that the final value of the interpolation function's convexity parameters in the continuation scheme should be carefully set to avoid the appearance of the non-physical intermediate densities in the final acquired topologies.

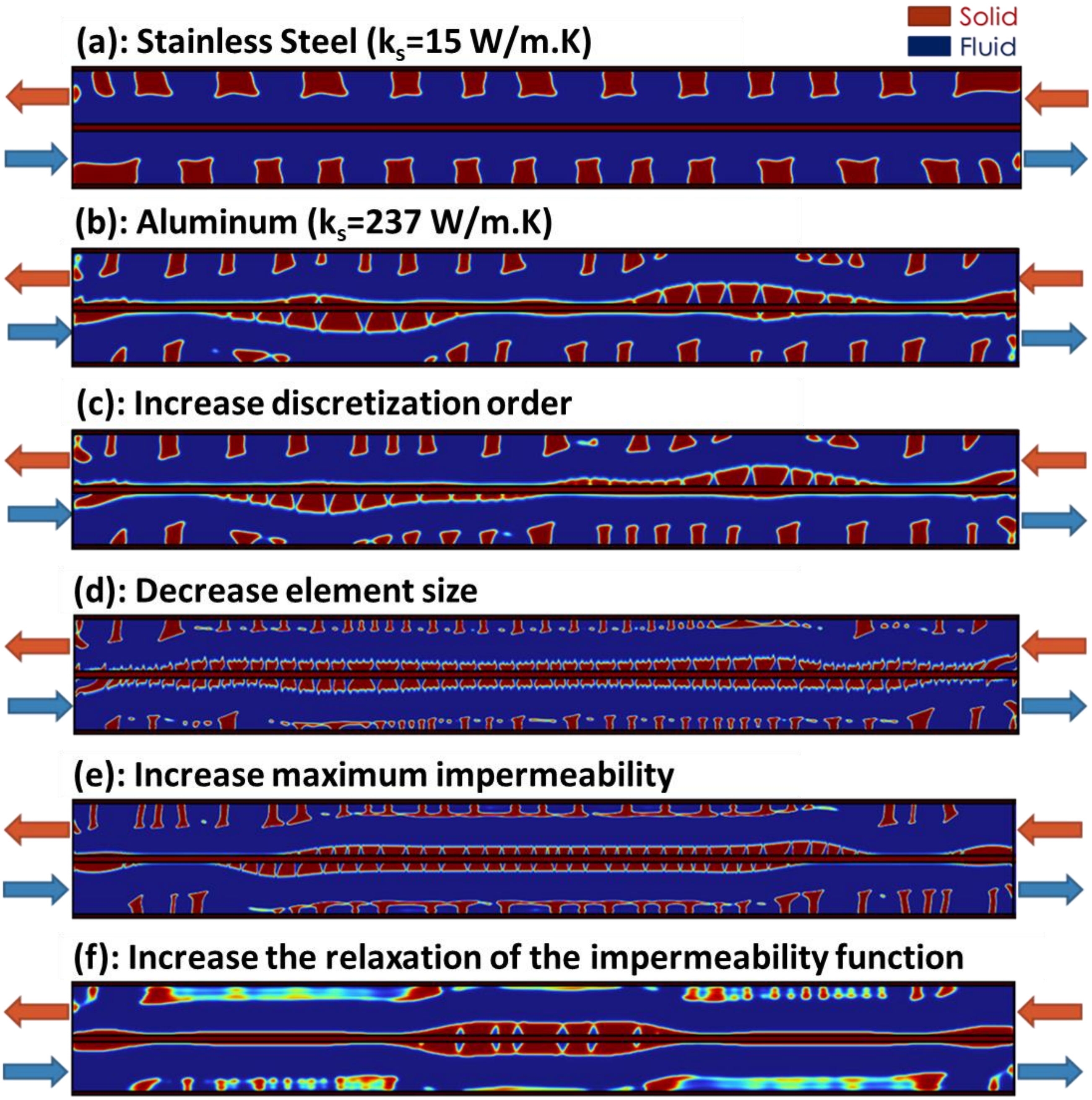

Figure 4.19: Acquired topologies using high conductive material (Aluminum) at *Re*=100.

The aforementioned problems raised from the utilization of high conductive material in the TO will be interpreted numerically and physically here. The appearance of non-physical intermediate densities can be explained by the higher thermal conductivity of the intermediate densities compared to the water used as a working fluid in the TO. Therefore, the optimizer will try to generate intermediate densities instead of water, which will increase more the objective function (heat transfer rate) and will not effectively prevent the flowing of the fluid through them, thereby ensuring the feasibility of the imposed pressure drop constraint.

Physically, the blocking of the outlets can be elucidated by the high temperature gradient between cold and hot fluids at the outlets of the flow channels. By setting a very high thermal conductivity of the solid phase, the conduction thermal resistance became negligible compared to the convective effect leading to the outlet partial blocking of HX's flow channels. To substantiate the preceding interpretation, the TO is carried out on a parallel-flow HX unit instead of the counter-flow configuration. As delineated in Figure 4.20, the partial blocking issues occur at the inlets of the HX's flow channels, where the highest temperature gradient occurs in the parallel-flow arrangement.

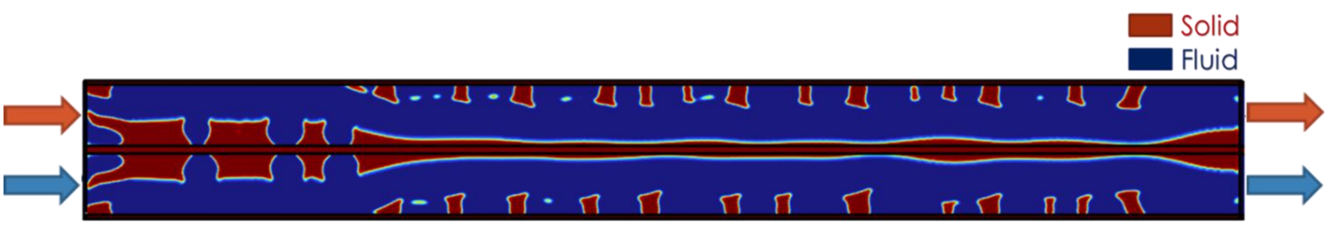

Figure 4.20: Obtained topology using parallel flow arrangement and high conductive material (Aluminum) at *Re*=100.

Furthermore, due to the significant difference between the thermal conductivity of the Stainless Steel (15 $W.m^{-1}.K^{-1}$) and Aluminum (237 $W.m^{-1}.K^{-1}$), it is valuable to execute the density-based TO using solid materials with intermediate thermal conductivity like Steel [279] and Silicon nitrates [280], [281]. This will facilitate the interpretation and observation of the transition phase from moderate to high conductive material. Figure 4.21 presents the acquired topologies using different solid materials with thermal conductivities spanning from moderate to high values. As the thermal conductivity increases, the problem's non-linearity increases, leading to lesser stable results characterized by a significant occurrence of the non-physical intermediate densities. Additionally, by increasing the thermal conductivity in TO, the optimizer attempts to generate solids at the HX's interface wall. This solid allocation can be physically explained by the reduced conduction thermal resistance associated with increased thermal conductivity. Thus, allocating high conductive solids at the HX's interface wall will not adversely affect the thermal performance of HXs.

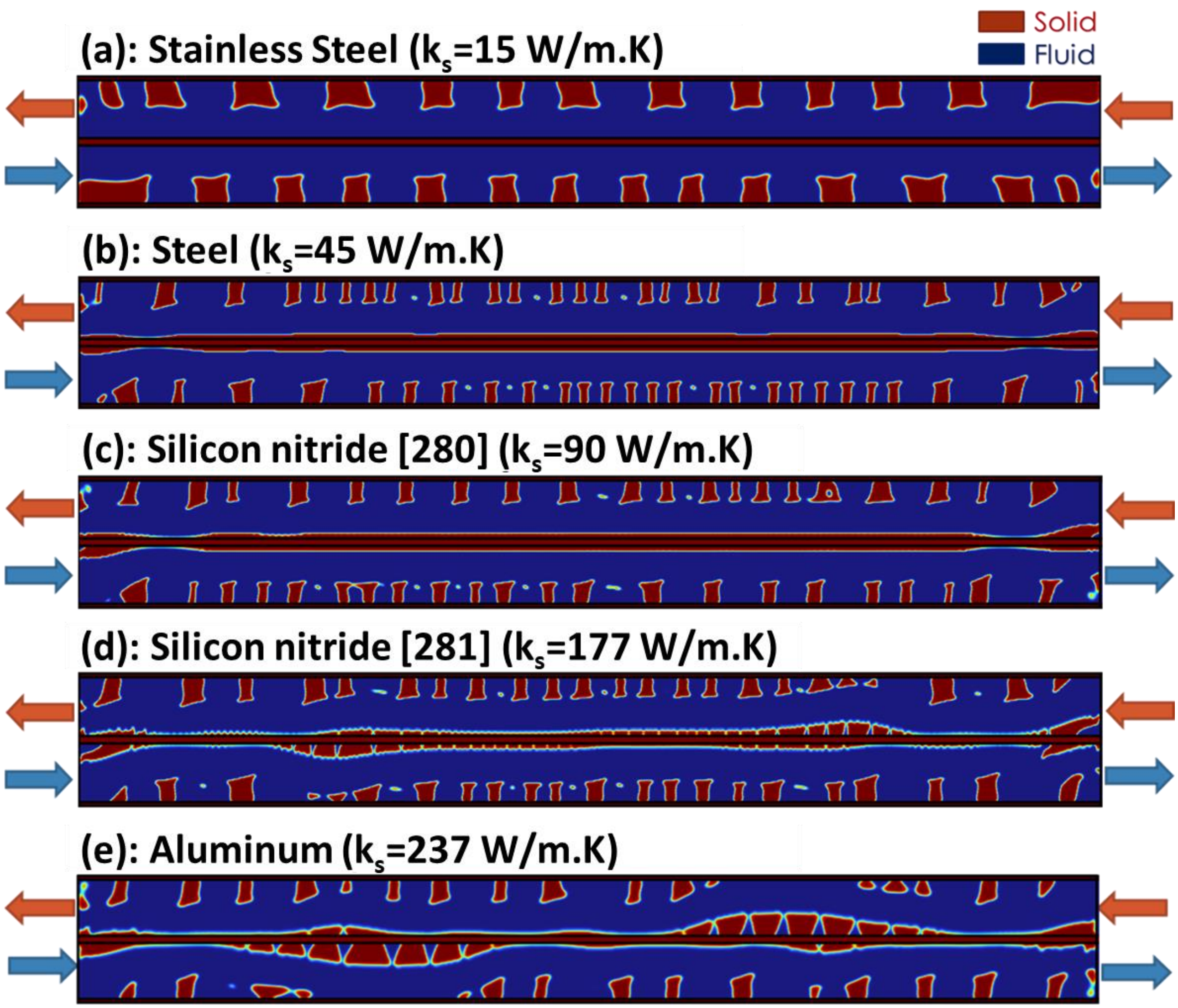

Figure 4.21: Acquired topologies using different solid materials at *Re*=100.

4.4.2.14 Short summary

In summary, the topologies obtained through TO exhibit sensitivity to variations in input parameters. Furthermore, it is noteworthy that the identical solid allocation persists on both the upper and lower plates of DP2 regardless of the prevailing conditions using moderate conductive material (Stainless Steel). Additionally, the evolution of the Pe number distribution in the TO process demonstrates that this distinct manner of fins allocation aims to increase the local velocity near the HX's interface wall (where heat is exchanged), resulting in a reduction in the convection and conduction thermal resistances and thereby improving the overall heat transfer rate. Lastly, the utilization of highly conductive materials, such as aluminum, in the TO gives rise to challenges in the final acquired topology mainly presented by the appearance of intermediate densities associated with the outlets partial blocking and closed regions issues. This elucidates the limitations of the density-based TO when employing materials with elevated thermal conductivity. Lastly, an extensive physical interpretation of the optimized topology for DP2 will be provided in the upcoming chapter 5.

4.5 Conclusions

This chapter is dedicated to the application of density-based TO on dual-flow HX units, aiming to rectify the encountered unphysical issue outlined in Chapter 3 which is attributed to the substantial velocity exhibited by the solid phase of generated topology (C-D). To solve this issue, a dual strategy is pursued by elevating the maximum impermeability value and imposing a pressure drop constraint within the TO process concurrently. Two distinct design problems are introduced: one represents the 2D periodic unit of the Plate Heat Exchanger (PHE), while the other disregards periodicity effects, presuming adiabatic conditions at the upper and lower boundaries. An investigation stage is undertaken to analyze the effect of the TO's input parameter on the acquired topology. The parameter examination stage reveals that the optimized topologies are mainly featured by the allocation of the generated solids in the flow channels central region for DP1 and by the positioning of the solids on the upper and lower plates of the HX unit for DP2. Subsequently, the limitations associated with the utilization of high-conductive materials in TO are underscored through both physical and numerical interpretations of the challenges encountered in the ultimate topological outcomes.

In the upcoming chapters 5 and 6, the optimized topology for DP2 will be numerically, physically and experimentally tested, interpreted and validated.

Chapter 5: Performance evaluation of the topology-optimized thermo-fluidic structure with insulated side walls: A 3D computational fluid dynamic analysis

Chapter Summary

In this chapter, a 3D numerical analysis is conducted using the FVM (finite volume method)-based solver FLUENT of ANSYS on the TO (topology optimization)-optimized structure for the design problem 2 (DP2) introduced in the preceding chapter 4. The reason of choosing the optimal topology for DP2 (insulated HX's top and bottom walls) and not for DP1 (thermal periodic boundary condition on the HX's top and bottom walls) is the difficulties associated of representing a variable local heat flux on the upper and low plates of the HX unit using experimental equipment. This selection facilitates the experimental validation of the optimal topology for DP2, which will be discussed in the forthcoming chapter 6. For the purpose of performing a comparative analysis, two additional HX units having rectangular fins with identical and opposite solid allocation of the TO-optimized design are introduced and named simplified and Benchmark HX units, respectively. The numerical results demonstrate that the allocation of solids in proximity to the insulation as in the optimized and simplified HX units results in an enhanced thermo-hydraulic performance compared to the solid positioning at the HX's interface wall as in the benchmark case, precisely when low/moderate conductive solid materials (i.e., Stainless Steel) are employed in the HX. Furthermore, a physical interpretation is conducted to interpret the thermal intensification exhibited in the TO-optimized and simplified HX units compared to the benchmark case. The physical interpretation stage reveals that the positioning of moderate conductive solids (Stainless Steel) near the HX's insulation reduces simultaneously the convective and conductive thermal resistances leading to an augmentation in the overall performance.

Keywords of the Chapter:

Computational fluid dynamics, Conjugate heat transfer, thermo-hydraulic performance, Physical interpretation, Finite volume method, heat exchanger.

5.1 Introduction

In the previous chapter 4, the density-based topology optimization (TO) is conducted on different counter-flow heat exchanger (HX) units for the purpose of maximizing their thermo-hydraulic performances. A full investigation stage was conducted to test the effect of the TO's various input parameters on the acquired topology. The investigation stage reveals that the TO-derived topologies are mainly featured by the allocation of the moderate conductive solids (Stainless Steel) near the insulated walls, which have not been reported in literature of the HXs, to our best knowledge. Despite all acquired topologies, additional work is still needed to assess the efficacy of the optimized HX, since the density-based TO is not able to evaluate accurately the thermo-hydraulic performance due to several reasons mentioned in the introduction of chapter 3. Thus, the main objective of this chapter is the validation of the TO design methodology by conducting high fidelity CFD simulations using the Ansys Fluent code to precisely evaluate the thermo-hydraulic performance of the optimized HX design.

For the purpose of conducting a comparative analysis, two additional HX units having rectangular fins are introduced. One HX unit is designed inspiring from the TO-derived design by positioning the fins in adjacency with the insulated walls and is designated as the simplified HX unit. The reason of attributing the nomenclature simplified for the previous mentioned design, stems from the several simplifications made in the transition from the optimized to the simplified case. These simplifications were necessitated due to the inability of considering all complicated features of the TO-optimized design. The other introduced design is named benchmark HX and is featured by the allocation of fins at the HX's interface wall contrary to the TO-optimized and simplified designs. Several criteria have been adopted to compare the thermal and hydraulic performances of the three HX units (optimized, simplified and benchmark). Lastly, a physical interpretation is delivered to analyze carefully the physical mechanisms behind the TO-derived HX.

This chapter is decomposed as follows: Section 5.2 presents the transformation procedure from 2D to 3D designs and the details of the investigated 3D HX units. Section 5.3 introduces the followed numerical methodology of the CFD analysis. Section 5.4 provides a detailed comparison of the thermal and hydraulic performances for the three HX units (optimized, simplified and benchmark). Lastly, section 5.5 summarizes the main conclusions.

5.2 3D HX design

The TO-optimized HX unit illustrated in Figure 4.7b of chapter 4 is selected for the present CFD investigation stage and is named TO-optimized HX. Subsequently, a threshold with a 0.5 value (50% solid, 50 % fluid) should be applied on the TO-acquired structure in order to remove the remaining intermediate densities at the solid/fluid interface created by the TO's filtering process as depicted by Figure 5.1 [259]. The length of the optimized HX is increased few millimeters (9 mm) to avoid the existence of solids at the inlets/outlets boundaries.

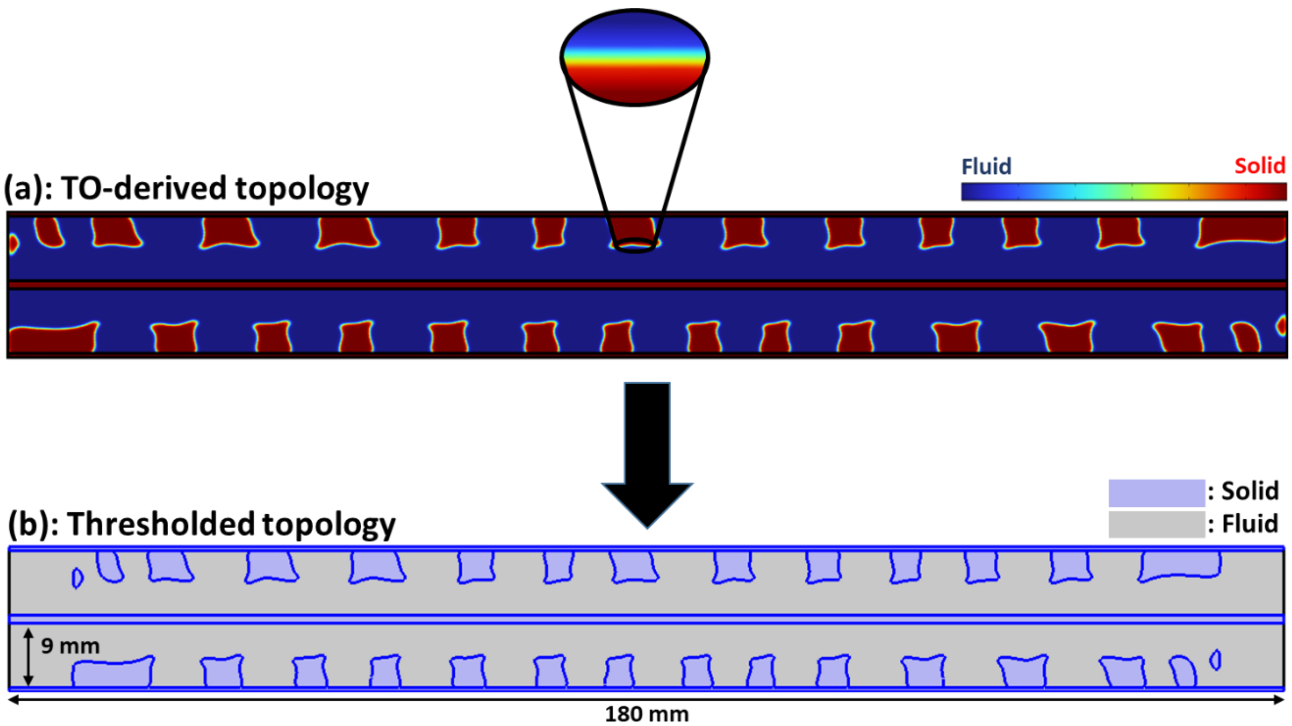

Figure 5.1: (a): TO-derived structure, **(b):** Thresholded topology.

Thereafter, the 2D HX unit is extended to 3D as seen in figure 5.2 for the purpose of being fabricated and experimentally validated in the forthcoming chapter 6. This 3D transformation uniformly extends the 2D HX design in the third direction assuming that the fluid flow effect in the third direction is negligible.

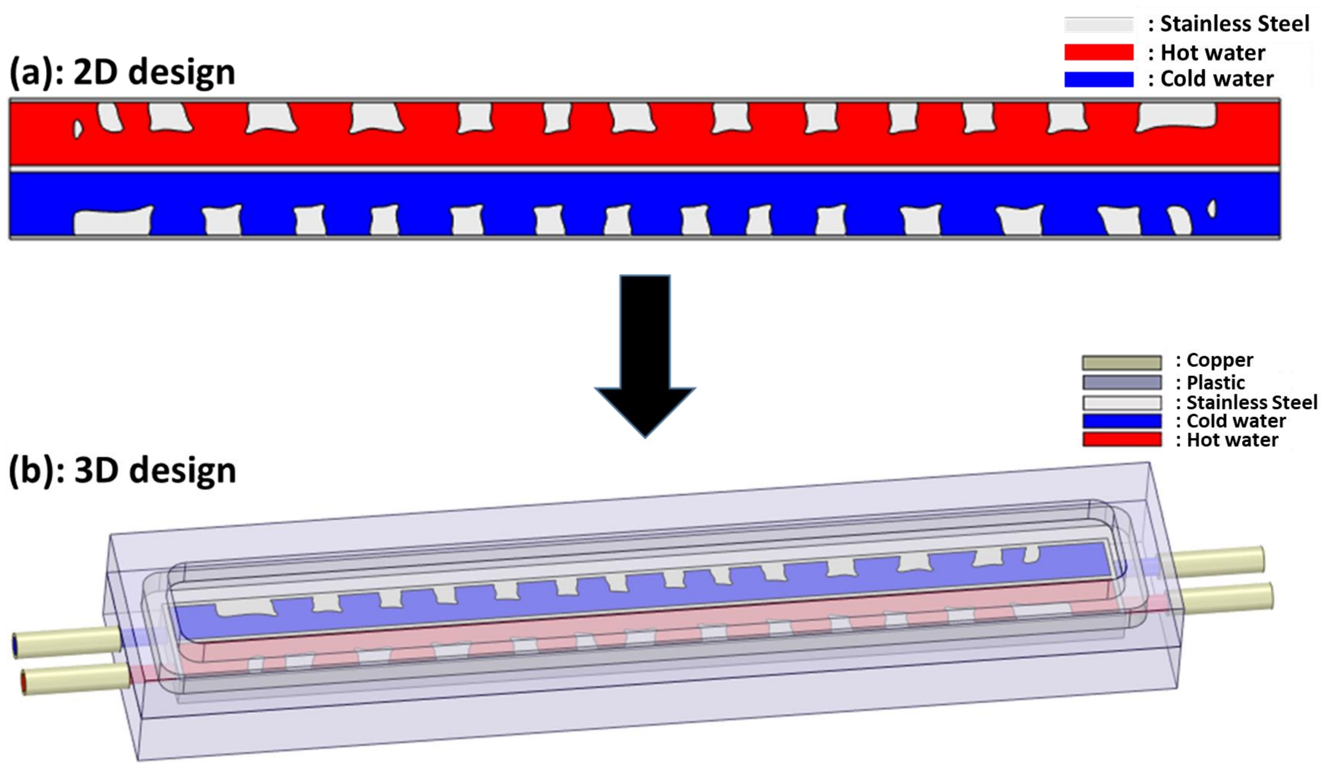

Figure 5.2: 3D transformation.

The 3D HX design has a sandwich concept and is decomposed of a plastic cage that covers the HX unit from the bottom and side boundaries to minimize the heat losses to the surrounding. Moreover, the HX unit is covered from the top by a plastic plate with a sapphire window in the middle for IR measurement. The 3D design is illustrated in the figure 5.3 with the corresponding dimensions and materials.

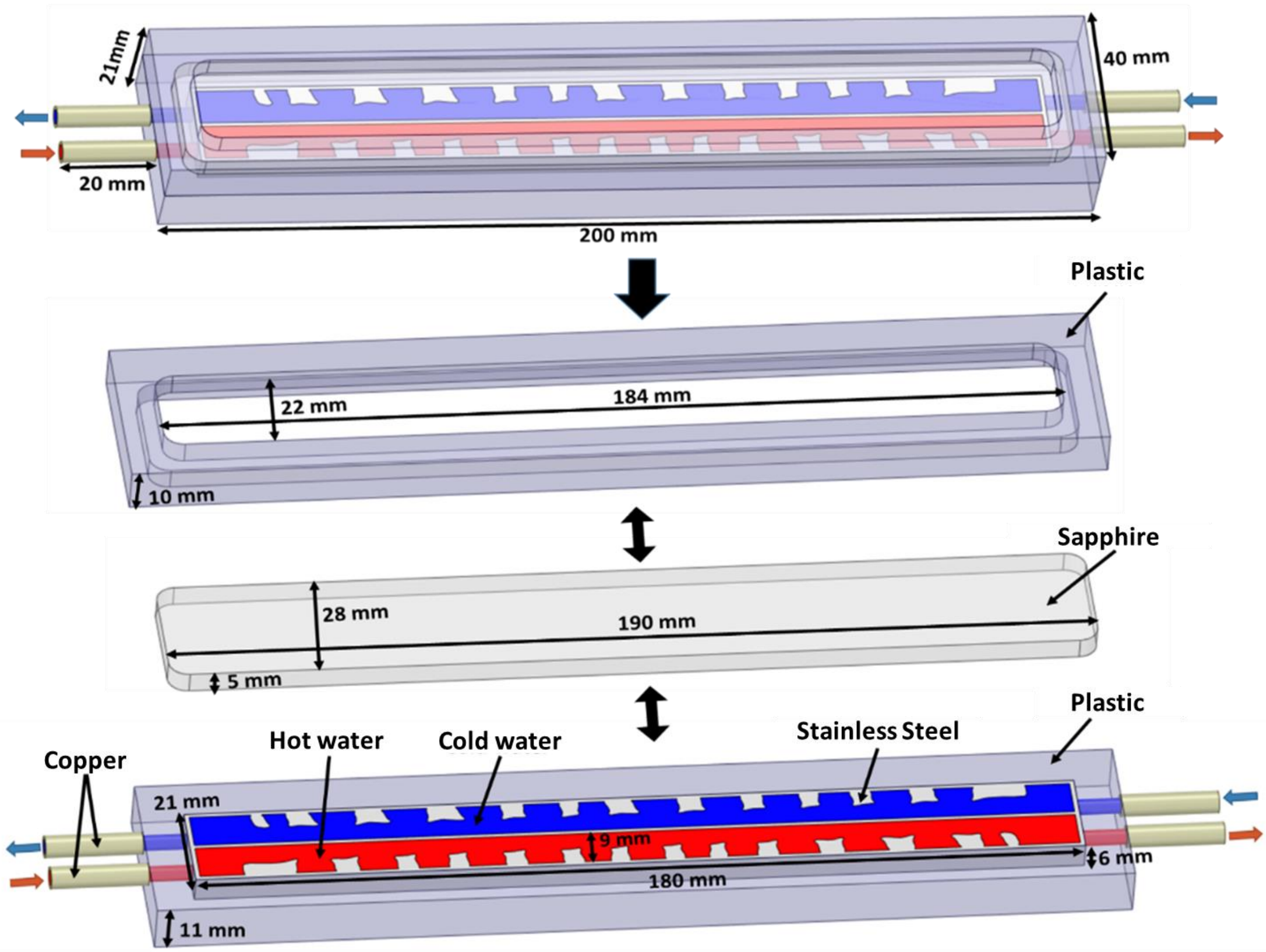

Figure 5.3: 3D design with the corresponding dimensions and materials.

With the intention of performing a performance comparison with the previously presented TO HX unit, two other HX units that have conventional rectangular fins are introduced as depicted by Fig. 5.4: one possesses identical fins allocation at the adiabatic boundary and is named Simplified HX unit, and the other has opposite usual fins allocation at the separating wall of hot and cold fluids and is designated as Benchmark HX unit. To make a fair comparison, all HX units (TO-optimized, simplified and benchmark) have the same solid fraction, external dimensions and materials.

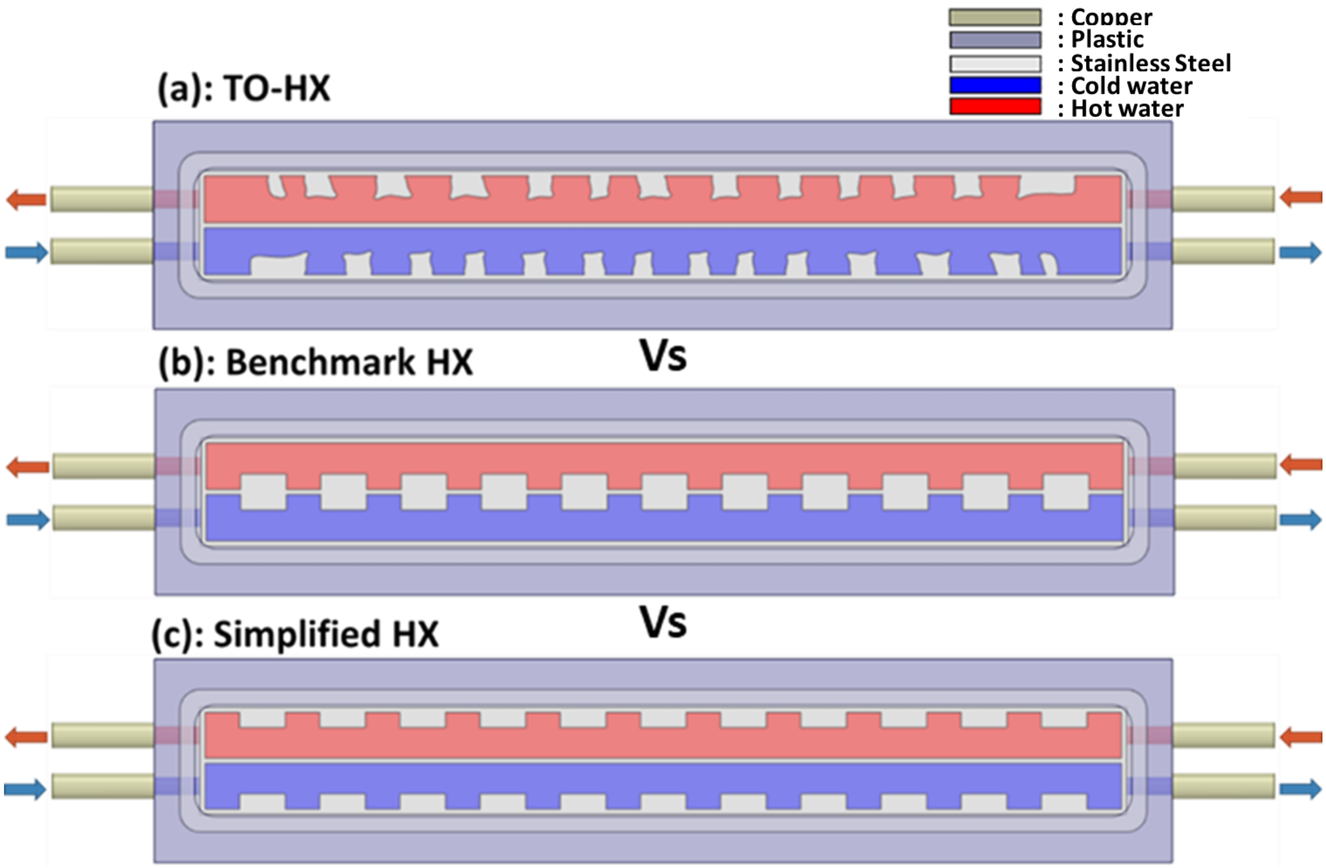

Figure 5.4: Top view of the **(a):** TO-optimized, **(b):** Benchmark and **(c):** Simplified HX units.

5.3 Methodology

In this subsection, the detailed methodology of the CFD (Computation fluid dynamics) analysis is presented.

First, the geometries of the three HX units (TO-optimized, simplified and benchmark) and the meshes were built using different modules of ANSYS Workbench 19.2. In the present study, the working fluid is set to the water while the solid part of the HX is the Stainless Steel for maintaining the consistency between the TO and CFD analysis. Furthermore, the bottom cage material is the polycarbonate and the top plates materials are the sapphire and polycarbonate, respectively. The flow connections situated at the inlets and outlets of the HX unit are comprised of copper material. The thermo-physical properties of the water are considered as temperature dependent, employing the fitting polynomials presented in Table 5.1. By contrast, the thermo-physical properties of the solids (Stainless Steel, polycarbonate, polycarbonate and copper) utilized in the 3D HX design are assumed independent of the temperature as delineated in Table 5.1. At the inlets of the HX's channels, uniform velocity profile was imposed with inlet temperatures of 288.15 K and 333.15 K for the cold and hot fluids, respectively. The numerical simulations were conducted at ten different flow rates spanning between 0.035 $L.min^{-1}$ and 0.215 $L.min^{-1}$, which corresponds to ($\overline{Re_{cold}}$) and hot ($\overline{Re_{hot}}$) channels, $98 \leq \overline{Re_{cold}} \leq 555$ and $180 \leq \overline{Re_{hot}} \leq 1106$, respectively. Moreover, zero static pressure was imposed on the outlets of the HX and no-slip condition was applied on the walls of the flow channels. The bottom and side surfaces of the plastic cage and the side boundaries of the top plastic plate were considered as adiabatic. All other external walls were subjected to a heat transfer coefficient of 7 $W.m^{-2}.K^{-1}$ with an ambient temperature to consider the effect of the natural convection with the surrounding.

The numerical simulations were executed using the FVM (Finite volume method)-solver FLUENT 19.2. The laminar model was used for low Reynolds number ($\overline{Re_{hot}} \leq 400$), while the turbulent *k*-*w* SST model was employed for higher $\overline{Re_{hot}}$ (400-1106). The aim of utilizing the turbulent model in the numerical simulations within the theoretical laminar region is mainly to maintain the numerical stability when having local flow vortex, local flow separation and micro-turbulences in the HX's flow channels. As for the velocity-pressure coupling, the standard SIMPLE (semi-implicit method for pressure linked equations) was used. The standard method was utilized for the space discretization of the pressure field, while the first order upwind scheme was used for velocity and temperature field discretization. For the turbulent equations *k* (kinetic energy) and *w* (specific rate of dissipation) discretization, the second order upwind scheme was chosen to decrease the fluctuation of the turbulent equation's residuals leading to an enhanced convergence rate. The solution is judged to be converged when the residuals of all governing equations are less than 1e-5 and the iterative variation of the inlet static pressure and the outlet temperature of the cold fluid is below 0.5 %. A mesh dependency study was conducted following the same methodology of chapter 4 to ensure the reliability of the numerical results. The results are considered to be mesh independent when the number of elements hit 13.38 million, 13.07 million and 12.97 million for the optimized, benchmark and simplified HX units, respectively. Lastly, it is essential to mention that the value of y+ (a dimensionless distance representing the viscous sub-layer) used in the present CFD analysis is about 1 to ensure the accuracy of the acquired results.

Table 5.1: Physical properties of the fluid and solids used for the numerical simulations (283.15 K <T< 343.15 K) [282]–[285]

Water	*Density [kg.m^{-3}]*	$\rho = -3.3\times10^{-7}T^4 + 4.3\times10^{-4}T^3 - 0.217T^2 + 47.95T + 2962.83$
	Specific heat [J kg^{-1} K^{-1}]	$C_P = 4.81\times10^{-6}T^4 - 6.1\times10^{-3}T^3 + 2.98T^2 - 643.2T + 56148.51$
	Viscosity [Pa.s]	$\mu = 2.96\times10^{-11}T^4 - 4\times10^{-8}T^3 + 2\times10^{-5}T^2 - 4.6\times10^{-3}T + 0.4$
	Thermal conductivity [W m^{-1} K^{-1}]	$k = -6.4\times10^{-11}T^4 + 1.34\times10^{-7}T^3 - 9.91\times10^{-5}T^2 + 3.2\times10^{-2}T - 3$
Copper	*Density [kg.m^{-3}]*	$\rho = 8850$
	Specific heat [J kg^{-1} K^{-1}]	$C_P = 392$
	Thermal conductivity [W m^{-1} K^{-1}]	$k = 398$
Polycarbonate	*Density [kg.m^{-3}]*	$\rho = 1200$
	Specific heat [J kg^{-1} K^{-1}]	$C_P = 1100$
	Thermal conductivity [W m^{-1} K^{-1}]	$k = 0.2$
Sapphire	*Density [kg.m^{-3}]*	$\rho = 3980$
	Specific heat [J kg^{-1} K^{-1}]	$C_P = 763$
	Thermal conductivity [W m^{-1} K^{-1}]	$k = 37$
Stainless Steel	*Density [kg.m^{-3}]*	$\rho = 7800$
	Specific heat [J kg^{-1} K^{-1}]	$C_P = 468$
	Thermal conductivity [W m^{-1} K^{-1}]	$k = 15$

5.4 Results and Discussion

5.4.1 Parameters definition for performance evaluation

First, the Reynolds number of the cold and hot fluids is calculated based on the average properties and velocities inside the HX flow channels using the following equation:

$$\overline{Re} = \frac{\overline{\rho_f}.\bar{v}.Dh}{\bar{\mu}} \tag{47}$$

where $\overline{\rho_f}$ is the fluid average density (kg.m^{-3}), $\bar{\mu}$ is the fluid average dynamic viscosity (Pa.s), $\bar{v}$ is the volume-weighted average velocity inside the cold or hot flow channels (m.s^{-1}) and Dh is the hydraulic diameter calculated according the cross-sectional dimensions of the HX's flow channel which is equal to 0.0072 m.

For the intention of evaluating the thermal performance of the HXs, the heat transfer rate is selected as a criterion and is evaluated using the following equation:

$$Q = \dot{m}\overline{C_p}(T_{out} - T_{in}) \tag{48}$$

where Q is the heat transfer rate (W), $\dot{m}$ is the mass flow-rate of the cold fluid (kg.s^{-1}), T_{out} and T_{in} are the mass-flow average temperatures at the outlet and inlet of the cold fluid (K), respectively, and $\overline{C_p}$ is the average specific heat of the cold channel (J.kg^{-1}.K^{-1}). As demonstrated by Fig 5.5, the heat transfer rate exhibits an intensification in the optimized and simplified HX units compared to the benchmark case with an augmentation rate up to 16.4% and 10.23%, respectively. The higher intensification rate in the optimized design compared to the simplified one can be explained by the neglection of the several topological features in the designing of the simplified HX unit. Additionally, the physical reasons and the interpretations behind the heat transfer intensification are kept to the upcoming physical interpretation subsection.

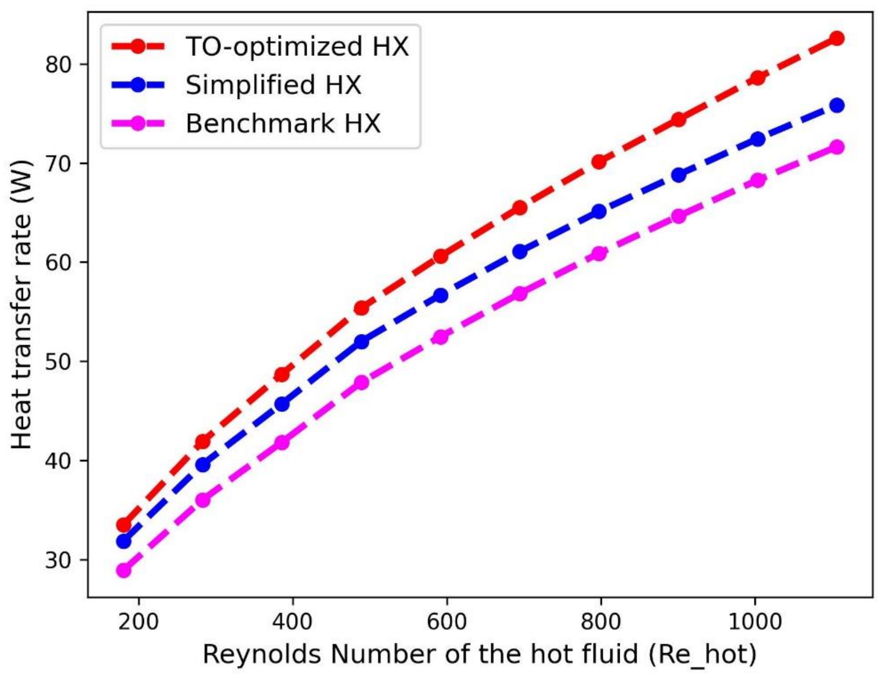

Figure 5.5: Heat transfer rate variation with respect to the Reynolds number for the optimized, simplified and benchmark HX units.

Furthermore, the friction coefficient (*f*) of the hot fluid is evaluated for the three HX units with the intention of comparing their hydraulic performance. As illustrated by Fig 5.6, the hydraulic losses in the optimized HX are slightly higher compared to the benchmark case while the friction coefficient of the simplified HX unit almost coincides with the one of the benchmark design.

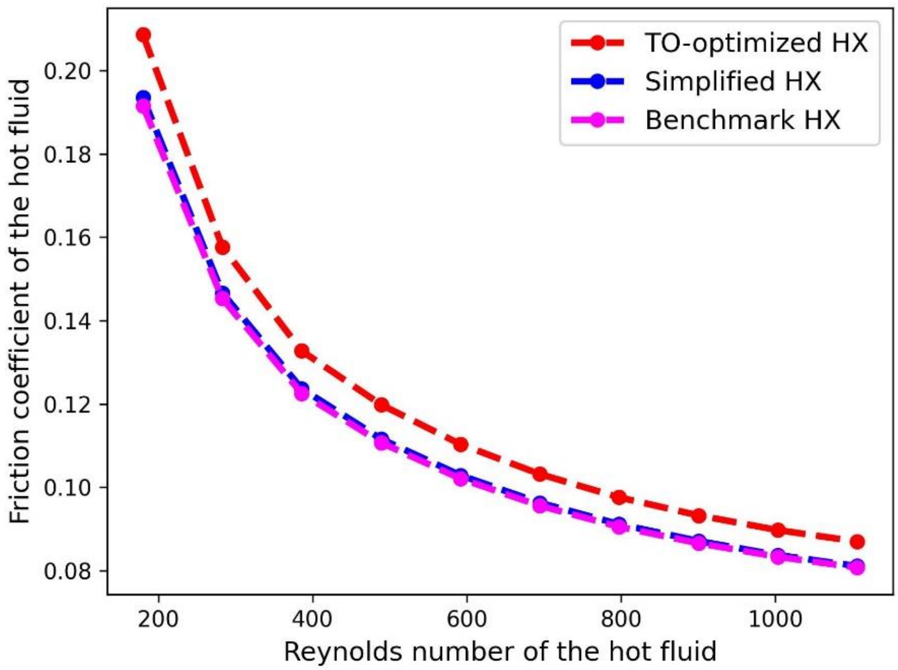

Figure 5.6: Variation of the friction coefficient with respect of the Reynolds number for all HX units.

To consider the thermo-hydraulic performance simultaneously, the performance evaluation criteria (PEC) number is first evaluated for all HX units. As seen in the equation below, the PEC is modified by adding the ratio of heat transfer areas as originally defined by Webb and Eckert [264] in order to consider the difference in the heat transfer areas of the optimized, simplified and benchmark HX units.

$$PEC = \frac{Nu/Nu_0}{(f/f_0)^{1/3}} \times \left(\frac{A}{A_0}\right)^{2/3} \tag{49}$$

where Nu is the Nusselt number, f is the friction coefficient and A is the heat transfer area (m^2). The parameters with a subscript 0 are the parameters of the reference case which is considered the benchmark HX unit. It should be noted that the Nu and f are calculated using the equations presented in section 3.5 of chap.3. The heat transfer areas are equal to 0.00109 m^2, 0.00109 m^2 and 0.00148 m^2 for the optimized, simplified and benchmark HX units, respectively. The heat transfer area for each HX unit is calculated based on the multiplication of the solid/fluid interface length (at the middle plate) with the depth of the flow channel (6mm). As seen in Fig. 5.7, the optimized HX units possess higher thermo-hydraulic performance compared to the benchmark case under a wide range of the Reynolds number with an improvement in the PEC number up to 21%. As for the simplified HX unit, better thermo-hydraulic is observed under $\overline{Re_{hot}}$ of 700 with an enhancement in the PEC number up to 15 %. By contrast, the benchmark HX unit possess higher PEC up to 4.5% compared to the simplified design for $\overline{Re_{hot}}$ higher than 700. The performance advantage of the benchmark HX unit over the simplified one contradicts with the previous plots (Fig 5.5 and Fig 5.6) that show higher thermal performance (heat transfer rate) of the simplified HX unit compared to the benchmark design and almost similar hydraulic performance under a wide flow operation. This contradiction can be attributed to the limitations considered in the derivation of the PEC number [264], particularly the obligation to have identical heat transfer area and pumping power for the optimized and reference cases. Additionally, the variation of the PEC with respect of the Reynolds number is a descending variation and the maximum thermo-hydraulic improvement is acquired at the lowest $\overline{Re_{hot}}$. This may be explained by the optimization of the HX unit through the TO under low Reynolds number (Re=100) as identified in the previous chapter 4. Another reason may be attributed to the inconsistent variation of the thermal and hydraulic performances with respect to the flowrate.

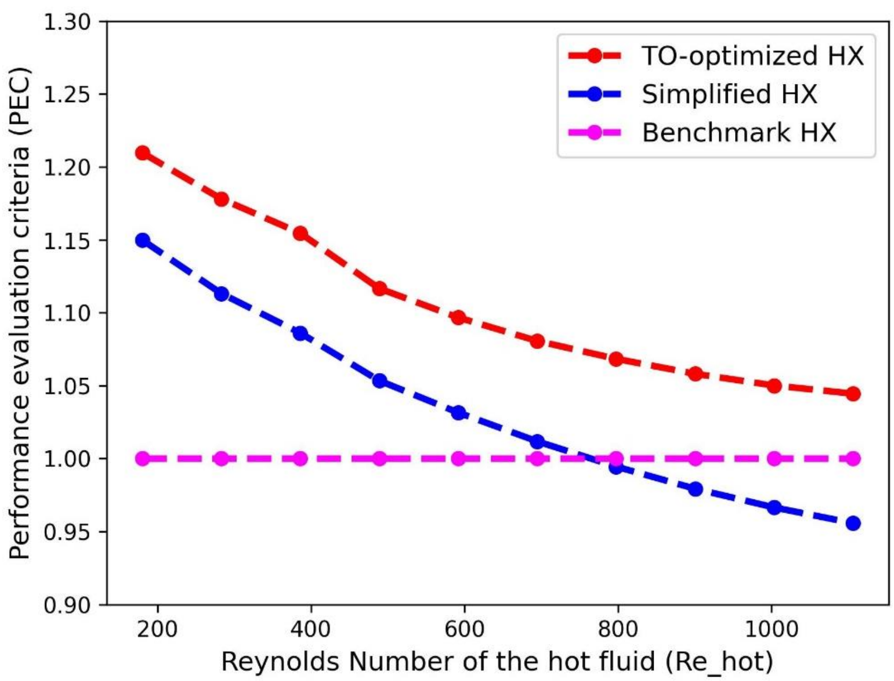

Figure 5.7: Variation of the PEC with regards to the Reynolds number for all HX units.

For further comparison of the simultaneous thermo-hydraulic performance of the three HX units and to avoid the constraints/limitations of the PEC number, the heat transfer rate Q is evaluated and compared under the same pumping power. As evidenced by the figure 5.8, the heat transfer rate of the TO-optimized and simplified HX units is intensified under the same pumping power compared to the benchmark case with an intensification rate in the laminar region up to 13.7% and 5.8 %, respectively.

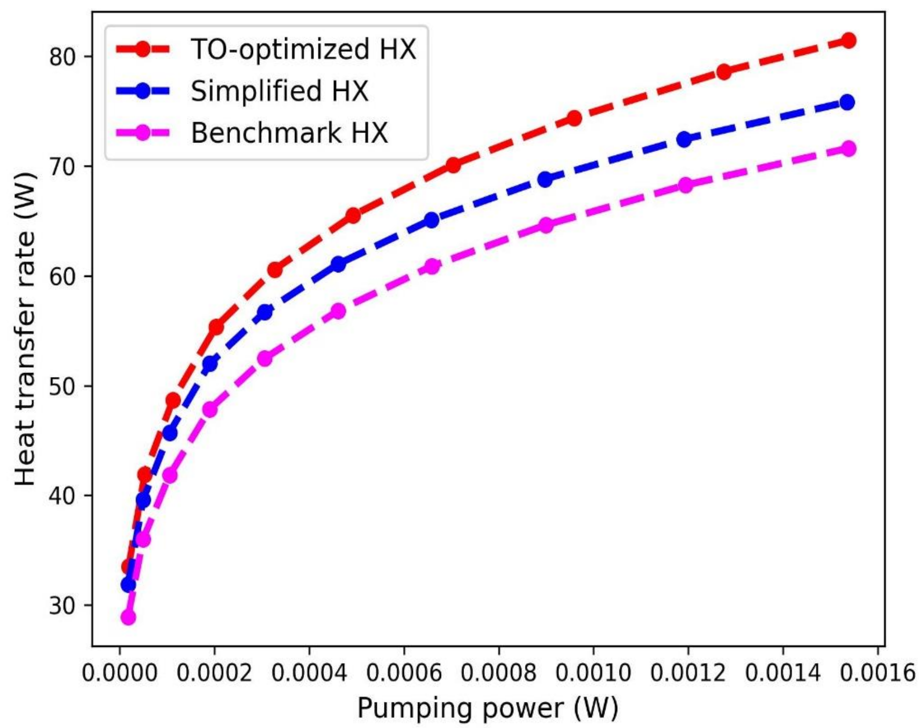

Figure 5.8: Variation of the heat transfer rate with respect to the pumping power for all HX units.

All of the aforementioned comparison criteria witness that the TO-optimized and simplified design possess better and higher thermo-hydraulic performance compared to the benchmark case. This will emphasize that the allocation of the solids (fins) in proximity to the insulation (as in the optimized and simplified designs) leads to superior thermo-hydraulic performance compared to the solid allocation at the HX's interface wall (as in the benchmark design), particularly when low or moderate conductive material is utilized as in the present case.

5.4.2 Physical interpretation

In this subsection, the thermal intensification exhibited in the TO-optimized and simplified HX units is physically interpreted. First, the velocity contours evaluated through the CFD analysis are plotted on the three HX units (optimized, simplified and benchmark) at $\overline{\mathrm{Re}_{\mathrm{hot}}}$= 695 as seen in Figure 5.9.

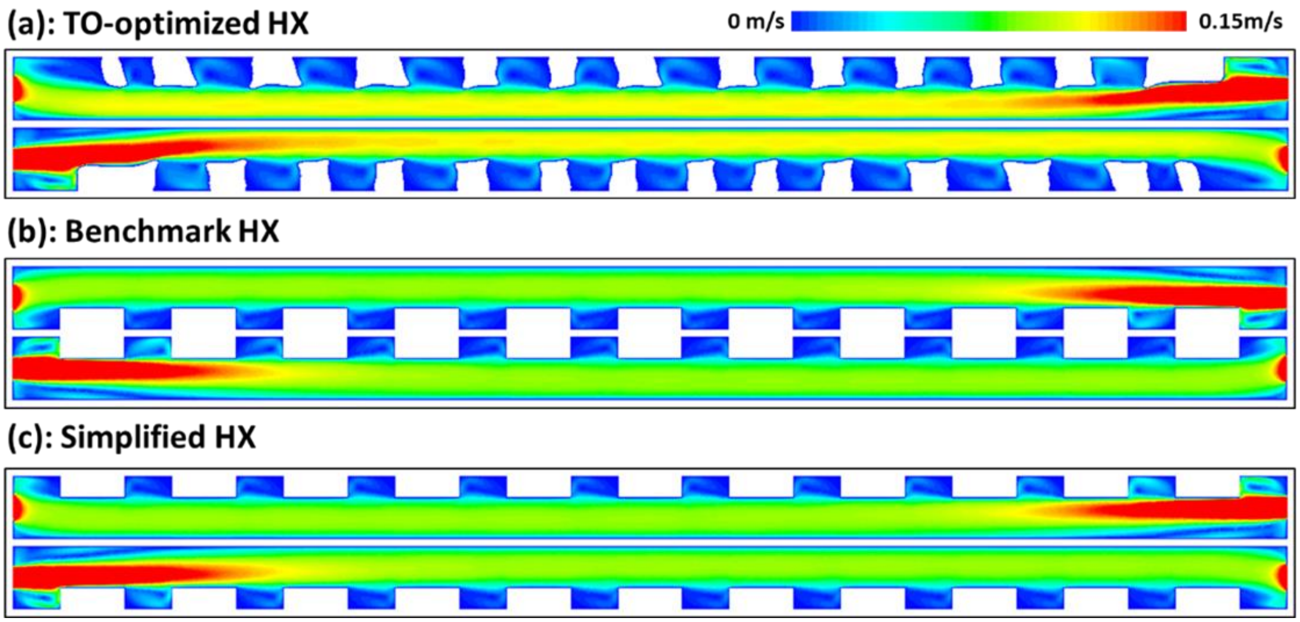

Figure 5.9: Velocity contours of the **(a):** TO-optimized, **(b):** Simplified and **(c):** Benchmark HX units at $\overline{Re_{hot}}$= 695.

Apparently, the optimized and simplified designs attempt to increase the velocity locally near the interface where heat is exchanged between two fluids, leading to a decrease in the convective thermal resistance and thus an augmentation in the overall thermal performance. By contrast, the benchmark design seeks to disturb the fluid near the interface wall but actually results in numerous dead zones between the solids, leading to an increase in the convective thermal resistance and thus a decrease in the overall thermal performance. Furthermore, allocating the solids at the interface wall as in the benchmark design will directly increase the conduction thermal resistance and thus will decrease the thermal performance notably when using low or moderate conductive material as in the present case (Stainless Steel). In order to confirm the previous mentioned interpretations, the overall thermal resistance (R_{th}) is calculated for the three HX units using the following equation:

$$R_{th} = \frac{\Delta T_m}{Q} \tag{50}$$

where ΔT_m is the logarithmic mean temperature difference (K) calculated as follows:

$$\Delta T_m = \frac{\left(T_{in,hot} - T_{out,cold}\right) - \left(T_{out,hot} - T_{in,cold}\right)}{ln\frac{\left(T_{in,hot} - T_{out,cold}\right)}{\left(T_{out,hot} - T_{in,cold}\right)}} \tag{51}$$

where $T_{in,hot}$ and $T_{out,hot}$ are the mass-flow averaged temperature at the inlet and outlet of the hot fluid (K), respectively and $T_{in,cold}$ and $T_{out,cold}$ are the are the mass-flow averaged temperature at the inlet and outlet of the cold fluid (K), respectively. As illustrated by Fig. 5.10, the benchmark case has up to 18.64% and 12.65% higher overall thermal resistance compared to the optimized and simplified HX units in the laminar region, respectively. This confirms the aforementioned physical interpretations and elucidates that the optimal allocation of the low/moderate conductive solids for maximized thermo-hydraulic performance is the distant positioning of the interface wall.

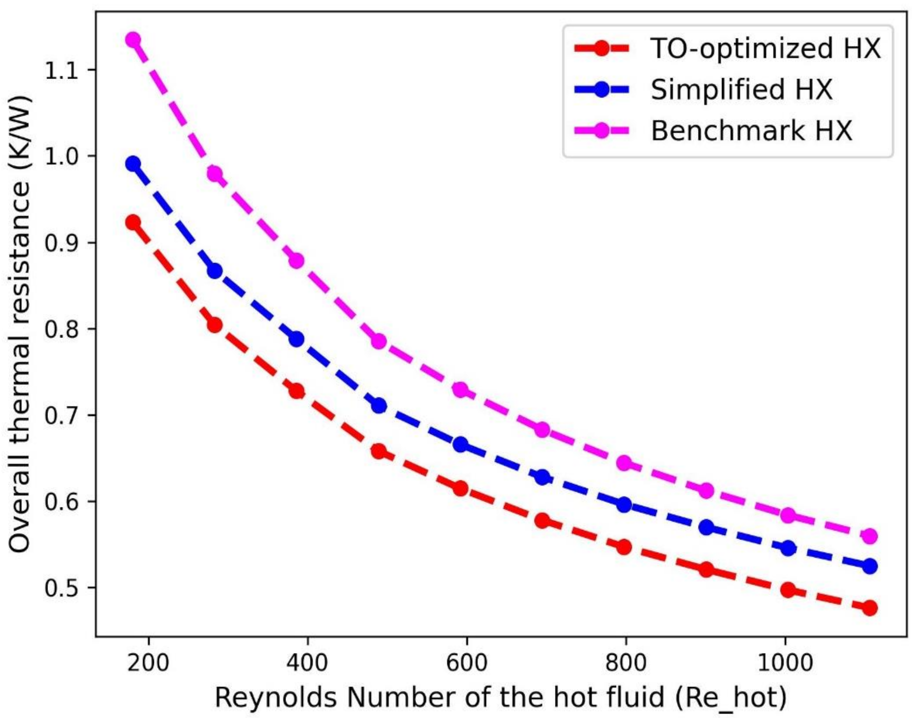

Figure 5.10: Variation of the overall thermal resistance with respect to the Reynolds number for all HX units.

Besides, the Biot number that delineates the importance of the fluid's convective heat transfer over the conduction heat transfer inside the solid is assessed for the three HX units as follows:

$$Bi = \frac{h_{hot} D_h}{k_s} \tag{52}$$

where k_s is the thermal conductivity of the Stainless Steel (W.m^{-1}.K^{-1}) and h_{hot} is the convective heat transfer coefficient of the hot fluid (W.m^{-2}.K^{-1}) computed using Eq. 53.

$$h_{hot} = \frac{Q_{hot}}{A_{hot}(\overline{T_{hot}} - T_{i,hot})} \tag{53}$$

where Q_{hot} is the heat transfer rate calculated on the hot flow side (W), A_{hot} is the heat transfer area on the hot flow side (m^2), $\overline{T_{hot}}$ is the mass-flow averaged temperature in the hot flow channel (K) and $T_{i,hot}$ is the area-weighted average temperature at the interface wall (interface wall between the hot fluid and the HX's middle plate) of the hot channel (K). As outlined by the figure 5.11, the Biot number is higher for the optimized and simplified HX units compared to the benchmark case with an augmentation rate up to 52.75% and 41.66%, respectively. This underscores the ability of the optimized and simplified designs in intensifying the convective heat transfer of the HXs, which are frequently dominated by the convective heat transfer as demonstrated by the Biot number.

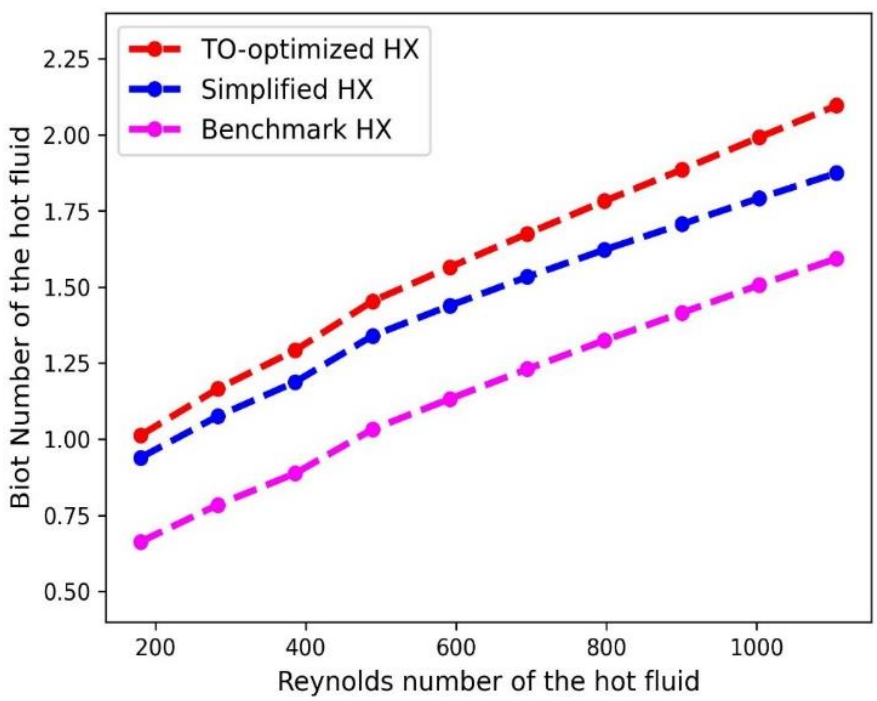

Figure 5.11: Variation of the Biot number with respect to the Reynolds number for all HX units.

5.4.3 Local temperature field comparison (Further analysis)

The local temperature distribution over the outer surface of the sapphire plate is compared for the three HX units for further analysis and comparison as illustrated by Fig. 5.12. It should be noted that the comparison and validation of the local fluid temperatures between the three HXs will be differed to the upcoming chapter 6. According to the figure below, the maximum temperature of the sapphire plate's outer surface for the optimized HX unit is higher by 1.2°C and 1.7°C compared to one of the simplified and benchmark designs, respectively, and the minimum temperature of the outer sapphire plate for the TO-optimized is lower by 1.12°C and 1.46°C compared to one of the simplified and benchmark designs, respectively, under the same Reynolds number ($\overline{Re_{cold}}$ = 354, $\overline{Re_{hot}}$ = 695) and boundary conditions. This indicates that the highest temperature gradient (highest exchanged heat) occurs in the TO-optimized HX unit, reflecting the thermal performance superiority of the optimized design over the simplified and benchmark cases.

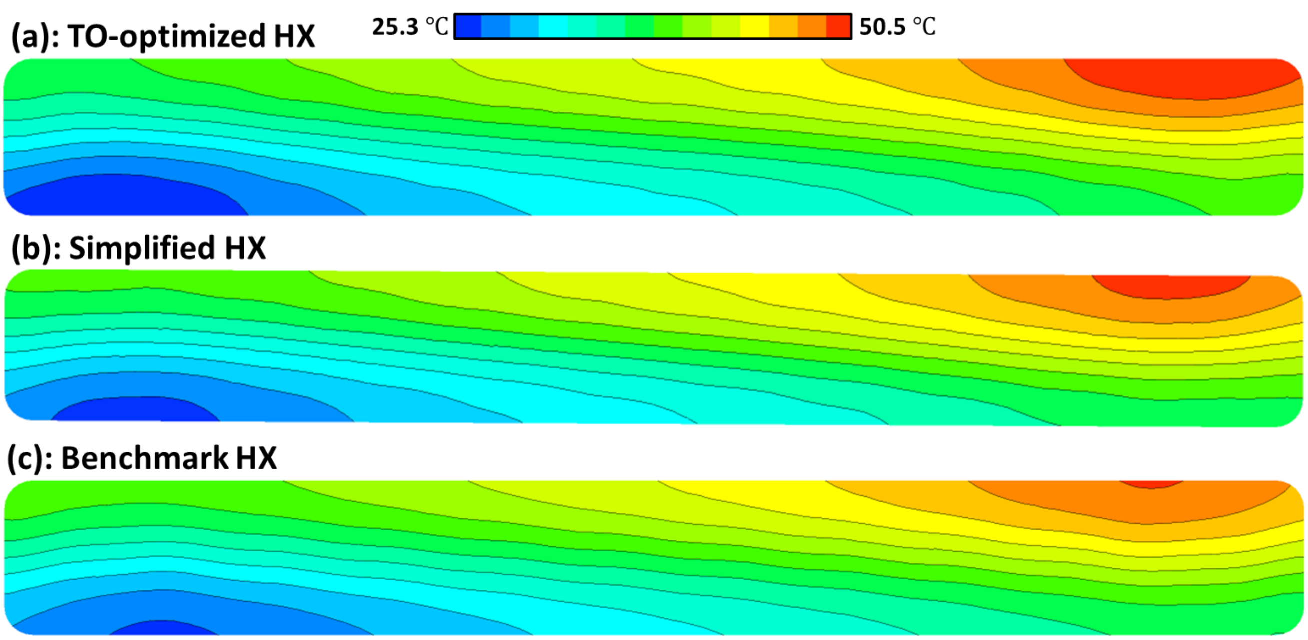

Figure 5.12: Temperature contours on the outer surface of the sapphire plate for the **(a):** TO-optimized, **(b):** Simplified and **(c):** Benchmark HX units at $\overline{Re_{hot}}$= 695.

5.5 Conclusions and Perspectives

This chapter has been dedicated to the performance evaluation of several HX designs using high fidelity numerical approaches. Three HX units (TO-optimized, simplified and benchmark) have been examined numerically using the ANSYS Fluent code under a wide range of flow rate operations in the laminar region. The major conclusions of the present chapter can be illustrated as follows:

- Among the three tested HX units, the TO-optimized HX have the highest heat transfer rate showing better thermal performance compared to the benchmark and simplified HX units in the laminar region.
- As for the simultaneous thermo-hydraulic performance, several criteria have been used (PEC, heat transfer rate at the same pumping power) to examine the three HX units. The results demonstrate that the TO-optimized HX unit possess the best thermo-hydraulic performance under a wide range of flow rate operations.
- The physical interpretation stage reveals that the TO-optimized and simplified designs that are principally featured by the solid allocation in proximity of the insulation decrease the thermal resistance leading to an intensification in the overall thermal performance.
- As for the HX design guidelines based on the inspiration from the topological features, when low or moderate conductive materials are employed in the HX, the optimal allocation of the fins is the distant allocation from the interface wall (where heat is exchanged) in order to achieve the maximized thermo-hydraulic performance.

All the aforementioned conclusions prove that the TO is a robust method to design HXs for magnified performance thanks to the elevated number of the employed design variables. After demonstrating numerically the efficacy of the TO, it is now indispensable to validate the numerical results and the design methodology using experimental approaches which will be discussed and presented in details in the next chapter 6.

Chapter 6: Experimental validation of the topology optimization design methodology

Chapter Summary

This chapter introduces the experimental approach to evaluate experimentally the thermo-hydraulic performance of the investigated HX (heat exchanger) units (TO-optimized, simplified and benchmark) in the previous chapter 5 with the intention of validating the TO (topology optimization) design methodology. The three HX units are fabricated using the water jet cutting process and an experimental setup is built, allowing the global performances evaluation of the machined HX units, while the IR (Infrared) thermography is used to compare and validate the local temperature fields. The acquired experimental results are compared with the numerical results obtained through the CFD analysis presented in the preceding chapter 5, demonstrating good agreement between each other, confirming the robustness and superiority of the TO-optimized HX unit over the benchmark design.

Keywords of the Chapter:

Experimental approach, Heat exchangers, Performance evaluation, Infrared (IR) thermography, Design methodology validation.

6.1 Introduction

Despite all encouraging numerical results obtained in the previous chapters that prove the thermo-hydraulic performance superiority of the TO-optimized and the simplified HX units (mainly featured by the solid allocation in proximity of the insulation) over the benchmark case (characterized by the solid allocation at the HX's interface wall), further efforts are still required to experimentally validate the numerical results and the TO's design methodology. For the purpose of intensifying the exchanged heat as reported by the literature, fins are inserted at the HX's interface wall (where heat is exchanged) to extent the heat transfer area leading to an improvement of the overall thermal performance. However, the optimal solid allocation derived by the TO for maximizing thermo-hydraulic performance is proved numerically in the previous chapter 5 not to be at the interface wall (near the insulation) of HXs that employs moderate conductive materials. Moreover, few researchers (about 18%) in the TO of HXs literature (chapter 2) fabricated the TO-derived structures and the majority (about 82%) limit their researches to the numerical approaches by performing CFD analysis to evaluate the performances of the TO-optimized structures. As for the TO of dual-flow HXs specifically, our statistics indicate that no existing researches have experimentally tested the TO-derived structures [12]. However, the experimental approach is considered an indispensable step to validate the numerical models. These previous aspects motivate us to perform the work of the present chapter. Therefore, the main aim of this chapter is to experimentally validate the design methodology of the TO by confirming the CFD results of the foregoing chapter 6 that demonstrate the efficacy of the TO-derived design and prove its advantage over other configurations.

An experimental setup was built in the LTeN, which allows us to evaluate the thermal performance (heat transfer rate) of the HX units using thermocouples, while the hydraulic performance (pressure losses) is measured using a manometer. For further comparison and validation, an optical-based technique, the IR thermography was utilized to confirm and compare the local temperature field.

This chapter is decomposed as follows: Section 6.2 presents the experimental setup built in the LTeN laboratory to evaluate the thermo-hydraulic performances of the different HX units. Section 6.3 introduces the fabricated HX units using the water jet cutting process. Section 6.4 delves into the IR thermography methodology by providing the details of the input parameters, imaging and post processing details. Section 6.5 provide a detailed comparison between the experimental and numerical results. Eventually, Section 6.6 encapsulates the main conclusions.

6.2 Experimental set-up

Figure 6.1 illustrates the experimental setup built in the LTeN laboratory for the aim of experimentally evaluating the thermo-hydraulic performance of TO-optimized, benchmark and simplified HX units. The setup permits the circulation of the cold and hot pure water with controlled inlet temperatures and flow rates thanks to two LAUDA RP855. Two manual valves were installed at the discharge section of each LAUDA RP855 for more control precision of the flow rate. Furthermore, a Kobold DPM-1103 flow meter (± 2.5% precision) was located at the suction section of each LAUDA in each circuit (cold and hot) to measure the flow rate. The inlet and outlet temperatures of the hot and cold fluids were measured using four thermocouples of type K (± 0.2K precision) and a central acquisition system with an acquisition frequency of 0.1 seconds. The hydraulic performance of the HX units was experimentally evaluated by measuring the static pressure at the inlets and outlets of the HX's cold and hot channels using a vertical manometer. Lastly, an IR camera has been used to measure and compare the local temperature field at the targeted surface.

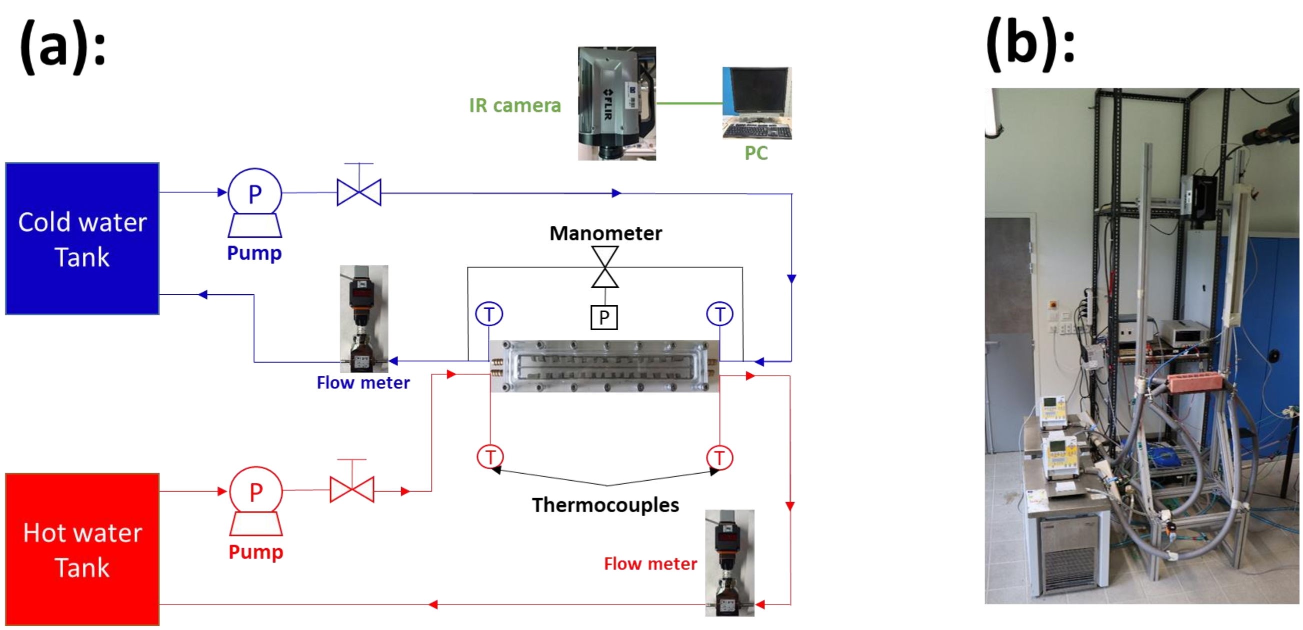

Figure 6.1: (a): Schematic view and **(b):** Photo view of the experimental setup built in the LTeN laboratory.

6.3 Heat exchanger prototypes

The three investigated HX units (TO-optimized, simplified and benchmark) presented in the figure 5.4 of the previous chapter 5 were machined using the water jet-cutting machine as depicted by figure 6.2. The machined HX units have an overall dimensions of 200mm × 40mm × 21 mm without considering the water copper connections at the inlets and outlets of the HX's flow channels. As illustrated in the preceding chapter, the 3D HX design has a sandwich concept composed of a bottom cage with 11 mm thickness made of polycarbonate that surrounds the HX unit fabricated from Stainless Steel from the side and bottom faces. A sapphire plate with dimensions of 190 mm × 28mm × 5 mm was placed at the upper face of the HX unit to authorize optical access for the IR camera, enabling the measurement the temperature distribution. Moreover, a cover plate with 10 mm thickness made of polycarbonate is positioned on the sapphire plate, allowing its fixation using fourteen screws. The detailed dimensions of the bottom cage, HX unit, sapphire plate and cover plates are presented in the figure 5.5 of chapter 5. Lastly, sealing strips were used to avoid the water leakage to the exterior, while strong glue was used at the upper and bottom surfaces of the HX's interface wall to prevent the mixing between cold and hot fluids.

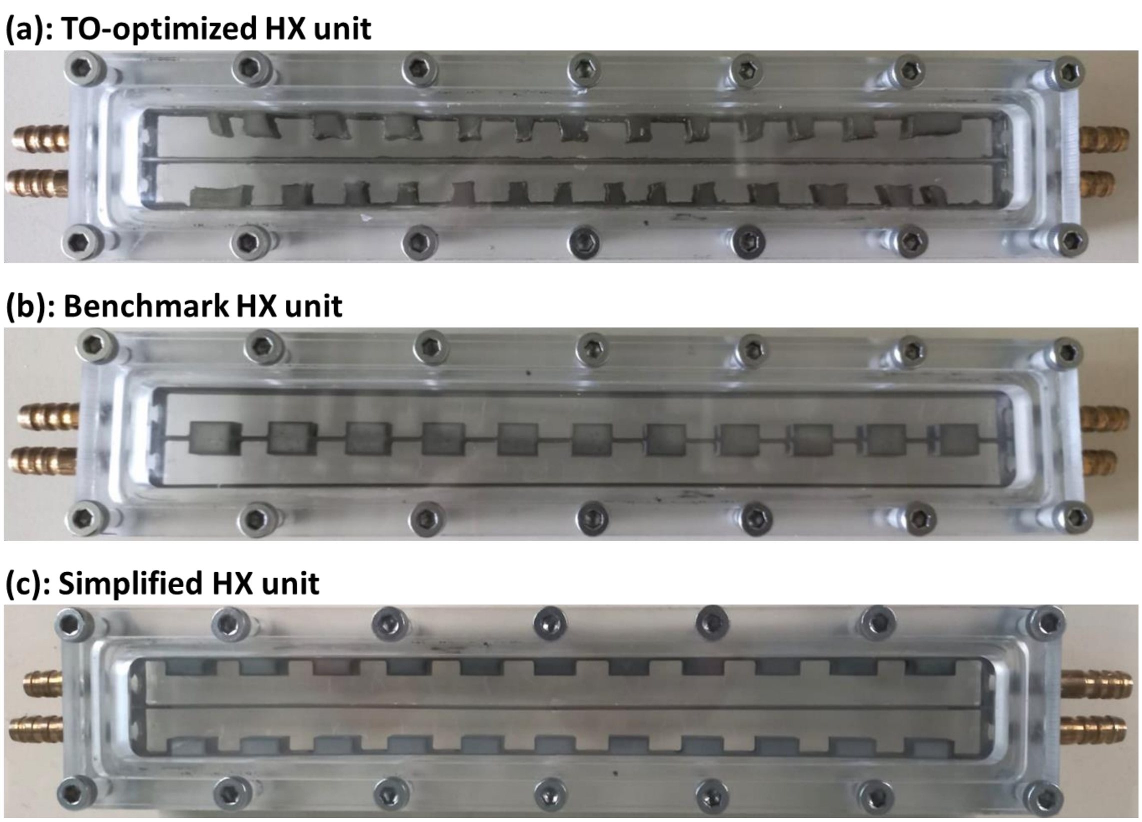

Figure 6.2: Fabricated **(a):** TO-optimized, **(b):** Benchmark and **(c):** Simplified HX units using the water jet cutting process.

6.4 Infrared thermography and measurement schemes

The fundamental principal of the IR thermography lies in the detection of radiation emitted by an object through infrared lens, which is subsequently converted to an electrical signal. Following amplification and data processing, the signal ultimately undergoes a transformation to display the temperature distribution values. According the literature [287], most of the used IR camera are sensitive in the middle and long wavelength ranges. In the present study, the employed IR camera (FLIR, X-series) can detect radiation with a wavelength span from 1.5 μm to 5 μm. Within this range, the sapphire plate with a 5 mm has a transmission over 60 % [288], while the emissivity of the water ranges between 0.92 and 0.96 [289]. Hence, the IR camera is capable of detecting the thermal radiation emitted by the water via the sapphire window.

The machined HX units (TO-optimized, simplified and benchmark) were tested under ten different flow rate operations, spanning from 0.035 L.min^{-1} ($\overline{Re_{cold}}$= 98, $\overline{Re_{hot}}$ =180) to 0.215 L.min^{-1} ($\overline{Re_{cold}}$= 555, $\overline{Re_{hot}}$ =1106). For each flow rate, the temperature and pressure measurements were carried out once the steady-state has been achieved, i.e., the outlet temperature of the cold fluid is stable (see Annex 6A). Upon reaching the thermal stability (steady-state), a real time image recording was performed using the commercial software ResearchIR with a frame frequency of 60 Hz. After obtaining 1000 successive temperature images (matrices), an element-wise average was performed to acquire the final measured temperature field with a resolution of 82×512 pixels. The selection of 1000 images was based on observations indicating that this number of images was sufficient to obtain a stable temperature contour. Moreover, it is noteworthy to mention that the IR measurement targets the inner surface of the sapphire plate (targeted surface) that is in direct contact with the water inside the HX. This is because the IR radiation can be transmitted through the semi-transparent sapphire, but not through the water. Lastly, it should be noted that temperature fields of the solid phase acquired by the IR camera must be hidden using the solid phase coordinates within the HX's domain.

6.5 Results

6.5.1 Uncertainty analysis

An uncertainty analysis was performed, employing the methodology of Moffat [290] to quantify the uncertainties of the experimental approach. Moffat [290] estimated the error between the mean value (true value) for different repeated trials and the measured value to be the twice of the standard deviation ($\pm 2\sigma$) for single sample experiments. Therefore, the experiments have been repeated three times first, showing an acceptable uncertainty of the experimentally measured heat transfer rate and friction coefficient with an error up to $\pm 4.15\ \%$ and $\pm 4.38\ \%$ for the TO-optimized HX unit, up to $\pm 4.65\ \%$ and $\pm 4.95\ \%$ for the simplified HX unit and up to $\pm 4.77\ \%$ and $\pm 5.07\ \%$ for the benchmark HX units, respectively as seen in Fig 6.3. The reason of repeating the experiments only three times due to the acceptable volatility error observed in the recurring experimental measurements of the heat transfer rate and friction coefficient. Eventually, the experimental validation and comparison of the thermo-hydraulic performance are kept to the following subsection.

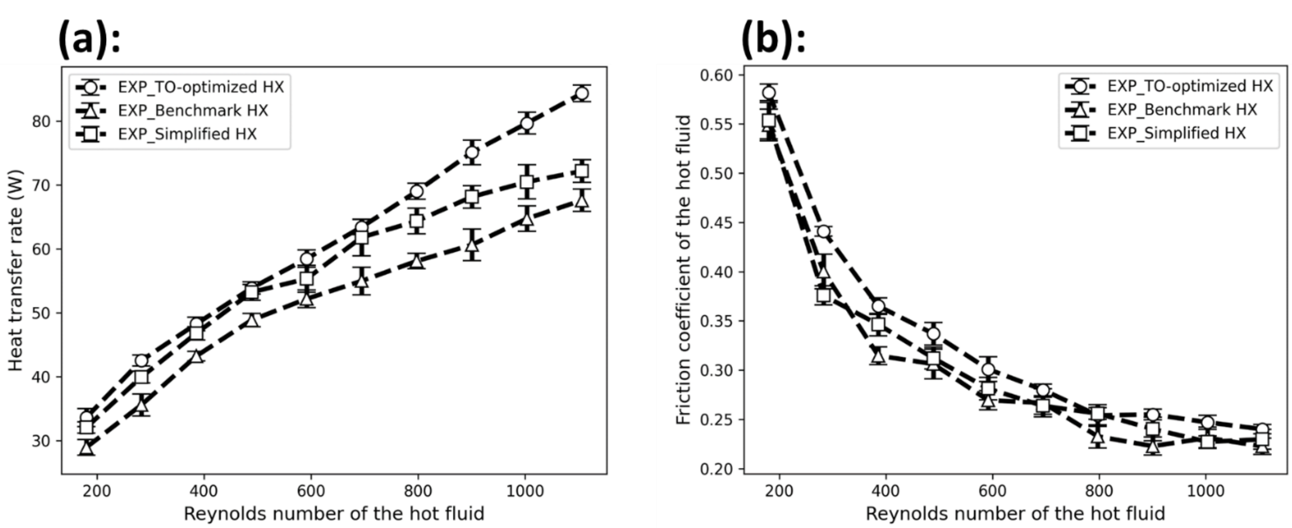

Figure 6.3: Uncertainty analysis of the **(a):** heat transfer rate and **(b):** friction coefficient of the three investigated HX units measured experimentally.

6.5.2 Thermo-hydraulic performance evaluation and validation

First, the Reynolds number of the cold and hot fluids is calculated based on the area-averaged flow properties and velocities inside the HX's flow channels using the following equation:

$$\overline{Re} = \frac{\overline{\rho_f}.\bar{v}.Dh}{\bar{\mu}} \tag{54}$$

where $\overline{\rho_f}$ is the fluid average density (kg.m^{-3}), $\bar{\mu}$ is the fluid average dynamic viscosity (Pa.s), $\bar{v}$ is the volume-weighted average velocity inside the cold or hot flow channels (m.s^{-1}) and Dh is the hydraulic diameter calculated according the cross-sectional dimensions of the HX's flow channel which is equal to 0.0072 m.

The heat transfer rate of the cold fluid side is utilized as criteria to evaluate the HX's thermal performance and is calculated using the equation 47 of the previous chapter 5. It should be noted that the highest heat loss to the ambient, calculated by the difference between the heat transfer rates on the hot and cold sides, is approximately 4% (1.32 W) at the lowest flow rate (0.035 L.min^{-1}). This small percentage indicates that the heat losses have a negligible effect on the evaluation of the HX's thermal performance. As seen by fig 6.4, a good agreement between the heat transfer evaluated experimentally (through four thermocouples and flowmeters) and numerically (CFD analysis) has been observed, with a maximum deviation up to 3.5%, 4.81% and 5.61% for the TO-optimized, simplified and benchmark HX unit, respectively. The experimental results demonstrate a higher exchanged heat in the TO-optimized and simplified HX units compared to the benchmark case with an enhancement up to 18.09% and 10.23 %, respectively. This validates and confirms the thermal efficacy and superiority of the TO-optimized and simplified design that are mainly featured by the solid allocations proximate to the insulation over the benchmark configuration typified by the solid positioning on the HX's interface wall.

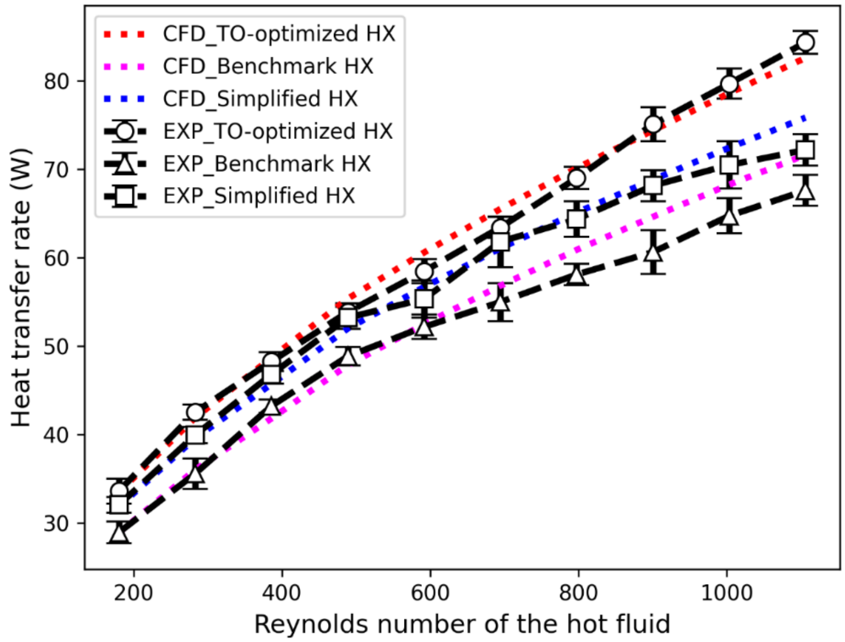

Figure 6.4: Variation of the heat transfer rate of the three HX units evaluated numerically and experimentally with respect to *Re*.

Moreover, the pressure drop is experimentally measured using a vertical manometer to validate and compare it with that evaluated through the CFD analysis. Thereafter, the friction coefficient can be directly computed from the measured pressure drop using the equation 29 of chapter 3. As illustrated by Fig 6.5, a noteworthy concurrence between the friction coefficients evaluated experimentally and numerically for all designs is evident with a maximum deviation up to 5.5%, 5.78% and 6.17% for the TO-optimized, simplified and benchmark HX units, respectively. This deviation is considered an acceptable deviation by considering the experimental uncertainty for measuring the friction coefficient is about 4.381%, 4.95% and 5.07% for the TO-optimized, simplified and benchmark HX units, which represents a small difference about 1%. Moreover, the error bars of the three-plotted curves in figure 6.5 that represents the experimental uncertainty for measuring the friction coefficient for the three HX units overlaps between each other's at different flow rate condition. This elucidates the small difference in the measured friction coefficient of the three HX units, confirming the slight increase in the hydraulic losses predicted numerically (figure 5.6) of the TO-optimized HX units compared to the simplified and benchmark designs.

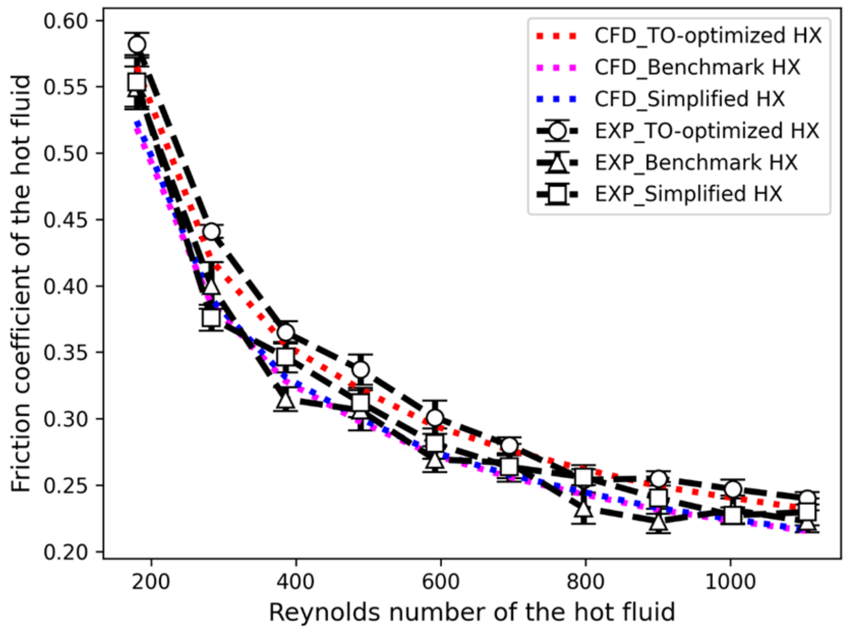

Figure 6.5: Variation of the friction coefficient of the three HX units evaluated numerically and experimentally with respect to the *Re*.

To consider the thermo-hydraulic performance simultaneously, the heat transfer rates for the three HX configurations are plotted as a function of the pumping power (Q_{pump}) calculated thought the following equation:

$$Q_{pump} = (\dot{v}\Delta P)_{cold} + (\dot{v}\Delta P)_{hot} \tag{55}$$

where $\dot{v}$ is the volumetric flow rate ($m^3.s^{-1}$). As seen by figure 6.6, a notable agreement between the numerical and experimental plots is conspicuous, substantiating the thermo-hydraulic performance advantage of the TO-optimized HX unit over the simplified and benchmark cases with a heat transfer intensification up to 8.7 % and 15.08 % under the same pumping power, respectively. It important to mention that the PEC number is not employed in this chapter to compare the thermo-hydraulic performance due to the limitations outlined in section 5.4.1 of the previous chapter 5.

By summarizing this subsection, the thermo-hydraulic performance of the TO-derived design is experimentally evaluated and compared with the numerical results acquired through CFD analysis (previous chapter 5). The comparison stage illustrates a good agreement between numerical and experimental results with acceptable deviations. This serves to confirm and substantiate that the optimal allocation of the low/moderate conductive solids for obtaining maximized thermo-hydraulic performance is in proximity to the insulation (as in the optimized and simplified designs) and not at the HX's interface wall (as in the benchmark design).

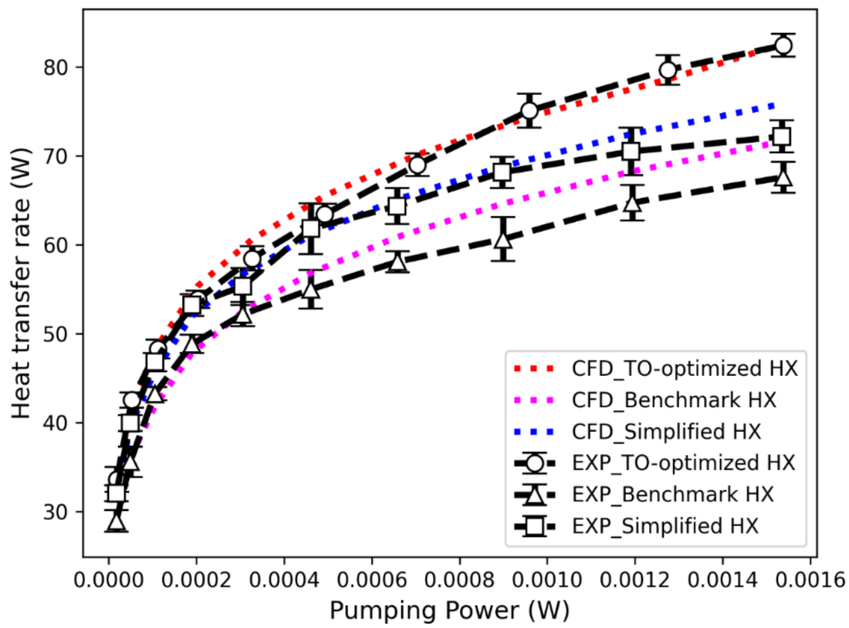

Figure 6.6: Evolution of the heat transfer rate computed experimentally and numerically with respect to the Pumping power.

6.5.3 Comparison between CFD and IR camera results (Fluid local temperature distribution comparison and validation)

- Fluid Temperature contours

Figures 6.7a, 6.7b & 6.7c expose the fluid temperature contours measured by the IR camera measurements and figures 6.7d, 6.7e & 6.7f illustrate the local fluid temperature contours acquired through the CFD analysis for the TO-optimized, benchmark and simplified HX units, respectively, under the same volumetric flow rate of 0.135 L.min^{-1} ($\overline{Re_{cold}}$ = 354, $\overline{Re_{hot}}$ = 695). For the three HX units, the isotherms acquired through IR camera and CFD exhibit a well correspondence, on the global range. As seen by Figure 6.7, the main differences in the IR and CFD isotherms can be observed at the solid/fluid interfaces. Moreover, the isotherms computed numerically tends to move forward in the flow direction compared to the one measured through the IR camera. As for the TO-optimized HX unit, the minimum and maximum temperatures measured at the targeted surface are

290.68 K (CFD), 291.83 K (IR) and 331.23 K (CFD), 330.14 K (IR), respectively. Moreover, the minimum and maximum temperatures measured at the targeted surface of the simplified HX unit are 292.9 (CFD), 293.25 K (IR) and 329.09 K (CFD), 328.2 K (IR camera), respectively. As for the benchmark case, the minimum and maximum temperatures observed at the targeted surface are 293.9 (CFD), 294.5 K (IR) and 328.09 K (CFD), 327.047 K (IR). This small difference (about 1 K) between the border temperatures of the cold and hot fluids for the three HX units serve as an additional evidence to authenticate the well conformity between the local temperature distributions evaluated numerically (CFD) and experimentally (IR camera).

By comparing the temperature contours of the three different HX units, a higher temperature gradient (The difference between the highest temperature of the hot fluid and the lowest temperature of the cold fluid) between the cold and hot fluid has been observed in the TO-optimized (38.31 K) and simplified (34.95 K) HX units compared to the benchmark HX unit (32.547 K). A heightened temperature gradient signifies an elevated exchanged heat between the two fluids, confirming the superior thermal performance of the TO-optimized and simplified designs over the benchmark case.

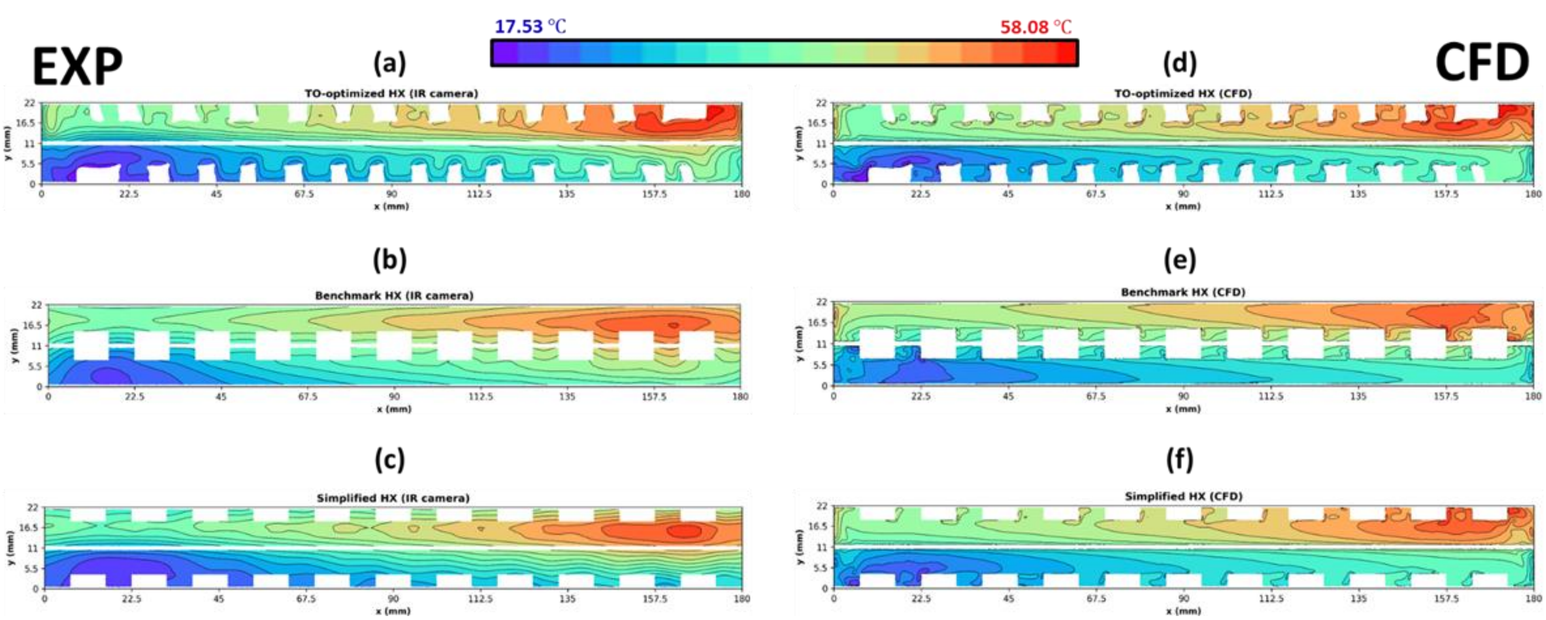

Figure 6.7: Comparison between the temperature contours acquired through IR measurements and CFD analysis for the three HX units at $\overline{Re_{cold}}$ = 354, $\overline{Re_{hot}}$ = 695.

- Local Temperature along sampling lines

For further analysis and comparisons between IR thermography measurement and CFD analysis, the local temperature profiles of the TO-optimized HX unit are compared and plotted as seen in Figure 6.8 at two sampling lines: one for the cold fluid at the position of y=7 mm and the other for the hot fluid at the position of y = 15.8 mm and x spans from 0 mm to 180 mm for both sampling lines. Evidently, the IR and CFD local temperature profiles are generally corresponded, for both sampling lines. Nonetheless, two peak deviations between the IR and CFD curves can be observed once for the cold fluid sampling line at x= 169 mm about 13.8% and the hot sampling line at x=0.5mm about 21.75%.

The reason behind this high discrepancy could potentially stem from the existence of multi-materials inside the HX, causing IR radiation emissions to the camera leading to a divergence in the measured temperature in certain regions. Another reason may arise from the limitation of the fabrication precision in manufacturing small channels with complicated geometries. Moreover, the difference between the fluid velocity profiles between the CFD analysis and experimental at the inlets of the HX could be another possible reason.

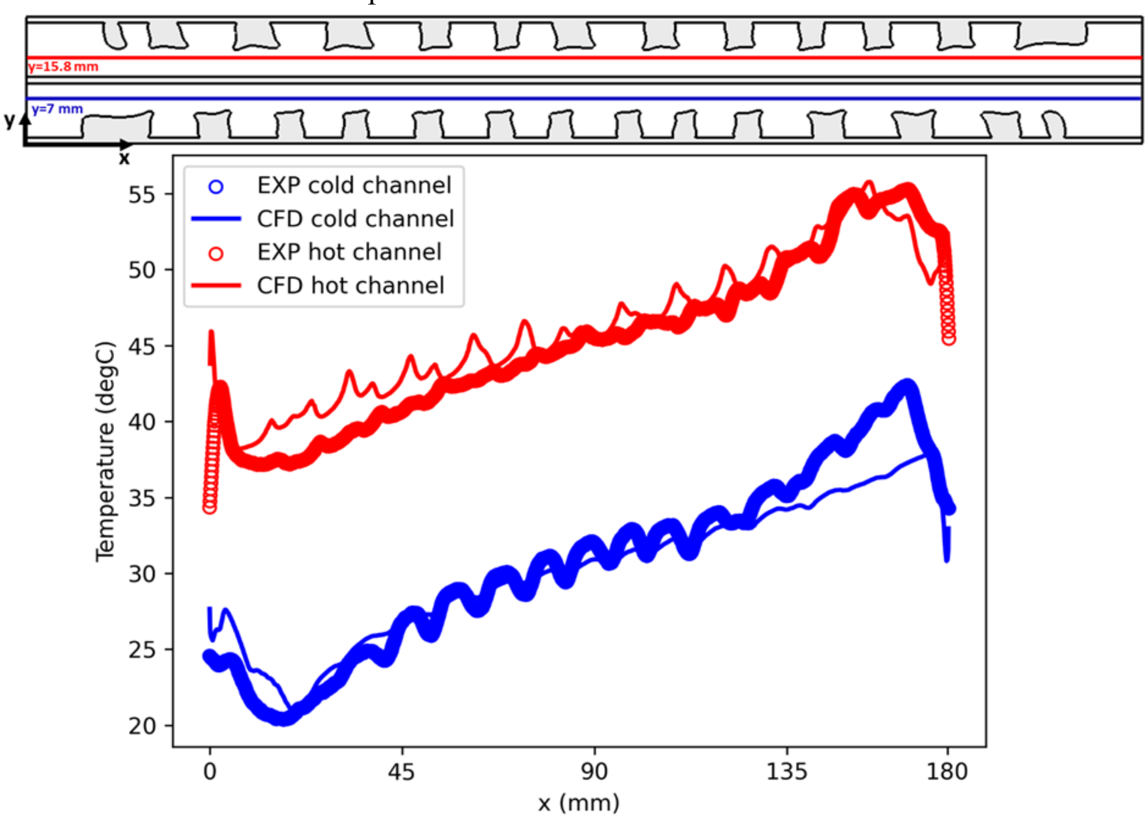

Figure 6.8: Comparison of the local temperature profiles at different sampling lines of the TO-optimized HX unit at $\overline{\mathrm{Re}_{\mathrm{cold}}} = 354$, $\overline{\mathrm{Re}_{\mathrm{hot}}} = 695$.

Furthermore, by visualizing the figure, it is apparent that the IR and CFD curves generally match at the majority of x positions. Thus, it will be not appropriate to solely consider the maximum deviation to compare both curves. Therefore, the mean errors between IR and CFD temperature profiles for both cold and hot fluids sampling lines yield percentages of approximately 4.45% and 3.3 %, respectively, which underscores the consistency between CFD and experimental curves.

Following the same strategy, the local temperature profiles evaluated experimentally (IR camera) and numerically (CFD) for the simplified HX unit are compared as illustrated in Fig 6.9 along two sampling lines: one for the cold fluid at the position of y=6 mm and the other for the hot fluid at the position of y = 15.8 mm and x spans from 0 mm to 180 mm for both sampling lines. A good consistency is evident between the temperature curves evaluated numerically and experimentally along the HX length. The maximum deviations observed in the temperature contours along the cold and hot sampling line are 16.8 % (x=0 mm) and 14.3 % (x=175 mm), respectively. Additionally, the mean error between the numerical and experimental temperature profiles along the cold and hot sampling lines are 5.1% and 3.5 %, respectively, which authenticates the good concordance between the numerical and experimental temperature profiles for the simplified HX unit.

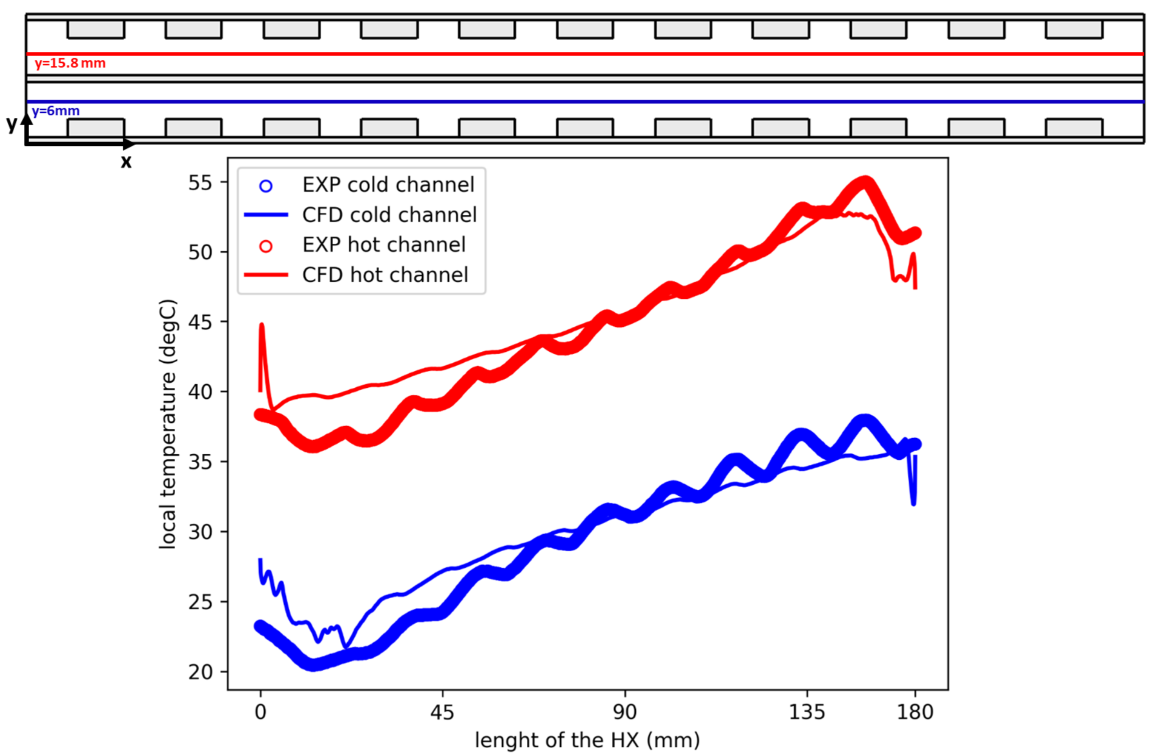

Figure 6.9: Comparison of the local temperature profiles at different sampling lines of the simplified HX unit at $\overline{\mathrm{Re}_{\mathrm{cold}}} = 354$, $\overline{\mathrm{Re}_{\mathrm{hot}}} = 695$.

Lastly, the temperature profiles of the benchmark HX unit evaluated numerically and experimentally are also compared for numerical validation purposes along two sampling lines: one for the cold fluid at the position of y=3 mm and the other for the hot fluid at the position of y = 15.8 mm and x spans from 0 mm to 180 mm for both sampling lines. The numerical and experimental temperature profiles exhibit a good match along both sampling lines as depicted by Fig 6.10. The maximum deviation between numerical and experimental curves at the cold sampling line is 11.6% (x=172 mm) and 12.29% (x=3 mm) along the hot sampling line. Unlike the previous presented plots for the TO-optimized and simplified HX units, the CFD and IR temperature profiles of the cold fluid in the benchmark design do not match well at the global trend. The main reason behind this discrepancy may be attributed to the micro leakage between fluids, which cannot be observed during the experiments due to the transparency of the water and sapphire plate. Nevertheless, the mean absolute errors calculated at the cold and hot sampling lines are 7.5% and 3.1 %, respectively. This confirms the consistency between the numerical and experimental temperature profiles for the benchmark HX unit.

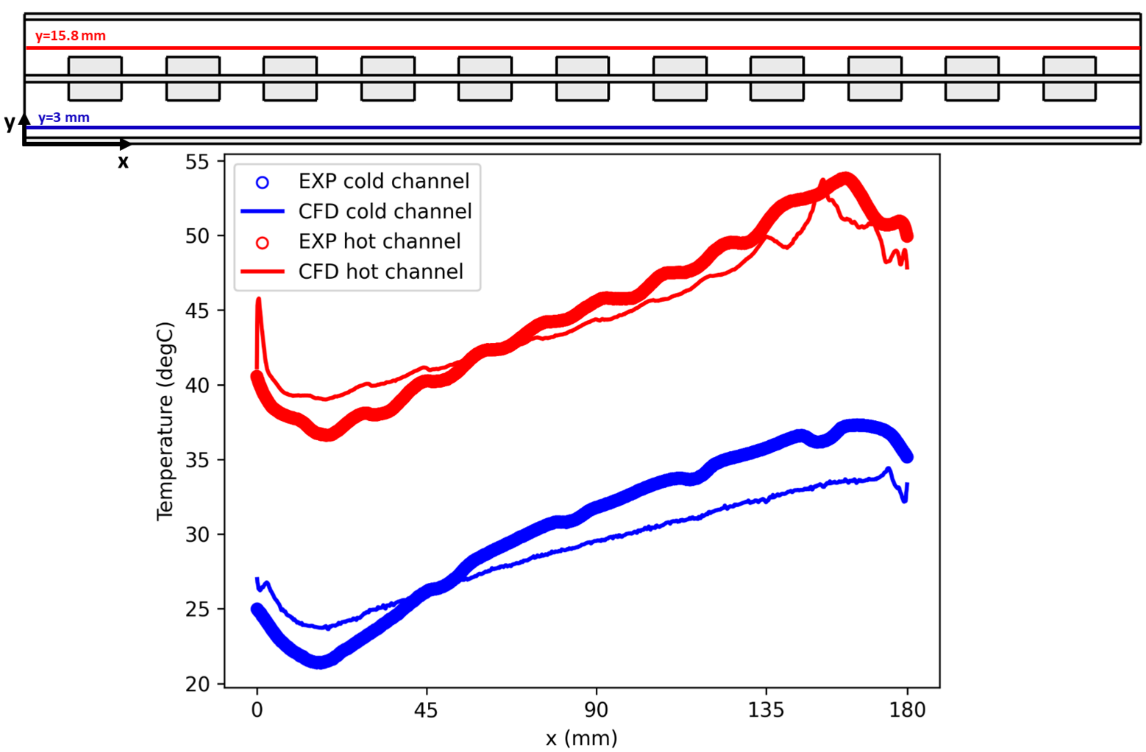

Figure 6.10: Comparison of the local temperature profiles at different sampling lines of the benchmark HX unit at $\overline{\mathrm{Re}_{\mathrm{cold}}} = 354$, $\overline{\mathrm{Re}_{\mathrm{hot}}} = 695$.

As a summary, the local temperature profiles for the three HX units measured experimentally using the IR camera and evaluated numerically through the CFD analysis are compared, showing a good agreement between each other. This serves as additional evidence to prove the high fidelity of the CFD analysis in evaluating the heat transfer characteristics of the three investigated HX units at the local level.

6.4 Conclusions

This chapter focuses on the experimental validation of the TO's design methodology and the numerical model. Three HX units (TO-optimized, simplified and benchmark) were machined and tested under different flow conditions. An experimental setup was built in the LTeN laboratory to experimentally evaluate the global thermal and hydraulic performances through four thermocouples, two flow meters and a manometer. Moreover, the IR thermography has been employed to compare and measure the local temperature field of the fluid. The conclusions can be summarized as follows:

- Good agreement between the thermal and hydraulic performances evaluated numerically (CFD) and experimentally has been observed with a maximum deviation in the evaluated heat transfer rate and friction coefficient up to 5.61% and 6.17%, respectively, thus affirming the validation of our CFD simulations.
- IR measurements and CFD calculations of the fluid temperature distribution demonstrates a good consistency, thereby confirming the fidelity of the CFD simulations.
- Among the three examined HX units, the TO-optimized design exhibits the highest heat transfer rate with an improvement up to 8.7 % and 15.08 % under the same pumping power compared to the simplified and benchmark HX units, respectively, reflecting the robustness of the TO in designing structures for maximized thermo-hydraulic performance.
- The conclusion of the previous chapter 5 regarding the design guidelines is then verified, which confirms that the optimal allocation of the low/moderate solids is in proximity to the insulated wall (for the present case) and not on the HX's interface wall. This will also validate the physical interpretation provided in the previous chapter and authenticates that

the allocation of the low/moderate conductive solid near the insulation reduces the thermal resistances (convective and conductive) leading to an intensification in the overall thermal performance.

All of the aforementioned conclusions demonstrate the effectiveness of the TO-derived design in attaining maximized thermo-hydraulic performance, which has been proved, confirmed and validated physically, numerically and experimentally.

Appendix 6A: Steady state establishment of the water outlet temperature in the experiments

The CFD simulations of chapter 5 were conducted under steady state conditions. Therefore, it is imperative to attain the steady state in the experiments to compare between the results obtained experimentally and numerically. Figure 6.A1 exposes the thermal transient behavior of the cold water outlet temperature over the time. As seen, it is evident that the steady-state condition of the outlet temperature is reached at about 900 sec (15min). Hence, a stabilization period of 15 min is needed at each flow rate adjustment to ensure the stability of the outlet temperatures.

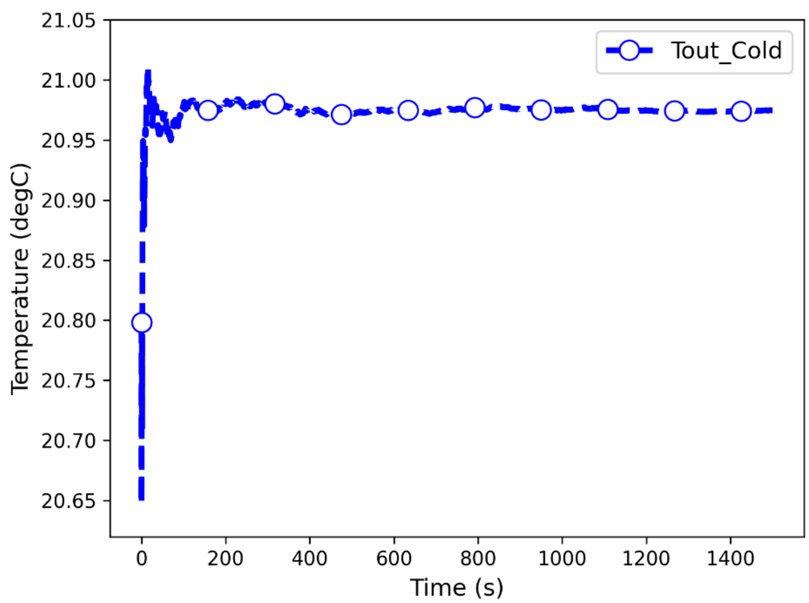

Figure 6.A1: Thermal transient state of the cold-water outlet temperature under a 0.195 $L.min^{-1}$ volumetric flow rate ($\overline{Re_{hot}}$=1003) of the TO-optimized HX unit.

Chapter 7: General conclusions and perspectives

7.1 Conclusions

This thesis is dedicated to the density-based (TO) topology optimization of dual-flow HXs, with the main objective of maximizing the thermo-hydraulic performance. A sensitivity analysis is conducted to test the influence of various TO's input parameters on the acquired topology. Moreover, both numerical and experimental approaches are adopted to test and validate the efficacy of the TO-derived designs, through a comparative analysis with other HX designs. The major conclusions drawn from each chapter can be summarized as follows:

In chapter 2, a detailed literature review is provided on the TO of HXs over the past decades revealing the following gaps: (1): Among the conducted researches in the literature, the majority about 92% focused on the single flow HX, while most of the industrial HXs typically operate with multi-flow streams. (2): a significant portion of the conducted researches employs HXs with wide domains, which may be inconsistent with some actual application like compact HXs. (3): Only 18% of the researchers in the literature tested and fabricated the TO-derived HXs, while the experimental validation is an indispensable step to validate the design methodology and the numerical model. (4): A lack of physical interpretations for the TO-derived structures and an in-depth investigation of the TO's input parameters is evident. (5): lack of addressing the limitations of the density-based TO.

In chapter 3, the density-based topology generation (TG) has been executed on a counter flow HX unit with narrow flow domains for thermal intensification purposes. An investigation stage was performed to study the influence of the crucial TG's input parameter on the generated topology. The investigation analysis reveals that the TG-derived topologies are mainly featured by a novel convergent-divergent (C-D) distribution of the generated fins along the HX's flow channels. Thereafter, a 2D CFD analysis has been conducted to assess numerically the performance of the proposed design and compare it with benchmark cases under different conditions. The results show the efficacy of the TG-derived designs that are mainly featured by the C-D fins distribution in improving the thermal performance compared to the benchmark case with an intensification in the Nu number up to 46.3% and 42.19% for case 1 and 2, respectively. Furthermore, the PEC number that represents the simultaneous thermo-hydraulic performance is improved in the TG-acquired HX units compared to the benchmark case with an enhancement up to 22.5% and 36.11% for case 1 and 2, respectively. Thereafter, a physical interpretation of the TG-derived designs was delivered, demonstrating that the C-D distribution of fins aims to increase the thermal performance in the convergent section and improve the hydraulic performance in the divergent one leading the simultaneous thermo-hydraulic improvement. Upon scrutinizing the correctness of the generated topology, an unphysical issue regarding the velocity field of the generated solids was identified, demonstrating that the imposed impermeability on the solid phase was inadequate to achieve zero velocity of the solid phase. The recognized deficiency in the employed methodology characterizes it as a generation process (TG) rather than an optimization one (TO).

In chapter 4, the solution of the unphysical issue identified in the previous chapter 3 was presented. A dual strategy was followed to solve the lack of the generated solids in resisting the fluid flow: the maximum impermeability imposed on the solid phase was increased and a pressure constraint has been imposed inside the HX's flow channel. Hence, the density-based TO was conducted to maximize the thermo-hydraulic performance of two dual-flow HX units (DP1 and DP2) employing moderately conductive material (Stainless Steel) under periodic and adiabatic wall conditions, respectively. An in-depth investigation was carried out to test the effect of TO's numerous parametric settings on the acquired topology. The investigation stage exemplified that the acquired topologies for DP1 are mainly featured by the positioning of the moderate conductive (Stainless Steel) solids at the central line of the HX's flow channels, while the TO-derived topologies for DP2 are primary featured by the allocation of the moderate conductive (Stainless Steel) solids near the insulation. Furthermore, the limitations of employing high conductive materials (Aluminum) in the TO were discussed and interpreted.

In chapter 5, a 3D CFD analysis was performed to numerically evaluate the thermo-hydraulic performance of the 3D extended TO-optimized HX unit for DP2 obtained in the previous chapter 4. Two additional HX units having rectangular fins are introduced for comparison purposes: one possesses similar solid allocation (near the insulation) of the TO-optimized design and is named simplified HX unit and the other one has an opposite solid allocation (at the HX interface wall). The results demonstrate an intensification of the exchanged heat in the TO-optimized and simplified HX units compared to the benchmark one with an intensification up to 17% and 10%, respectively. Moreover, upon comparing the simultaneous thermo-hydraulic performance, the heat transfer rate was plotted for the three HX units under the same pumping power, illustrating that the TO-optimized and simplified HX units have higher thermo-hydraulic performance compared to the benchmark case with an augmentation in the heat transfer rate up to 14% and 6% under the same pumping power. The performance intensification was physically interpreted disclosing that the allocation of low/moderate near the insulation (as in the TO-optimized and simplified designs) reduces the convective and conductive thermal resistances leading to an intensification in the overall thermal performance.

In chapter 6, the three HX units (TO-optimized, simplified and benchmark) were machined and then experimentally tested to substantiate the efficacy of the TO's design methodology through an experimental validation of the numerical model. Therefore, an experimental setup was built allowing the evaluation and comparison of the global thermal and hydraulic performances for three HX designs. In addition, the IR thermography was employed to compare and validate the fluid local temperature distribution. The experimental and numerical results exhibit good concurrence between each other with a maximum deviation in the evaluated heat transfer rate and friction coefficient up to 5.61% and 6.17%, respectively. This will consequently validate and demonstrates the thermo-hydraulic performance superiority of the TO-optimized and simplified HX units over the benchmark case with an enhancement in the heat transfer rate up to 15.08 % and 8.7 % under the same pumping power, respectively. Therefore, the experimental/numerical validation authenticates the robustness of the TO in designing novel designs for magnifying the thermo-hydraulic performance of dual-flow HXs.

7.2 Perspectives

Based on the progress of the present work, several perspectives can be proposed for further advancing in the field as follows:

- **Tuning TO's various input parameters using an optimizer**

In the present work, the various input parameters of the TO were manually tuned to solve the deficiency discovered in the employed methodology of chapter 3, allowing a transfer from topology generation process to topology optimization one. Tunning manually those parameters to obtain an optimized design was actually a time-consuming task. Therefore, gradient-based or gradient-free optimizers can be employed to determine the optimal input parameter setting of the TO, enabling the derivation of optimized topologies with maximized performance and accelerating the identification and resolution of some limitations inherent in density-based TO [291].

- **TO in the turbulent regions**

In this thesis, the TO was conducted on a 2D counter-flow HX unit within the laminar flow region by virtue of the computational resource limitations. Executing the TO in the turbulent region is essential as several industrial heat exchangers operates in the turbulent region. However, adding a turbulent model to the TO will exponentially increase the computational time. Moreover, the selection of the suitable turbulent model that can accurately simulate the turbulence effect inside the TO-acquired complicated configurations could be also another future work.

- **TO of 3D HXs with practical size**

For simplification purposes, the TO is conducted in this thesis on 2D HX (chapters 3 & 4), then the 2D acquired topologies are extended uniformly in the third direction for the CFD validation stage (chapter 5), with the assumption of neglecting the flow circulation effect in the third dimension. Nevertheless, the effect of the flow circulation in the third direction is paramount in the industrial HXs and cannot be disregarded, emphasizing the necessity of executing the TO on 3D HXs.

- **Machine learning assisted with the TO**

One of the major disadvantages of the TO is the huge computational time needed to solve the governing equations in each iteration for computing the state variables. Integrating the machine learning techniques with the TO will significantly increase its efficiency by reducing the required computational time. This can be done by replacing of the TO's numerical solver (FEM-solver in the present thesis) by a pre-learned ML predictor that can predict the state variable distribution, thereby obviating the necessity of iteratively solving the governing equations.

- **Comparison between gradient with stochastic optimizers**

Theoretically, the stochastic optimizers (i.e., genetic algorithm) can achieve global optimum in the optimization process unlike the gradient optimizers that can easily trap in a local optimum especially when the objective function has several local optimums as in the conjugate heat transfer problems. Nonetheless, in the present work of this thesis, a conservative continuation scheme was built to mitigate the possibility of converging toward a poor local optimum as discussed in chapter 5. Thereafter, comparing the performance of the topologies acquired using gradient and stochastic optimizers could be considered another future work.

- **TO with compressible flows**

In this thesis, the TOs were conducted on a counter-flow HX employing water (incompressible fluid) as a working fluid. Moreover, several industrial HXs (i.e., shell and tube HX) employs compressible fluid (i.e., Air) in the heat transfer mechanism. Thus, considering the compressibility of the working fluid in the TO could be also considered another research direction.

- **Physical interpretation based on the boundary layer phenomena**

In chapters 3, 4 and 5, physical interpretations were delivered to analyze the physics behind the acquired topology. For further analysis of the topology optimized design, the boundary layer concept can be used, which is considered a crucial parameter in the laminar flow regions. During the TO process, fins are generated in the flow channels of the HX in order to disrupt the fluid flow by increasing locally its velocity, which can apparently affect the thermal and hydraulic boundary layers. Therefore, using the boundary layer concept to physically interpret the TO-derived topologies could be important for a clearer understanding of the underlying physics phenomena.

REFERENCES:

[1] A. Fawaz et al., 'Topology optimization of heat exchangers: A review', *Energy*, p. 124053, Apr. 2022 [Online]. Available: 10.1016/j.energy.2022.124053.

[2] O. P. Arsenyeva et al., 'Optimal design of plate-and-frame heat exchangers for efficient heat recovery in process industries', *Energy*, vol. 36, no. 8, pp. 4588–4598, Aug. 2011 [Online]. Available: 10.1016/j.energy.2011.03.022.

[3] H. Jouhara et al., 'Experimental and theoretical investigation of a flat heat pipe heat exchanger for waste heat recovery in the steel industry', *Energy*, vol. 141, pp. 1928–1939, Dec. 2017 [Online]. Available: 10.1016/j.energy.2017.10.142.

[4] H. Jouhara et al., 'Investigation on a full-scale heat pipe heat exchanger in the ceramics industry for waste heat recovery', *Energy*, vol. 223, p. 120037, May 2021 [Online]. Available: 10.1016/j.energy.2021.120037.

[5] Q. Li et al., 'Compact heat exchangers: A review and future applications for a new generation of high temperature solar receivers', *Renewable and Sustainable Energy Reviews*, vol. 15, no. 9, pp. 4855–4875, Dec. 2011 [Online]. Available: 10.1016/j.rser.2011.07.066.

[6] L. Luo et al., 'Design, Fabrication And Experimental Study Of New Compact Mini Heat-Exchangers', in *Microreaction Technology*, M. Matlosz, W. Ehrfeld, and J. P. Baselt, Eds. Berlin, Heidelberg: Springer Berlin Heidelberg, 2001, pp. 68–69[Online]. Availablehttp://link.springer.com/10.1007/978-3-642-56763-6_7[Accessed: 12January2022].

[7] L. Luo et al., 'Heat exchanger: from micro- to multi-scale design optimization', *Int. J. Energy Res.*, vol. 31, no. 13, pp. 1266–1274, Oct. 2007 [Online]. Available: 10.1002/er.1298.

[8] Y. Fan and L. Luo, 'Recent Applications of Advances in Microchannel Heat Exchangers and Multi-Scale Design Optimization', *Heat Transfer Engineering*, vol. 29, no. 5, pp. 461–474, May 2008 [Online]. Available: 10.1080/01457630701850968.

[9] L. Luo et al., 'Integration of constructal distributors to a mini crossflow heat exchanger and their assembly configuration optimization', *Chemical Engineering Science*, vol. 62, no. 13, pp. 3605–3619, Jul. 2007 [Online]. Available: 10.1016/j.ces.2007.02.058.

[10] C. Pistoresi et al., 'Thermal performances of a multi-scale fluidic network', *Applied Thermal Engineering*, vol. 147, pp. 1096–1106, Jan. 2019 [Online]. Available: 10.1016/j.applthermaleng.2018.11.015.

[11] L. Luo, Ed., *Heat and Mass Transfer Intensification and Shape Optimization*. London: Springer London, 2013[Online]. Availablehttp://link.springer.com/10.1007/978-1-4471-4742-8[Accessed: 6November2021].

[12] D. Tondeur and E. Kvaalen, 'Equipartition of entropy production. An optimality criterion for transfer and separation processes', *Ind. Eng. Chem. Res.*, vol. 26, no. 1, pp. 50–56, Jan. 1987 [Online]. Available: 10.1021/ie00061a010.

[13] A. E. Bergles, 'ExHFT for fourth generation heat transfer technology', *Experimental Thermal and Fluid Science*, vol. 26, no. 2–4, pp. 335–344, Jun. 2002 [Online]. Available: 10.1016/S0894-1777(02)00145-0.

[14] Z. Y. Guo et al., 'The field synergy (coordination) principle and its applications in enhancing single phase convective heat transfer', *International Journal of Heat and Mass Transfer*, vol. 48, no. 9, pp. 1797–1807, Apr. 2005 [Online]. Available: 10.1016/j.ijheatmasstransfer.2004.11.007.

[15] H. S. Dizaji et al., 'Proposing an innovative and explicit economic criterion for all passive heat transfer enhancement techniques of heat exchangers', *Energy*, vol. 239, p. 122271, Jan. 2022 [Online]. Available: 10.1016/j.energy.2021.122271.

[16] R. Boichot and L. Luo, 'A simple Cellular Automaton algorithm to optimise heat transfer in complex configurations', *International Journal of Exergy*, vol. 7, pp. 51–64, 2010.

[17] L. Luo et al., 'Heuristic shape optimization of baffled fluid distributor for uniform flow distribution', *Chemical Engineering Science*, vol. 123, pp. 542–556, Feb. 2015 [Online]. Available:

10.1016/j.ces.2014.11.051.
[18] Y. Du et al., ‘Size optimization of heat exchanger and thermoeconomic assessment for supercritical CO2 recompression Brayton cycle applied in marine’, *Energy*, vol. 239, p. 122306, Jan. 2022 [Online]. Available: 10.1016/j.energy.2021.122306.
[19] R. Hilbert et al., ‘Multi-objective shape optimization of a heat exchanger using parallel genetic algorithms’, *International Journal of Heat and Mass Transfer*, vol. 49, no. 15–16, pp. 2567–2577, Jul. 2006 [Online]. Available: 10.1016/j.ijheatmasstransfer.2005.12.015.
[20] L. Wang et al., ‘Lattice Boltzmann method for shape optimization of fluid distributor’, *Computers & Fluids*, vol. 94, pp. 49–57, May 2014 [Online]. Available: 10.1016/j.compfluid.2014.01.034.
[21] L.-Z. Zhang, ‘Conjugate Heat Transfer in Plate-Fin and Tube Heat Exchangers’, in *Conjugate Heat and Mass Transfer in Heat Mass Exchanger Ducts*, Elsevier, 2013, pp. 255–274[Online]. Availablehttps://linkinghub.elsevier.com/retrieve/pii/B9780124077829000095[Accessed: 6November2021].
[22] P. Papazoglou, ‘Topology Optimization of Heat Exchangers’, Master’s thesis, Delft University of Technology, 2015.
[23] R. T. Marler and J. S. Arora, ‘The weighted sum method for multi-objective optimization: new insights’, *Struct Multidisc Optim*, vol. 41, no. 6, pp. 853–862, Jun. 2010 [Online]. Available: 10.1007/s00158-009-0460-7.
[24] K. Deb et al., ‘A fast and elitist multiobjective genetic algorithm: NSGA-II’, *IEEE Trans. Evol. Computat.*, vol. 6, no. 2, pp. 182–197, Apr. 2002 [Online]. Available: 10.1109/4235.996017.
[25] M. Mani et al., ‘Design Rules for Additive Manufacturing: A Categorization’, in *Volume 1: 37th Computers and Information in Engineering Conference*, Cleveland, Ohio, USA, 2017, p. V001T02A035[Online]. Availablehttps://asmedigitalcollection.asme.org/IDETC-CIE/proceedings/IDETC-CIE2017/58110/Cleveland,%20Ohio,%20USA/259177[Accessed: 26October2021].
[26] J. Zhu et al., ‘A review of topology optimization for additive manufacturing: Status and challenges’, *Chinese Journal of Aeronautics*, vol. 34, no. 1, pp. 91–110, Jan. 2021 [Online]. Available: 10.1016/j.cja.2020.09.020.
[27] X. Chen, ‘Topology optimization of microfluidics — A review’, *Microchemical Journal*, vol. 127, pp. 52–61, Jul. 2016 [Online]. Available: 10.1016/j.microc.2016.02.005.
[28] T. Dbouk, ‘A review about the engineering design of optimal heat transfer systems using topology optimization’, *Applied Thermal Engineering*, vol. 112, pp. 841–854, Feb. 2017 [Online]. Available: 10.1016/j.applthermaleng.2016.10.134.
[29] J. Alexandersen and C. S. Andreasen, ‘A Review of Topology Optimisation for Fluid-Based Problems’, *Fluids*, vol. 5, no. 1, p. 29, Mar. 2020 [Online]. Available: 10.3390/fluids5010029.
[30] N. van Dijk et al., ‘Critical study of design parameterization in topology optimization; The influence of design parameterization on local minima’, in *TU Delft Research Portal*, Lisbon, Portugal, 2010, p. 11[Online]. Availablehttps://research.tudelft.nl/en/publications/critical-study-of-design-parameterization-in-topology-optimizatio.
[31] M. P. Bendsøe, ‘Optimal shape design as a material distribution problem’, *Structural Optimization*, vol. 1, no. 4, pp. 193–202, Dec. 1989 [Online]. Available: 10.1007/BF01650949.
[32] T. Borrvall and J. Petersson, ‘Topology optimization of fluids in Stokes flow’, *Int. J. Numer. Meth. Fluids*, vol. 41, no. 1, pp. 77–107, Jan. 2003 [Online]. Available: 10.1002/fld.426.
[33] T. Matsumori et al., ‘Topology optimization for fluid–thermal interaction problems under constant input power’, *Struct Multidisc Optim*, vol. 47, no. 4, pp. 571–581, Apr. 2013 [Online]. Available: 10.1007/s00158-013-0887-8.
[34] A. A. Koga et al., ‘Development of heat sink device by using topology optimization’, *International Journal of Heat and Mass Transfer*, vol. 64, pp. 759–772, Sep. 2013 [Online]. Available: 10.1016/j.ijheatmasstransfer.2013.05.007.
[35] J. H. K. Haertel and G. F. Nellis, ‘A fully developed flow thermofluid model for topology optimization of 3D-printed air-cooled heat exchangers’, *Applied Thermal Engineering*, vol. 119, pp. 10–24, Jun. 2017

[Online]. Available: 10.1016/j.applthermaleng.2017.03.030.
[36] J. H. K. Haertel et al., 'Topology optimization of a pseudo 3D thermofluid heat sink model', *International Journal of Heat and Mass Transfer*, vol. 121, pp. 1073–1088, Jun. 2018 [Online]. Available: 10.1016/j.ijheatmasstransfer.2018.01.078.
[37] C. Sun et al., 'Thermal enhancement of fin and tube heat exchanger with guiding channels and topology optimisation', *International Journal of Heat and Mass Transfer*, vol. 127, pp. 1001–1013, Dec. 2018 [Online]. Available: 10.1016/j.ijheatmasstransfer.2018.08.093.
[38] C. Saglietti et al., 'Topology optimization of heat sinks in a square differentially heated cavity', *International Journal of Heat and Fluid Flow*, vol. 74, pp. 36–52, Dec. 2018 [Online]. Available: 10.1016/j.ijheatfluidflow.2018.08.004.
[39] V. Subramaniam et al., 'Topology optimization of conjugate heat transfer systems: A competition between heat transfer enhancement and pressure drop reduction', *International Journal of Heat and Fluid Flow*, vol. 75, pp. 165–184, Feb. 2019 [Online]. Available: 10.1016/j.ijheatfluidflow.2019.01.002.
[40] Ł. Łaniewski-Wołłk and J. Rokicki, 'Adjoint Lattice Boltzmann for topology optimization on multi-GPU architecture', *Computers & Mathematics with Applications*, vol. 71, no. 3, pp. 833–848, Feb. 2016 [Online]. Available: 10.1016/j.camwa.2015.12.043.
[41] J. Zhao et al., 'Topology optimization of turbulent forced convective heat sinks using a multi-layer thermofluid model', *Struct Multidisc Optim*, Sep. 2021[Online]. Availablehttps://link.springer.com/10.1007/s00158-021-03064-1[Accessed: 16November2021].
[42] X. Mo et al., 'Topology optimization of cooling plates for battery thermal management', *International Journal of Heat and Mass Transfer*, vol. 178, p. 121612, Oct. 2021 [Online]. Available: 10.1016/j.ijheatmasstransfer.2021.121612.
[43] S. B. Dilgen et al., 'Density based topology optimization of turbulent flow heat transfer systems', *Struct Multidisc Optim*, vol. 57, no. 5, pp. 1905–1918, May 2018 [Online]. Available: 10.1007/s00158-018-1967-6.
[44] T. V. Oevelen and M. Baelmans, 'APPLICATION OF TOPOLOGY OPTIMIZATION IN A CONJUGATE HEAT TRANSFER PROBLEM', Kos Island, Greece, 2014.
[45] S. Zeng et al., 'Experimental and numerical investigation of a mini channel forced air heat sink designed by topology optimization', *International Journal of Heat and Mass Transfer*, vol. 121, pp. 663–679, Jun. 2018 [Online]. Available: 10.1016/j.ijheatmasstransfer.2018.01.039.
[46] S. Ghosh and J. S. Kapat, 'Topology Optimization of Serpentine Channels for Minimization of Pressure Loss and Maximization of Heat Transfer Performance As Applied for Additive Manufacturing', in *Volume 5B: Heat Transfer*, Phoenix, Arizona, USA, 2019, p. V05BT21A006[Online]. Availablehttps://asmedigitalcollection.asme.org/GT/proceedings/GT2019/58653/Phoenix,%20Arizona,%20USA/1066892[Accessed: 18November2021].
[47] E. M. Dede, 'Multiphysics Topology Optimization of Heat Transfer and Fluid Flow Systems', in *the Proceedings of the COMSOL Conference 2009 Boston*, 2009.
[48] Y. Lv and S. Liu, 'Topology optimization and heat dissipation performance analysis of a micro-channel heat sink', *Meccanica*, vol. 53, no. 15, pp. 3693–3708, Dec. 2018 [Online]. Available: 10.1007/s11012-018-0918-z.
[49] H. Kobayashi et al., 'Freeform winglet design of fin-and-tube heat exchangers guided by topology optimization', *Applied Thermal Engineering*, vol. 161, p. 114020, Oct. 2019 [Online]. Available: 10.1016/j.applthermaleng.2019.114020.
[50] S. Zeng and P. S. Lee, 'Topology optimization of liquid-cooled microchannel heat sinks: An experimental and numerical study', *International Journal of Heat and Mass Transfer*, vol. 142, p. 118401, Oct. 2019 [Online]. Available: 10.1016/j.ijheatmasstransfer.2019.07.051.
[51] S. Yan et al., 'Topology optimization of microchannel heat sinks using a two-layer model', *International Journal of Heat and Mass Transfer*, vol. 143, p. 118462, Nov. 2019 [Online]. Available: 10.1016/j.ijheatmasstransfer.2019.118462.
[52] H. Li et al., 'Experimental and numerical investigation of liquid-cooled heat sinks designed by topology

optimization', *International Journal of Thermal Sciences*, vol. 146, p. 106065, Dec. 2019 [Online]. Available: 10.1016/j.ijthermalsci.2019.106065.
[53] B. Zhang and L. Gao, 'Topology optimization of convective heat transfer problems for non-Newtonian fluids', *Struct Multidisc Optim*, vol. 60, no. 5, pp. 1821–1840, Nov. 2019 [Online]. Available: 10.1007/s00158-019-02296-6.
[54] B. Zhang et al., 'Topology optimization design of nanofluid-cooled microchannel heat sink with temperature-dependent fluid properties', *Applied Thermal Engineering*, vol. 176, p. 115354, Jul. 2020 [Online]. Available: 10.1016/j.applthermaleng.2020.115354.
[55] X. Han et al., 'Topology optimization for spider web heat sinks for electronic cooling', *Applied Thermal Engineering*, vol. 195, p. 117154, Aug. 2021 [Online]. Available: 10.1016/j.applthermaleng.2021.117154.
[56] A. Liu et al., 'Study on the thermal and hydraulic performance of fin-and-tube heat exchanger based on topology optimization', *Applied Thermal Engineering*, vol. 197, p. 117380, Oct. 2021 [Online]. Available: 10.1016/j.applthermaleng.2021.117380.
[57] T. Zeng et al., 'Topology optimization of heat sinks for instantaneous chip cooling using a transient pseudo-3D thermofluid model', *International Journal of Heat and Mass Transfer*, vol. 154, p. 119681, Jun. 2020 [Online]. Available: 10.1016/j.ijheatmasstransfer.2020.119681.
[58] K. Yaji et al., 'Topology optimization in thermal-fluid flow using the lattice Boltzmann method', *Journal of Computational Physics*, vol. 307, pp. 355–377, Feb. 2016 [Online]. Available: 10.1016/j.jcp.2015.12.008.
[59] J. S. Lee et al., 'A topology optimization based design of a liquid-cooled heat sink with cylindrical pin fins having varying pitch', *International Journal of Heat and Mass Transfer*, vol. 172, p. 121172, Jun. 2021 [Online]. Available: 10.1016/j.ijheatmasstransfer.2021.121172.
[60] H. Li et al., 'Optimal design and thermal modelling for liquid-cooled heat sink based on multi-objective topology optimization: An experimental and numerical study', *International Journal of Heat and Mass Transfer*, vol. 144, p. 118638, Dec. 2019 [Online]. Available: 10.1016/j.ijheatmasstransfer.2019.118638.
[61] S. Qian et al., 'The influence of temperature dependent fluid properties on topology optimization of conjugate heat transfer', *International Journal of Thermal Sciences*, vol. 173, p. 107424, Mar. 2022 [Online]. Available: 10.1016/j.ijthermalsci.2021.107424.
[62] K. Yaji et al., 'Data-driven multifidelity topology design using a deep generative model: Application to forced convection heat transfer problems', *Computer Methods in Applied Mechanics and Engineering*, vol. 388, p. 114284, Jan. 2022 [Online]. Available: 10.1016/j.cma.2021.114284.
[63] X. Dong and X. Liu, 'Multi-objective optimization of heat transfer in microchannel for non-Newtonian fluid', *Chemical Engineering Journal*, vol. 412, p. 128594, May 2021 [Online]. Available: 10.1016/j.cej.2021.128594.
[64] G. Marck et al., 'Topology Optimization of Heat and Mass Transfer Problems: Laminar Flow', *Numerical Heat Transfer, Part B: Fundamentals*, vol. 63, no. 6, pp. 508–539, Jun. 2013 [Online]. Available: 10.1080/10407790.2013.772001.
[65] J. Alexandersen et al., 'Topology optimisation for natural convection problems: TOPOLOGY OPTIMISATION FOR NATURAL CONVECTION PROBLEMS', *Int. J. Numer. Meth. Fluids*, vol. 76, no. 10, pp. 699–721, Dec. 2014 [Online]. Available: 10.1002/fld.3954.
[66] X. Qian and E. M. Dede, 'Topology optimization of a coupled thermal-fluid system under a tangential thermal gradient constraint', *Struct Multidisc Optim*, vol. 54, no. 3, pp. 531–551, Sep. 2016 [Online]. Available: 10.1007/s00158-016-1421-6.
[67] J. Alexandersen et al., 'Large scale three-dimensional topology optimisation of heat sinks cooled by natural convection', *International Journal of Heat and Mass Transfer*, vol. 100, pp. 876–891, Sep. 2016 [Online]. Available: 10.1016/j.ijheatmasstransfer.2016.05.013.
[68] S. Qian et al., 'Topology optimization of fluid flow channel in cold plate for active phased array antenna', *Struct Multidisc Optim*, vol. 57, no. 6, pp. 2223–2232, Jun. 2018 [Online]. Available: 10.1007/s00158-017-1852-8.
[69] T. Lei et al., 'Investment casting and experimental testing of heat sinks designed by topology

optimization', *International Journal of Heat and Mass Transfer*, vol. 127, pp. 396–412, Dec. 2018 [Online]. Available: 10.1016/j.ijheatmasstransfer.2018.07.060.

[70] M. Yu et al., 'Topology optimization of thermal–fluid problem using the MMC-based approach', *Struct Multidisc Optim*, vol. 60, no. 1, pp. 151–165, Jul. 2019 [Online]. Available: 10.1007/s00158-019-02206-w.

[71] X. Dong and X. Liu, 'Multi-objective optimal design of microchannel cooling heat sink using topology optimization method', *Numerical Heat Transfer, Part A: Applications*, vol. 77, no. 1, pp. 90–104, Jan. 2020 [Online]. Available: 10.1080/10407782.2019.1682872.

[72] D. Hu et al., 'Numerical study on flow and heat transfer characteristics of microchannel designed using topological optimizations method', *Sci. China Technol. Sci.*, vol. 63, no. 1, pp. 105–115, Jan. 2020 [Online]. Available: 10.1007/s11431-019-1438-8.

[73] S. Sun et al., '3D topology optimization of heat sinks for liquid cooling', *Applied Thermal Engineering*, vol. 178, p. 115540, Sep. 2020 [Online]. Available: 10.1016/j.applthermaleng.2020.115540.

[74] B. Zhang et al., 'Design of nanofluid-cooled heat sink using topology optimization', *Chinese Journal of Aeronautics*, vol. 34, no. 2, pp. 301–317, Feb. 2021 [Online]. Available: 10.1016/j.cja.2020.05.023.

[75] T. Zhou et al., 'Study of the Performance of a Novel Radiator with Three Inlets and One Outlet Based on Topology Optimization', *Micromachines*, vol. 12, no. 6, p. 594, May 2021 [Online]. Available: 10.3390/mi12060594.

[76] X. Liu et al., 'Topology optimization of the manifold microchannels with triple-objective functions', *Numerical Heat Transfer, Part B: Fundamentals*, vol. 80, no. 5–6, pp. 89–114, Dec. 2021 [Online]. Available: 10.1080/10407790.2021.1946309.

[77] J. Zhao et al., 'Topology optimization of planar cooling channels using a three-layer thermofluid model in fully developed laminar flow problems', *Struct Multidisc Optim*, vol. 63, no. 6, pp. 2789–2809, Jun. 2021 [Online]. Available: 10.1007/s00158-021-02842-1.

[78] F. Chen et al., 'Topology optimization design and numerical analysis on cold plates for lithium-ion battery thermal management', *International Journal of Heat and Mass Transfer*, vol. 183, p. 122087, Feb. 2022 [Online]. Available: 10.1016/j.ijheatmasstransfer.2021.122087.

[79] L. Xie et al., 'Topology optimization of heat sink based on variable density method', *Energy Reports*, vol. 8, pp. 718–726, Apr. 2022 [Online]. Available: 10.1016/j.egyr.2021.11.214.

[80] S. Ghosh et al., 'Fluid-Thermal Topology Optimization of Gas Turbine Blade Internal Cooling Ducts', *Journal of Mechanical Design*, vol. 144, no. 5, p. 051703, May 2022 [Online]. Available: 10.1115/1.4053042.

[81] P. Huang et al., 'Pseudo 3D topology optimization of microchannel heat sink with an auxiliary objective', *International Journal of Heat and Mass Transfer*, vol. 187, p. 122526, May 2022 [Online]. Available: 10.1016/j.ijheatmasstransfer.2022.122526.

[82] M. Yu et al., 'A synergic topology optimization approach on distribution of cooling channels and diverse-intensity heat sources for liquid-cooled heat sink', *Struct Multidisc Optim*, vol. 65, no. 2, p. 48, Feb. 2022 [Online]. Available: 10.1007/s00158-021-03113-9.

[83] A. Zou et al., 'Topology optimization for a water-cooled heat sink in micro-electronics based on Pareto frontier', *Applied Thermal Engineering*, vol. 207, p. 118128, May 2022 [Online]. Available: 10.1016/j.applthermaleng.2022.118128.

[84] T. Zhou et al., 'A Novel Mini-Channel Heat Sink Design with Arc-Type Design Domain by Topology Optimization', *Micromachines*, vol. 13, no. 2, p. 180, Jan. 2022 [Online]. Available: 10.3390/mi13020180.

[85] S. D. Marshall and P. S. Lee, '3d Topology Optimisation of Liquid-Cooled Microchannel Heat Sinks', *SSRN Journal*, 2022[Online]. Availablehttps://www.ssrn.com/abstract=4031308[Accessed: 28February2022].

[86] K. Yeranee et al., 'Design of a Serpentine Cooling Channel Under Turbulent Flow Using Density-Based Topology Optimization', *SSRN Journal*, 2022[Online]. Availablehttps://www.ssrn.com/abstract=4001458[Accessed: 26February2022].

[87] G. Wang et al., 'Design and performance enhancement of thermal-fluid system based on topology optimization', *Applied Mathematical Modelling*, vol. 116, pp. 168–186, Apr. 2023 [Online]. Available:

10.1016/j.apm.2022.11.031.
[88] H. Wang et al., 'Deep-learning accelerating topology optimization of three-dimensional coolant channels for flow and heat transfer in a proton exchange membrane fuel cell', *Applied Energy*, vol. 352, p. 121889, Dec. 2023 [Online]. Available: 10.1016/j.apenergy.2023.121889.
[89] M.-S. Wu, 'Multi-objective topology optimization of cold plates featuring branched and streamlined mini-channels for thermal management system of lithium-ion battery module', *Journal of Energy Storage*, vol. 72, p. 108362, Nov. 2023 [Online]. Available: 10.1016/j.est.2023.108362.
[90] N. Adil et al., 'Rational design process for gas turbine exhaust to supercritical CO2 waste heat recovery heat exchanger using topology optimization', *Applied Thermal Engineering*, vol. 236, p. 121670, Jan. 2024 [Online]. Available: 10.1016/j.applthermaleng.2023.121670.
[91] S. Zhan et al., 'Effect of inlet and outlet positions on heat dissipation performance of lithium-ion battery cold plates: An analysis based on topology optimization', *International Journal of Heat and Mass Transfer*, vol. 215, p. 124436, Nov. 2023 [Online]. Available: 10.1016/j.ijheatmasstransfer.2023.124436.
[92] C. Sun et al., 'Thermal design of composite cold plates by topology optimization', *International Journal of Mechanical Sciences*, vol. 259, p. 108594, Dec. 2023 [Online]. Available: 10.1016/j.ijmecsci.2023.108594.
[93] C. Tang et al., 'Thermal Performance and Parametrical Analysis of Topologically-optimized Cross-flow Heat Sinks Integrated with Impact Jet', *Applied Thermal Engineering*, vol. 235, p. 121310, Nov. 2023 [Online]. Available: 10.1016/j.applthermaleng.2023.121310.
[94] T. Zhang et al., 'Topology optimization of regenerative cooling channel in non-uniform thermal environment of hypersonic engine', *Applied Thermal Engineering*, vol. 219, p. 119384, Jan. 2023 [Online]. Available: 10.1016/j.applthermaleng.2022.119384.
[95] D. Wang et al., 'Experimental and numerical study of plate heat exchanger based on topology optimization', *International Journal of Thermal Sciences*, vol. 195, p. 108659, Jan. 2024 [Online]. Available: 10.1016/j.ijthermalsci.2023.108659.
[96] Y. Xia et al., 'Numerical investigation of microchannel heat sinks with different inlets and outlets based on topology optimization', *Applied Energy*, vol. 330, p. 120335, Jan. 2023 [Online]. Available: 10.1016/j.apenergy.2022.120335.
[97] Q. Zhong et al., 'A comprehensive numerical study based on topology optimization for cooling plates thermal design of battery packs', *Applied Thermal Engineering*, vol. 236, p. 121918, Jan. 2024 [Online]. Available: 10.1016/j.applthermaleng.2023.121918.
[98] B. Rogié and C. S. Andreasen, 'Design complexity tradeoffs in topology optimization of forced convection laminar flow heat sinks', *Struct Multidisc Optim*, vol. 66, no. 1, p. 6, Jan. 2023 [Online]. Available: 10.1007/s00158-022-03449-w.
[99] D. S. Makhija and P. S. Beran, 'Concurrent shape and topology optimization for steady conjugate heat transfer', *Struct Multidisc Optim*, vol. 59, no. 3, pp. 919–940, Mar. 2019 [Online]. Available: 10.1007/s00158-018-2110-4.
[100] X. Zhao et al., 'A "poor man's approach" to topology optimization of cooling channels based on a Darcy flow model', *International Journal of Heat and Mass Transfer*, vol. 116, pp. 1108–1123, Jan. 2018 [Online]. Available: 10.1016/j.ijheatmasstransfer.2017.09.090.
[101] E. A. Kontoleontos et al., 'Adjoint-based constrained topology optimization for viscous flows, including heat transfer', *Engineering Optimization*, vol. 45, no. 8, pp. 941–961, Aug. 2013 [Online]. Available: 10.1080/0305215X.2012.717074.
[102] E. M. Dede, 'Optimization and Design of a Multipass Branching Microchannel Heat Sink for Electronics Cooling', *Journal of Electronic Packaging*, vol. 134, no. 4, p. 041001, Dec. 2012 [Online]. Available: 10.1115/1.4007159.
[103] D. Ramalingom et al., 'A new interpolation technique to deal with fluid-porous media interfaces for topology optimization of heat transfer', *Computers & Fluids*, vol. 168, pp. 144–158, May 2018 [Online]. Available: 10.1016/j.compfluid.2018.04.005.
[104] J. Asmussen et al., 'A "poor man's" approach to topology optimization of natural convection problems',

Struct Multidisc Optim, vol. 59, no. 4, pp. 1105–1124, Apr. 2019 [Online]. Available: 10.1007/s00158-019-02215-9.

[105] M. Pietropaoli et al., ‘Three-dimensional fluid topology optimization for heat transfer’, *Struct Multidisc Optim*, vol. 59, no. 3, pp. 801–812, Mar. 2019 [Online]. Available: 10.1007/s00158-018-2102-4.

[106] M. Pietropaoli et al., ‘Three-Dimensional Fluid Topology Optimization and Validation of a Heat Exchanger With Turbulent Flow’, in *Volume 7A: Heat Transfer*, Virtual, Online, 2020, p. V07AT15A006[Online]. Availablehttps://asmedigitalcollection.asme.org/GT/proceedings/GT2020/84164/Virtual,%20Online/1094945[Accessed: 10November2021].

[107] A. Ghasemi and A. Elham, ‘Multi-objective topology optimization of pin-fin heat exchangers using spectral and finite-element methods’, *Struct Multidisc Optim*, vol. 64, no. 4, pp. 2075–2095, Oct. 2021 [Online]. Available: 10.1007/s00158-021-02964-6.

[108] G. H. Yoon, ‘Topological design of heat dissipating structure with forced convective heat transfer’, *J Mech Sci Technol*, vol. 24, no. 6, pp. 1225–1233, Jun. 2010 [Online]. Available: 10.1007/s12206-010-0328-1.

[109] M. S. Santhanakrishnan et al., ‘Performance assessment of density and level-set topology optimisation methods for three dimensional heat sink design’, *Journal of Algorithms & Computational Technology*, vol. 12, no. 3, pp. 273–287, Sep. 2018 [Online]. Available: 10.1177/1748301818779019.

[110] S. A. Lurie et al., ‘Topology optimization of the wick geometry in a flat plate heat pipe’, *International Journal of Heat and Mass Transfer*, vol. 128, pp. 239–247, Jan. 2019 [Online]. Available: 10.1016/j.ijheatmasstransfer.2018.08.125.

[111] S. Jahan et al., ‘Thermo-fluid Topology Optimization and Experimental Study of Conformal Cooling Channels for 3D Printed Plastic Injection Molds’, *Procedia Manufacturing*, vol. 34, pp. 631–639, 2019 [Online]. Available: 10.1016/j.promfg.2019.06.120.

[112] P. Francisco et al., ‘Multi-objective and multi-load topology optimization and experimental validation of homogenized coupled fluid flow and heat transfer and structural stiffness’, *Struct Multidisc Optim*, vol. 62, no. 5, pp. 2571–2598, Nov. 2020 [Online]. Available: 10.1007/s00158-020-02625-0.

[113] G. Lee et al., ‘Topology optimization of a heat sink with an axially uniform cross-section cooled by forced convection’, *International Journal of Heat and Mass Transfer*, vol. 168, p. 120732, Apr. 2021 [Online]. Available: 10.1016/j.ijheatmasstransfer.2020.120732.

[114] T. L. E. Tang et al., ‘Multi-Physics Topology Optimization for Thermal-Flow Problems Applied to Additively Manufactured Heat Exchangers’, in *Volume 2D: Turbomachinery — Multidisciplinary Design Approaches, Optimization, and Uncertainty Quantification; Radial Turbomachinery Aerodynamics; Unsteady Flows in Turbomachinery*, Virtual, Online, 2021, p. V02DT36A019[Online]. Availablehttps://asmedigitalcollection.asme.org/GT/proceedings/GT2021/84935/V02DT36A019/1119851[Accessed: 10November2021].

[115] F. Navah et al., ‘Thermofluid topology optimization for cooling channel design’, *Applied Thermal Engineering*, vol. 236, p. 121317, Jan. 2024 [Online]. Available: 10.1016/j.applthermaleng.2023.121317.

[116] R. Tawk et al., ‘Topology optimization of heat and mass transfer problems in two fluids—one solid domains’, *Numerical Heat Transfer, Part B: Fundamentals*, vol. 76, no. 3, pp. 130–151, Sep. 2019 [Online]. Available: 10.1080/10407790.2019.1644919.

[117] L. C. Høghøj et al., ‘Topology optimization of two fluid heat exchangers’, *International Journal of Heat and Mass Transfer*, vol. 163, p. 120543, Dec. 2020 [Online]. Available: 10.1016/j.ijheatmasstransfer.2020.120543.

[118] M. Troya et al., ‘Two Dimensional Topology Optimization of Heat Exchangers with the Density and Level-Set Methods’, in *14th WCCM-ECCOMAS Congress*, 2021[Online]. Availablehttps://www.scipedia.com/public/Troya_et_al_2021a[Accessed: 15November2021].

[119] H. Kobayashi et al., ‘Topology design of two-fluid heat exchange’, *Struct Multidisc Optim*, vol. 63, no. 2, pp. 821–834, Feb. 2021 [Online]. Available: 10.1007/s00158-020-02736-8.

[120] G. Lee et al., ‘Dual-fluid topology optimization of printed-circuit heat exchanger with low-pumping-power design’, *Case Studies in Thermal Engineering*, vol. 49, p. 103318, Sep. 2023 [Online]. Available: 10.1016/j.csite.2023.103318.

[121] C. F. Hvejsel and E. Lund, ‘Material interpolation schemes for unified topology and multi-material optimization’, *Struct Multidisc Optim*, vol. 43, no. 6, pp. 811–825, Jun. 2011 [Online]. Available: 10.1007/s00158-011-0625-z.

[122] O. Sigmund and J. Petersson, ‘Numerical instabilities in topology optimization: A survey on procedures dealing with checkerboards, mesh-dependencies and local minima’, *Structural Optimization*, vol. 16, no. 1, pp. 68–75, Aug. 1998 [Online]. Available: 10.1007/BF01214002.

[123] F. Wang et al., ‘On projection methods, convergence and robust formulations in topology optimization’, *Struct Multidisc Optim*, vol. 43, no. 6, pp. 767–784, Jun. 2011 [Online]. Available: 10.1007/s00158-010-0602-y.

[124] N. Vermaak et al., ‘Topological Optimization with Interfaces’, in *Architectured Materials in Nature and Engineering*, vol. 282, Y. Estrin, Y. Bréchet, J. Dunlop, and P. Fratzl, Eds. Cham: Springer International Publishing, 2019, pp. 173–193[Online]. Availablehttp://link.springer.com/10.1007/978-3-030-11942-3_6[Accessed: 30September2021].

[125] S. Osher and J. A. Sethian, ‘Fronts propagating with curvature-dependent speed: Algorithms based on Hamilton-Jacobi formulations’, *Journal of Computational Physics*, vol. 79, no. 1, pp. 12–49, Nov. 1988 [Online]. Available: 10.1016/0021-9991(88)90002-2.

[126] J. A. Sethian and A. Wiegmann, ‘Structural Boundary Design via Level Set and Immersed Interface Methods’, *Journal of Computational Physics*, vol. 163, no. 2, pp. 489–528, Sep. 2000 [Online]. Available: 10.1006/jcph.2000.6581.

[127] M. Y. Wang et al., ‘A level set method for structural topology optimization’, *Computer Methods in Applied Mechanics and Engineering*, vol. 192, no. 1–2, pp. 227–246, Jan. 2003 [Online]. Available: 10.1016/S0045-7825(02)00559-5.

[128] G. Allaire et al., ‘Structural optimization using sensitivity analysis and a level-set method’, *Journal of Computational Physics*, vol. 194, no. 1, pp. 363–393, Feb. 2004 [Online]. Available: 10.1016/j.jcp.2003.09.032.

[129] M. Yoshimura et al., ‘Topology optimization of fluid problems using genetic algorithm assisted by the Kriging model: TOPOLOGY OPTIMIZATION USING A KRIGING-BASED GENETIC ALGORITHM’, *Int. J. Numer. Meth. Engng*, vol. 109, no. 4, pp. 514–532, Jan. 2017 [Online]. Available: 10.1002/nme.5295.

[130] F. Dugast et al., ‘Topology optimization of thermal fluid flows with an adjoint Lattice Boltzmann Method’, *Journal of Computational Physics*, vol. 365, pp. 376–404, Jul. 2018 [Online]. Available: 10.1016/j.jcp.2018.03.040.

[131] S. Kambampati et al., ‘Level Set Topology Optimization of Load Carrying Heat Exchangers’, in *AIAA Scitech 2020 Forum*, Orlando, FL, 2020[Online]. Availablehttps://arc.aiaa.org/doi/10.2514/6.2020-0891[Accessed: 7October2021].

[132] F. Feppon et al., ‘Body-fitted topology optimization of 2D and 3D fluid-to-fluid heat exchangers’, *Computer Methods in Applied Mechanics and Engineering*, vol. 376, p. 113638, Apr. 2021 [Online]. Available: 10.1016/j.cma.2020.113638.

[133] P. Mario et al., ‘Optimization of Fin Topology for Heat Transfer Within Lightweight Plate-Fin Heat Exchangers’, *Journal of Thermophysics and Heat Transfer*, vol. 35, no. 4, pp. 677–685, Oct. 2021 [Online]. Available: 10.2514/1.T6121.

[134] K. Yaji et al., ‘A topology optimization method for a coupled thermal–fluid problem using level set boundary expressions’, *International Journal of Heat and Mass Transfer*, vol. 81, pp. 878–888, Feb. 2015 [Online]. Available: 10.1016/j.ijheatmasstransfer.2014.11.005.

[135] P. Coffin and K. Maute, ‘A level-set method for steady-state and transient natural convection problems’, *Struct Multidisc Optim*, vol. 53, no. 5, pp. 1047–1067, May 2016 [Online]. Available: 10.1007/s00158-015-1377-y.

[136] Y. Sato et al., ‘An Optimum Design Method for a Thermal-Fluid Device Incorporating Multiobjective Topology Optimization With an Adaptive Weighting Scheme’, *Journal of Mechanical Design*, vol. 140, no. 3, p. 031402, Mar. 2018 [Online]. Available: 10.1115/1.4038209.

[137] H. Li et al., ‘Optimum design and thermal modeling for 2D and 3D natural convection problems

incorporating level set-based topology optimization with body-fitted mesh†', *Numerical Meth Engineering*, p. nme.6923, Jan. 2022 [Online]. Available: 10.1002/nme.6923.
[138] Y. Lin et al., 'A stabilized parametric level-set XFEM topology optimization method for thermal-fluid problem', *Numerical Meth Engineering*, vol. 123, no. 4, pp. 924–952, Feb. 2022 [Online]. Available: 10.1002/nme.6883.
[139] D. Chen et al., 'Multi-objective topology optimization of heat transfer surface using level-set method and adaptive mesh refinement in OpenFOAM', *International Journal of Heat and Mass Transfer*, vol. 221, p. 125099, Apr. 2024 [Online]. Available: 10.1016/j.ijheatmasstransfer.2023.125099.
[140] J. Luo et al., 'Topology optimization of convective heat transfer by the lattice Boltzmann method', *Numerical Methods in Fluids*, vol. 95, no. 3, pp. 421–452, Mar. 2023 [Online]. Available: 10.1002/fld.5153.
[141] T. Zhang et al., 'Level set-based topology optimization for thermal-fluid system based on the radial basis functions', *Applied Mathematical Modelling*, vol. 113, pp. 144–159, Jan. 2023 [Online]. Available: 10.1016/j.apm.2022.09.005.
[142] X. Li et al., 'Heat transfer augmentation in microchannel heat sink based on isogeometric topology optimization framework', *Applied Mathematical Modelling*, vol. 104, pp. 163–187, Apr. 2022 [Online]. Available: 10.1016/j.apm.2021.11.021.
[143] N. P. van Dijk et al., 'Level-set methods for structural topology optimization: a review', *Struct Multidisc Optim*, vol. 48, no. 3, pp. 437–472, Sep. 2013 [Online]. Available: 10.1007/s00158-013-0912-y.
[144] G. Fabbri, 'A genetic algorithm for fin profile optimization', *International Journal of Heat and Mass Transfer*, vol. 40, no. 9, pp. 2165–2172, Jun. 1997 [Online]. Available: 10.1016/S0017-9310(96)00294-3.
[145] E. Duplain and B. R. Baliga, 'Computational optimization of the thermal performance of internally finned ducts', *International Journal of Heat and Mass Transfer*, vol. 52, no. 17–18, pp. 3929–3942, Aug. 2009 [Online]. Available: 10.1016/j.ijheatmasstransfer.2009.03.030.
[146] H. Moon et al., 'Heat Transfer Enhancement of Single-Phase Internal Flows using Shape Optimization and Additively Manufactured Flow Structures', *International Journal of Heat and Mass Transfer*, vol. 177, p. 121510, Oct. 2021 [Online]. Available: 10.1016/j.ijheatmasstransfer.2021.121510.
[147] P. Rostami and J. Marzbanrad, 'Cooperative coevolutionary topology optimization using moving morphable components', *Engineering Optimization*, vol. 53, no. 6, pp. 962–983, Jun. 2021 [Online]. Available: 10.1080/0305215X.2020.1759579.
[148] B. S. Mekki et al., 'Genetic algorithm based topology optimization of heat exchanger fins used in aerospace applications', *International Journal of Heat and Mass Transfer*, vol. 170, p. 121002, May 2021 [Online]. Available: 10.1016/j.ijheatmasstransfer.2021.121002.
[149] K. Shimoyama and A. Komiya, 'Multi-objective Bayesian topology optimization of a lattice-structured heat sink in natural convection', *Struct Multidisc Optim*, vol. 65, no. 1, p. 1, Jan. 2022 [Online]. Available: 10.1007/s00158-021-03092-x.
[150] A. Hrennikoff, 'Solution of Problems of Elasticity by the Framework Method', *Journal of Applied Mechanics*, vol. 8, no. 4, pp. A169–A175, Dec. 1941 [Online]. Available: 10.1115/1.4009129.
[151] D. McHenry, 'Discussion: "Solution of Problems of Elasticity by the Framework Method" (Hrennikoff, A., 1941, ASME J. Appl. Mech., 8, pp. A169–A175)', *Journal of Applied Mechanics*, vol. 9, no. 3, pp. A144–A145, Sep. 1942 [Online]. Available: 10.1115/1.4009210.
[152] S. R. Idelsohn and E. Oñate, 'Finite volumes and finite elements: Two "good friends"', *Int. J. Numer. Meth. Engng.*, vol. 37, no. 19, pp. 3323–3341, Oct. 1994 [Online]. Available: 10.1002/nme.1620371908.
[153] G. Dhatt et al., *Finite Element Method.* London: Wiley, 2013[Online]. Availablehttp://public.ebookcentral.proquest.com/choice/publicfullrecord.aspx?p=1120636[Accessed: 9November2021].
[154] M. Zhou et al., 'Industrial application of topology optimization for combined conductive and convective heat transfer problems', *Struct Multidisc Optim*, vol. 54, no. 4, pp. 1045–1060, Oct. 2016 [Online]. Available: 10.1007/s00158-016-1433-2.
[155] K. R. Saviers et al., 'Design and validation of topology optimized heat exchangers', in *AIAA Scitech 2019*

Forum, San Diego, California, 2019[Online]. Availablehttps://arc.aiaa.org/doi/10.2514/6.2019-1465[Accessed: 8October2021].

[156] T. Li et al., 'Design of an internally cooled turning tool based on topology optimization and CFD simulation', *Int J Adv Manuf Technol*, vol. 91, no. 1–4, pp. 1327–1337, Jul. 2017 [Online]. Available: 10.1007/s00170-016-9804-9.

[157] L. Noël and K. Maute, 'XFEM level set-based topology optimization for turbulent conjugate heat transfer problems', *Struct Multidisc Optim*, vol. 66, no. 1, p. 2, Jan. 2023 [Online]. Available: 10.1007/s00158-022-03353-3.

[158] L. Bush and V. Ginting, 'On the Application of the Continuous Galerkin Finite Element Method for Conservation Problems', *SIAM J. Sci. Comput.*, vol. 35, no. 6, pp. A2953–A2975, Jan. 2013 [Online]. Available: 10.1137/120900393.

[159] T. E. Bruns, 'Topology optimization of convection-dominated, steady-state heat transfer problems', *International Journal of Heat and Mass Transfer*, vol. 50, no. 15–16, pp. 2859–2873, Jul. 2007 [Online]. Available: 10.1016/j.ijheatmasstransfer.2007.01.039.

[160] P. W. McDonald, 'The Computation of Transonic Flow Through Two-Dimensional Gas Turbine Cascades', in *ASME 1971 International Gas Turbine Conference and Products Show*, Houston, Texas, USA, 1971, p. V001T01A089[Online]. Availablehttps://asmedigitalcollection.asme.org/GT/proceedings/GT1971/79825/Houston,%20Texas,%20USA/234506[Accessed: 21September2021].

[161] A. W. Rizzi and M. Inouye, 'Time-Split Finite-Volume Method for Three-Dimensional Blunt-Body Flow', *AIAA Journal*, vol. 11, no. 11, pp. 1478–1485, Nov. 1973 [Online]. Available: 10.2514/3.50614.

[162] R. Eymard et al., 'Finite volume methods', in *Handbook of Numerical Analysis*, vol. 7, Elsevier, 2000, pp. 713–1018[Online]. Availablehttps://linkinghub.elsevier.com/retrieve/pii/S1570865900070058[Accessed: 2October2021].

[163] F. Moukalled et al., *The Finite Volume Method in Computational Fluid Dynamics: An Advanced Introduction with OpenFOAM® and Matlab*, vol. 113. Cham: Springer International Publishing, 2016[Online]. Availablehttp://link.springer.com/10.1007/978-3-319-16874-6[Accessed: 9October2021].

[164] A. Gersborg-Hansen et al., 'Topology optimization of heat conduction problems using the finite volume method', *Struct Multidisc Optim*, vol. 31, no. 4, pp. 251–259, Apr. 2006 [Online]. Available: 10.1007/s00158-005-0584-3.

[165] Z. J. Wang et al., 'High-order CFD methods: current status and perspective: HIGH-ORDER CFD METHODS', *Int. J. Numer. Meth. Fluids*, vol. 72, no. 8, pp. 811–845, Jul. 2013 [Online]. Available: 10.1002/fld.3767.

[166] A. R. Khoei, *Extended finite element method: theory and applications*. Chichester, West Sussex: John Wiley & Sons, Inc, 2015.

[167] A. Riccio et al., 'Robustness of XFEM Method for the Simulation of Cracks Propagation in Fracture Mechanics Problems', *American Journal of Engineering and Applied Sciences*, vol. 9, no. 3, pp. 599–610, Mar. 2016 [Online]. Available: 10.3844/ajeassp.2016.599.610.

[168] T. Belytschko and T. BLACK, 'Elastic crack growth in finite elements with minimal remeshing', *International Journal for Numerical Methods in Engineering*, vol. 45, no. 5, pp. 601–620, 1999.

[169] R. Merle and J. Dolbow, 'Solving thermal and phase change problems with the eXtended finite element method', *Computational Mechanics*, vol. 28, no. 5, pp. 339–350, May 2002 [Online]. Available: 10.1007/s00466-002-0298-y.

[170] A. A. Mohamad, *Lattice Boltzmann Method: Fundamentals and Engineering Applications with Computer Codes*. London: Springer London, 2019[Online]. Availablehttp://link.springer.com/10.1007/978-1-4471-7423-3[Accessed: 9November2021].

[171] G. R. McNamara and G. Zanetti, 'Use of the Boltzmann Equation to Simulate Lattice-Gas Automata', *Phys. Rev. Lett.*, vol. 61, no. 20, pp. 2332–2335, Nov. 1988 [Online]. Available: 10.1103/PhysRevLett.61.2332.

[172] J. Zhang, 'Lattice Boltzmann method for microfluidics: models and applications', *Microfluid Nanofluid*, vol. 10, no. 1, pp. 1–28, Jan. 2011 [Online]. Available: 10.1007/s10404-010-0624-1.

[173] T. Krüger et al., *The Lattice Boltzmann Method: Principles and Practice*. Cham: Springer International

Publishing, 2017[Online]. Availablehttp://link.springer.com/10.1007/978-3-319-44649-3[Accessed: 9January2022].
[174] D. Tarlet et al., 'Entropy generation analysis of a mini heat exchanger for heat transfer intensification', *Experimental Thermal and Fluid Science*, vol. 53, pp. 119–126, Feb. 2014 [Online]. Available: 10.1016/j.expthermflusci.2013.11.016.
[175] M. Gunzburger, 'Adjoint Equation-Based Methods for Control Problems in Incompressible, Viscous Flows', *Flow, Turbulence and Combustion*, vol. 65, no. 3/4, pp. 249–272, 2000 [Online]. Available: 10.1023/A:1011455900396.
[176] M. B. Giles and N. A. Pierce, 'An Introduction to the Adjoint Approach to Design', *Flow, Turbulence and Combustion*, vol. 65, no. 3/4, pp. 393–415, 2000 [Online]. Available: 10.1023/A:1011430410075.
[177] K. Svanberg, 'The method of moving asymptotes—a new method for structural optimization', *Int. J. Numer. Meth. Engng.*, vol. 24, no. 2, pp. 359–373, Feb. 1987 [Online]. Available: 10.1002/nme.1620240207.
[178] K. Svanberg, 'A Class of Globally Convergent Optimization Methods Based on Conservative Convex Separable Approximations', *SIAM J. Optim.*, vol. 12, no. 2, pp. 555–573, Jan. 2002 [Online]. Available: 10.1137/S1052623499362822.
[179] J. S. Arora, *Introduction to Optimum Design*. 2004.
[180] P. T. Boggs and J. W. Tolle, 'Sequential Quadratic Programming', *Acta Numerica*, vol. 4, pp. 1–51, Jan. 1995 [Online]. Available: 10.1017/S0962492900002518.
[181] J. C. Meza, 'Steepest descent', *WIREs Comp Stat*, vol. 2, no. 6, pp. 719–722, Nov. 2010 [Online]. Available: 10.1002/wics.117.
[182] SIMULIA-Tosca Manual, Dassault Systemes Simulia, 2015.
[183] T. Yamada et al., 'A topology optimization method based on the level set method incorporating a fictitious interface energy', *Computer Methods in Applied Mechanics and Engineering*, vol. 199, no. 45–48, pp. 2876–2891, Nov. 2010 [Online]. Available: 10.1016/j.cma.2010.05.013.
[184] F. Feppon et al., 'Null space gradient flows for constrained optimization with applications to shape optimization', *ESAIM: COCV*, vol. 26, p. 90, 2020 [Online]. Available: 10.1051/cocv/2020015.
[185] G. Venter, 'Review of Optimization Techniques', in *Encyclopedia of Aerospace Engineering*, R. Blockley and W. Shyy, Eds. Chichester, UK: John Wiley & Sons, Ltd, 2010, p. eae495[Online]. Availablehttps://onlinelibrary.wiley.com/doi/10.1002/9780470686652.eae495[Accessed: 11October2021].
[186] J. Fliege and A. I. F. Vaz, 'A Method for Constrained Multiobjective Optimization Based on SQP Techniques', *SIAM J. Optim.*, vol. 26, no. 4, pp. 2091–2119, Jan. 2016 [Online]. Available: 10.1137/15M1016424.
[187] J. H. Holland, 'Genetic Algorithms', *Sci Am*, vol. 267, no. 1, pp. 66–72, Jul. 1992 [Online]. Available: 10.1038/scientificamerican0792-66.
[188] A. Lipowski and D. Lipowska, 'Roulette-wheel selection via stochastic acceptance', *Physica A: Statistical Mechanics and its Applications*, vol. 391, no. 6, pp. 2193–2196, Mar. 2012 [Online]. Available: 10.1016/j.physa.2011.12.004.
[189] S. Mirjalili, 'Genetic Algorithm', in *Evolutionary Algorithms and Neural Networks*, vol. 780, Cham: Springer International Publishing, 2019, pp. 43–55[Online]. Availablehttp://link.springer.com/10.1007/978-3-319-93025-1_4[Accessed: 13October2021].
[190] Chang Wook Ahn and R. S. Ramakrishna, 'Elitism-based compact genetic algorithms', *IEEE Trans. Evol. Computat.*, vol. 7, no. 4, pp. 367–385, Aug. 2003 [Online]. Available: 10.1109/TEVC.2003.814633.
[191] L. Gosselin et al., 'Review of utilization of genetic algorithms in heat transfer problems', *International Journal of Heat and Mass Transfer*, vol. 52, no. 9–10, pp. 2169–2188, Apr. 2009 [Online]. Available: 10.1016/j.ijheatmasstransfer.2008.11.015.
[192] Y. Li et al., 'A genetic algorithm-based topology optimization (GATO) method for convective cooling of a heating surface with multiple heat sources', *International Journal of Heat and Mass Transfer*, vol. 224, p. 125349, Jun. 2024 [Online]. Available: 10.1016/j.ijheatmasstransfer.2024.125349.

[193] Y. Haimes et al., ‘On a Bicriterion Formulation of the Problems of Integrated System Identification and System Optimization’, *IEEE Trans. Syst., Man, Cybern.*, vol. SMC-1, no. 3, pp. 296–297, Jul. 1971 [Online]. Available: 10.1109/TSMC.1971.4308298.

[194] H. J. Kushner, ‘A New Method of Locating the Maximum Point of an Arbitrary Multipeak Curve in the Presence of Noise’, *Journal of Basic Engineering*, vol. 86, no. 1, pp. 97–106, Mar. 1964 [Online]. Available: 10.1115/1.3653121.

[195] A. G. Zhilinskas, ‘Single-step Bayesian search method for an extremum of functions of a single variable’, *Cybern Syst Anal*, vol. 11, no. 1, pp. 160–166, 1976 [Online]. Available: 10.1007/BF01069961.

[196] J. Mockus, *Bayesian Approach to Global Optimization: Theory and Applications*, vol. 37. Dordrecht: Springer Netherlands, 1989[Online]. Availablehttp://link.springer.com/10.1007/978-94-009-0909-0[Accessed: 14October2021].

[197] D. R. Jones et al., ‘Efficient Global Optimization of Expensive Black-Box Functions’, *Journal of Global Optimization*, vol. 13, no. 4, pp. 455–492, 1998 [Online]. Available: 10.1023/A:1008306431147.

[198] P. I. Frazier, ‘Bayesian Optimization’, in *Recent Advances in Optimization and Modeling of Contemporary Problems*, E. Gel, L. Ntaimo, D. Shier, and H. J. Greenberg, Eds. INFORMS, 2018, pp. 255–278[Online]. Availablehttp://pubsonline.informs.org/doi/10.1287/educ.2018.0188[Accessed: 14October2021].

[199] A. Klein et al., ‘Towards efficient Bayesian Optimization for Big Data’, 2015.

[200] M. E. Lynch et al., ‘Machine Learning to Aid Tuning of Numerical Parameters in Topology Optimization’, *Journal of Mechanical Design*, vol. 141, no. 11, p. 114502, Nov. 2019 [Online]. Available: 10.1115/1.4044228.

[201] J. Sacks et al., ‘Design and Analysis of Computer Experiments’, *Statist. Sci.*, vol. 4, no. 4, Nov. 1989[Online]. Availablehttps://projecteuclid.org/journals/statistical-science/volume-4/issue-4/Design-and-Analysis-of-Computer-Experiments/10.1214/ss/1177012413.full[Accessed: 11January2022].

[202] E. Merrill et al., ‘An Empirical Study of Bayesian Optimization: Acquisition Versus Partition’, *Journal of Machine Learning Research,22*, 2021.

[203] X. Garcia-Santiago et al., ‘Bayesian Optimization With Improved Scalability and Derivative Information for Efficient Design of Nanophotonic Structures’, *J. Lightwave Technol.*, vol. 39, no. 1, pp. 167–177, Jan. 2021 [Online]. Available: 10.1109/JLT.2020.3023450.

[204] S. Ford and M. Despeisse, ‘Additive manufacturing and sustainability: an exploratory study of the advantages and challenges’, *Journal of Cleaner Production*, vol. 137, pp. 1573–1587, Nov. 2016 [Online]. Available: 10.1016/j.jclepro.2016.04.150.

[205] M. Attaran, ‘The rise of 3-D printing: The advantages of additive manufacturing over traditional manufacturing’, *Business Horizons*, vol. 60, no. 5, pp. 677–688, Sep. 2017 [Online]. Available: 10.1016/j.bushor.2017.05.011.

[206] M. Petrovic et al., ‘Numerical and experimental performance investigation of a heat exchanger designed using topologically optimized fins’, *Applied Thermal Engineering*, vol. 218, p. 119232, Jan. 2023 [Online]. Available: 10.1016/j.applthermaleng.2022.119232.

[207] X. Liang et al., ‘An isogeometric analysis-based topology optimization framework for 2D cross-flow heat exchangers with manufacturability constraints’, *Engineering with Computers*, vol. 38, no. 6, pp. 4829–4852, Dec. 2022 [Online]. Available: 10.1007/s00366-022-01716-4.

[208] J. Alexandersen, ‘Topology Optimisation for Axisymmetric Convection Problems’, Technical University of Denmark, 2011a[Online]. Availablehttps://backend.orbit.dtu.dk/ws/portalfiles/portal/155591760/Alexandersen2011a.pdf.

[209] J. Wang et al., ‘Study of the influence of objective functions on the topology optimization design of battery cold plate’, *Applied Thermal Engineering*, vol. 226, p. 120326, May 2023 [Online]. Available: 10.1016/j.applthermaleng.2023.120326.

[210] A. B. Farimani et al., ‘Deep Learning the Physics of Transport Phenomena’, *arXiv:1709.02432 [physics]*, Sep. 2017[Online]. Availablehttp://arxiv.org/abs/1709.02432[Accessed: 9September2021].

[211] B. Kwon et al., ‘Machine learning for heat transfer correlations’, *International Communications in Heat and Mass Transfer*, vol. 116, p. 104694, Jul. 2020 [Online]. Available:

10.1016/j.icheatmasstransfer.2020.104694.
[212] L. Zhou et al., 'Machine learning algorithms to predict flow condensation heat transfer coefficient in mini/micro-channel utilizing universal data', *International Journal of Heat and Mass Transfer*, vol. 162, p. 120351, Dec. 2020 [Online]. Available: 10.1016/j.ijheatmasstransfer.2020.120351.
[213] G. Zhu et al., 'Machine learning based approach for the prediction of flow boiling/condensation heat transfer performance in mini channels with serrated fins', *International Journal of Heat and Mass Transfer*, vol. 166, p. 120783, Feb. 2021 [Online]. Available: 10.1016/j.ijheatmasstransfer.2020.120783.
[214] I. Sosnovik and I. Oseledets, 'Neural networks for topology optimization', *Russian Journal of Numerical Analysis and Mathematical Modelling*, vol. 34, no. 4, pp. 215–223, Aug. 2019 [Online]. Available: 10.1515/rnam-2019-0018.
[215] D. W. Abueidda et al., 'Topology optimization of 2D structures with nonlinearities using deep learning', *Computers & Structures*, vol. 237, p. 106283, Sep. 2020 [Online]. Available: 10.1016/j.compstruc.2020.106283.
[216] A. Chandrasekhar and K. Suresh, 'TOuNN: Topology Optimization using Neural Networks', *Struct Multidisc Optim*, vol. 63, no. 3, pp. 1135–1149, Mar. 2021 [Online]. Available: 10.1007/s00158-020-02748-4.
[217] H. Chi et al., 'Universal machine learning for topology optimization', *Computer Methods in Applied Mechanics and Engineering*, vol. 375, p. 112739, Mar. 2021 [Online]. Available: 10.1016/j.cma.2019.112739.
[218] D. P. Kingma and M. Welling, 'Auto-Encoding Variational Bayes', *arXiv:1312.6114 [cs, stat]*, May 2014[Online]. Availablehttp://arxiv.org/abs/1312.6114[Accessed: 27December2021].
[219] Q. Lin et al., 'Investigation into the topology optimization for conductive heat transfer based on deep learning approach', *International Communications in Heat and Mass Transfer*, vol. 97, pp. 103–109, Oct. 2018 [Online]. Available: 10.1016/j.icheatmasstransfer.2018.07.001.
[220] W. H. A. Schilders et al., Eds., *Model Order Reduction: Theory, Research Aspects and Applications*, vol. 13. Berlin, Heidelberg: Springer Berlin Heidelberg, 2008[Online]. Availablehttp://link.springer.com/10.1007/978-3-540-78841-6[Accessed: 30October2021].
[221] B. Moore, 'Principal component analysis in linear systems: Controllability, observability, and model reduction', *IEEE Trans. Automat. Contr.*, vol. 26, no. 1, pp. 17–32, Feb. 1981 [Online]. Available: 10.1109/TAC.1981.1102568.
[222] L. Sirovich, 'Turbulence and the dynamics of coherent structures. I. Coherent structures', *Quart. Appl. Math.*, vol. 45, no. 3, pp. 561–571, Oct. 1987 [Online]. Available: 10.1090/qam/910462.
[223] K. Glover, 'All optimal Hankel-norm approximations of linear multivariable systems and their *L* , ∞ -error bounds†', *International Journal of Control*, vol. 39, no. 6, pp. 1115–1193, Jun. 1984 [Online]. Available: 10.1080/00207178408933239.
[224] M. Behbahani-Nejad and Y. Shekari, 'The accuracy and efficiency of a reduced-order model for transient flow analysis in gas pipelines', *Journal of Petroleum Science and Engineering*, vol. 73, no. 1–2, pp. 13–19, Aug. 2010 [Online]. Available: 10.1016/j.petrol.2010.05.001.
[225] T. Lassila et al., 'Model Order Reduction in Fluid Dynamics: Challenges and Perspectives', in *Reduced Order Methods for Modeling and Computational Reduction*, A. Quarteroni and G. Rozza, Eds. Cham: Springer International Publishing, 2014, pp. 235–273[Online]. Availablehttp://link.springer.com/10.1007/978-3-319-02090-7_9[Accessed: 31October2021].
[226] X. Guo et al., 'Doing Topology Optimization Explicitly and Geometrically—A New Moving Morphable Components Based Framework', *Journal of Applied Mechanics*, vol. 81, no. 8, p. 081009, Aug. 2014 [Online]. Available: 10.1115/1.4027609.
[227] W. Zhang et al., 'A new topology optimization approach based on Moving Morphable Components (MMC) and the ersatz material model', *Struct Multidisc Optim*, vol. 53, no. 6, pp. 1243–1260, Jun. 2016 [Online]. Available: 10.1007/s00158-015-1372-3.
[228] W. Zhang et al., 'A new three-dimensional topology optimization method based on moving morphable components (MMCs)', *Comput Mech*, vol. 59, no. 4, pp. 647–665, Apr. 2017 [Online]. Available:

10.1007/s00466-016-1365-0.
[229] J. Sun et al., ‘Topology Optimization of a Three-Dimensional Flexible Multibody System Via Moving Morphable Components’, *Journal of Computational and Nonlinear Dynamics*, vol. 13, no. 2, p. 021010, Feb. 2018 [Online]. Available: 10.1115/1.4038142.
[230] T. Alam and M.-H. Kim, ‘A comprehensive review on single phase heat transfer enhancement techniques in heat exchanger applications’, *Renewable and Sustainable Energy Reviews*, vol. 81, pp. 813–839, Jan. 2018 [Online]. Available: 10.1016/j.rser.2017.08.060.
[231] P. Pongsoi et al., ‘Heat transfer and flow characteristics of spiral fin-and-tube heat exchangers: A review’, *International Journal of Heat and Mass Transfer*, vol. 79, pp. 417–431, Dec. 2014 [Online]. Available: 10.1016/j.ijheatmasstransfer.2014.07.072.
[232] A. A. Bhuiyan and A. K. M. S. Islam, ‘Thermal and hydraulic performance of finned-tube heat exchangers under different flow ranges: A review on modeling and experiment’, *International Journal of Heat and Mass Transfer*, vol. 101, pp. 38–59, Oct. 2016 [Online]. Available: 10.1016/j.ijheatmasstransfer.2016.05.022.
[233] M. M. Abu-Khader, ‘Plate heat exchangers: Recent advances’, *Renewable and Sustainable Energy Reviews*, vol. 16, no. 4, pp. 1883–1891, May 2012 [Online]. Available: 10.1016/j.rser.2012.01.009.
[234] L. Wang et al., *Plate heat exchangers: design, applications and performance*. Southampton: WIT Press, 2007.
[235] E. M. Sparrow and S. H. Lin, ‘Heat-transfer characteristics of polygonal and plate fins’, *International Journal of Heat and Mass Transfer*, vol. 7, no. 8, pp. 951–953, Aug. 1964 [Online]. Available: 10.1016/0017-9310(64)90150-4.
[236] H. Zabronsky, ‘Temperature Distribution and Efficiency of a Heat Exchanger Using Square Fins on Round Tubes’, *Journal of Applied Mechanics*, vol. 22, no. 1, pp. 119–122, Mar. 1955 [Online]. Available: 10.1115/1.4010981.
[237] J.-Y. Jang et al., ‘The thermal-hydraulic characteristics of staggered circular finned-tube heat exchangers under dry and dehumidifying conditions’, *International Journal of Heat and Mass Transfer*, vol. 41, no. 21, pp. 3321–3337, Nov. 1998 [Online]. Available: 10.1016/S0017-9310(98)00037-4.
[238] S. Sanaye and H. Hajabdollahi, ‘Thermal-economic multi-objective optimization of plate fin heat exchanger using genetic algorithm’, *Applied Energy*, vol. 87, no. 6, pp. 1893–1902, Jun. 2010 [Online]. Available: 10.1016/j.apenergy.2009.11.016.
[239] H. Nemati et al., ‘Shape optimisation of air-cooled finned-tube heat exchangers’, *International Journal of Thermal Sciences*, vol. 150, p. 106233, Apr. 2020 [Online]. Available: 10.1016/j.ijthermalsci.2019.106233.
[240] L. Luo, Ed., *Heat and Mass Transfer Intensification and Shape Optimization*. London: Springer London, 2013[Online]. Availablehttp://link.springer.com/10.1007/978-1-4471-4742-8[Accessed: 6November2021].
[241] M. Yang et al., ‘Experimental study on single-phase hybrid microchannel cooling using HFE-7100 for liquid-cooled chips’, *International Journal of Heat and Mass Transfer*, vol. 160, p. 120230, Oct. 2020 [Online]. Available: 10.1016/j.ijheatmasstransfer.2020.120230.
[242] T. Dbouk, ‘A review about the engineering design of optimal heat transfer systems using topology optimization’, *Applied Thermal Engineering*, vol. 112, pp. 841–854, Feb. 2017 [Online]. Available: 10.1016/j.applthermaleng.2016.10.134.
[243] J. Alexandersen and C. S. Andreasen, ‘A Review of Topology Optimisation for Fluid-Based Problems’, *Fluids*, vol. 5, no. 1, p. 29, Mar. 2020 [Online]. Available: 10.3390/fluids5010029.
[244] P. Papazoglou, ‘Topology Optimization of Heat Exchangers’, Master’s thesis, Delft University of Technology, 2015.
[245] R. Tawk et al., ‘Topology optimization of heat and mass transfer problems in two fluids—one solid domains’, *Numerical Heat Transfer, Part B: Fundamentals*, vol. 76, no. 3, pp. 130–151, Sep. 2019 [Online]. Available: 10.1080/10407790.2019.1644919.
[246] H. Kobayashi et al., ‘Topology design of two-fluid heat exchange’, *Struct Multidisc Optim*, vol. 63, no. 2, pp. 821–834, Feb. 2021 [Online]. Available: 10.1007/s00158-020-02736-8.

[247] W.-Q. Tao et al., ‘A comprehensive review and comparison on heatline concept and field synergy principle’, *International Journal of Heat and Mass Transfer*, vol. 135, pp. 436–459, Jun. 2019 [Online]. Available: 10.1016/j.ijheatmasstransfer.2019.01.143.

[248] M. P. Bendsøe, ‘Optimal shape design as a material distribution problem’, *Structural Optimization*, vol. 1, no. 4, pp. 193–202, Dec. 1989 [Online]. Available: 10.1007/BF01650949.

[249] K. Thulukkanam, *Heat Exchanger Design Handbook*, 0 ed. CRC Press, 2013[Online]. Availablehttps://www.taylorfrancis.com/books/9781439842133[Accessed: 12February2023].

[250] M. B. Giles and N. A. Pierce, ‘An Introduction to the Adjoint Approach to Design’, *Flow, Turbulence and Combustion*, vol. 65, no. 3/4, pp. 393–415, 2000 [Online]. Available: 10.1023/A:1011430410075.

[251] K. Svanberg, ‘A Class of Globally Convergent Optimization Methods Based on Conservative Convex Separable Approximations’, *SIAM J. Optim.*, vol. 12, no. 2, pp. 555–573, Jan. 2002 [Online]. Available: 10.1137/S1052623499362822.

[252] O. Sigmund and J. Petersson, ‘Numerical instabilities in topology optimization: A survey on procedures dealing with checkerboards, mesh-dependencies and local minima’, *Structural Optimization*, vol. 16, no. 1, pp. 68–75, Aug. 1998 [Online]. Available: 10.1007/BF01214002.

[253] B. S. Lazarov and O. Sigmund, ‘Filters in topology optimization based on Helmholtz-type differential equations’, *Int. J. Numer. Meth. Engng.*, vol. 86, no. 6, pp. 765–781, May 2011 [Online]. Available: 10.1002/nme.3072.

[254] F. Wang et al., ‘On projection methods, convergence and robust formulations in topology optimization’, *Struct Multidisc Optim*, vol. 43, no. 6, pp. 767–784, Jun. 2011 [Online]. Available: 10.1007/s00158-010-0602-y.

[255] X. Han et al., ‘Topology optimization for spider web heat sinks for electronic cooling’, *Applied Thermal Engineering*, vol. 195, p. 117154, Aug. 2021 [Online]. Available: 10.1016/j.applthermaleng.2021.117154.

[256] F. A. S. Mota et al., ‘Modeling and Design of Plate Heat Exchanger’, in *Heat Transfer Studies and Applications*, M. S. N. Kazi, Ed. InTech, 2015[Online]. Availablehttp://www.intechopen.com/books/heat-transfer-studies-and-applications/modeling-and-design-of-plate-heat-exchanger[Accessed: 3May2022].

[257] S. Sun et al., ‘3D topology optimization of heat sinks for liquid cooling’, *Applied Thermal Engineering*, vol. 178, p. 115540, Sep. 2020 [Online]. Available: 10.1016/j.applthermaleng.2020.115540.

[258] H. Kobayashi et al., ‘Freeform winglet design of fin-and-tube heat exchangers guided by topology optimization’, *Applied Thermal Engineering*, vol. 161, p. 114020, Oct. 2019 [Online]. Available: 10.1016/j.applthermaleng.2019.114020.

[259] S. B. Dilgen et al., ‘Density based topology optimization of turbulent flow heat transfer systems’, *Struct Multidisc Optim*, vol. 57, no. 5, pp. 1905–1918, May 2018 [Online]. Available: 10.1007/s00158-018-1967-6.

[260] I. B. Celik et al., ‘Procedure for Estimation and Reporting of Uncertainty Due to Discretization in CFD Applications’, *J. Fluids Eng.*, vol. 130, no. 7, p. 078001, 2008 [Online]. Available: 10.1115/1.2960953.

[261] J. R. Welty, Ed., *Fundamentals of momentum, heat, and mass transfer*, 5. ed. Hoboken, NJ: Wiley, 2008.

[262] M. Cavazzuti et al., ‘Compressible Fanno flows in micro-channels: An enhanced quasi-2D numerical model for laminar flows’, *Thermal Science and Engineering Progress*, vol. 10, pp. 10–26, May 2019 [Online]. Available: 10.1016/j.tsep.2019.01.003.

[263] S. Zeng et al., ‘Experimental and numerical investigation of a mini channel forced air heat sink designed by topology optimization’, *International Journal of Heat and Mass Transfer*, vol. 121, pp. 663–679, Jun. 2018 [Online]. Available: 10.1016/j.ijheatmasstransfer.2018.01.039.

[264] R. L. Webb and E. R. G. Eckert, ‘Application of rough surfaces to heat exchanger design’, *International Journal of Heat and Mass Transfer*, vol. 15, no. 9, pp. 1647–1658, Sep. 1972 [Online]. Available: 10.1016/0017-9310(72)90095-6.

[265] Z. Y. Guo et al., ‘A novel concept for convective heat transfer enhancement’, *International Journal of Heat and Mass Transfer*, vol. 41, no. 14, pp. 2221–2225, Jul. 1998 [Online]. Available: 10.1016/S0017-9310(97)00272-X.

[266] W.-Q. Tao et al., ‘Field synergy principle for enhancing convective heat transfer––its extension and

numerical verifications', *International Journal of Heat and Mass Transfer*, vol. 45, no. 18, pp. 3849–3856, Aug. 2002 [Online]. Available: 10.1016/S0017-9310(02)00097-2.

[267] Z. Y. Guo et al., 'The field synergy (coordination) principle and its applications in enhancing single phase convective heat transfer', *International Journal of Heat and Mass Transfer*, vol. 48, no. 9, pp. 1797–1807, Apr. 2005 [Online]. Available: 10.1016/j.ijheatmasstransfer.2004.11.007.

[268] J. Guo et al., 'The application of field synergy number in shell-and-tube heat exchanger optimization design', *Applied Energy*, vol. 86, no. 10, pp. 2079–2087, Oct. 2009 [Online]. Available: 10.1016/j.apenergy.2009.01.013.

[269] T. Zhao et al., 'Irreversibility evaluation for transport processes revisited', *International Journal of Heat and Mass Transfer*, vol. 189, p. 122699, Jun. 2022 [Online]. Available: 10.1016/j.ijheatmasstransfer.2022.122699.

[270] L. C. Høghøj et al., 'Topology optimization of two fluid heat exchangers', *International Journal of Heat and Mass Transfer*, vol. 163, p. 120543, Dec. 2020 [Online]. Available: 10.1016/j.ijheatmasstransfer.2020.120543.

[271] E. M. Dede, 'Optimization and Design of a Multipass Branching Microchannel Heat Sink for Electronics Cooling', *Journal of Electronic Packaging*, vol. 134, no. 4, p. 041001, Dec. 2012 [Online]. Available: 10.1115/1.4007159.

[272] J. H. K. Haertel et al., 'Topology optimization of a pseudo 3D thermofluid heat sink model', *International Journal of Heat and Mass Transfer*, vol. 121, pp. 1073–1088, Jun. 2018 [Online]. Available: 10.1016/j.ijheatmasstransfer.2018.01.078.

[273] C. F. Hvejsel and E. Lund, 'Material interpolation schemes for unified topology and multi-material optimization', *Struct Multidisc Optim*, vol. 43, no. 6, pp. 811–825, Jun. 2011 [Online]. Available: 10.1007/s00158-011-0625-z.

[274] J. Alexandersen et al., 'Topology optimisation for natural convection problems: TOPOLOGY OPTIMISATION FOR NATURAL CONVECTION PROBLEMS', *Int. J. Numer. Meth. Fluids*, vol. 76, no. 10, pp. 699–721, Dec. 2014 [Online]. Available: 10.1002/fld.3954.

[275] 'IAPWS (2016). Revised release on the IAPWS formulation 1995 for the thermodynamic properties of ordinary water substance for general and scientific use.' .

[276] P. E. Gill et al., 'SNOPT: An SQP Algorithm for Large-Scale Constrained Optimization', *SIAM Rev.*, vol. 47, no. 1, pp. 99–131, Jan. 2005 [Online]. Available: 10.1137/S0036144504446096.

[277] A. Wächter and L. T. Biegler, 'On the implementation of an interior-point filter line-search algorithm for large-scale nonlinear programming', *Math. Program.*, vol. 106, no. 1, pp. 25–57, Mar. 2006 [Online]. Available: 10.1007/s10107-004-0559-y.

[278] Y. Hua et al., 'Heat Spreading Effect on the Optimal Geometries of Cooling Structures in A Manifold Heat Sink'. 2023[Online]. Availablehttps://www.ssrn.com/abstract=4625528[Accessed: 8July2024].

[279] 'Thermal and physical properties of the Steel'. [Online]. Availablehttps://matweb.com/search/DataSheet.aspx?MatGUID=ee25302df4b34404b21ad67f8a83e858.

[280] H. S. Dow et al., 'Thermal and electrical properties of silicon nitride substrates', *AIP Advances*, vol. 7, no. 9, p. 095022, Sep. 2017 [Online]. Available: 10.1063/1.4996314.

[281] Y. Zhou et al., 'Development of high-thermal-conductivity silicon nitride ceramics', *Journal of Asian Ceramic Societies*, vol. 3, no. 3, pp. 221–229, Sep. 2015 [Online]. Available: 10.1016/j.jascer.2015.03.003.

[282] 'Thermal physical properties of 304 Stainless Steel'. [Online]. Availablehttps://matweb.com/search/DataSheet.aspx?MatGUID=abc4415b0f8b490387e3c922237098da&ckck=1.

[283] 'Thermal physical properties of Sapphire'. [Online]. Availablehttps://www.guildoptics.com/sapphire-properties/sapphire-properties/.

[284] 'Thermal Physical properties of Copper'. [Online]. Availablehttps://matweb.com/search/DataSheet.aspx?MatGUID=9aebe83845c04c1db5126fada6f76f7e.

[285] 'Thermal physical properties of Polycarbonate'. [Online]. Availablehttps://matweb.com/search/DataSheet.aspx?MatGUID=d16a64a389df424f8e53ed481e77477b&ckck=1.
[286] 'COMSOL Multiphysics® v. 6.1. www.comsol.com. COMSOL AB, Stockholm, Sweden'. .
[287] T. Astarita and G. M. Carlomagno, *Infrared Thermography for Thermo-Fluid-Dynamics*. Berlin, Heidelberg: Springer Berlin Heidelberg, 2013[Online]. Availablehttps://link.springer.com/10.1007/978-3-642-29508-9[Accessed: 29April2024].
[288] 'Crystan Ltd, Sapphire (Al2O3), Crystan Ltd (2019).' [Online]. Availablehttps://www.crystran.co.uk/optical-materials/sapphire-al2o3.
[289] K. E. Kaylegian et al., 'Influence of fatty acid chain length and unsaturation on mid-infrared milk analysis', *Journal of Dairy Science*, vol. 92, no. 6, pp. 2485–2501, Jun. 2009 [Online]. Available: 10.3168/jds.2008-1910.
[290] R. J. Moffat, 'Describing the uncertainties in experimental results', *Experimental Thermal and Fluid Science*, vol. 1, no. 1, pp. 3–17, Jan. 1988 [Online]. Available: 10.1016/0894-1777(88)90043-X.
[291] Y. Hua et al., 'Heat spreading effect on the optimal geometries of cooling structures in a manifold heat sink', *Energy*, vol. 308, p. 132948, Nov. 2024 [Online]. Available: 10.1016/j.energy.2024.132948.

COLLEGE DOCTORAL PAYS DE LA LOIRE | SCIENCES DE L'INGENIERIE ET DES SYSTEMES

Nantes Université

Titre : Optimisation topologique basée sur la méthode de densité des échangeurs de chaleur à plaques

Mots clés : Optimisation topologique, échangeurs de chaleur, mécanique des fluides numérique, approche expérimentale, interprétations physiques.

Résumé: Les échangeurs de chaleur (HX) jouent un rôle essentiel dans divers systèmes énergétiques, ce qui peut grandement influencer leur efficacité globale. Plus récemment, l'intérêt pour l'optimisation topologique (TO) pour les problèmes de transfert de chaleur connaît une croissance rapide, ce qui peut donner lieu à des conceptions thermiques innovantes. Par conséquent, la présente thèse étudie l'utilité du TO basé sur la densité pour les unités HX à double flux avec un domaine de conception étroit, ainsi que la CFD (dynamique des fluides computationnelle) et des vérifications expérimentales. Une conception convergente-divergente (C-D) d'ailettes est acquise à l'aide d'un générateur de topologie (TG), dont l'efficacité peut être prouvée par les simulations CFD, malgré une déficience identifiée dans le champ de vitesse de la topologie dérivée du TG. De plus, après résolution de cette déficience, une nouvelle topologie a été acquise en allouant les solides générés à proximité des limites adiabatiques pour maximiser les performances thermohydrauliques de l'unité HX avec un matériau conducteur modéré. Des approches numériques haute fidélité sont utilisées pour examiner l'efficacité de cette nouvelle conception à travers une analyse comparative avec un cas de référence, et des expériences sont menées pour valider les résultats numériques. Les approches numériques et expérimentales démontrent que l'unité HX dérivée du TO présente les meilleures performances thermohydrauliques, reflétant sa faisabilité en pratique. De plus, des interprétations physiques détaillées sont fournies pour analyser la physique sous-jacente aux topologies obtenues.

Title : Density-based topology optimization of plate heat exchangers

Keywords: Topology optimization, heat exchangers, Computational Fluid dynamics, experimental approach, physical interpretations.

Abstract: Heat exchangers (HXs) play a critical role in various energy systems, which can largely influence their overall efficiency. Most recently, the interest in the topology optimization (TO) for heat transfer problems is growing rapidly, which can derive innovative thermal designs. Therefore, the present thesis investigates the utility of the density-based TO for dual-flow HX unit with narrow design domain, along with CFD (computational fluid dynamics) and experimental verifications. A convergent-divergent (C-D) design of fins is acquired using a topology generator (TG), of which efficacy can be proven by the CFD simulations, despite an identified deficiency in the velocity field of the TG-derived topology. Furthermore, upon the resolution of this deficiency, a new topology has been acquired by allocating the generated solids in proximity to the adiabatic boundaries for maximizing the thermo-hydraulic performance of the HX unit with moderate conductive material. High fidelity numerical approaches are employed to examine the efficacy of this new design through a comparative analysis with a benchmark case, and experiments are conducted to validate the numerical results. Both numerical and experimental approaches demonstrate that the TO-derived HX unit has the best thermo-hydraulic performance, reflecting its feasibility in practice. Furthermore, detailed physical interpretations are delivered to analyze the underlying physics behind the obtained topologies.